Mesoporous Thin-film Materials Studied by Optical Waveguide Spectroscopy

Peic, Antun

Award date:
2009

Awarding institution:
University of Bath

Mesoporous Thin-film Materials Studied by Optical Waveguide Spectroscopy

Antun Peić

A thesis submitted for the degree of Doctor of Philosophy

University of Bath

Department of Chemistry

November 2009

Antun Peić

ABSTRACT

A method was developed to access the interior of light-guiding structures in order to exploit the enhanced sensing potential of the highly confined electromagnetic field distributions, located within the core of a waveguide.

The work presented in this thesis explores therefore the possibilities of optical waveguide spectroscopy utilising transparent mesoporous thin-film waveguides deposited on top of a thin gold layer. These multi-layer assemblies are employed in a prism-coupling attenuated total internal reflection (ATR) configuration. The angular read-out of the reflected light intensity allows label-free detection schemes with high sensitivity to changes of the dielectric environment in the case of the presence of analyte molecules within the probing region.

This optical waveguide spectroscopy technique has been used to study the real-time diffusion of Ruthenium 535-bisTBA (N-719) dye into mesoporous nanocrystalline titanium dioxide films. The porous films were prepared on top of gold substrates and prism coupling was used to create a guided wave in the nanocrystalline film. Dying was carried out by bring the film into contact with a 3×10^{-4} $moldm^{-3}$ dye solution and using optical waveguide spectroscopy to monitor the change in both the refractive index and the extinction coefficient of the nanoporous layer as dye diffused into the porous network. Dye uptake in a 1.27 μm film was slow with the refractive index of the film still increasing after 22 hours.

Mesoporous Thin-Film Materials Studied by Optical Waveguide Spectroscopy

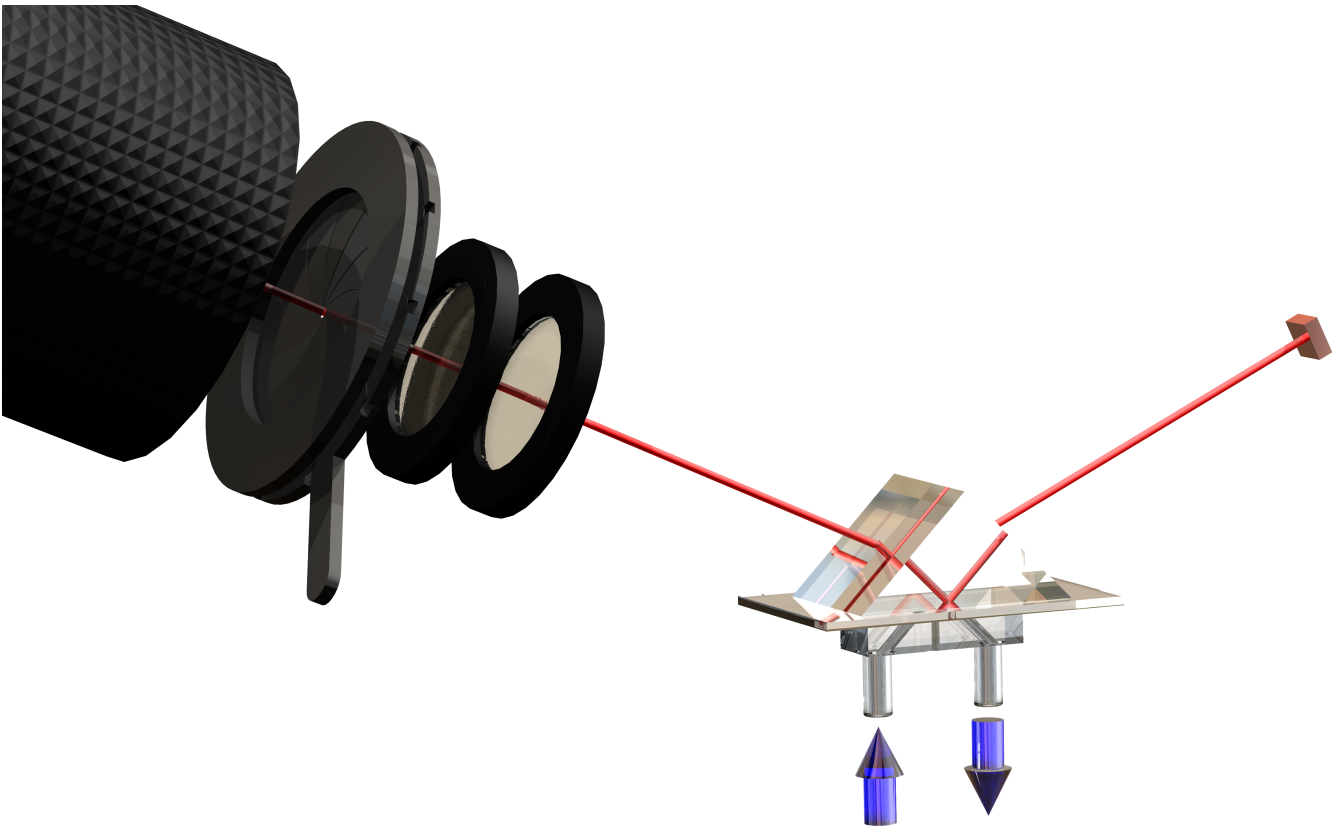

Antun Peić

Mesoporous Thin-film Materials Studied by Optical Waveguide Spectroscopy

Antun Peić

February 17, 2010

A thesis submitted for the degree of Doctor of Philosophy

University of Bath

Department of Chemistry

2009

_____

Antun Peić

Acknowledgements

I am pleased to take this opportunity to thank the many people who helped me to get here.

Firstly, and most importantly, I would like to thank Prof. Dr. Wolfgang Knoll for giving me the great opportunity to work in his group at the Max-Planck-Institute for Polymere Research in Mainz and to learn to be a scientist. I really appreciate the wide range of support, as well as the guidance, while giving me full responsibility for my project, and the advice he has given me, which has been astute and profound.

There are so many people who have been crucial to my motivation while working on this thesis, who have created a very pleasant and scientifically interesting working environment, which was very fruitful for my work. The many hours spent socially after work, the great dinners and nights will truly be missed.

There are several people who I like to thank individually:

Bernhard Menges, for his thorough supervision, for his great scientific guidance and for all the interesting discussions, as well as for the many fruitful meetings, his critical suggestions, and his generous support during the course of my work at the MPIP.

Dr. Toby Jenkins, for opening the great opportunity for me to come to the University of Bath, which was of invaluable significance to me. Whithout him I wonder if I would ever have made it through. I will never forget some of the advices he gave me, the many fruitful discussions, and his generous and special support during the course of my work at the University of Bath. I would also like to thank him for the many kilos of coffee he provided.

Dr. Petra Cameron, for the thorough supervision, the financial support, the very careful proof reading of the manuscript along with the many scientific discussions and suggestions, the great patience and support during the writing of the thesis, and the sushis. She gave me the great opportunity to work in her research group in Bath, while giving me all the support I needed during my stay. I have the utmost respect for her opinions and her abilities as a scientist and also as the person she is.

Furthermore, I would also like to thank the whole group for the support and the friendly environment in the office and the labs.

Last, but not least, I would like to give my thanks to my parents and my brother, who have always been and will always be an important support in my life. Thank you for everything, particularly your great patience and support during the writing of the thesis.

Contents

Nomenclature

DSSC	dye-sensitised solar cell
AFM	atomic force microscopy
OWS	optical waveguide spectroscopy
APCE	absorbed photon-to-current efficiency
RH	relative humidity
ATR	attenuated total reflection
BK7	borosilicate crown glass
CB	conduction band
C	cover medium
CMC	critical micellar concentration
COO	carboxyl group
CRT	cathode-ray tube
DSSC	dye sensitised solar cell
EISA	evaporation induced self assembly
EMA	effective medium approximation
EM	electromagnetic (field)
EMT	Effective Medium Theory
EO	ethylene oxide
eV	electron volt
eV	electron volts
F	(waveguide) film
FTO	fluorine-doped tin oxide
GOWS	grating-coupled optical waveguide spectroscopy
HeNe	Helium-Neon (laser)
IO	integrated optics
IPCE	incident photon-to-current efficiency

IR infrared

IUPAC International Union of Pure and Applied Chemistry

LOT Lens-less Optical Trapping

meso-nc-TiO2 mesoporous nanocrystalline titanium oxide

meso-nc meoporous nanocrystalline

N719 Ruthenium 535 bis-TBA

NIR near-infrared

NR normal reflection

NSOM near-field scanning optical microscopy

OCP open-circuit potential

OR alkoxide

OWG optical waveguide

OWS optical waveguide spectroscopy

PCM Partial Charge Model

PO propylene oxide

QSPR quantitative structure property relation

RH relative humidity

RIBE reactive ion beam etching

RI refractive index

RT room temperature

SEM scanning electron microscopy

SPP surface plasmon polariton

SPR surface plasmon resonance

SP surface plasmon

S substrate

STP standard conditions for temperature and pressure

TEM transmission electron microscopy

TEOH titanium(IV) ethoxide

TE transverse electric (polarisation)

TiPO titanium(IV) iso-propoxide

TIR-FM total internal reflection fluorescence microscope

TIR	total internal reflection
TM	transverse magnetic (polarisation)
TnBO	titanium(IV) n-butoxide
TnEO	titanium(IV) ethoxide
UV	ultraviolet
VB	valence band
Vis	visible
XRD	x-ray powder diffraction

List of Symbols

A	amplitude
$\mathbf{B}$	magnetic flux density
c	phase velocity in empty space
$\mathbf{D}$	electric displacement field
D	diffusion coefficient
d	thickness
D_{eff}	effective diffusion constant
D_s	self-diffusion coefficient
D_t	transport diffusion coefficient
$\mathbf{E}$	electrical field strength
$\mathbf{E}_0$	electric field amplitude
e	elementary charge
$erfc(x)$	error function
$\mathbf{F}$	Lorentz force
G	grating vector
h	(groove) depth
$\mathbf{H}$	magnetic field strength
H^+	proton
H_2O	water
I	(evanescent field) intensity
$Im\{\}$	imaginary part
$\mathbf{j}$	current density
$\mathbf{k}$	wave vector
L	propagation length
L_{eff}	effective trajectory
L_s	direct path
l	path length
l_p	decay length / penetration depth
m	mode order
m_e	electron mass
N	effective refractive index
N_A	Avogadro's number
$\bar{N_j}$	particle density
n	real part of refractive index
$\tilde{n}$	complex refractive index

n_e	electron density
OH^-	hydroxyl
P	(light) power
$\mathbf{P_j}$	propagation matrix
p	porosity
p_j	filling factor
$\mathbf{Q}$	Fresnel matrix
q	geometry factor
q_m	matrix factor
R	reflectivity
$Re\{\}$	real part
$\mathbf{r}$	denoting the position vector
r_{light}	reflection coefficient
s	screening factor
$\mathbf{T}$	transfer matrix
T_D	tortuousity
t	time
t_{light}	transmission coefficient
V	(total) volume
V_j	volume fraction
$\mathbf{v}$	particle velocity
Γ_{rad}	radiation damping
Δn	refractive index change
ΔT	temperature difference
$\Delta\theta$	angular shift
Λ	grating constant (groove spacing)
α	polarisability
β	(complex) propagation constant
δ	constrictivity
ϵ	molar absorption coefficient
ε	relative permittivity / real part of dielectric function
ε''	imaginary part of complex dielectric constant
ε'	real part of complex dielectric constant

ε_0	electric permittivity of free space
$\varepsilon(\omega)$	material's electric permeability
$\tilde{\varepsilon}(\omega)$	complex dielectric function
$\zeta(x)$	profile curve
θ_B	Brewster angle
$\theta_{critical}$	critical angle
θ_i	angle of incidence
θ_r	angle of reflection
θ_t	angle of transmission
κ	imaginary part of refractive index / extinction coefficient
λ	wavelength
μ_0	magnetic permeability of free space
$\mu(\omega)$	material's magnetic permeability
v_p	phase velocity in a given medium
ρ	charge density
ρ_q	charge on particle
σ	specific electric conductivity
σ_a	absorption cross section
τ	collision time
τ_i	internal transmittance
φ	surface concentration
ω	angular frequency
ω_p	plasma frequency
∇	Nabla symbol / vector differential operator 'del'
Ø	diameter

Chapter 1

Introduction

Contents

1.1 Introduction

The accessible functionality of any material is determined by the interplay of its elementary constituents. Functional materials often consist of fairly complex systems, thus new properties appear that are not observed for each individual component separately. While it is commonly known that subatomic particles like, e.g. electrons and nuclei, form atoms (sub-ångstrom scale), which again form molecules (ångstrom scale) which may be arranged into polymers (early nanometre scale), this is just a little insight into the potential of assemblies or of large multifunctional objects (e.g. copolymers of complex architecture). Whereas nature virtuously handles the full range of "materials" on the length scale from femtometres (a unit of measure for subatomic particles; a proton has a diameter of about 1.6 to 1.7 femtometres) to parsecs (a unit of measure for interstellar space that is equal to 3.26 light-years), mankind is somewhat limited to the length scale between subatomic particles and the size of our planet (equatorial radius 6,378.1 km). Even though the accessible range to mankind is drastically reduced, only a little fraction thereof is available to us for manipulation. Within this limited range, again, a particularly interesting length scale exists; thinking of the nanoscopic organisation of matter. Using at this point the example of life as the most impressive and complex feature of organised matter, it appears that nature strictly restricts the size of any life form (in the definition of life as we know it) to a minimum size within nanoscopic to microscopic dimension. It is exactly this particular length scale, which seems to bear so much importance that is so promising and just being explored.

Due to rapid progress in various scientific and technological disciplines new methods and materials become accessible and new phenomena are being exploited and may help to advance our state of knowledge, regarding fundamental insights in nature's "construction plan". Besides the fundamental aspects, inherent to the pursuit for higher states of knowledge, as scientists we have also always been interested in designing practical applications of scientific advances in the form of devices and technological methodologies. However, scientific progress generally comes about as a result of symbiotic interplay of several advances in various (sub)disciplines. Therefore, many ongoing studies are focusing on copious approaches to control and characterise matter on an atomic and molecular scale, whereas this exploration of the nanometre regime is intuitively associated with the phenomenon of visible light ($\lambda = 400 - 700nm$), and its properties as the tool for investigation. As a consequence, a whole new scientific field of nano-photonics or nano-optics arouse, with the aim to study the behaviour of light or the interaction of light with particles or substances at sub-wavelength length scales. Within this advancing area,

again, the main focus of research is on nano-optical and nano-photonic systems where optical excitation of a device leads to useful processes such as light-energy conversion in the form of electricity in solar cells, photochromic and photoelectrochromic systems for digital display, smart windows that on one hand can control the amount of light passing through and also assist indirectly in cost-saving measures, and of course optical sensors for the detection of trace quantities of chemicals, just to mention a few.

Due to extensive research on the sub-nanometre level, more precisely in molecular electronics, it was revealed how photons are used as power to make a system work and as input/output signals to be processed. In nature, vision is based on a light-induced chemical reaction[87,93], and in the process of photosynthesis light harvesting takes place by migration of the excitation energy within molecular arrays.[29,66] This photosystem successfully provides all life directly or indirectly with energy[19], however, it is just one example of how nature applies the precise spatial assembly of a functional molecular machine for its needs.

In artificial systems, on the other hand, controlled manipulation of photons has been achieved by molecules, and used to transmit (molecular wires[15]), harvest (antenna systems[12,34,26,24,36]), store (photochromic systems[32]), disclose (fluorescent sensors[73]), and process (switching[91] and logic[72,80,64]elaboration) information. In most cases, however, the experiments have been performed on bulk systems. Until now little attention has been devoted to the development of nano-structured photonic technology, implicating also the molecular level. One reason is that the wavelength of light in the IR, visible, and even UV spectral regions is by far greater than the molecular dimensions of interest, so that spatially selective detection or excitation of a specific molecule in a supramolecular arrangement is prevented. Traditional microscopy makes use of diffractive elements to focus light tightly in order to increase resolution. But because of the diffraction limit (also known as the Rayleigh Criterion), propagating light may be focused to a spot with a minimum diameter of roughly half the wavelength of the light. Thus, even with diffraction-limited confocal microscopy, the maximum resolution obtainable is on the order of a couple of hundred nanometres. The scientific and industrial communities are becoming more interested in the characterisation of materials and phenomena on the scale of a few nanometres, so alternative techniques must be utilised. Such technologies in the realm of nano-optics today include near-field scanning optical microscopy (NSOM), photoassisted scanning tunnelling microscopy, surface plasmon optics, and optical waveguide spectroscopy. Devices for guiding electromagnetic radiations on a scale below the diffraction limit are also needed for future design of molecular-level optical circuits. Progress in near-field

optical techniques[33,27,65,94,56] and electromagnetic energy transport in metal nanoparticle plasmon waveguides[47] might open this possibility. It should also be noted that energy transfer from a donor to an acceptor can occur along a molecular wire "waveguide" without any problem.[71]

However, the design of these new nano-optical devices requires ability to organise matter (e.g. molecules and inorganic nano building blocks) on a nanometric scale, with fine control on their arrangement: distribution, mobility, spectral and redox properties.

Even though scientists have successfully adopted the mechanism of photosynthesis from nature and implemented the principles of that photon-to-current conversion mechanism in the promising development of the dye sensitised solar cell (DSSC), materials science is not yet as far advanced to efficiently utilise the evolutionary developments present everywhere in nature. This approach of photon harvesting, the working principle of a DSSC, does not involve a charge-recombination process between electrons and holes because electrons are only injected from the photo-sensitiser molecules into the semiconductor electrode and a hole is not formed in the valence band of the semiconductor, as in classical photovoltaics. In addition, charge transport takes place in the semiconductor film, which is separated from the photon absorption site (i.e. the photo-sensitiser); thus, effective charge separation is expected. The approach of sensitising a suitable material is similar to the mechanism for photosynthesis in nature, in which chlorophyll functions as the photo-sensitiser and charge transport occurs in the membrane.

The key to successful exploitation of nature's knowledge, in order to harvest energy at maximum efficiency might be found in nanocomposite thin films which comprise at least two phases. The general characteristics of nanocomposite materials as a host material with another material homogeneously embedded in it, with one (or both) of these materials having a characteristic length scale of $1\text{–}100nm$. With this new advances also new techniques are needed to support rapid development with precise and reliable information about manufacturing, operating and quality control of the final device. Nano-optics can operate below the diffraction limit, thus offer suitable (sensing) methods for this task.

Nanocomposite thin films also represent a new class of materials which exhibit special mechanical[86,61,85], electronic[51,57] magnetic[52] and optical properties due to their size-dependent phenomena[3,11]. Nowadays increasing interest is attracted by nanocomposite films due to the endless possibilities of synthesising these materials of unique properties. Whereas the properties of two- and multiphase thin films often significantly exceed what is expected by the rule of mixture.

A particular interesting class of nanocomposite materials, again, is represented by meso-

porous materials, especially in the form of thin and ultra-thin films. Thus mesoporous materials in general, and mesoporous oxides in particular, are good host material for label-free optical (bio-)chemical sensing applications because their nano-optical readout properties (e.g. photo-luminescence, reflectance) are highly sensitive to the presence of chemical and biological species inside the pores[78]. Starting from Si-based approaches, nowadays a broad variety of mesoporous metal oxides is synthetically available. Especially mesoporous titanium oxide, a form of titanium oxide with unique properties, distinct from those of crystalline, micro-crystalline, or amorphous titanium oxide, has gained great attention as promising nano-structured electrode in DSSCs. The optical properties of such composite materials comprise an interesting field of study *per se*, since their properties may differ significantly from those of the individual constituents (i.e. titanium dioxide and void-filling material). Due to this fact it is conceivable that materials may be designed with properties meeting a set of desirable conditions. A key advantage of such an approach is that the target species is confined to a three-dimensional region with dimensions on the same scale as the target itself, which, again, fulfills the prerequisite for an effective medium approach. It has been shown that porous metal oxides can be used as a base material for passive or active optical devices like Bragg reflectors, Fabry–Perrot cavities[18], Bragg mirrors[74], rugate filters[17], planar waveguides[35] and micro-cavities[13,59,58] have been experimentally demonstrated for the detection of toxins[75], DNA[13], and proteins[58,18]. Because of its porous nature, the refractive index of such porous structures is lower than that of bulk material (if the void-filling material has a lower refractive index than the matrix). The capture of biological or chemical molecules inside the pore volume changes the composite refractive index of the porous oxide structures, thus causing a shift in the light coupling condition (e.g. surface plasmon resonance or waveguide modes) thus change the reflectance spectra when nano-optical methods are used. The composite refractive index of a porous layer is, again, related to its porosity by the Bruggeman effective medium model[82]. On this basis the principles of optical waveguide spectroscopy can be applied to monitor dye-sensitisation of a mesoporous DSSC electrode film *in-situ*. This new concept was developed by the author in the frame of this thesis and is presented in the following chapters.

In this chapter, an overview is given on preparatory work done on theoretical considerations regarding the design of a mesoporous thin film for waveguide sensor application. Furthermore, the general benefits behind the idea of a mesoporous waveguide structure, applied as optical sensor, will be demonstrated.

First the general sensing probabilities of bulk optical slab waveguides are elucidated before

being compared with porous waveguide films. Also the analysis of the field confinement of the applied guided light and accordingly obtained reflectivity spectra is explained in detail, with emphasis on the characteristic read-out features which are used for characterisation of the mesoporous thin-films as well as the features drawn on for sensing purposes.

1.2 Optical Waveguide Sensor

In general, (integrated) nano-optical sensors often make use of guided optical waves (i.e. EM field modes), in particular of the orthogonally polarised TM and TE modes in thin-film planar waveguides with high refractive index. Inherent to *all* 'direct' waveguide sensors is the principle of sensing their environment at the transducer surface through the change of refractive index of adjacent media (more precisely to say, the optical changes within the volume of their penetration depth into the surrounding medium *via* evanescent field(s) of their resonance feature(s)). This principle of 'direct' signal transduction eliminates the need for any kind of labelling (e.g. fluorescence) and therefore does not require any kind of cumbersome pretreatment of the specimen, contrary to 'indirect' methods. Thus analogy between optical waveguide (OWG) sensors and surface plasmon resonance (SPR) sensors appears obvious, as both applie guided waves (wave-guided modes being guided by total internal reflection (TIR) within in the waveguiding film and the surface plasmons being guided by the metal/dielectric interface) that cause evanescent waves to penetrate into the cover medium. Therefore, such sensors may be summarised by their utilised sensor effect as evanescent field sensors, which are, in general, basically exhibiting the qualities of a differential refractometer, which is measuring the refractive index of the surrounding medium as shown in figure 1.1*(a)*.

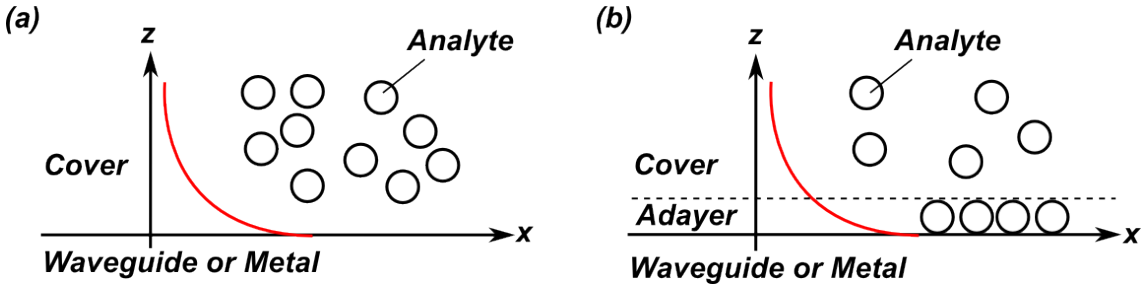

Figure 1.1: Schematic illustration of the basic sensor effect of evanescent field sensor. According to molecular transport (be it diffusion or convection) into the evanescent field of the guided wave a change in refractive index will cause a transformation into directly measurable physical qualities, e.g. into reflected light intensity. The left scheme (a) illustrates a change in refractive index of the cover medium Δn_{cover}, whereas the right scheme (b) depicts the formation of an adlayer of a thickness $d_{adlayer}$ and a refractive index $n_{adlayer}$ due to adsorption of molecules on the sensor surface.

If, however, the adsorption of molecules at the surface results in the formation of an adlayer on top of the surface (referring to figure 1.1*(b)*), the optical waveguide sensor shows to

advantage, as it allows for the coherent excitation of both, transverse magnetic (TM) *and* transverse electric (TE) modes and therefore the read-out of more information is possible, whereas the SPR sensor only supports the readout of either $d_{adlayer}$ or $n_{adlayer}$, since only one mode (referred to as surface plasmon, SP) is applied for sensing. More precisely, as a consequence of applying two different polarisation states, multiple modes are available for sensing, thus it is possible to determine both the adlayer thickness *and* the refractive index of the adsorbed or bound species[55,43,42], while analogous measurements with SPR sensors are limited, depending on whether the value for the refractive index or the adlayer thickness, respectively, is assumed.

The EM field is highly sensitive to refractive index changes within its evanescent tail. Nevertheless, the EM field distribution within the optical transducer (and consequently also its evanescent fraction(s)) is also highly dependent on the chosen materials. In other words, the EM field geometry may be adjusted for a given application to a high degree by the choice of the optimum material combination. In the very basic form such an evanescent optical sensor is represented by a planar multi-layer assembly with the possibility to exchange the cover medium, as well as the substrate in order to manipulate the EM field distributions of a given transducer (metal or waveguide layer), and accordingly the evanescent tail which is used for sensing in this 'direct' perturbation concept.

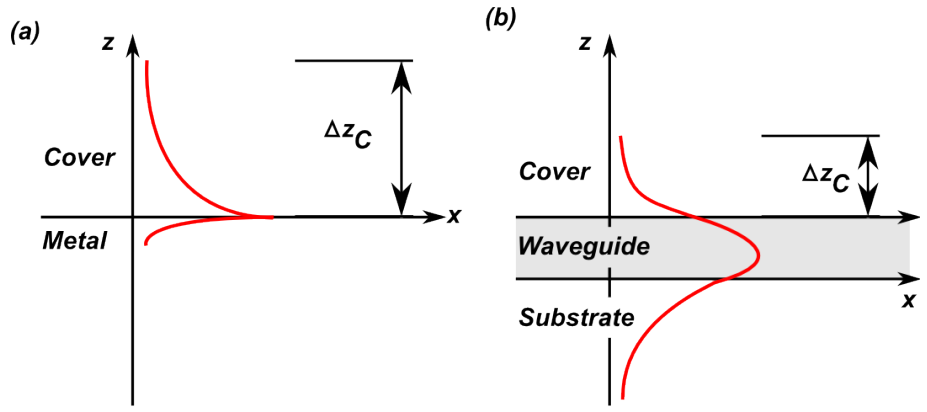

Figure 1.2: Shows schematically the analogous transverse EM field distribution $\mathbf{H_y(z)}$ *for (a) the SPR and (b) the planar OWG within the multi layer structure.*

Typically optical sensing devices are made of inorganic materials in order to assure robustness and stability for both the device in general and the optical transduction mechanism, in particular. In fact, the most frequently applied material groups are represented by metals and their oxides, though recently also partly organic and all-organic designs were demonstrated to suit special applications. Especially attempts for optofluidic devices are focusing on this concepts where fluidic replacement or modification leads to reconfigurable optical systems[62].

Whatever materials are chosen to assemble the device, in the case of a plane waveguide structure it is essential for a good sensor performance that the materials assembly forms an asymmetric refractive index profile around the waveguiding layer, rather than a symmetric geometry[76,68]. The reason for this is given by the light-focusing property of matter in regions with high refractive index, which act as lens-like media[84]. This principle also leads to a historically important rule of waveguide optics, namely, the rule of refractive index, which postulates that a light wave tends to propagate in the region where the refractive index is the largest, or, the wave velocity is the slowest[84]. As a consequence of this, the maximum intensity of the field distribution is allocated throughout the multi-layer system following the refractive index profile. For evanescent optical sensing application this field confinement is designed to predominantly direct towards the cover medium[77], thus increasing the sample volume which is penetrated by the evanescent field, and consequently increasing the amount of potentially probed analyte.

For the detection and characterisation of thin adlayer films, however, it is not favourable to extend the evanescent field as far as possible into the sample solution. On the contrary, it is desired to minimise the disturbing effect of refractive index changes of the bulk solution volume Δn_{cover}, caused by, for example, temperature or concentration fluctuations. For optimised evanescent field sensors, this parasitic effect is 2-3 times smaller in optical waveguide systems as compared to the SPR based sensor[44], because the penetration depth of the guided optical modes is smaller by this factor than those of the surface-bound SPs.

Therefore, it is crucial to tailor the penetration depth of the evanescent field, or rather to adjust the EM field distribution of the guided modes in order to achieve maximised sensitivity for a variety of different sensing schemes. From an optical point of view, several approaches can be used to develop an evanescent field sensing scheme. Figure 1.3 depicts the classical high-sensitivity optical sensing mechanisms, while 1.3*(a)* allowes for the real-time monitoring of adsorbing (or desorbing) molecules at the waveguide surface, whereas the effect in 1.3*(b)* is basically the application of the optical waveguide (OWG) sensor as refractometer. This basic planar waveguide configuration was introduced for the first time for sensing purposes by Tiefenthaler and Lukosz[83] who applied it as a humidity and gas sensor by detecting a change in the refractive index (RI) of the cover medium.

The sensing effects depicted in figure 1.4, on the other hand, represent the sensing principles applied in chemically selective (bio)chemical evanescent field sensors. More precisely, the sensing scheme illustrated in 1.4*(a)* is used as affinity sensor. Such (bio)chemical sensors have to be chemically specific or highly selective in order to precisely detect and quantify the presence of target analyte.

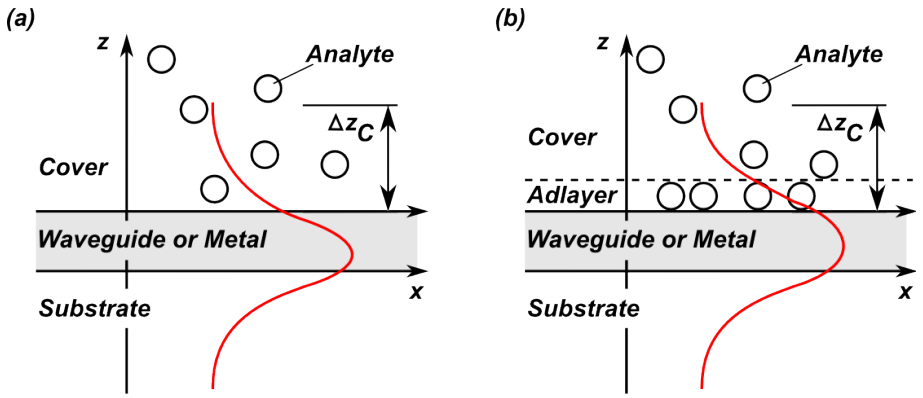

Figure 1.3: Schematic illustration of the classical high sensitivity sensor effects. (a) Sensing mechanism for refractive index changes of the bulk sample volume (measured variable is n_{cover}). (b) Sensing of the formation of an adlayer caused by unspecific molecular adsorption to the surface (measured variables are $n_{adlayer}$ and $d_{adlayer}$). The EM field distribution is shown schematically for the case of OWG sensing, whereas for SPR sensors exclusively the evanescent tail above the metal surface is present.

Affinity sensors are characterised by a chemoresponsive coating consisting of immobilised (e.g. antigen) molecules which attrackt and finally bind the corresponding (e.g. antibody) molecules.

Also the scheme depicted in 1.4*(b)* is used for affinity sensors, but, however, applies a 3D-matrix as chemoresponsive layer of typical thickness in the range of $0.1 - 2\mu m$. The receptor molecules for this technique are immobilised at the inside of the 3D-matrix in order to accumulate analyte molecules within a spatially restricted volume. The target analyte then diffuses into the porous coating, such as a hydrogel, and binds to the receptors. This process leads to a potentially significant increase in RI of the porous adlayer. However, since in most cases the porous matrix is thicker than the penetration depth of the evanescent field, the sensor effect does not take into account the analyte distributed within the sensing matrix which is out of reach for the evanescent field. Therefore, in recent approaches this sensing scheme for evanescent field sensors is optimised by subsequent collapsing of the hydrogel film (e.g. ΔT) after saturation with analyte was reached[25]. As a consequence of matrix-volume shrinkage a thinner layer (amount shrinkage depends on the type of hydrogel but approximate factors of 10 can easily be achieved) with significantly higher refractive index is formed.

The above-described sensing mechanisms are applicable for both SPR and OWG sensors. The SPR system is restricted to metallic surfaces (e.g. Ag, Au, Al) and according surface chemistry, whereas the OWG systems only requires a high refractive index material (relative to its surrounding) and, therefore allowes for rich variety of surface functionalisation.

SPR and OWG sensors, applying sensor effects as illustrated in figures 1.3 and 1.4 are considered to be state-of-the-art label-free technologies for bio-molecular interaction

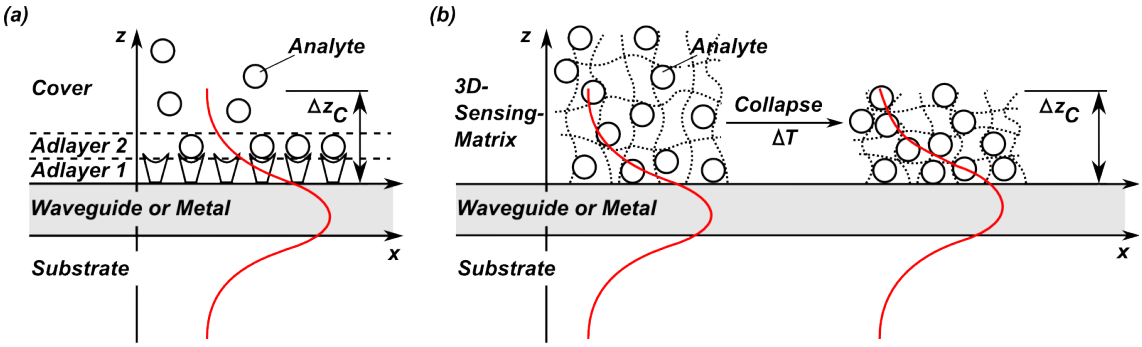

Figure 1.4: Schematic illustration of sensor effects applied in (bio)chemical sensors. (a) Affinity sensing of specific molecular binding to a previously formed (bio)chemically selective target layer and the according formation of a double layer (measured variables are $n_{adlayer1}$, $d_{adlayer1}$, $n_{adlayer2}$, and $d_{adlayer2}$). (b) Sensing of molecular binding to a 3D-binding matrix above the waveguide layer (measured variables are n_{matrix}, d_{matrix}, Δn_{matrix}, and Δd_{matrix}). The EM field distribution is shown schematically for the case of OWG sensing, whereas for SPR sensors exclusively the evanescent tail above the metal surface is present.

studies[28]. Nevertheless, the detection of very small analyte or analyte with very small RI contrast still remains a challenge to SPR sensors, which are restricted to limited surface area, and therefore only allow a finite number of molecules to make up the sensing signal.

For OWG sensors, however, the predominant fraction of the EM field distribution to potentially contribute to the sensor effect, is guided within the high refractive index layer. In order to exploit a greater fraction of this EM field for sensing purposes, the waveguiding layer has to be made accessible for analyte molecules. For this purpose, microporous slab waveguide films have been produced by a variety of different techniques, for example 1D-microporosities (as shown in 1.5*(a)*) have been introduced by electrochemical etching or ion beam drilling, whereas approaches for achieving 3D-microporosity (as shown in 1.5*(a)*) include sputtering techniques, sol-gel synthesis, pulsed laser deposition etc.. The main characteristic of these microporous films is the large internal surface area within the volume of the high RI film. The general sensing mechanism in optical systems in combination with these microporous structures is mainly the RI change, $\Delta n_{waveguide}$, of the waveguiding film introduced by gas adsorption and/or capillary condensation. Consequently, a range of properties such as photo-luminescence[7], impedance changes[6], capacitance[2,1] interference of reflected light[54], and intensity modulation of guided modes[4] are altered when molecules are adsorbed. These parameters can be utilised and measured, hence accordingly be related to interfacial reactions. Alternative approaches made use of slab waveguides with micro-pores fabricated of composite material, which react with the gaseous species and thereby alter the light propagation proportionally due to interactions at these specific centres within the waveguide[21,20].

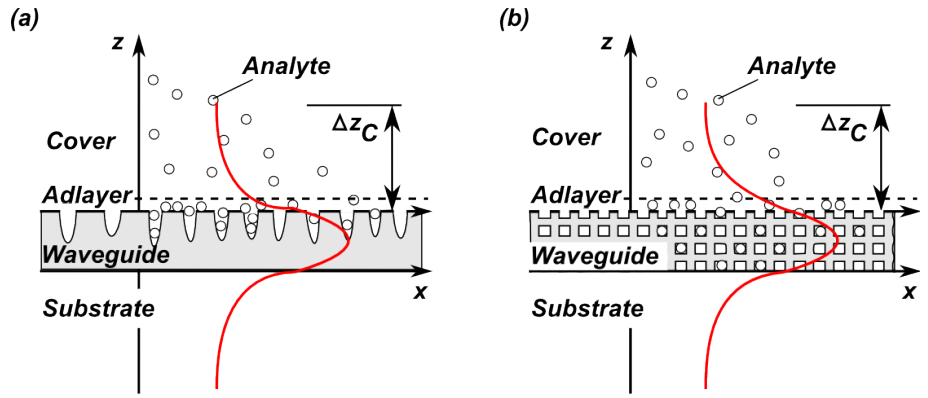

Figure 1.5: Schematic illustration of sensor effects based on sorption of small (gas) molecules in microporous slab waveguide films. The scheme in (a) depicts the application of 1D-micropores for sensing of small (gas) molecules and the eventual formation of an adlayer (measured variables are $\Delta n_{waveguide}$, $d_{adlayer}$, and $n_{adlayer}$). (b) Sensing of small (gas) molecules by adsorption into a 3D-microporous waveguide matrix (measured variables are $\Delta n_{waveguide}$, $d_{adlayer}$, and $n_{adlayer}$). The EM field distribution is shown schematically for the case of OWG sensing.

1.3 Materials for Mesoporous Waveguides

In recent years, mesoporous materials have been extensively studied with the aim to understand and control their inherent properties like the large internal surface area, their functional properties, and the high hydrothermal stability, and make these features accessible for potential applications[5,9,14,16,38,48,88,89,31,30,81,70,90,63]. A classification of nanoporous materials according to their properties or technical characteristics is given in table 1.1

	Polymeric	**Glass**	**Oxide**	**Metal**
Pore Size	Meso-macro	Meso-macro	Micro-meso	Meso-macro
Surface Area	Low	Low	Medium	Low
Porosity	>0.6	0.3-0.6	0.3-0.6	0.1-0.7
Permeability	Low	High	Medium	High
Refractive index	Low	Medium	High	Low (Complex)
Strength	Medium	Strong	Medium	Strong
Thermal Stability	Low	Good	Medium	High
Chemical Stability	Low	High	Very High	High
Cost	Low	High	Medium	Medium
Lifetime	Short	Long	Long	Long

Table 1.1: Classification of nanoporous materials[41]

Among the available nanoporous materials mainly metal oxides, and particularly titania (TiO_2) stimulated immense research activity, as it is a material with numerous of almost unique properties (see table 1.1) desirable for a whole range of applications (e.g. photocatalysis, self-cleaning surfaces, solar cells, catalysis, doping, biomedics, ceramics etc.).

The application of titania in waveguide optical application evolved mainly due to its good

optical properties (highly transparent in the visible range $\lambda > 410nm$, high refractive index $n_{titania}(anatase) = 2.1775$) and its ability to form various stable mesoporous structures (e.g. sol-gel, block copolymer templated, anodised).

1.3.1 Mesoporous sensing matrix

While microporous materials are generally restricted to the adsorption of small molecules, the pore size of mesoporous films allowes for waveguides that can be adjusted to accommodate (bio-)molecules in the size range of approximately $1 - 100nm$. Porous materials are classified into several kinds by their size. The definition of pore size according to the International Union of Pure and Applied Chemistry (IUPAC) is that microporous materials have pore diameters of less than $2nm$ and macroporous materials have pore diameters of greater than $50nm$; the pore size for mesoporous media, by definition, lies typically between 2 and $50nm$, This deinition is somewhat in conflict with the definition of nanoscale objects. The term nanoporous will therefore only be used within this thesis to relate to porous materials, typically having large porosities (> 0.4), and pore diameters between $1 - 100nm$.

As a consequence of the very large internal surface area of porous waveguide materials, those sensors which incorporate nanoporous materials accomplish higher sensitivities due to an increased interaction with the guided EM fields, compared to aforementioned surface-sensitive examples where various surface interactions and/or coatings are used. Certainly, the theoretical sensitivity can be enhanced by the application of porous waveguides, however, various factors affecting adsorption have to be considered, in particular regarding specific surface area and pore diameter as well as external influences from ambient water (relative humidity (RH)) and temperature. In a first approach, considering the range of all sub-groups of nanoporous materials, the molecular adsorption capacity in a microporous material proportionally depends on the adsorbent surface area. But, since micropores (by definition) do not extend a pore diameter of $2nm$, the molecular size of adsorbing species has to be much smaller to achieve quick diffusion inside the pore volume, in order to avoid size exclusion effects but rather to reach the adsorption sites and finally the maximum adsorption capacity of the pore volume.

Another important factor (besides the pore diameter) to be taken into account for the optimum design of a nanoporous waveguide sensor is the influence of the molecular architecture of the analyte (i.e. size and volume and functional groups present in the molecules, e.g. amine, alcohol, acid halogen etc.). Molecules may therefore introduce certain degrees of polarisation, causing interference with the sensing mechanism. It

is known that adsorption parameters are significantly influenced by the quantitative structure property relation (QSPR)[8,79,60]. A mixture of different molecules, again, results in an adsorption competition between the molecules, and therefore reduces the overall adsorption capacity compared to the pure analyte. The situation is comparable to the presence of ambient water (RH) which is also competing for adsorption sites with the adsorbate. In other words this is to say, a high humidity level has in most cases parasitic effects on the sensor effect.

Bearing in mind the above listed qualities, a reasonably universally applicable nanoporous waveguide sensor should posses large pores (meso-scale $2 - 50nm$) and offer large pore volume and large internal surface area. Nevertheless, it has to be composed of a material with high refractive index (at the utilised wavelength of interrogating light) in order to successfully confine light into guided modes, all this despite the great fraction of pore volume which decrease the average refractive index according to the (lower) refractive index of the void-filling material.

Microporous materials, as listed above, are widely-used in many technological processes (e.g. purification, chromatography) that involve a liquid/solid interface. The efficiency of these processes is mainly determined by the utilised materials (i.e. surface chemistry) and structural properties (i.e. pore size, pore size distribution, spatial organisation), whereas the pore size and the surface chemistry predominantly affect the overall accessibility of the pore space and thermodynamic parameters (i.e. adsorption energy and affinity), while the pore size distribution and the spatial arrangement of the pores (i.e. interconnectivity, tortuousity, and their geometrical shape) have pronounced impact on the kinetics of adsorption processes.

For the purpose of designing a versatile porous waveguide sensor it also has to be accounted for the applicability in different surrounding media, especially in liquids, be they aqueous or of other nature. While adsorption from gaseous phase is relatively straightforward, in this case of liquid/solid interfaces adsorption phenomena become generally more complex[67]. The problem of competing adsorption processes was already mentioned, however, in the case of aqueous solutions, the circumstances are extremely complicated, since the reactivity of water depends on the pH and according formation of various concentrations of its inherent constituents (H_2O, H^+, and OH^-). In the (common) case of the additional present of an electrolyte already six components are present in the solution that actively influence the adsorption process.

Also the formation of a surface charge due to the reactivity of water molecules with many surfaces, its conditions and progression as a function of pH, ionic strength and

temperature remain a challenge since these properties have not been studied for porous materials to such an extend as for the case of bulk films[45].

The variability (and complexity) of analyte molecules, involved in adsorption processes at liquid/solid interfaces has indeed also to be considered. Therefore, in order to allow application on a broad range of analyte, from simple organic molecules (in particular interesting in chromatographic applications) to large and multi functional (macro)molecules, good knowledge of the surface chemistry of the porous material is crucial to understand its adsorption behaviour.

Particularly interesting is the utilisation of the mesoporous OWG sensing concept as a nano-optical tool for *in-situ* characterisation in the emerging field of DSSCs, in order to fully understand the processes intrinsic to energy conversion on the (sub-)nano-scale.

1.4 Mesoporous Waveguide Sensor Analysis

In the following the general optical properties of thin film materials with relevance for application in DSSCs, i.e. transparent porotrode (mesoporous electrode) will be discussed, which are inhomogeneous on the nanometre scale. Particular emphasis will be given to the specific optical behaviour of these mesoporous (non-metallic) structures, which is controlled by pore shape, pore size, and the pore distribution. When the refractive indices, or alternatively, the dielectric functions of the constituent materials are given, the influence of these spatial parameters on the optical properties may be understood in terms of the Effective Medium Theory (EMT). More precisely, in this present work, the EMT approach introduced by Bruggeman is applied, which provides a quantitative description to the optical behaviour of such systems, no matter whether the pore/matter arrangement is preferably one-, two-, or three-dimensional or of any order in particular. This approach is well-qualified for the presented case of mesoporous titania films as long as one phase is that of spherical shape and dispersed at a ratio of nearly $1:1$ in the other medium. As practical examples, in later sections, mesoporous titania films in different environments will be discussed.

The pore diameter of mesoporous titania films is much smaller than the wavelength of light used for the experiments in this presented thesis ($\lambda_{HeNe} = 632.8nm$). Therefore, the porous thin-film waveguides can be treated as an effective medium whose refractive index is a weighted average of the refractive index of the matrix material (titania in its anatase phase) and the refractive index of the material inside the pores at the time. When molecules are bound inside the pores, the resulting composite refractive index of the

mesoporous waveguide increases and correspondingly changes the optical properties of the waveguide. In order to achieve the largest sensing response for a given concentration of target material, the pores should be large enough to permit infiltration, but small enough to ensure a large refractive index change when air or water in the pores is partially replaced by the target material.

In this work, the performance of the mesoporous titanium dioxide waveguide sensor is demonstrated with the focus on adsorption studies, relevant for efficient DSSC production, operation and *in-situ* investigation of those processes.

1.4.1 Effective Medium Theory

Concerning the refractive index of a mesoporous film, as it is a monotonic function of density, it is naturally to assume that the optical constants of the mixture represent some kind of superposition of the optical constants of their constituents. Assuming further that each component occupies a certain volume fraction of the material, and this volume fraction V_j determines the filling factor p_j of the material *via*:

$$p_j \equiv \frac{V_j}{V} \tag{1.1}$$

where V is the volume occupied by the whole mixture. It becomes obvious that

$$\sum_j p_j = 1 \tag{1.2}$$

Consequently, the resulting dielectric response of the composite material depends on its composition, i.e. the volume fractions or filling factor of the individual constituents, besides their inherent material characteristics. Mesoporous nanocrystalline titanium oxide is therefore a form of titanium oxide with unique properties, distinct from those of crystalline, micro-crystalline, or amorphous titanium oxide. Its properties result from the composition of the two composites it consists of, namely titanium oxide nanocrystals and voids. Each constituent is present in the whole in spatial dimensions large enough that it may be described by its bulk optical properties. At the same time the typical structure dimensions and spacings are much smaller than an optical wavelength applied to the film, so that the composite may be described as a bulk film by effective optical parameters which are related to the constituent parameters.

Even if these films appear macroscopically homogeneous, it is well known that the UV/Vis optical properties of thin films are significantly affected by inhomogeneities on the micro-

structure, such as disordered regions, grain boundaries and voids. The macroscopic dielectric response of a heterogeneous thin film is therefore connected in an intimate way with the compositional and micro-structural parameters that determine its other physical properties. Therefore, the quantitative description of the macroscopic dielectric function ε of a heterogeneous material in terms of its composition and meso-structure can be given by combining the known individual dielectric responses of the constituents in an effective medium model, which in effect defines a uniform, prototypical composite structure with a dielectric response that is, on average, equivalent to ε. The principal idea is illustrated in figure 1.6.

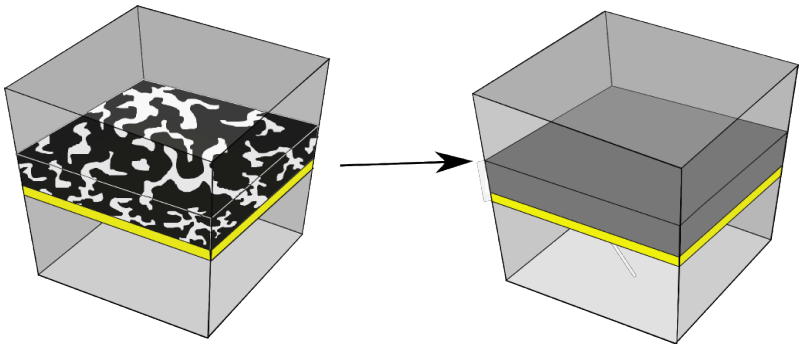

Figure 1.6: Illustration of the heterogeneous two-component structure of a mesoporous waveguide material (left), and the corresponding effective medium model (right), which in effect defines a uniform, prototypical composite structure with a dielectric response that is given by combining the known individual dielectric responses of the constituents. Given that the dimensions of the pore structure $d \ll \lambda$, the EMT model effectively describes the optical parameters of porous materials equivalent to as they are seen by the probing light.

Effective-medium theory (EMT) has been a tool for the evaluation of the optical properties of composite media for a long time. The main objective is the characterisation of properties of composite systems from the known macroscopic variables of its constituents (i.e. bulk material dielectric constants, domain morphology and volume fractions).

The simplest approach for application in the optical regime, dating back to 1904, was derived by Maxwell-Garnett[50,49] and is a replication of the Clausius-Mossotti formula. In the 1930s the more recent Bruggeman theory was developed[10]. The validity of the different approaches to predict the optical properties of composite materials has been discussed frequently. Reviews concerning the subject and its elaboration can be found, for instance, in[92] and[23,22].

1.4.2 Two-component medium

For a two-component medium the EMT approach is derived following the Lorentz-Lorenz equation (also known as the Clausius–Mossotti relation and Maxwell's formula), which relates the refractive index of a substance to its polarisability.

$$\frac{\varepsilon - 1}{\varepsilon + 2} = \frac{4\pi}{3} n\alpha \tag{1.3}$$

The simplest assumption to estimate the effective dielectric function ε of a heterogeneous two-component medium is one in which the points of a given medium are randomly assigned to different polarisabilities α_a and α_b.

$$\frac{\varepsilon - 1}{\varepsilon + 2} = \frac{4\pi}{3} (n_a\alpha_a + n_b\alpha_b) \tag{1.4}$$

This expression, however, involves micro-structural parameters which can not be directly measured by means of optical methodology. If, on the other hand, the individual dielectric functions ε_a and ε_b of phase a and b, respectively, are known in their pure forms are available, then equation 1.3 can be used to rewrite equation 1.4 as

$$\frac{\varepsilon - 1}{\varepsilon + 2} = f_a \frac{\varepsilon_a - 1}{\varepsilon_a + 2} + f_b \frac{\varepsilon_b - 1}{\varepsilon_b + 2} \tag{1.5}$$

where $f_{a,b} = \frac{n_{a,b}}{n_a + n_b}$ are the volume fractions of the phases a and b. This is the Lorentz-Lorenz effective medium expression[40,39].

1.4.3 The Maxwell-Garnett Theory

According to Maxwell-Garnett theory it is assumed that inclusion of particles in dielectric medium are randomly dispersed. Taking the particles to be spherical in shape and the inclusion radius much smaller than the typical spacing between inclusions which in turn is much smaller than an optical wave length. The dielectric constant of the composites is determined.

The Clausius-Mossotti equation can be modified to describe spherical nanoparticles that are in a host matrix, supposing that the separate phases a and b are not mixed on an atomic scale but rather consist of regions large enough to possess their own dielectric identity. Then the assumption of vacuum ($\varepsilon = 1$) as the host medium in which to embed points is not good. Supposing that the host dielectric function is ε_h, then equation 1.5 becomes

$$\frac{\varepsilon - \varepsilon_h}{\varepsilon + 2\varepsilon_h} = f_a \frac{\varepsilon_a - \varepsilon_h}{\varepsilon_a + 2\varepsilon_h} + f_b \frac{\varepsilon_b - \varepsilon_h}{\varepsilon_b + 2\varepsilon_h} \tag{1.6}$$

Specifically, if b represents the dilute phase then $\varepsilon_h = \varepsilon_a$, in which case

$$\frac{\varepsilon - \varepsilon_a}{\varepsilon + 2\varepsilon_a} = f_b \frac{\varepsilon_b - \varepsilon_a}{\varepsilon_b + 2\varepsilon_a} \tag{1.7}$$

Equation 1.6 and the alternative equation obtained with $\varepsilon_h = \varepsilon_b$ are the Maxwell-Garnett effective medium expressions[49].

Maxwell Garnett theory can be generalised for non-spherical geometry also by generalising the equation by a screening factor s.

$$\frac{\varepsilon - \varepsilon_a}{\varepsilon + s\varepsilon_a} = f_b \frac{\varepsilon_b - \varepsilon_a}{\varepsilon_b + s\varepsilon_a} \tag{1.8}$$

This new parameter s depends on the shape of the particles and their orientation to the electric field. The screening factor s is related to the depolarisation factor of Lorentz by the following relation :

$$s = \frac{1-q}{q} \tag{1.9}$$

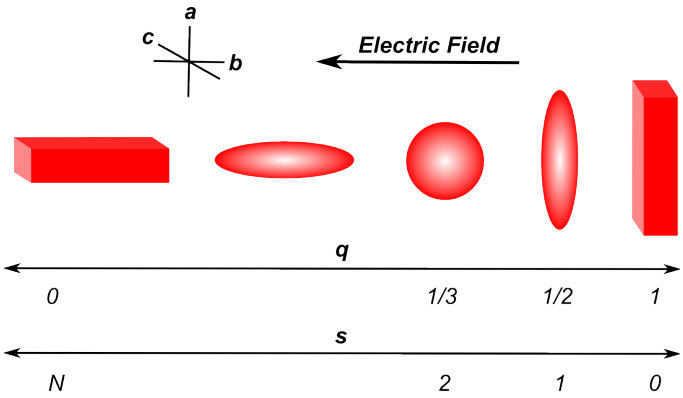

Figure 1.7: Illustration of the range for values of q and s as a function of the geometrical shape of the constituents.

If ellipsoidal particles are considered, with major and minor axes measuring a and b respectively, with the incident electric field parallel to the minor axis, the relationship that interlinks q and the geometric parameters a and b of the particles is as follows (see figure 1.7 above)

$$q = \frac{\frac{1}{b}}{\frac{1}{a} + \frac{2}{b}} \tag{1.10}$$

1.4.4 The Bruggeman theory

This theory treats the constituent symmetrically. The model assumes that grains of two or more materials are randomly interspersed. To analyse such a composite a single grain

is considered within the whole. This grain will be surrounded by grains of each type of constituent material including its own type. It is also assumed that the grain will be surrounded by a material of uniform dielectric constant given by that of the effective medium. Just as in the case of the Maxwell-Garnett equation, Bruggeman's equation can be applied to quasi-static condition (very small particles) of nanoparticles in a matrix. In addition to this, the density of particles present in the matrix is so high that the phenomena of percolation needs to be taken into consideration. In these conditions (figure 1.8): $f_a \sim f_b$ and $f_b = 1 - f_a$.

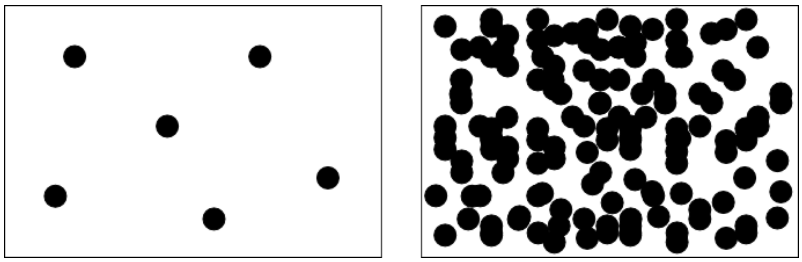

Figure 1.8: Nanocomposite used in approximation of Maxwell-Garnett with $f_a \ll f_b$ (left) and the approximation of Bruggeman with $f_a \ll f_b$ (right).

In cases where f_a and f_b are comparable, it may not be clear whether a or b is the host medium. One alternative is simply to make the self-consistent choice $\varepsilon_h = \varepsilon$, in which case equation 1.6 reduces to

$$0 = f_a \frac{\varepsilon_a - \varepsilon}{\varepsilon_a + 2\varepsilon} + f_b \frac{\varepsilon_b - \varepsilon}{\varepsilon_b + 2\varepsilon} \tag{1.11}$$

This equation is known as the Bruggeman expression, commonly called the Bruggeman effective medium approximation (EMA). Although they are related, equation 1.8 actually describes a coated-sphere microstructure where a is completely surrounded by b while equation 1.11 refers to the aggregate or random-mixture microstructure where a and b are inserted into the effective medium itself (compare sketches in figure 1.8).

The salient feature of this model is, that it presents a successful description of a system even when the volume fraction of one constituent increases to a point at which the grains begin to join and form continuous threads throughout the composite. For the material this causes changes in properties like conductivity etc. that may change significantly due to this percolation.

All here presented EMA types are used for the description of porous thin films. In this work, however, only the Bruggeman EMA is used for the investigations of porous thin titania films, it is derived as

$$0 = f_{matrix}\frac{\varepsilon_{matrix} - \varepsilon_{eff}}{\varepsilon_{matrix} + 2\varepsilon_{eff}} + f_{pore}\frac{\varepsilon_{pore} - \varepsilon_{eff}}{\varepsilon_{pore} + 2\varepsilon_{eff}} \tag{1.12}$$

The Bruggeman effective medium model shows that the effective medium refractive index increases as the porosity decreases, as long as the voids are filled with a medium with a lower refractive index than the nanocrystalline TiO_2 matrix. This concept will be applied to all OWS experiments in the following chapters.

1.5 Mesoporous Waveguide Configuration

The development of optical mesoporous titania waveguides has been very challanging due to many difficulties in producing suitable transparent, homogeneous metal oxide thin-films. Also the scattering losses and reduction of average refractive index accompanied with introduced mesoporosity have been hindering optical thin-film applications.

However, various attempts have been made to produce mesoporous metal oxide waveguides, using different configurations. For a long time attempts to integrate porous metal oxide have been limited to configurations where the waveguide core material had a higher refractive index than the porous metal oxide cladding[46], thus resulting in optical sensing schemes comparable to the ones depicted in figure 1.5(a). Only recently development was reported on the for application of mesoporous oxide films with higher refractive index than the supporting substrate. For example, mesoporous metal oxide semiconductor-clad waveguides have been reported[53], where a mesoporous layer of titania has been formed on top of glass slide. Another example was reported[63] wherein an ultra thin-film of mesoporous metal oxides (WO_3 and SnO_2) was prepared on a tin-diffused glass slides.

Actually, the latter reported structure was not a waveguide but a conventional attenuated total reflection (ATR) element because of the microscopy glass, which was used as the core of the 'waveguide' is too thick ($d = 2mm$) to result in a standing wave along the substrate normal and a transverse travelling wave in the direction parallel to the substrate.

However, these and similar approaches have successfully applied a porous metal oxide matrix to the sensing scheme, but, nevertheless, only shifted a comparably small portion of the EM field towards the analyte within the voids of the oxide materials, as shown in figure 1.9.

The mesoporous titania waveguide system developed in the framework of this thesis, however, has a feature within the multilayer structure, allowing for great confinement of the EM fields of the guided modes within the porous structure. A thin metal layer ($50nm$)

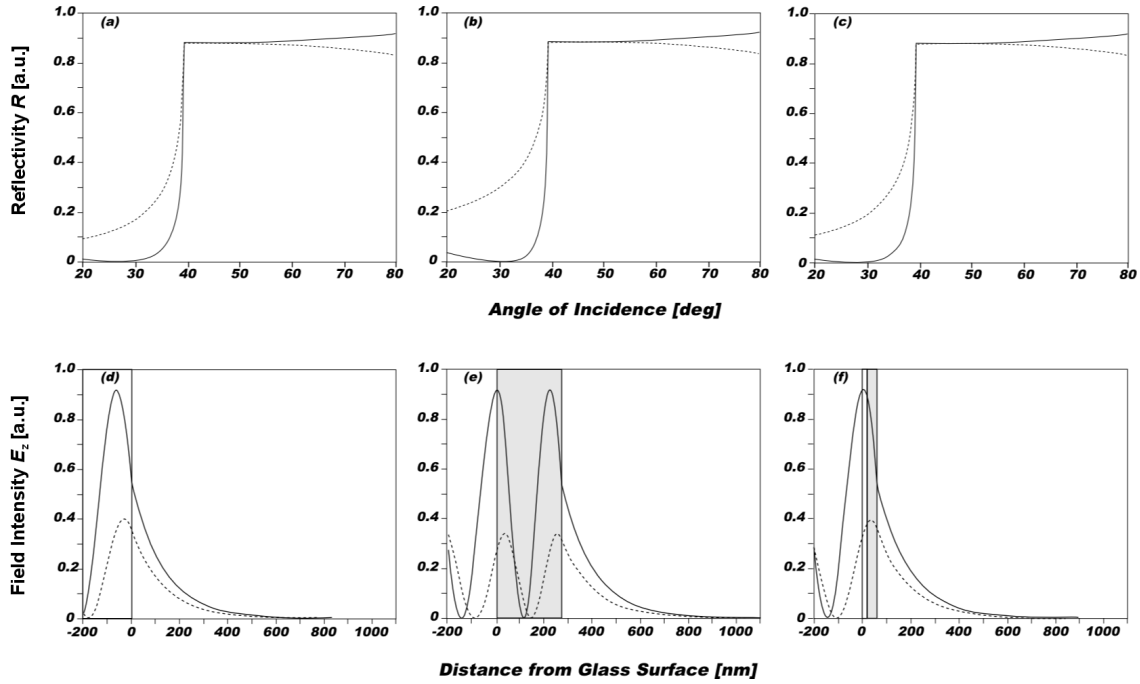

Figure 1.9: EM field calculations for the reported examples of mesoporous waveguide sensing schemes from literature are presented in this overview. The sketch in (a) shows the angular reflectivity spectrum for just the glass slide ($n_{BK7} = 1.51513$) in air as cover medium ($n_C = 1.00027$) without any mesoporous adlayer for reference. (b) and (c) show the corresponding spectra for the two reported systems, consulted for this exemplification. (b) shows the angular reflectivity scan of a mesoporous titania layer ($n_{meso-TiO_2} = 1.8$, $d_{meso-TiO_2} = 270nm$) deposited on a BK7 glass slide, (c) illustrates the thin-film mesoporous SnO_2 waveguide ($n_{meso-SnO_2} = 1.64$, $d_{meso-SnO_2} = 41.2nm$), formed on a tin-diffused glass slide. The spatial distributions of the electric field intensities in z-direction for each example at operational conditions at the coupling angle of $45°$ are depicted in (d), (e), and (f).

was evaporated on the glass slide before the mesoporous titania film was formed. This metal layer was the key to achieve this high confinement within the mesoporous waveguide (refer to figure 1.10).

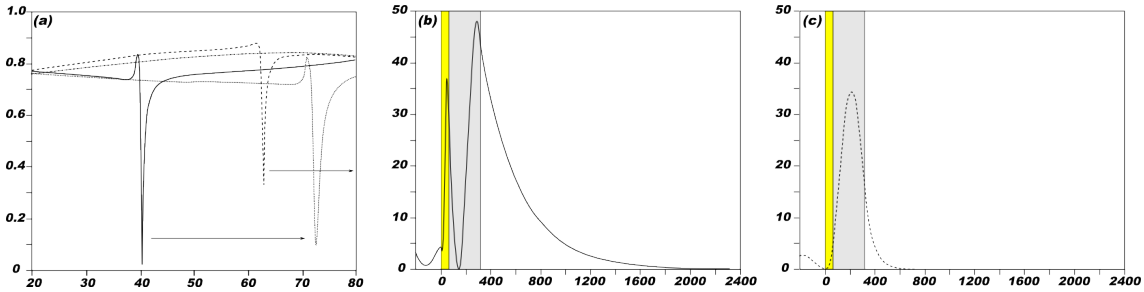

Figure 1.10: (a) shows the Fresnel simulation for angular dependent reflectivity (in air $n_{air} = 1.000$) of a thin mesoporous titania film ($n_{meso-TiO_2} = 1.4968$, $d_{meso-TiO_2} = 270nm$) deposited on a thin gold layer ($n_{Au} = 0.312$, $k_{Au} = 3.823$, $d_{Au} = 48nm$) on top of a glass slide ($n_{BK7} = 1.51513$). When the mesoporous oxide layer is infiltrated with water, the composite refractive index is increased and the spectrum of the monomodal waveguide shifts to higher angles. The spatial electric field distribution in z-direction under initial conditions with air-filled pores is schematically illustrate for the present TM_1 mode (b) and the TE_0 mode (c).

The configuration of this sensor is thus similar to the conventional dielectric waveguide sensor but with an extra layer of metal introduced between the substrate and the waveguide

film. This architecture can also be compared to the structure of a SPR sensor. The difference between those two structures is simply that a waveguide film is added on top of the metal-coating.

If the film thickness of the waveguide is sufficiently increased, multiple nonradiative modes (i.e. guided optical waves) can be observed. The excitation of these modes of different order *m* can be seen if the reflected intensity is recorded as a function of the angle of incidence: narrow dips in the reflectivity curve above the critical angle indicate the existence of the various guided waves (shown in figure 1.11(a)). Each observable mode characterises an individual field profile (see figure 1.11(b) and (c)) which, again, can be utilised for sensing purposes by interaction with the analyte. For a mesoporous titania film with a thickness of $\approx 1.4\mu m$, several waveguide modes can be excited at visible wavelengths, therefore it is referred to as multimode waveguide (refer to figure 1.11(a)). Analysis of multiple modes can give rich information on the anisotropy or structural properties of the film. The optical coupling depends on the dimensions and refractive indices of the different parts of the waveguiding system. This makes multimodal optical waveguide highly suitable for sensing purposes.

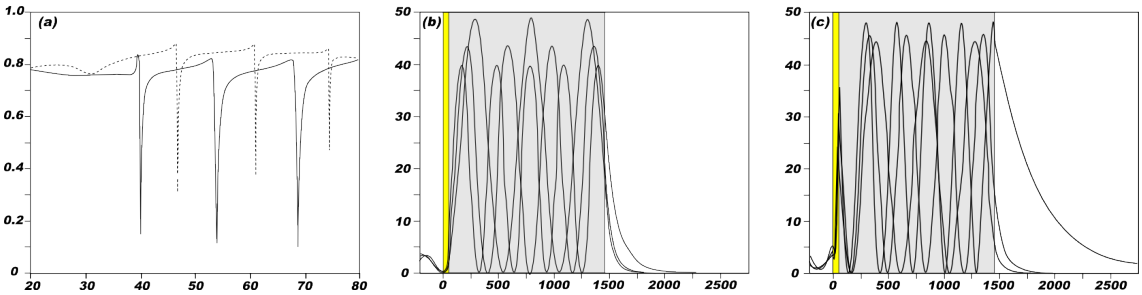

Figure 1.11: (a) Illustration of angular dependent reflectivity (in air $n_{air} = 1.000$) of a mesoporous titania film ($n_{meso-TiO_2} = 1.4968$, $d_{meso-TiO_2} \approx 1.4\mu m$) deposited on a thin gold layer ($n_{Au} = 0.312$, $k_{Au} = 3.823$, $d_{Au} = 48nm$) on top of a glass slide ($n_{BK7} = 1.51513$). The spatial electric field distributions in z-direction with air-filled pores are schematically illustrate for the all present TE modes (b) and in (c) for the TM modes, respectively.

If, for example, small molecules like sensitiser dyes adsorb on top or within the pore network of the mesoporous oxide film, this can lead to large change in the optical coupling conditions. Further analysis of the coupling conditions (angle of incidence, and per cent reflected light intensity) gives quantitative and structural information about the adsorbed species. The propagation in the waveguide is restricted only to light with specific momentum and energy.

Further it has to be considered, that exposure to another environment with different refractive index also has a profound impact on the sensing signal: When the pore volume is infiltrated by a given medium the composite refractive index is accordingly shifted. Commonly aqueous solutions are applied for target analyte delivery to the sensing unit

(dyeing bath), therefore the identical mesoporous waveguide system as shown in figure 1.11 is simulated again for the case of water being the pore filling medium, instead of air. Figure 1.12 depicts the situation after the environment is switched.

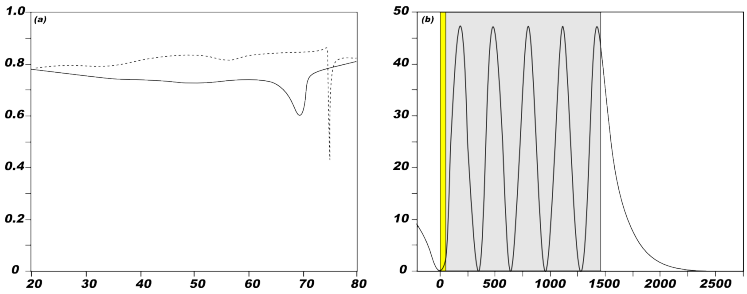

Figure 1.12: (a) When the mesoporous oxide layer is infiltrated with water ($n_{water} = 1.333$), the composite refractive index is increased and the spectrum of the multimodal waveguide shifts to higher angles. (compare with 1.11) (b) The spatial electric field distribution in z-direction with water-filled pores is schematically illustrate for the present TE_4 mode.

As demonstrated above in figure 1.12, a substantial shift in the angular position of the mode spectrum is occurred after water entered the pores. The TE_4-mode experienced an angular shift of $30.21°$, from $47.45°$ to$77.66°$, and remains the only observable mode coupling angle after the shift due to water infiltration. In order to allow for multiple resonant mode angles to be observed in the available angular range, the sensor configuration had to be modified, and BK7 glass was no longer used as substrate, but high refractive index LaSF9 glass instead. This increased the refractive index of the glass support by $\Delta n \approx 0.33$ and made (at the same film thickness and refractive index) a whole range of guided optical modes accessible for sensing effects. The angular reflectivity spectrum available for operation in air and associated spatial field distributions of the confined guided modes are presented in figure 1.13.

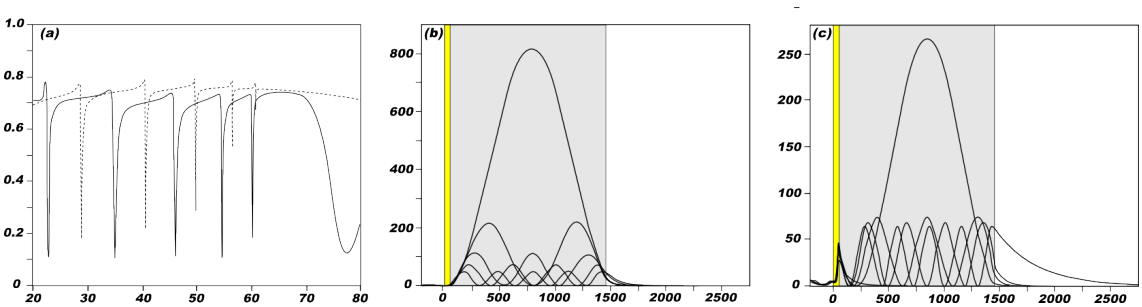

Figure 1.13: Illustration of angular dependent reflectivity (in air $n_{air} = 1.000$) of a mesoporous titania film ($n_{meso-TiO_2} = 1.4968$, $d_{meso-TiO_2} \approx 1.4\mu m$) deposited on a thin gold layer ($n_{Au} = 0.312$, $k_{Au} = 3.823$, $d_{Au} = 48nm$) on top of a glass slide ($n_{BK7} = 1.51513$). The spatial field distributions in z-direction with air-filled pores are schematically illustrate for the all present TE modes (b) and in (c) for the TM modes, respectively.

With this optimised configuration on high refractive index supports, multiple modes became available also in aqueous environments, as the spectrum in figure 1.12 clearly indicates.

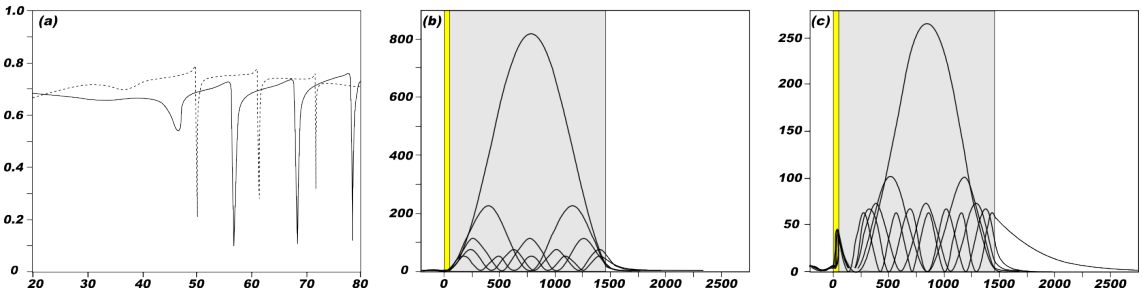

Figure 1.14: Illustration of angular dependent reflectivity (in water $n_{water} = 1.333$) of a mesoporous titania film ($n_{meso-TiO_2} = 1.4968$, $d_{meso-TiO_2} \approx 1.4\mu m$) deposited on a thin gold layer ($n_{Au} = 0.312$, $k_{Au} = 3.823$, $d_{Au} = 48nm$) on top of a glass slide ($n_{BK7} = 1.51513$). The spatial field distributions in z-direction with air-filled pores are schematically illustrate for the all present TE modes (b) and in (c) for the TM modes, respectively.

Conceptually, such metal supported or plasmon coupled OWG sensors have already been presented[68,37,69] but so far, no general (thorough theoretical) study of this type of OWG sensor has been presented in literature. Moreover, literature reporting a sensing scheme which utilises mesoporous oxide layers as slab waveguide on top of the metal layer was not found till date.

Bibliography

[1] Ali, M. B., Milka, R., Ouada, H. B., M'ghaieth, R. & Maaref, H. *Sens. Actuators* **74**, 123 (1999).

[2] Anderson, R. C., Muller, R. S. & Tobias, C. W. *Sens. Actuators A* **21-23**, 835 (1990).

[3] Andrievski, R. & Glezer, A. Size effects in properties of nanomaterials. *Scripta Mater.* **44**, 1621–1624 (2001).

[4] Arrand, H. F. *et al. J. Luminescence 80, 119 1999* **80**, 119 (1999).

[5] Baeck, S., Choi, K., Jaramillo, T. F., Stucky, G. D. & McFarland, E. W. *Adv. Mater.* **15**, 1269 (2003).

[6] Baratto, C. *et al.* **2**, 121 (2002).

[7] Ben-Chorin, M. & Kux, A. *Appl. Phys. Lett.* **64**, 481 (1994).

[8] Brasquet, C., Bourges, B. & Cloirec, P. L. Quantitative structure - property relationship (qspr) for the adsorption of organic compounds onto activated carbon cloth - comparison between multiple linear regression and neural network. *Environ. Sci. Technol.* **33**, 4226–4231 (1999).

[9] Brinker, C. J., Lu, Y., Sellinger, A. & Fran, H. *Adv. Mater.* **11**, 579 (1999).

[10] Bruggeman, D. A. G. Berechnung verschiedener physikalischer konstanten von heterogenen substanzen. i. dielektrizitaetskonstanten und leitfaehigkeiten der mischkoerper aus isotropen substanzen. *Annalen der Physik* **416**, 636–664 (1935).

[11] Cantor, B. *et al.* Applications of nanocomposites. *Scripta Mater.* **44**, 2055–2059 (2001).

[12] Ceroni, P., Bergamini, G., Marchioni, F. & Balzani, V. *Prog. Polym. Sci.* **30**, 453 (2005).

[13] Chan, S., Li, Y., Rothberg, L. J., Miller, B. L. & Fauchet, P. M. Nanoscale silicon microcavities for biosensing. *Mat. Sci. & Eng. C* **15**, 277–282 (2001).

[14] Cheng, W., Baudrin, E., Dunn, B. & Zink, J. I. *J. Mater. Chem.* **11**, 92 (2001).

[15] Cola, L. D. Special volume on molecular wires. *Top. Curr. Chem.* 257 (2005).

[16] Crepaldi, E. L., de A. A. Soler-Illia, G. J., Grosso, D. & Sanchez, C. Nanocrystallised titania and zirconia mesoporous thin films exhibiting enhanced thermal stability. *New J. Chem.* **27**, 9–13 (2003).

[17] Cunin, F. *et al.* Biomolecular screening with encoded porous-silicon photonic crystals. *Nat. Mater.* **1**, 39–44 (2002).

[18] Dancil, K.-P. S., Greiner, D. P. & Sailor, M. J. A porous silicon optical biosensor: Detection of reversible binding of igg to a protein a-modified surface. *J. Am. Chem. Soc.* **121**, 7925–7930 (1999).

[19] Decher, G. *Layered Nanoarchitectures via Directed Assembly of Anionic and Cationic Molecules, in Comprehensive Supramolecular Chemistry, Vol. 9, Templating, Self-Assembly and Self-Organization* (Pergamon Press, New York, pp. 507-528, 1996).

[20] Garces, I. *et al. Sens. Actuators B* **60**, 191 (1999).

[21] Garces, I. *et al. Sens. Actuators B* **60**, 191 (1999).

[22] Granqvist, C. G. & Hunderi, O. Optical properties of ag-sio2 cermet films: A comparison of effective-medium theories. *Phys. Rev. B* **18**, 2897–2906 (1978).

[23] Granqvist, C. G., O. & Hunderi. Optical properties of ultrafine gold particles. *Phys. Rev. B* **16**, 3513–3534 (1977).

[24] Gust, D., Moore, T. A. & Moore, A. L. Mimicking photosynthetic solar energy transduction. *Acc. Chem. Res.* **34**, 40–48 (2001).

[25] Hassan, C., Doyle, F. & Peppas, N. Dynamic behavior of glucose-responsive poly(methacrylic acidÐg-ethylene glycol) hydrogels. *Macromolecules* **30**, 6166–6173 (1997).

[26] Hecht, S. & Frechet, J. M. J. Dendritic encapsulation of function - applying nature's site isolation principle from biomimetics to materials science. *Angew. Chem. Int. Ed.* **40**, 74–91 (2001).

[27] Hillenbrand, R., Taubner, T. & Keilmann, F. Phonon-enhanced lightÐmatter interaction at the nanometre scale. *Nature 2002* **418**, 159–168 (2002).

[28] Homola, J., Koudela, I. & Yee, S. S. Surface plasmon resonance sensors based on diffraction gratings and prism couplers: sensitivity comparison. *Sensors and Actuators B - Chemical* **54**, 16–24 (1999).

[29] Hu, X., Damjanovic, A., Ritz, T. & Schulten, K. *Proc. Natl. Acad. Sci. USA* **95**, 5935 (1998).

[30] Hyodo, T., Abe, S., Shimizu, Y. & Egashira, M. *Sens. Actuators B* **93**, 590 (2003).

[31] Hyodo, T., Nishida, N., Shimizu, Y. & Egashira, M. *Sens. Actuators B* **83**, 209 (2002).

[32] Irie, M. Special issue on photochromism - memories and switches. *Chem. Rev.* **100**, 1683 (2000).

[33] Irie, M. & Matsuda, K. *Electron Transfer in Chemistry, Vol. 5, p. 215* (Wiley-VCH, Weinheim, Germany, 2001).

[34] Jiang, D.-L. & Aida, T. *Prog. Polym. Sci.* **30**, 403 (2005).

[35] Jiao, Y., Rong, G. & Weiss, S. M. Porous waveguide in the kretschmann configuration for small molecule detection. *Photonic Microdevices/Microstructures for Sensing* **7322**, 732205 (2009).

[36] Kim, D. & Osuka, A. Directly linked porphyrin arrays with tunable excitonic interactions. *Acc. Chem. Res.* **37**, 735–745 (2004).

[37] Knoll, W. Interfaces and thin films as seen by boun electromagnetic waves. *Annual Review of Physical Chemistry* **49**, 569–638 (1998).

[38] Kresge, C. T., Leonowicz, M. E., Roth, W. J., Vartuli, J. C. & Beck, J. S. *Nature London* **359**, 710 (1992).

[39] Lorentz, H. *The Theory of Electrons* (Teubner, Leipzig, 1909, 2nd edn 1916).

[40] Lorenz, L. Ueber die refractionsconstante. *Annalen der Physik und Chemie* **247**, 70–103 (1880).

[41] Lu, G. Q. & Zhao, X. S. *Nanoporous Materials - Science and Engineering* (Imperial Colege Press, London, 2004).

[42] Lukosz (1990).

[43] Lukosz (1989).

[44] Lukosz, W. *Biosensors and Bioelectronics* **6**, 215–225 (1991).

[45] Lyklema, J. *Fundamentals of Interface and Colloid Science - I Fundamentals. II Solid-Liquid Interfaces* (Academic Press, London, 1995).

[46] MacCraith, B. D. *Sens. Actuators B 1995* **29**, 51 (1995).

[47] Maier, J. A. *et al.* Plasmonics - a route to nanoscale optical devices. *Adv. Mater. 2001, 13, 1501* **13**, 1501 (2001).

[48] Marlow, F., McGehee, M. D., Zhao, D., Chmelka, B. F. & Stucky, G. D. *Adv. Mater.* **11**, 632 (1999).

[49] Maxwell-Garnett, J. Colours in metal glasses, in metallic films, and in metallic solutions. ii. *Phil. Trans. R. Soc. Lond. A* **205**, 237–288 (1906).

[50] Maxwell-Garnett, J. Colours in metal glasses and in metallic films. *Phil. Trans. R. Soc. Lond. A* **203**, 385–420 (1904).

[51] Maya, L., Allen, W., Glover, A. & Mabon, J. Gold nanocomposites. *Vac. Sci. Technol. B* **13**, 361–365 (1995).

[52] Mazaleyrat, F. & Varga, L. Ferromagnetic nanocomposites. *J. Magnetism and Magnetic Mater* **215-216**, 253–259 (2000).

[53] Miller, L. W., Tejedor, M. I., Nelson, B. P. & Anderson, M. A. Mesoporous metal oxide semiconductor-clad waveguides. *J. Phys. Chem. B* **103**, 8490–8492 (1999).

[54] Min, H., Yang, H. & Cho, S. M. *Sens. Actuators B* **67**, 199 (2000).

[55] Nellen & Lukosz (1990).

[56] Novotny, L. & Stranick, S. J. Near-field optical microscopy and spectroscopy with pointed probes. *Annu. Rev. Phys. Chem.* **57**, 303–331 (2006).

[57] Onishi, T., Iwamura, E., Takagi, K. & Yashikawa, K. Influence of adding transition metal elements to an aluminum target on electrical resistivity and hillock resistance in sputter-deposited aluminum alloy thin films. *J. Vac. Sci. Technol. A* **14**, 2728–2735 (1995).

[58] Ouyang, H., Christophersen, M., Viard, R., Miller, B. L. & Fauchet, P. M. Macroporous silicon microcavities for macromolecule detection. *Adv. Funct. Mater.* **15**, 1851–1859 (2005).

[59] Pavesi, L. *Riv. Nuovo Cimento* **1**, 20 (1997).

[60] Preist, P., Delage, F., Faur-Brasquet, C. & Cloirec, P. L. Quantitative structure-activity relationships for the prediction of vocs adsorption and desorption energies onto activated carbon. *Fuel Process. Technol.* **77-78**, 345–351 (2002).

[61] Provenzano, V. & Holtz, R. *Mater. Sci. Eng. A* **204**, 125–134 (1995).

[62] Psaltis, D., Quake, S. R. & Yang, C. Developing optofluidic technology through the fusion of microfluidics and optics. *Nature* **442**, 381–386 (2006).

[63] Qi, Z.-M., Wei, M., Honma, I. & Zhoua, H. Sensitive slab optical waveguides composed of mesoporous metal-oxide thin films on the tin-diffused layers of float glass substrates. *JOURNAL OF APPLIED PHYSICS* **100**, 83102 (2006).

[64] Qu, D. H., Ji, F. Y., Wang, Q. C. & Tian, H. *Adv. Mater.* **18**, 2035 (2006).

[65] Rasmussen, A. & Deckert, V. New dimension in nano-imaging - breaking through the diffraction limit with scanning near-field optical microscopy. *Anal. Bioanal. Chem. 2005, 381, 165* **381**, 165–172 (2005).

[66] Rogl, H., Schoedel, R., Lokstein, H., Kuehlbrandt, W. & Schubert, A. Assignment of spectral substructures to pigment-binding sites in higher plant light-harvesting complex lhc-ii. *Biochemistry* **41**, 2281–2287 (2002).

[67] Rouquerol, F., Rouquerol, J. & Sing, K. *Adsorption by Powders and Porous Solids - Principles, Methodology and Applications,* (Academic Press, London, 1999).

[68] Salamon, Z., Macleod, H. & Tollin, G. Coupled plasmon-waveguide resonators - a new spectroscopic tool for probing proteolipid film structure and properties. *Biophys. J.* **73**, 2791–2898 (1997).

[69] Salamon, Z. & Tollin, G. Optical anisotropy in lipid bilayer membranes: coupled plasmon waveguide resonance measurements of molecular orientation, polarisability, and shape. *Biophys. J.* **80**, 1557–1567 (2001).

[70] Santato, C., Odziemkowski, M., Ulmann, M. & Augustynski, J. *J. Am. Chem. Soc.* **123**, 10639 (2001).

[71] Schlicke, B., Belser, P., Cola, L. D., Sabbioni, E. & Balzani, V. Photonic wires of nanometric dimensions. electronic energy transfer in rigid rodlike ru(bpy)32+-(ph)n-os(bpy)32+ compounds (ph = 1,4-phenylene n = 3, 5, 7). *J. Am. Chem. Soc.* **121**, 4207 (1999).

[72] de Silva, A. P. & McClenaghan, N. D. *Chem. Eur. J.* **10**, 574 (2004).

[73] de Silva, A. P. & Tecilla, P. Special issue on fluorescent sensors. *J. Mater. Chem.* **15**, 2617 (2005).

[74] Snow, P. A., Squire, E. K., Russell, P. S. J. & Canham, L. T. Vapor sensing using the optical properties of porous silicon bragg mirrors. *J. Appl. Phys.* **86**, 1781 (1999).

[75] Sohn, H., Letant, S., Sailor, M. J. & Trogler, W. C. Detection of fluorophosphonate chemical warfare agents by catalytic hydrolysis with a porous silicon interferometer. *J. Am. Chem. Soc.* **122**, 5399–5400 (2000).

[76] Srivastava, R., Bao, C. & Gomez-Reino, C. *Sens. Actuators A* **51**, 165 (1996).

[77] Stewart, G., Muhammad, A. & Culshaw, B. *Sens. Actuators B* **11**, 521 (1993).

[78] Stewart, M. P. & Buriak, J. M. Chemical and biological applications of porous silicon technology. *Adv. Mater.* **12**, 859 (2000).

[79] Suzuki, M. *Adsorption Engineering* (Elsevier, Amsterdam, The Netherlands, 1990).

[80] Szacilowski, K. *Chem. Eur. J.* **10**, 2520 (2004).

[81] Teoh, L. G., Hon, Y. M., Shieh, J., Lai, W. H. & Hon, M. H. *Sens. Actuators B* **96**, 219 (2003).

[82] Theiss, W. Optical properties of porous silicon. *Surf. Sci. Rep.* **91-192**, 91–192 (1997).

[83] Tiefenthaler, K. & Lukosz, W. Sensitivity of grating couplers as integrated-optical chemical sensors. *J. Opt. Soc. Am. B* **6**, 209–220 (1989).

[84] Tien, P. K. Integrated optics and new wave phenomena in optical waveguides. *Rev. Mod. Phys.* **49**, 361–420 (1977).

[85] Veprek, S. & Argon, A. Mechanical properties of superhard nanocomposites. *Surf. Coat. Technol.* **146-147**, 175–182 (2001).

[86] Veprek, S. & S. Reiprich, T. S. F. . . Đ. A concept for the design of novel superhard coatings. *Thin Solid Films* **268**, 64–71 (1995).

[87] Wald, G. Molecular basis of visual excitation. *Science* **162**, 230–239 (1968).

[88] Wang, J. & Stucky, G. D. *Adv. Funct. Mater.* **14**, 409 (2004).

[89] Yang, P., Zhao, D., Margolese, D. I., Chmelka, B. F. & Stucky, G. D. *Nature London* **396**, 152 (1998).

[90] Zhou, H. *et al. Jpn. J. Appl. Phys., Part 1* **40**, 7098 (2001).

[91] Feringa, B. L. (ed.) *Molecular Switches* (Wiley-VCH, Weinheim, Germany, 2001).

[92] Garland, J. C. & Tanner, D. B. (eds.). *Electrical Transport and Optical Properties of Inhomogeneous Media*, vol. 2. American Institute of Physics (American Institute of Physics, New York, 1978, 1978).

[93] Stavenga, D. G., DeGrip, W. J. & E. N. Pugh, J. (eds.) *Handbook of Biological Physics, Vol. 3* (Elsevier, Amsterdam, 2000).

[94] Yao, N. & Wang, Z. L. (eds.) *Handbook of Microscopy for Nanotechnology, Vol. 1* (Springer, Berlin, 2005).

Chapter 2
2 Theory

Contents

Introduction

In this chapter all the fundamental concepts needed for the complete comprehension of the presented thesis are outlined. A major part of this work is concerned with the excitation of surface waves and their interaction with the dielectric media they are associated with. Therefore, the mathematical description of electromagnetic (EM) waves and their interaction with an interface is introduced. Accordingly optical phenomena at interfaces will be presented in detail. Then, the case of one of the two media forming the interface being a metal is presented. Two different ways of exciting plasmons, namely prism and grating coupling, are addressed. Accordingly, optical waveguides will then be introduced and a detailed presentation of spatially confined, guided modes and their inherent properties is given. Next, the transfer-matrix method will be introduced, which is able to describe the optical transmission and reflection behaviour of a multi-layer system. This section will finally also discuss a method that allows to take continuous refractive index profiles in multi-layer systems to be taken into account.

Material properties, and the geometry of the media in general, influence the propagation of light through different materials. Mathematically, the description is based on the Maxwell equations, which form the basis of classical electrodynamics. Bearing in mind that optical phenomena such as the excitation of evanescent optical waves take place at the interfaces between two media, the most important processes at such an interface, i.e. refraction, reflection and transmission, are addressed.

2.1 General consideration

For the purpose of fundamentally understanding the optical behaviour of thin-films and thin-film systems in general, it is mandatory to become familiar with the optical constants of materials, their origins, magnitudes and their dependence on the way such films are produced, processed, and finally assembled. Therefore, the purpose of this section is to provide a brief survey of this topic.

The unifying concept that describes all optical properties in general is the interaction of EM radiation with (the electrons of) materials. On this basis, optical properties of all materials are interpretable from the electronic structure and how it is affected by atomic structure, bonding, impurities, and defects. For an exact description, quantum mechanical approaches are required, but this is well beyond the scope intended in this introductory chapter. Discussions will stress meanings and implications, allowing an understanding of

the optical behaviour of nano-structured materials like the titania thin-films presented in this thesis, rather than mathematical rigour.

In contrast to propagation in free space, where the velocity of all EM radiation is constantly the same ($c \approx 3 \cdot 10^8 ms^{-1}$), EM waves that travel in matter undergo refraction. Refraction is the change in direction due to a change in velocity, caused by the presence of charge. Therefore, optical properties of given materials are to a large degree encoded in what is called the index of refraction, often referred to as refractive index (RI) n. Where n in general is defined as the ratio of the phase velocity, c, of a plane harmonic EM wave of a specific frequency in empty space to the phase velocity, v_p, in a given medium:

$$n = \frac{c}{v_p} \tag{2.1}$$

On the micro scale, an EM wave's phase velocity is slowed down while travelling within a material because its electric field creates a disturbance in the charges of each atom - primarily through interaction with the circumjacent electrons - proportional to the permittivity of the material. The charges will, in general, oscillate slightly out of phase with respect to the driving electric field. The charges thus radiate their own EM wave that is at the same frequency but with a phase delay. The macroscopic sum of all such contributions in the material is a wave with the same frequency but shorter wavelength than the original, leading to a slowing of the wave's phase velocity. Most of the radiation from oscillating material charges will modify the incoming wave, changing its velocity. However, some net energy will be radiated in other directions, resulting in scattered light.

2.1.1 Interaction of EM waves and matter

A full description of the properties of electric and magnetic fields and their relation to charge density and current density is given by Maxwell's equations, a set of four partial differential equations connecting the electric displacement field $\mathbf{D}$ (also called the electric flux density), the magnetic flux density $\mathbf{B}$ (also called the magnetic induction or the magnetic field), the electrical field strength $\mathbf{E}$, and the magnetic field strength $\mathbf{H}$ (also called the auxiliary field). Nowadays the Maxwell's equations are most often written in vector notation:

$$\nabla \cdot \mathbf{D}(\mathbf{r}, t) = \rho(\mathbf{r}, t) \tag{2.2}$$

$$\nabla \cdot \mathbf{B}(\mathbf{r}, t) = 0 \tag{2.3}$$

$$-\nabla \times \mathbf{E}(\mathbf{r},t) = \frac{\partial \mathbf{B}(\mathbf{r},t)}{\partial t} \tag{2.4}$$

$$\nabla \times \mathbf{H}(\mathbf{r},t) = \frac{\partial \mathbf{D}(\mathbf{r},t)}{\partial t} + \mathbf{j}(\mathbf{r},t) \tag{2.5}$$

Symbols in bold represent vector quantities, whereas symbols in italics represent scalar quantities, where $\mathbf{E}$ is the electrical field vector, $\mathbf{B}$ the magnetic field vector, $\mathbf{j}$ the current density vector, ρ the charge density, and $\varepsilon_0 = 8.854 \cdot 10^{-12} F/m$ the permittivity of vacuum, and with $\mathbf{r}$ denoting the position vector, t the time.

Individually, these equations are known as Gauss's law (eq. 2.2), Gauss' law for magnetism (absence of magnetic monopoles) (eq. 2.3), Faraday's law of induction (eq. 2.4), and Ampère's Circuital law with Maxwell's correction (eq. 2.13). The force exerted upon a charged particle by the electric field and magnetic field is given by the Lorentz force equation:

$$\mathbf{F} = \rho_q(\mathbf{E} + \mathbf{v} \times \mathbf{B}) \tag{2.6}$$

where ρ_q is the charge on the particle and $\mathbf{v}$ is the particle velocity. The four Maxwell equations, together with the Lorentz force law are the complete set of laws of classical electromagnetism.

The index of refraction is closely linked to the electronic structure, more precisely to the material's relative permittivity ε *via* a simple relation which can be derived from the Maxwell equations. Therefore, assuming materials with linear polarisation and magnetisation responses in respect to the external fields, both the electric as well as the magnetic quantities are interconnected *via* the material equations (2.7) and (2.8) and with consideration of Ohm's law (eq.2.9), and can be expressed as:

$$\mathbf{D}(\mathbf{r},t) = \varepsilon_0 \mathbf{E}(\mathbf{r},t) + \mathbf{P}(\mathbf{r},t) = \varepsilon_0 \varepsilon(\omega)\mathbf{E}(\mathbf{r},t) = \varepsilon(\omega)\mathbf{E}(\mathbf{r},t) \tag{2.7}$$

$$\mathbf{B}(\mathbf{r},t) = \mu_0 \mathbf{H}(\mathbf{r},t) + \mathbf{M}(\mathbf{r},t) = \mu_0 \mu(\omega)\mathbf{H}(\mathbf{r},t) = \mu(\omega)\mathbf{H}(\mathbf{r},t) \tag{2.8}$$

$$\mathbf{j}(\mathbf{r},t) = \sigma \mathbf{E}(\mathbf{r},t) \tag{2.9}$$

where ε_0 is the electric permittivity of free space, μ_0 is the magnetic permeability of free space, ω is the angular frequency, $\varepsilon(\omega)$ is the material's electric permeability, $\mu(\omega)$ is the

magnetic permeability, and σ is the specific electric conductivity.

As it fulfils the requirements for solving the problems discussed within the frame of this thesis, in the following, only homogeneous, isotropic ($\varepsilon(\omega)$ = constant, $\mu(\omega)$ = constant), and non-magnetic materials will be considered, which allows equation 2.8 to be simplified as $\mu(\omega) = \mu_0$ and $\sigma = 0$. Consequently $\varepsilon(\omega)$ and $\mu(\omega)$ are reduced to scalar quantities, while they are rank two tensors in the general treatment. However, they still remain complex functions of the angular frequency ω of the exciting EM field. Under these circumstances Maxwell's equations become:

$$\nabla \times \mathbf{H}(\mathbf{r}, t) = \varepsilon \frac{\partial \mathbf{E}(\mathbf{r}, t)}{\partial t} + \sigma \mathbf{E}(\mathbf{r}, \mathbf{t}) \tag{2.10}$$

$$-\nabla \times \mathbf{H}(\mathbf{r}, t) = \mu \frac{\partial \mathbf{H}(\mathbf{r}, t)}{\partial t} \tag{2.11}$$

$$\varepsilon(\omega) \nabla \cdot \mathbf{E}(\mathbf{r}, t) = \rho \tag{2.12}$$

$$\mu(\omega) \nabla \cdot \mathbf{H}(\mathbf{r}, t) = 0 \tag{2.13}$$

and can be solved by electric plane waves

$$\mathbf{E}(\mathbf{r}, t) = \mathbf{E}_0 e^{i(\mathbf{k} \cdot \mathbf{r} - \omega \cdot t)} \tag{2.14}$$

with $\mathbf{r}$ denoting the position vector, t the time, $\mathbf{E}_0$ the electric field amplitude and $\mathbf{k}$ the wave vector. Due to the transverse nature of light, $\mathbf{E}_0$ is always orthogonal to the direction of propagation, which is along $\mathbf{k}$. Alternatively, a magnetic plane wave of analogous design can be used to fully describe the solution since both fields are linked in this case to each other by purely algebraic relations:

$$\mathbf{H}(\mathbf{r}, t) = \frac{c}{\omega \mu_0 \mu(\omega)} \mathbf{k} \times \mathbf{E}(\mathbf{r}, t) \tag{2.15}$$

$$\mathbf{E}(\mathbf{r}, t) = \frac{c}{\omega \varepsilon_0 \varepsilon(\omega)} \mathbf{k} \times \mathbf{H}(\mathbf{r}, t) \tag{2.16}$$

$\mathbf{k}$ and ω are not independent of each other but rather satisfy the photonic dispersion relation:

$$\frac{\omega^2}{|\ \mathbf{k}\ |^2} = \frac{1}{\mu_0 \mu(\omega) \varepsilon_0 \varepsilon(\omega)} \tag{2.17}$$

With the assumption of nonmagnetic media ($\mu(\omega) = 1$) from now on and with the identity

$$c^2 = \frac{1}{\mu_0 \varepsilon_0} \tag{2.18}$$

the magnitude of $\mathbf{k}$ can be expressed in a way that is more convenient for the following considerations:

$$\mid \mathbf{k} \mid = \omega \sqrt{\mu_0 \varepsilon_0 \varepsilon(\omega)} = \mid \mathbf{k} \mid = \frac{\omega}{c} \sqrt{\varepsilon(\omega)} \tag{2.19}$$

2.1.2 Optical properties of conductors and insulators

As introduced in equation 2.1 the refractive index governs the macroscopic response of a material to an external EM field. This value, however, is in most cases complex, taking into account intrinsic loss-pathways. Also it usually is defined as a complicated function of frequency ω, since it is a superimposed description of dispersion phenomena occurring at multiple frequencies. Accordingly, the dielectric function $\varepsilon(\omega)$ must have poles only for frequencies with positive imaginary parts, and therefore satisfies the Kramers–Kronig relations. However, in the narrow frequency range that is studied in the framework of this thesis, the permittivity can be approximated as frequency-independent or by model functions. At a given frequency, the imaginary part of the complex dielectric function, $\tilde{\varepsilon}(\omega) = \varepsilon'(\omega) + i\varepsilon''(\omega)$, leads to absorption loss if it is positive and gain if it is negative. In Figure 2.1 a *schematic* overview *is given of the dielectric permittivity spectrum over a wide range of frequencies.*

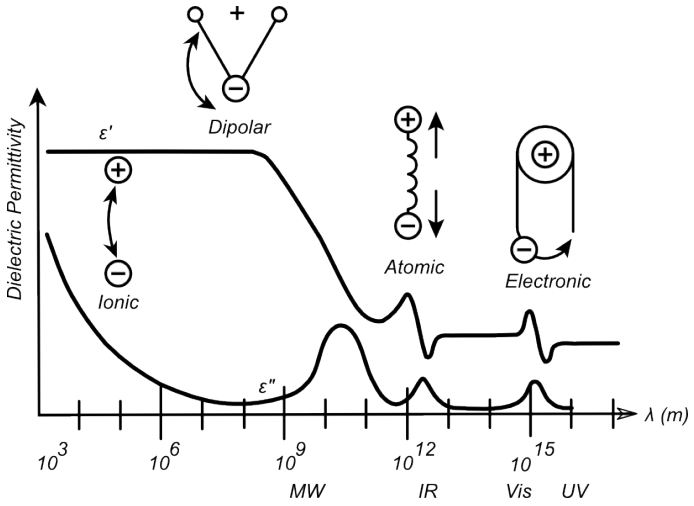

Figure 2.1: A dielectric schematic permittivity spectrum over a wide range of frequencies. ε' and ε'' denote the real and the imaginary part of the permittivity, respectively. Various processes are labelled on the image: ionic and dipolar relaxation, and atomic and electronic resonances at higher energies.

More generally, in the case of solids, the complex dielectric function is intimately connected to band structure. The primary quantity that characterises the electronic structure of any

crystalline material is the probability of photon absorption, which is directly related to the imaginary part of the complex optical dielectric function $\tilde{\varepsilon}(\omega)$.

Alternatively, the optical properties of materials can be characterised by the complex refractive index $\tilde{n}(\omega) = n(\omega) + i\kappa(\omega)$, with the real part n being the (ordinary) refractive index and the imaginary part κ being the extinction coefficient. This description is equivalent to the usage of the dielectric function of the material and both properties are converted into each other *via* the following equations[1]:

$$(n - i\mathbf{k})^2 = \varepsilon' + i\varepsilon'' = \tilde{\varepsilon} \tag{2.20}$$

$$\varepsilon' = n^2 - \kappa^2 \tag{2.21}$$

$$\varepsilon'' = 2n\kappa \tag{2.22}$$

It is therefore important to have an understanding of the complex optical properties, encoded in $\tilde{\varepsilon}$ for materials employed in this thesis. Two general categories of material need to be distinguished: *(1)* conductors (e.g. silver, gold) and *(2)* dielectrics/insulators (e.g. water, glasses, oxides, (conductive) polymers, proteins). In the latter the electrons are strongly localised at the atomic sites. Only substantial electric fields will create electron mobility. Therefore, insulators typically show a small positive value for ε' and an almost vanishingly small value for ε'' in the visible and infrared spectral range.

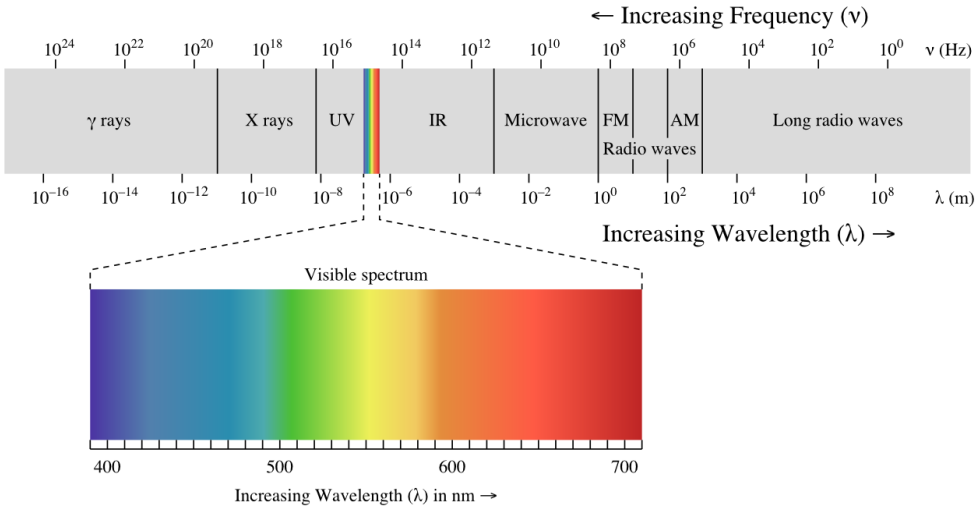

Figure 2.2: EM radiation is classified according to the frequency (or wavelength) of the light wave. This includes (in order of increasing frequency): natural EM waves, radio waves, microwaves, terahertz radiation, infrared (IR) radiation, visible light (Vis), ultraviolet (UV) radiation, X-rays and gamma rays. A small window of frequencies, called the visible spectrum or light, is sensed by the eye of various organisms, with variations of the limits of this narrow spectrum, hence referred to as the visible portion (highlighted above).

[1] The ω-dependence is still implied but suppressed from now on for better readability.

Metals and conductors in general, on the other hand, possess conduction band electrons that can easily move to different lattice sites under the influence of an external electric field. This behaviour at the microscopic level gives rise to many of their macroscopic characteristics like the typical metallic lustre, ductility, conduction of heat and electric currents. Thus metals feature a negative value for ε' and a smaller, but positive value for ε'' at visible and longer wavelengths.

The dielectric properties of metals can be described by the Drude model[4]. It works well for a spectral range starting from the visible up to the microwave regime. Amazingly, Drude developed his theory of electrical and thermal conduction prior to the development of quantum theory[26,27]. It is based on the kinetic theory of gases. Hence, metals are essentially described as a gas of electrons (i.e. electron-gas) governed by Newtonian mechanics. The average electron velocity is determined by the thermal energy of the metal. The electrons experience mutual collisions with each other after time intervals equal to the collision time τ. Other electron-electron interactions taking place between collisions are neglected. Ion-electron interactions, however, can not be fully ignored. This situation is summarised with the term "quasi-free" electron approximation. The response of the metal to an externally applied electric field is primarily determined by the acceleration imposed on the electrons. Within this framework the dielectric function of a metal as a function of the angular frequency of the external applied field is derived as:

$$\varepsilon(\omega) = 1 - \frac{\omega_p^2}{\omega^2 + i\frac{\omega}{\tau}} \tag{2.23}$$

The plasma frequency ω_p is given by

$$\omega_p = \sqrt{\frac{n_e e^2}{\varepsilon_0 m_e}} \tag{2.24}$$

where n_e is the electron density, e the electron charge and m_e the effective electron mass. Equation 2.24 can be applied to frequencies lower than the plasma frequency. If the frequency of the impinging EM wave approaches or exceeds the frequency of ω_p, the material exhibits transparent behaviour. This is true for the alkali metals in the UV, but different in other metals as other contributions to $\varepsilon(\omega)$ become significant which require further theoretical treatment based on quantum mechanics. This, however, would go beyond the scope of theory, relevant for this thesis.

2.1.3 Polarisation of light

Not only the material properties but also the properties of the light source itself affect the way light interacts with materials. In particular the spatial orientation of the polarisation of light has to be considered. The simplest manifestation of polarisation to visualise is that of a plane wave, which is a good approximation of most light waves (a plane wave is a wave with infinitely long and wide wave fronts). For plane waves Maxwell's equations, specifically Gauss's laws, impose the transversality requirement, that is to say the electric and magnetic field be perpendicular to the direction of propagation and to each other. Conventionally, when considering polarisation, only the electric field vector is described and the magnetic field is ignored since it is perpendicular to the electric field and proportional to it. The electric field vector of a plane wave may be arbitrarily divided into two perpendicular components labelled $\mathbf{E}$ (electric field vector) and $\mathbf{H}$ (magnetic field vector) (with $\mathbf{k}$ indicating the direction of travel). For a simple harmonic wave, where the amplitude of the electric vector varies in a sinusoidal manner in time, the two components have exactly the same frequency. However, these components have two other defining characteristics that can differ. First, the two components may not have the same amplitude. Second, the two components may not have the same phase, that is they may not reach their maxima and minima at the same time. For the purpose of this introductory chapter, however, the components are generally assumed to be of the same amplitude and also in-phase.

In principle the origin of different polarisation states lies in the nature of the radiation source, where most sources of EM radiation contain a large number of atoms or molecules that emit light. Therefore, natural sunlight and almost every other form of artificial illumination transmits light waves whose electric field vectors vibrate in all perpendicular planes with respect to the direction of propagation. Such a collection of waves, which have an equal distribution of electric field orientations for all directions, i.e. where the electric field vectors are not restricted to a single plane, is referred to as unpolarised light. While each individual wave may be linearly polarised, there is no preferred direction of polarisation when all the waves are averaged together. Polarisation is principally of importance as polarised light interacts with anisotropic materials, which is the basis for birefringence, for example. This is an optical phenomenon usually seen in crystalline materials. In such a case the polarised light is 'double refracted', as the refractive index in those materials is different for horizontally and vertically polarised light. This is to say, the polarisability of anisotropic materials is not equivalent in all directions. As a consequence, the material's anisotropy causes changes in the polarisation of the incident beam, and

is easily observable using certain optical techniques that use the effect of polarisation of light, e.g. cross-polar microscopy or polarimetry.

Light in the form of a plane EM wave, which has a uniform distribution of electric field orientations in only one direction, i.e. where the electric field vectors are restricted to a single plane, is said to be linearly polarised. The transverse electric field wave is accompanied by a magnetic field wave as illustrated in figure 2.3.

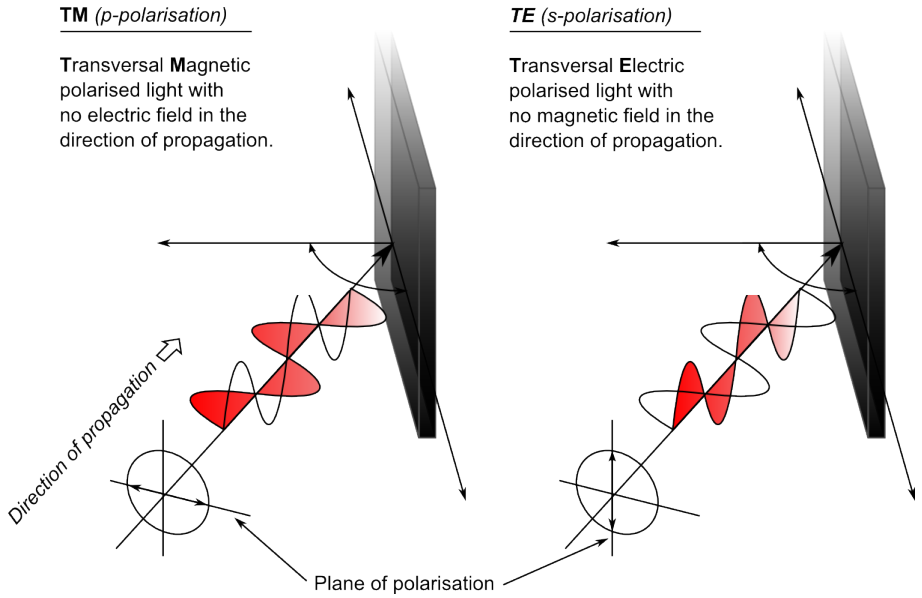

Figure 2.3: Schematic illustration of a linearly polarised plane electromagnetic wave. The transverse electric field wave is accompanied by a magnetic field wave as illustrated above. By convention, the polarisation of light is described by specifying the direction of the wave's electric field (coloured) being either in the plane if incidence (TM or p-polarised) or perpendicular to it (TE or s-polarised).

EM waves in materials, and in particular the guided-wave phenomena in waveguides or fibres show a polarisation dependency, which can be reduced to an analysis of two orthogonal linear polarisations. They are treated separately for the case of an ideal waveguide. The orientation of this two polarisations is defined by the orientation of the electric field component of the EM fields of a plane wave with respect to a plane interface. The component of the electric field parallel to this plane is termed p-like (parallel) and the component perpendicular to this plane is termed s-like (from *senkrecht*, German for perpendicular). Light with a p-like electric field is said to be p-polarised, π-polarised, tangential plane polarised, or in other words, to be a transverse-magnetic (TM) wave. Light with an s-like electric field is s-polarised, also known as σ-polarised or sagittal plane polarised, or most often it is called a transverse-electric (TE) wave. For a transverse magnetic (TM) wave the electric field oscillates in the plane of incidence. For a transverse electric (TE) wave, the same is true for the magnetic field. In both cases the electric and magnetic fields oscillate in the plane perpendicular to the direction of propagation $(\mathbf{k})$ of the plane wave. Figure 2.4 illustrates the definition in detail.

2.1.4 Electromagnetic waves at interfaces

The behaviour of EM waves at interfaces in terms of reflection and refraction of light was first studied in ancient times. In 130 A. D. Claudius Ptolemy measured the angles of incidence and refraction for several media but was not able to find a mathematical framework to describe his results. Later, but still long before the formulation of the EM theory of light by J. C. Maxwell, R. W. van Snell discovered the law of refraction empirically in 1621. It was later reformulated by R. Descartes in terms of sines. P. de Fermat derived the law from his principle of least time, stating that light propagates from one point in space to another along a route that takes the least time.

This interrelations may be exemplified by the illustration in figure 2.4, where two different materials (with different refractive indices n_1 and n_2, respectively), each occupying a semi-infinite half-space, share a common, flat interface at $z = 0$. In this example a light ray (representing the k-vector, $\mathbf{k}$, of the EM wave) is impinging upon the interface from the side of 'optically thinner' medium, penetrating into the 'optically thicker' material.

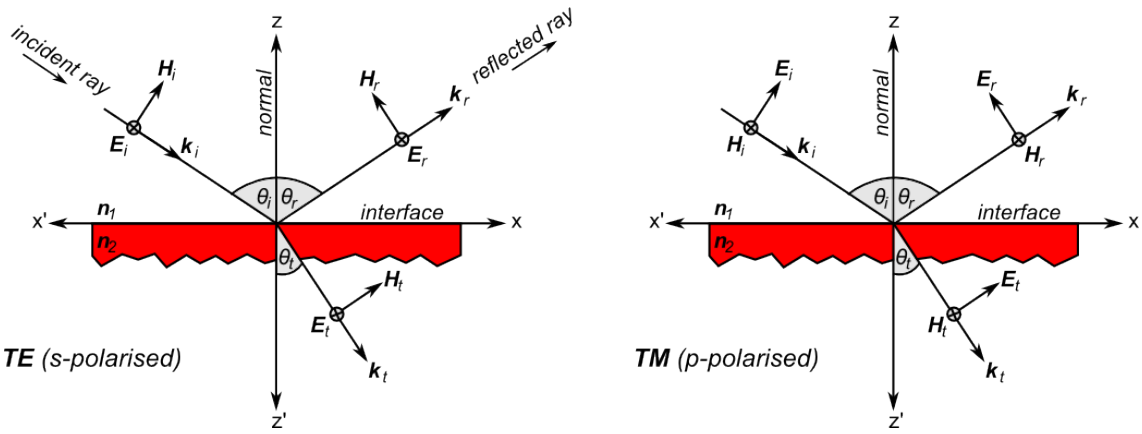

Figure 2.4: Reflection of a plane wave from a surface perpendicular to the page. The cases are illustrated for both TE polarised light (left), with s-components of the wave perpendicular to the plane of the page, and TM polarised light (right) where p-components of the wave are perpendicular to the surface.

For the case of a plane EM wave with an angle of incidence θ_i (measured from the surface normal) the angle of transmission θ_t can be found via Snell's law of refraction:

$$\frac{n_1}{n_2} = \frac{sin(\theta_t)}{sin(\theta_i)} \tag{2.25}$$

Reflection occurs at the angle of reflection θ_r, where $\theta_r = -\theta_i$. For $n_2 < n_1$, θ_t is always larger than θ_i, but θ_r always equals θ_i. In the case where the angle of tranmittance θ_t

would result in $\theta_t \geqq 90°$, no light is transmitted into the optically thinner medium and the full intensity is reflected. This condition is termed total internal reflection (TIR). The angle of incidence above which TIR occurs is called the critical angle $\theta_{critical}$. It is also given by Snell's law in the extreme case when the numerator on the right side of equation 2.25 becomes unity, and can be written as:

$$\theta_{critical} = arcsin(\frac{n_2}{n_1}) \tag{2.26}$$

Accordingly, the optical phenomenon of TIR occurs only when a ray of light strikes a medium boundary at an angle of incidence, θ_i, larger than the critical angle, $\theta_{critical}$, with respect to the normal to the surface. However, if θ_i > $\theta_{critical}$ then the light will change from being a normal propagating ray of light (crossing the boundary) to being bent away from the normal, so the angle of reflection θ_r is greater then the angle of incidence θ_i. Such reflection is commonly called internal reflection. The angle of transmission θ_t will then approach 90° for the critical angle of incidence $\theta_{critical}$. For angles of incidence $\theta_i > \theta_{critical}$, therefore, the total light beam power will be reflected back internally, and the TIR-condition is fulfilled. This, however, can only be achieved for light propagating in a medium with higher RI, n, and directed towards a medium with lower RI, n, see figure 2.5 for illustration of reflection at the film/cover-boundary.

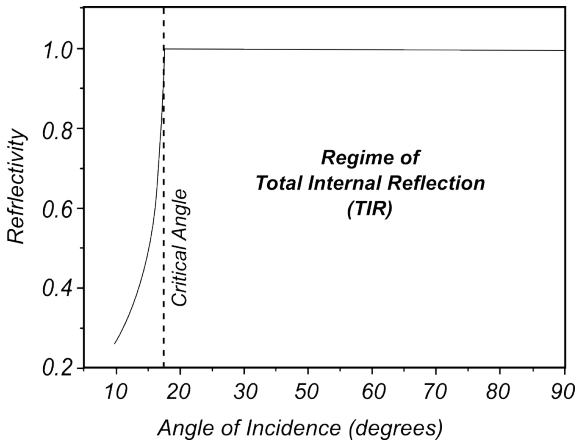

Figure 2.5: Reflectivity as a function of the incident angle, θ_i. The critical angle, $\theta_{critical}$, denotes the lowest angle at which total internal reflection occours. It is given by $sin(\theta_{critical}) = \sqrt{\frac{\varepsilon_1}{\varepsilon_2}}$. This particular curve was calculated with $\varepsilon_1 = 1.778$, $\varepsilon_2 = 3.4036$.

Since reflection and transmission constitute competing propagation channels, the question arises how the impinging intensity is split up quantitatively between the two. Fresnel has solved this problem. His deduction [10,36] is based on the continuity conditions for the tangential (interfacial) components of $\mathbf{E}$ and $\mathbf{H}$. This is expressed in Snell's Law of Refraction, that follows from Fermat's principle of least time, which in turn follows from the

propagation of light as EM waves. Certainly, the different polarisations of the transversal field have to be distinguished for these calculations, since they behave differently at the interface.

With its wave vector (**E** and **H**) situated within the $x-z$-plane, any arbitrary plane electric field can be decomposed into a component that is lying within the $x-z$-plane and a orthogonal component that runs parallel to the y-axis. The latter corresponds to an electric field of s-polarisation (TE-mode). The in-plane component is of p-polarisation (TM-mode). Fresnel's formulae express the ratio of the electric field amplitude of the reflected (or transmitted) wave divided by the incident wave amplitude for the two polarisations:

$$r_{TE} = \frac{n_2 cos(\theta_i) - n_1 cos(\theta_t)}{n_2 cos(\theta_i) + n_1 cos(\theta_t)} \qquad t_{TE} = \frac{2n_1 cos(\theta_i)}{n_2 cos(\theta_i) + n_1 cos(\theta_t)} \tag{2.27}$$

$$r_{TM} = \frac{n_2 cos(\theta_t) - n_1 cos(\theta_i)}{n_2 cos(\theta_t) + n_1 cos(\theta_i)} \qquad t_{TM} = \frac{2n_1 cos(\theta_i)}{n_2 cos(\theta_t) + n_1 cos(\theta_i)} \tag{2.28}$$

Here r represents the reflected intensity, whereas t stands for the transmitted intensity of the individual polarised component of light.

2.1.5 Brewster's Angle

One in particular interesting phenomenon related to the discriminative behaviour of TM and TE polarised light at the interface (of non-magnetic materials) of different refractive index materials is given at the so called polarisation angle. At this angle of incidence, light with a particular polarisation is perfectly transmitted through a surface, with no reflection. The angle at which this occurs is named after the Scottish physicist, Sir David Brewster (1781–1868). He discovered that light, when it moves between two transparent dielectric (or insulating) media of differing refractive index one particular angle of incidence exists where light with one particular polarisation cannot be reflected. This angle of incidence is referred to as Brewster's angle, θ_B.

The one polarisation state that is perfectly transmitted at this angle is the TM polarisation (p-polarisation) for which the electric field of the light waves lies in the same plane as the incident ray and the surface normal (i.e. the plane of incidence). Therefore, an interface may be used as polarisation device (i.e. polariser) when unpolarised light is impinged at the surface at Brewster's angle; the reflected portion of light is always purely TE polarised (s-polarisation) . Although s and p polarisation states were not named for this convention, it may be convenient to remember that s-polarised light will 'skip' off a Brewster boundary and p-polarised light will 'plunge' through, as sketched in figure 2.6.

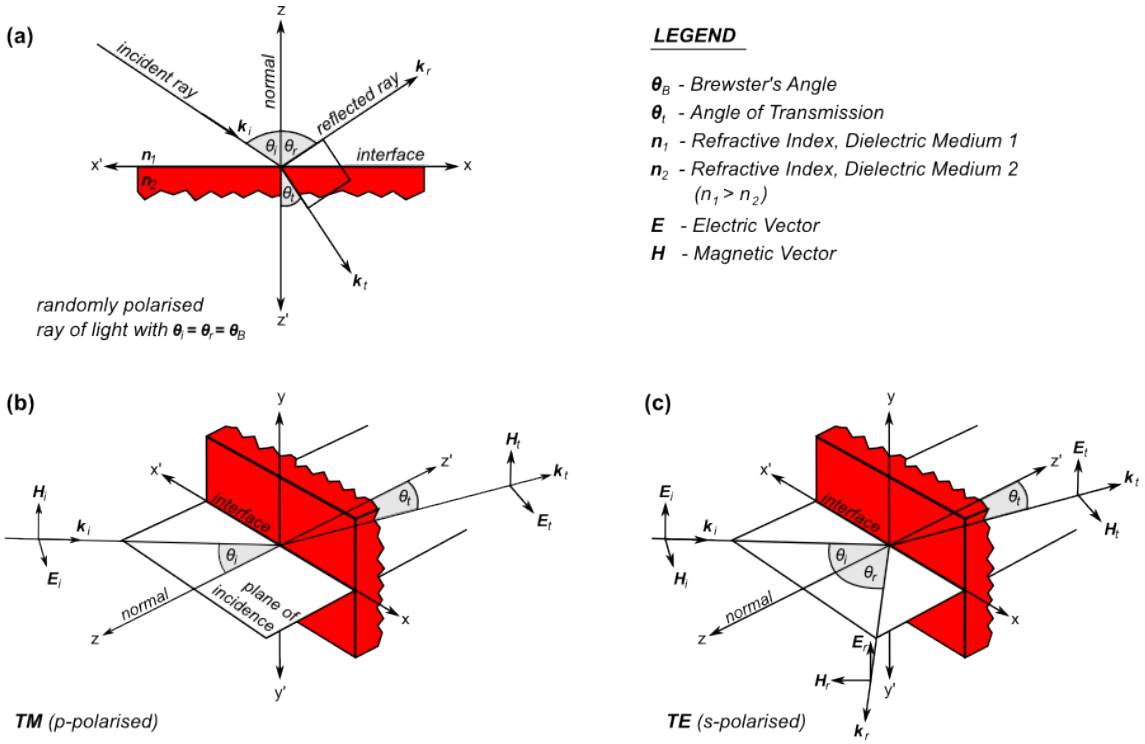

Figure 2.6: (a) Illustration of a randomly polarised ray of light impinging upon an interface at Brewster's angle, given when the **k***-vectors of the reflected and the transmitted light form a 90° angle to each other. (b) Linearly TM-polarised (***E***-vector parallel to the plane of interface). No light is reflected. (c) Linearly TE-polarised (***E***-vector perpendicular to the plane of interface). For n_1 being air and n_2 being glass, approximately 15% of the impinged light intensity is reflected and 85% transmitted.*

The physical mechanism for this can be qualitatively understood from the manner in which electric dipoles in the media respond to TM light. One can imagine that light incident on the surface is absorbed, and then re-radiated by oscillating electric dipoles at the interface between the two media. The polarisation of freely propagating light is always perpendicular to the direction in which the light is travelling. The dipoles that produce the transmitted (refracted) light oscillate in the polarisation direction of that light. These same oscillating dipoles also generate the reflected light. However, dipoles do not radiate any energy in the direction along which they oscillate. Consequently, if the direction of the refracted light is perpendicular to the direction in which the light is predicted to be specularly reflected, the dipoles will not create any reflected light. Since, by definition, the s-polarisation (TE) is parallel to the interface, the corresponding oscillating dipoles will always be able to radiate in the specular-reflection direction. This is why there is no Brewster's angle for TE-polarised light.

The value for the unique angle θ_B at which the reflected light waves are all polarised into a single plane can be easily calculated from utilising Fresnel's equations; the reflection coefficient r_{TM} (TM radiation) will equal zero when the indices of refraction are equal, so $n_1 = n_2$ or

$$n_2 cos(\theta_2) = n_1 cos(\theta_1) \tag{2.29}$$

which, after solving for $cos^2(\theta_1)$ in Snell's law, yields

$$\theta_B = tan^{-1}(\frac{n_2}{n_1}). \tag{2.30}$$

θ_B is the Brewster angle as measured from the normal. Equation 2.30 is known as Brewster's law.

Since the refractive index for a given medium changes depending on the wavelength of light, Brewster's angle and the reflectivity (i.e. reflected intensity, $\frac{I_{reflected}}{I_{in}}$) will also vary with the light's wavelength. Brewster showed that this angle, however, is a function of the refractive index, and can therefore be utilised to easily measure the refractive index of a material. Although Brewster's angle is generally presented as a zero-reflection angle in textbooks from the late 1950s onwards, as illustrated below in figure 2.7, it truly is a polarising angle.

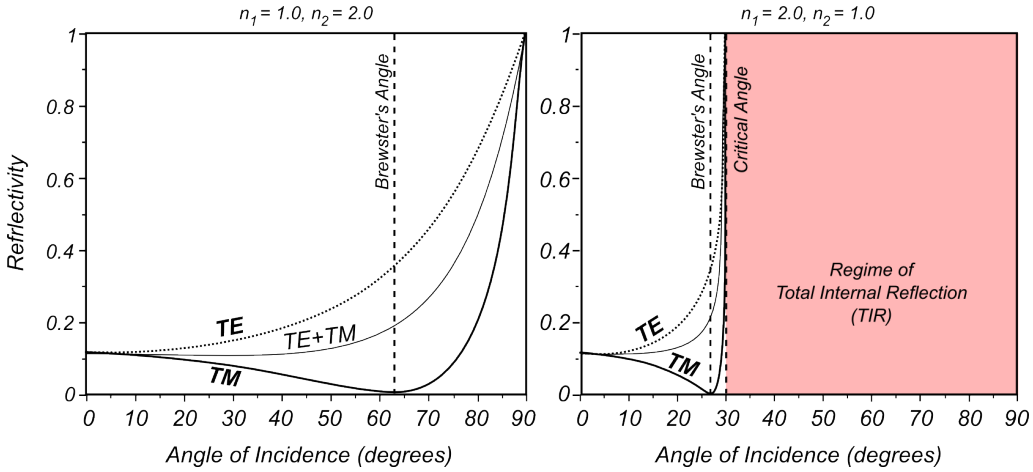

Figure 2.7: Fresnel reflected intensity (i.e. reflectivity, $\frac{I_{reflected}}{I_{in}}$) at an interface of two materials with $n_1 = 1.0$ and $n_2 = 2.0$ at $\lambda = 632.8nm$ versus angle of incidence θ_i from air. For TM-polarisation, the reflectivity vanishes at the Brewster angle of incidence, whereas the reflectivity increases monotonously for TE-polarisation with increasing incidence angle.

After discussing the phenomenon of light polarisation at material interfaces, it may be appropriate at this point to also raise the question provide a deeper insight into the behaviour of light at an interface. Especially the behaviour of light at, but also after exceeding the critical angle of TIR is fundamental for the understanding of evanescent field-based optical devices. The following subsection will therefore enter in this topic.

2.1.6 Goos-Hänchen shift

One particularly interesting feature associated with light being incident on a flat surface in an angular range above TIR is the violation of the specular reflection law. The Law of Reflection of a light ray incident upon a mirror ($\theta_i = \theta_r$) was first formulated by Euclid around $300\ B.C.$ in his book Catoptrics[35]; it has been a tenet of geometrical optics ever since. The law of specular reflection simply expresses that the incoming and reflected beam meet exactly at the interface, and that the reflected angle is equal to the incoming angle. However, more recently, a small angular deviation of the Law of Reflection has been predicted for a physical light beam when this is regarded as the implementation of a ray[67,3,16,2].

In the case of a beam of light being reflected at the air-glass interface, below the critical angle of incidence $\theta_{critical}$ one part is reflected and one part is transmitted. Above $\theta_{critical}$, total internal reflection will occur at the interface between dielectric materials with different RIs. That shows the first violation of the specular reflection law: the reflected beam is shifted a little in the propagation direction which is equal to a slightly lowered reflection plane (dashed line in figure 2.8(b)). This shift was conjectured by Newton 300 years ago, but only measured in 1947 by Goos and Hänchen[32].

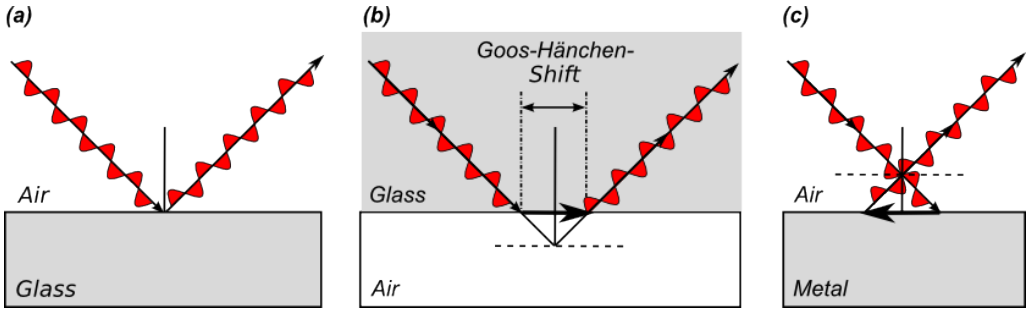

Figure 2.8: (a) Specular reflection, (b) internal reflection, (c) metallic reflection.

The so-called Goos-Hänchen effect is the displacement, with respect to geometrical reflection, of a TE or TM polarised (s- and p-polarised, respectively) light beam when it is reflected by a medium with a complex and angle-dependent reflection coefficient. This displacement generally lies in the order of $10 - 1000nm$. During the Goos-Hänchen shift at total reflection, light waves will consequently enter a few nanometres into the surrounding medium. This causes a phase shift and also higher losses, in the case where the absorption of the surroundings is higher than the absorption of the medium the wave is travelling in (compare illustrations (a) and (b) in figure 2.8.

The second case of violation of the specular reflection law can be observed if the reflection is monitored at a metallic surface (e.g. reflecting layer). High-precision experiments with a

displacement sensitivity in the nanometre range have revealed the[61,60] shift to be directed backwards. In a metal, the refractive index has a large imaginary component and the free electrons, excited by the incoming light, oscillate in anti-phase. Therefore, the light can barely penetrate the metal and it looks like the mirror plane is closer (schematically illustrated in figure 2.8 (c)).

2.2 Evanescent Wave Optics

The term 'evanescent wave optics' summarises a variety of optical phenomena related to surface-bound, standing and exponentially (perpendicular to the interface between two media with different optical properties) decaying EM waves.

These evanescent waves form the basis of many experimental techniques for scientific as well as technological applications that characterise properties of, or in close proximity, to surfaces. Changes in the optical properties of the medium within the decay length of the field cause a change in the decay length of the field. This response is exploited by various types of spectroscopies such as total internal reflection fluorescence microscope (TIR-FM) [13].

In the framework of this thesis two main extensions of this concept, based on the optical phenomena arising from TIR, are combined in a synergistic manner to form a sophisticated experimental probing technique. The first one is concerned with surface plasmon polariton (SPP) or surface plasmon resonance (SPR) or just surface plasmon (SP). SPs are collective charge oscillations which can be excited for example at the interface between a conducting and a dielectric material. The second technique deals with guided optical waves, so called optical waveguide modes, which can be observed once an additional material layer with sufficient optical thickness is interfaced with the TIR-exhibiting material. In order to provide the required background knowledge to make these techniques completely accessible, further theoretical treatment of optical waves at interfaces is presented in the following subsections.

2.2.1 The Evanescent Wave

The term 'evanescent' is derived from the Latin verb 'evanescere', and means 'tending to vanish', which is appropriate because the intensity of evanescent waves decays exponentially (rather than sinusoidally) with distance from the interface at which they are formed. Evanescent waves, in general, are near-field standing waves which appear when sinusoidal waves are totally internally reflected from an interface at an angle greater

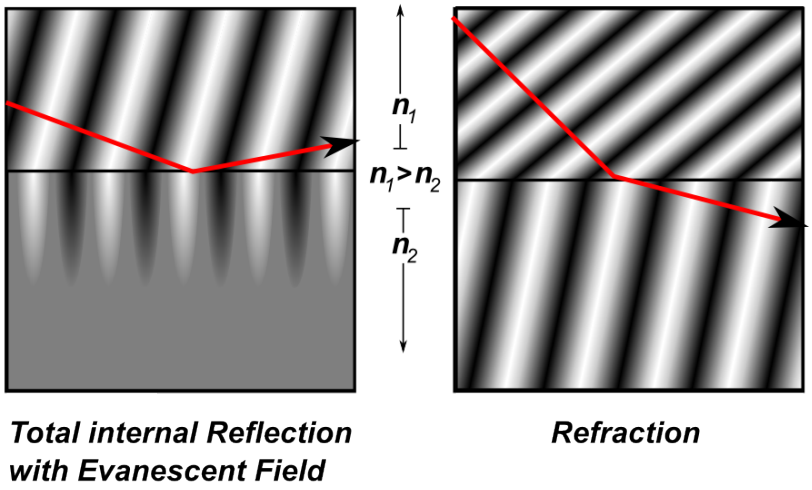

Figure 2.9: Left: Travelling EM waves in a medium undergo TIR at its boundary because they hit the interface at an angle equal or greater than the critical angle ($\theta_i > \theta_{critical}$) (for a detailed description, see subsection 2.1.4), accordingly the refracted light beam disappears. Surprisingly, when the light wave is totally reflected, there are still waves present in the less dense medium. Although no net energy is transferred through the interface under conditions of TIR, an optical disturbance occurs outside the material's surface which takes the form of an 'evanescent wave'. Thus only a spatially very restricted volume, very close to the interface is illuminated by the evanescent wave. The physical explanation for the existence of the evanescent wave is that the electric and magnetic fields cannot be discontinuous at a boundary, as it would be the case if there was no evanescent wave-field. Right: If the TIR condition is not fulfilled, the waves are refracted and propagate through the lower index medium.

than the critical angle $\theta_{critical}$. They are formed at the boundary between two media with different dielectric properties, and consequently with different properties in respect of wave motion. Evanescent waves are most intense within one-third of a wavelength from the surface of formation, as illustrated in figure 2.10 below.

The rigorous mathematical treatment of this problem shows that the electric field along the propagation direction at the interface is still oscillating as usual whereas its component perpendicular to the interface is decaying exponentially. The electric field strength of this evanescent mode (i.e. a standing wave) in z-direction is given by:

$$\mathbf{E}(z) = \mathbf{E}_0 e^{-\frac{z}{l_p}} \tag{2.31}$$

The decay length, or penetration depth (into the optically thinner medium), l_p, is of the order of the wavelength, λ, of the incident light wave. The distance beyond the interface, where the intensity decays to $\frac{1}{e}$ (approximately 37%) of the starting amplitude is described by the following equation:

$$l_p = \frac{\lambda}{2\pi n_1 \sqrt{sin^2\theta_i - (\frac{n_2}{n_1})^2}}, \quad \theta_i > \theta_{critical} \tag{2.32}$$

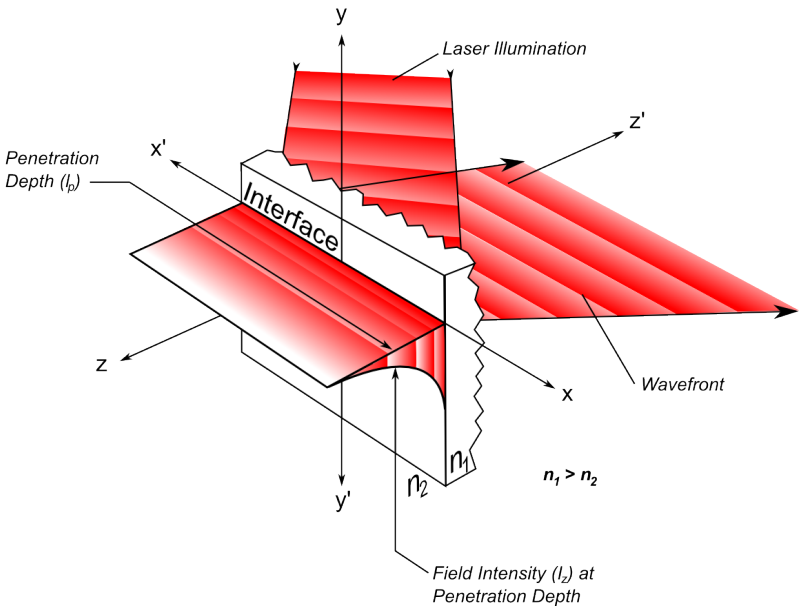

Figure 2.10: TIR of a plane wave of wavelength λ at the surface of a medium, n_1, in contact with a dielectric medium, n_2, where $n_2 < n_1$. For incident angles $\theta_i > \theta_{critical}$ the evanescent field at the interface decays exponentially into the dielectric with a penetration depth l_p. While wave solutions have real wave numbers, for evanescent modes they are purely imaginary.

Here n_1 and n_2 donate the refractive indices of the two dielectric media ($n_1 > n_2$) and θ_i represents the angle of incidence of the light.

2.2.1.1 Polarisation dependence

Evanescent wave intensity at the interface $(z = 0)$ is a function of both the incident angle and the polarisation components of the light beam. The intensities at $z = 0$ observed for polarised vibration vectors are discussed in terms of a coordinate system with the plane of incidence (the $x - z$ plane) defined as being parallel to the exciting light beam.

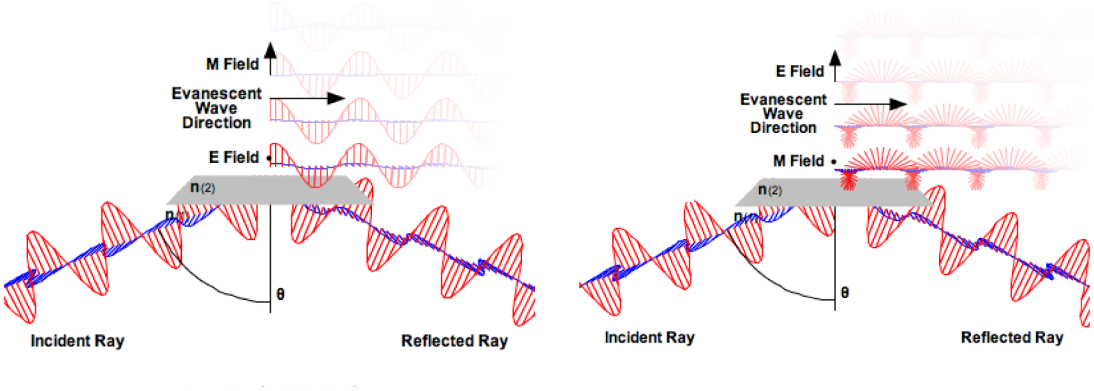

Figure 2.11: The evanescent electric field vector for TE-polarised incident light is perpendicular to the plane of incidence (left). A non-zero longitudinal component and phase lag manifests the TM-polarised incident light, which has an evanescent electric field vector direction that remains in the plane of incidence. The longitudinal component induces the p-polarised light electric field vector to 'rotate' along the interface and produce elliptical polarisation of the evanescent field in the plane of propagation (right).

The evanescent electric field vector for s-polarised incident light is perpendicular to the plane of incidence. A non-zero longitudinal component and phase lag is observed for the p-polarised incident light, which has an evanescent electric field vector direction that remains in the plane of incidence. The longitudinal component induces the TM-polarised light electric field vector to 'rotate' along the interface and produce elliptical polarisation of the evanescent field in the plane of propagation. When the incident angle is reduced from the super-critical range to the critical angle and lower, the longitudinal component disappears and the electric field component in the x-direction simultaneously vanishes.

The evanescent field intensities at the interface $(z = 0)$ for the incident TM- and TE-components are complex expressions given by the following series of equations:

$$I_x = \frac{(4cos^2(\theta))(sin^2(\theta) - (\frac{n_2}{n_1})^2)}{(1 - (\frac{n_2}{n_1})^2)\left[(1 + (\frac{n_2}{n_1})^2)sin^2(\theta) - (\frac{n_2}{n_1})^2\right]} \tag{2.33}$$

$$I_y = \frac{4cos^2(\theta)}{1 - (\frac{n_2}{n_1})^2} \tag{2.34}$$

$$I_z = \frac{(4cos^2(\theta))sin^2(\theta)}{(1 - (\frac{n_2}{n_1})^2)\left[(1 + (\frac{n_2}{n_1})^2)sin^2(\theta) - (\frac{n_2}{n_1})^2\right]} \tag{2.35}$$

where I is the orientation-dependent evanescent field intensity. For TE-polarised incident light, the total evanescent intensity is equal to the y-component, I_y, while the evanescent intensity for p-polarised incident light is composed of both the x and z components (I_x and I_z). As discussed above, the y-intensity is linearly polarised, but the x and z intensities are elliptically polarised due to the fact that the electric fields are $90°$ out of phase with each other. A mathematical description of the evanescent wave is provided by considering the amplitude of the electric field in z-direction. In this context, the EM field $\mathbf{E}$ of an EM plane wave, travelling in in a medium with refractive index n can be expressed as

$$\mathbf{E} = \mathbf{E}_0 e^{i(\omega t - \mathbf{k}\cdot\mathbf{r})} = \mathbf{E}_0 e^{i(\omega t - \mathbf{k}_x x - \mathbf{k}_y y - \mathbf{k}_z z)} \tag{2.36}$$

with the amplitude of the electric field donated as $\mathbf{E}_0$, the angular frequency ω, the wavevector $\mathbf{k}$, the position vector $\mathbf{r} = (x, y, z)$ and $i = \sqrt{-1}$. As it is apparent from equation 2.36, a travelling wave is only represented if the exponent is complex.

The magnitude of the wave vector $\mathbf{k}$, with its direction parallel to the direction of wave propagation, is given by

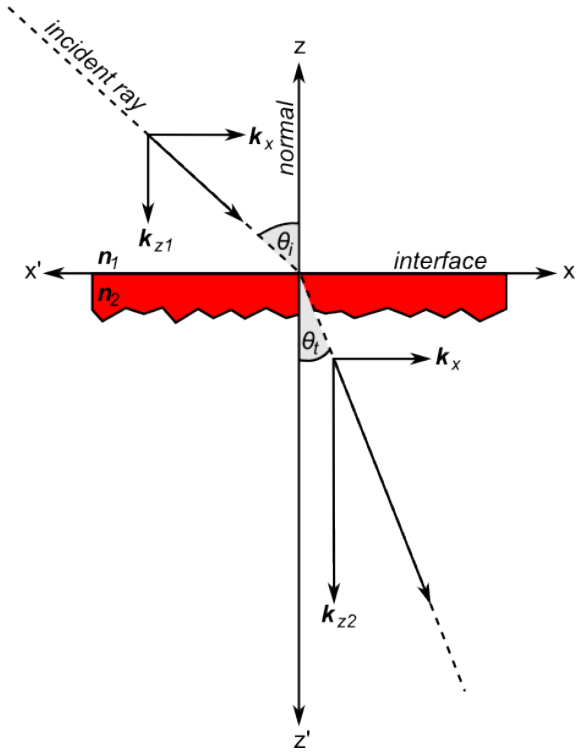

Figure 2.12: Schematic illustration of the wave vector components and their magnitudes for the evanescent wave.

$$\mathbf{k} = \sqrt{\mathbf{k}_x^2 + \mathbf{k}_y^2 + \mathbf{k}_z^2} = n\frac{2\pi}{\lambda} = n\frac{\omega}{c} \tag{2.37}$$

where λ and c are the wavelength and propagation velocity in vacuum, respectively. Considering the refraction of such a wave at an interface between two media with refractive indices n_1 and n_2, respectively, and choosing $\mathbf{k}_y = 0$ to reduce the problem to two dimensions, Snell's law holds

$$n_1 sin(\theta_i) = n_2 sin(\theta_t) \tag{2.38}$$

or, equivalently,

$$\mathbf{k}_{x1} = \mathbf{k}_{x2} \equiv \mathbf{k}_x \tag{2.39}$$

By combining the equations ($\mathbf{k} = \sqrt{\mathbf{k}_x^2 + \mathbf{k}_y^2 + \mathbf{k}_z^2} = n\frac{2\pi}{\lambda} = n\frac{\omega}{c}$) and ($\mathbf{k}_{x1} = \mathbf{k}_{x2} \equiv \mathbf{k}_x$) the component of the wavevector $\mathbf{k}_z$ perpendicular to the interface can be expressed as :

$$\mathbf{k}_{z2}^2 = n_1^2 \left(\frac{2\pi}{\lambda}\right)^2 \left(\frac{n_2^2}{n_1^2} - sin^2(\theta_i)\right) \tag{2.40}$$

Given that $n_1 > n_2$, from equation 2.40 it follows that for $sin(\theta_i) > n_2/n_1$ the right side of equation is negative, and, consequently, $\mathbf{k}_z$ is purely imaginary.

EM evanescent waves have been used to exert optical radiation pressure on small particles in order to trap them for experimentation, i.e. near-field optical micro-manipulation

(optical tweezers), or to cool them to very low temperatures. This work was first pioneered in 1992[81,80]. It has been shown that the field can be coupled to particles in proximity on the order of 100 nanometres to the surface. A recently updated and more sophisticated version of evanescent field optical tweezers is termed as Lens-less Optical Trapping (LOT)[30]. Other emerging applications include the application of evanescent waves to illuminate very small objects such as biological cells for microscopy (as in the total internal reflection fluorescence microscope) or using the evanescent wave from an optical fibre in gas sensors.

More generally, practical applications of evanescent waves can be classified in the following way.

(1) Those in which the energy associated with the wave is used to excite some other phenomenon within the region of space where the original travelling wave becomes evanescent (for example, as in total internal reflection fluorescence microscope).

(2) Those in which the evanescent wave 'couples' two media in which travelling waves are allowed, and hence permits the transfer of energy between the media, even though no travelling-wave solutions are allowed in the region of space between the two media. An example of this is so-called 'wave-mechanical tunnelling'. This second type of application is known generally as 'evanescent wave coupling'.

2.2.2 Evanescent Wave Coupling

In optics, evanescent wave coupling is a process by which EM waves are transmitted from one medium to another by means of the evanescent, exponentially decaying EM field (for details see section 2.2.1). This phenomenon is describable by quantum mechanics and in this context it is referred to as tunnelling. This phenomenon not only affects EM photons (whether in the form of visible light or microwaves) but is also an essential component of physical processes like radioactivity and nuclear fusion.

Wave-mechanical tunnelling (also called quantum-mechanical tunnelling, quantum tunnelling, and the tunnel effect) is an evanescent wave coupling effect that occurs in the context of quantum mechanics because the behaviour of particles is governed by Schrödinger's wave-equation. All wave equations exhibit evanescent wave coupling effects if the conditions are right. Wave coupling effects, mathematically equivalent to those called 'tunneling' in quantum mechanics, can occur with Maxwell's wave-equation (both with light and with microwaves).

Traditionally, imaginary parts have been ignored as 'imaginary numbers do not describe any real physical quantity', but it was discovered that purely imaginary solutions, that are called

evanescent modes, are mathematically identical with the solutions of the Schrödinger's equation, the fundamental equation describing quantum mechanical behaviour in the case of tunnelling. Moreover, evanescent modes are not just a theoretical concept, but occur in a number of physical devices that are collectively called photonic barriers. This can, for instance, be an air gap between double prisms to produce a condition called frustrated total reflection, a phenomenon hinted at by Newton.

2.2.3 Frustrated total internal reflection

Under 'ordinary conditions' it is true that the creation of an evanescent wave does not affect the conservation of energy, i.e. the evanescent wave transmits zero net energy. However, if a third medium with a higher refractive index than the second medium is placed within less than several wavelengths distance from the interface between the first medium and the second medium, the evanescent wave will be different from the one under 'ordinary conditions' and it will pass energy across the second into the third medium.

If two glss prisms are placed together with a small gap containing a less refracting substance (air, for instance), it is found that a small proportion of the light that should bounce back in the first prism (when it is at an angle that generates TIR) in fact 'jumps the gap', thus tunnelling through the gap into the second prism. Purely imaginary solutions of the wave equation seem to imply a zero shift in the phase of the wave – which would mean that the wave spent zero time in the barrier, crossing it instantaneously (or perhaps more accurately getting from one side of the barrier to the other without crossing the intervening space).

There are various TIR-based applications in science and technology making use of the possibility to access evanescent fields (e.g. Total internal reflection microfluorimetry and Fingerprint-scanning devices, which use frustrated total internal reflection in order to record an image of a person's fingerprint without the use of ink. Also the new generation of multi-touch screens uses frustrated total internal reflection in combination with a camera and appropriate software to pick up multiple targets.

2.3 Surface Plasma Wave

This section discusses an extension of the basic principle of evanescent waves, which is concerned with the excitation of surface plasma waves (also called surface plasmon resonance (SPR)) at the interface between a noble metal and a dielectric medium[14]. In such a configuration the (nearly) free electron gas in the metal acts as a resonator driven

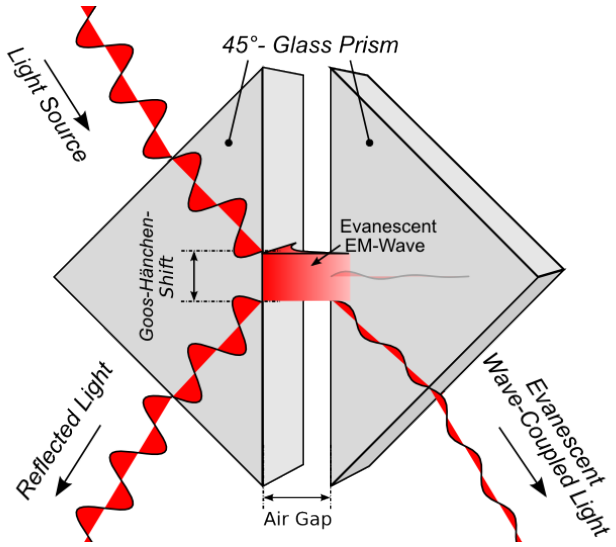

Figure 2.13: A transparent, low refractive index material (i.e.air) is sandwiched between two prisms of another material (i.e. glass). This allows the beam to 'tunnel' through from one prism to the next in a process very similar to quantum tunnelling while at the same time the emerging evanescent wave will pass energy across the air-gap into the glass medium.

by the incoming photon field, and giving rise to substantial intensity enhancements[50? ,90] compared to the mere dielectric configuration discussed in the previous section. Plasmons, as such, are quasi-particles, i.e. density waves of the charge carriers oscillating in a conducting medium such as a metal, semiconductor, or plasma (schematically depicted in figure 2.14).

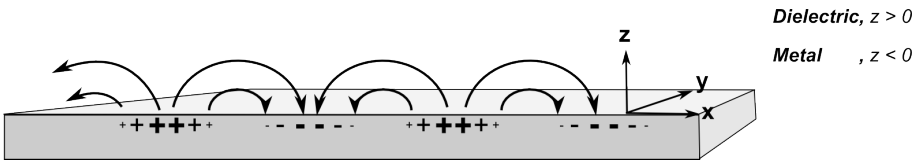

Figure 2.14: Scheme of a p-polarised surface wave and its electric field on the interface (dielectric/metal) between two semi-infinite half-spaces. The oscillating charge density being associated with the electromagnetic wave is indicated.

In this case, again, one is dealing with an evanescent, i.e. bound, EM mode propagating along the metal/dielectric interface. A number of examples is given of how this 'surface light' can be employed to monitor interfacial properties and processes sensitively, or to characterise the optical properties of ultra-thin coatings deposited onto the interface[6].

Plasmons play a major role in the optical properties of metals. Light of frequency below the plasma frequency is reflected, because the electrons in the metal screen the electric field of the light. Light of frequency above the plasma frequency it is transmitted, because the electrons cannot respond fast enough to screen it. In the majority of metals, the plasma frequency lies in the ultraviolet spectral range, making these materials appear shiny in the visible range. Some metals, however, have plasma frequencies in the visible range (e.g. gold and copper), giving them their distinctive colour. For doped semiconductors, the

plasma frequency usually lies in the infrared.

In the early twentieth century, the excitation of SPR, initially termed Wood's Anomaly, was observed as anomalous reflective patterns when polarised light was incident on a metal grating[95]. This optical phenomenon was attributed to the resonant coupling of the incoming EM field and the electron plasma on a metal surface. The resulting wave originates from the interaction of photons from the transverse magnetic-polarised (TM) light with the oscillation of free electrons in the metal. Research on surface plasmon resonance was originally limited to diffraction gratings[98,101,42,74]. Since the sixties of last century research has flourished in numerous fields[41,92,43] including non-linear optics (e.g. Raman scattering and second harmonic generation[23,82,96]), meteorology (e.g. surface roughness[100,69,70,29]) and optical properties of metals[77], SPP optics on nano-structured objects (e.g. metal nanoparticles[91,34], chains of metal nanoparticles[31,76] and sub-wavelength arrays of holes[55]) lasers[21], optical data storage[24], photonic band-gap structures[8,7], sub-diffraction imaging[28], surface plasmon-based integrated optics[52] and optical sensors[39,78,15,99,62,63,57].

Essential for the generation of SPs is the presence of (nearly) free electrons at the interface of two materials – in practise this almost always implies that one of these materials is a metal where free conduction electrons are abundant. This condition follows naturally from the analysis of a semi-infinite metal-dielectric interface by Maxwell's equations.

On an interface as sketched in figure 2.14, the electric field $\mathbf{E}$

$$\mathbf{E} = \mathbf{E}_0 e^{i(\mathbf{k}_x x - \omega t)} \left\{ \begin{array}{ccc} (1 & 0 & \frac{\mathbf{k}_x}{\mathbf{k}_{z,dielectric}}) e^{-i\mathbf{k}_{z,dielectric} z} \\ (1 & 0 & \frac{-\mathbf{k}_x}{\mathbf{k}_{z,metal}}) e^{+i\mathbf{k}_{z,metal} z} \end{array} \right\} for \left\{ \begin{array}{l} z > 0 \\ z < 0 \end{array} \right. \tag{2.41}$$

and the magnetic field $\mathbf{H}$

$$\mathbf{H} = \frac{\omega}{c} E_0 e^{i(\mathbf{k}_x x - \omega t)} \left\{ \begin{array}{ccc} (0 & \frac{-\varepsilon_{dielectric}}{\mathbf{k}_{z,dielectric}} & 0) e^{-i\mathbf{k}_{z,dielectric} z} \\ (0 & \frac{\varepsilon_{metal}}{\mathbf{k}_{z,metal}} & 0) e^{+i\mathbf{k}_{z,metal} z} \end{array} \right\} for \left\{ \begin{array}{l} z > 0 \\ z < 0 \end{array} \right. \tag{2.42}$$

fulfil Maxwell's equations and the continuity relations for the tangential electric and magnetic field components and for the normal components of the electric displacement, when

$$\mathbf{k}_x^2 + \mathbf{k}_{z,j}^2 = \left(\frac{\omega}{c}\right)^2 \varepsilon_j \quad j : dielectric, metal \tag{2.43}$$

In the case $\varepsilon_{dielectric} \geq 1$ and $\varepsilon'_{metal} < 0$, $\mid \varepsilon'_{metal} \mid > 1 > \varepsilon''_{metal} > \varepsilon_{dielectric}$, $\mathbf{k}_{zj}$ becomes

imaginary or complex, which means the electric field having its maximum in the surface at $z = 0$ with exponential decay into the media. This is characteristic for surface waves. SPs propagate along the interface and are characterised by the (complex) propagation constant β, this leads to the dispersion relationships (i.e. the energy-momentum relation) for surface plasmons at a metal/dielectric interface:

$$\mathbf{k}_x^2 + \mathbf{k}_{z,dielectric}^2 = \left(\frac{\omega}{c}\right)^2 \varepsilon_{dielectric} \tag{2.44}$$

$$\mathbf{k}_{z,dielectric}^2 = \sqrt{\varepsilon_{dielectric}\left(\frac{\omega}{c}\right)^2 - \mathbf{k}_x^2} \tag{2.45}$$

$$\mathbf{k}_x = \frac{\omega}{c}\sqrt{\frac{\tilde{\varepsilon}_{metal}\varepsilon_{dielectric}}{\tilde{\varepsilon}_{metal} + \varepsilon_{dielectric}}} = \frac{2\pi}{\lambda}\sqrt{\frac{\tilde{n}_{metal}^2 n_{dielectric}^2}{\tilde{n}_{metal}^2 + n_{dielectric}^2}} = \beta \tag{2.46}$$

where λ is the wavelength, ω is the angular frequency, c is the speed of light in vacuum, $n_{dielectric}$ is the refractive index of the dielectric and $\tilde{n}_{metal}$ is the (complex) refractive index of the metal.

A few details are noteworthy: (1) In the usual treatment, ω is taken to be real. Since $\tilde{n}_{metal}$ is complex, $\tilde{\mathbf{k}}_x$ is also complex, i.e. $\tilde{\mathbf{k}}_x = \tilde{\mathbf{k}}'_x + i\tilde{\mathbf{k}}''_x$. As a consequence, SP modes propagating along a metal/dielectric interface exhibit a finite propagation length, L_x , given by $L_x = \frac{1}{\mathbf{k}''_x}$. This decay has a strong impact on lateral resolution that is desirable in order to characterise laterally structured samples investigated with plasmon light in a microscopic setup. (2) The frequency (spectral) range of interest is given by:

$$\sqrt{\frac{\tilde{n}_{metal}^2 n_{dielectric}^2}{\tilde{n}_{metal}^2 + n_{dielectric}^2}} \geq \sqrt{n_{dielectric}^2} \tag{2.47}$$

This has two important consequences. The first can be seen from equation 2.45. Inserting equation 2.47 shows that in this case the z-component of the SP wave vector is purely imaginary. The surface plasmon is a bound, non-radiative evanescent wave with a field amplitude, the maximum of which is at the interface ($z = 0$) and which is decaying exponentially into the dielectric (as well as into the metal). The mode is propagating as a damped oscillatory wave (as illustrated in figure 2.15).

All parameters characterising the properties of SPs can be quantitatively described on the basis of the dielectric functions of the involved materials, e.g. the exponential decay of the optical field intensity normal to an metal/dielectric interface. The penetration depth, l_p, of this light into the dielectric medium is found to be a few hundred nanometre only, and again it is this surface specificity that makes it such an interesting probe field.

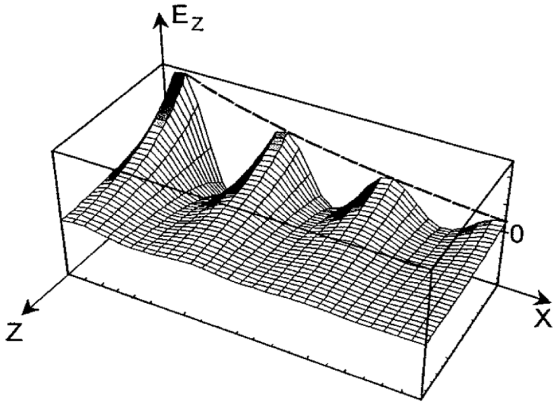

Figure 2.15: Schematic of evanescent character of a surface plasmon mode excited at a metal/dielectric interface in the x-, y-plane propagating as a damped oscillatory wave in the x-direction. The electric field components along the z-direction, normal to the interface,decay exponentially, here shown for the $\mathbf{E}_z$ component. [50]

Since TM-polarised light is used to excite SPs, their EM field is also transverse magnetically polarised. Therefore, in a Cartesian coordinate system, the field can be described by the nonzero components of the magnetic intensity parallel to the interface $\mathbf{H}_y$, the electric intensity parallel to the interface $\mathbf{E}_z$ and the electric intensity perpendicular to the interface $\mathbf{E}_x$. Figure 2.16 shows the spatial distribution of the exponentially decaying magnetic field along the x-coordinate, and the penetration depths from the metal/dielectric interface into the the dielectric $l_{p,dielectric}$ and the metal $l_{p,metal}$, respectively. These penetration depths depend on the material's optical properties (on the real part of the complex refractive index) and are defined as the distance perpendicular to the surface at which the field amplitude decreases by a factor $1/e$ ($l_{p,j} = Re\{\beta^2 - \mathbf{k}_0^2\mathbf{k}_j^2\}^{-\frac{1}{2}}$ where j stands either for the metal or dielectric). The propagation distance along the metal surface, on the other hand, depends (due to dissipation in the metal film) solely on the imaginary part of the complex refractive index. It is quantified by the propagation length L_x as the distance along the metallic surface at which the intensity of the SP mode drops to $1/e$ ($L_x = (2Im\{\beta\})^{-1}$ where $Im\{\}$ is the imaginary part of the complex refractive index).

The second consequence of equation 2.47 is that the momentum of a free photon propagating in a dielectric medium,

$$\mathbf{k}_{ph} = \frac{\omega}{c} \cdot n_{dielectric} \tag{2.48}$$

is always smaller than the momentum of a surface plasmon mode, $\mathbf{k}_{sp}$, propagating along an interface between that same medium and the metal [see figure 2.17(a)]. Therefore, the surface wave cannot directly couple light in the dielectric; coupling is forbidden by the law of conversion of momentum. The dispersion of photons is described by the light line, $\omega = c_d\mathbf{k}_{ph}$ [Figure 2.23 (a)], with $c_d = \frac{c}{\sqrt{n^2_{dielectric}}}$.

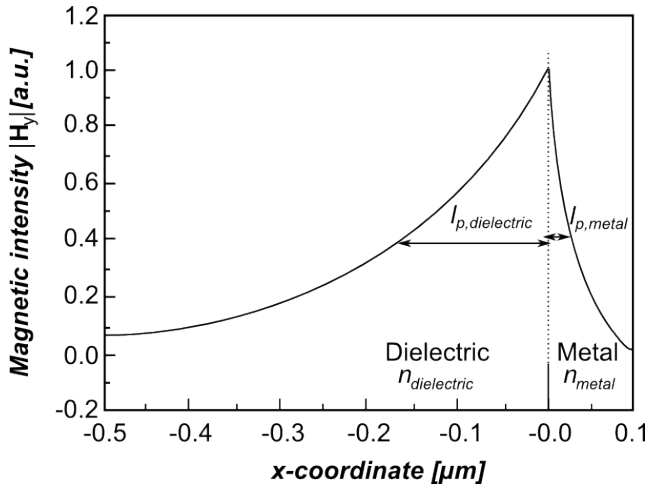

Characteristics of surface plasmon

Penetration depth in gold	$l_{p,metal} = 0.027\mu m$
Penetration depth in dielectric	$l_{p,dielectric} = 0.183\mu m$
Propagation length	$L_x = 7.2\mu m$

Figure 2.16: Distribution of the magnetic field intensity $\mathbf{H}_y$ of the SP propagating along the interface of gold ($\tilde{n}_{Au} = 0.3 + i3.8$) and water as the dielectric ($n_{H_2O} = 1.33$) at a wavelength of $\lambda = 0.633\mu m$. The table summarises the typical values for penetration depths and propagation lengths in an aqueous surrounding above a gold surface as illustrated in the figure. [25]

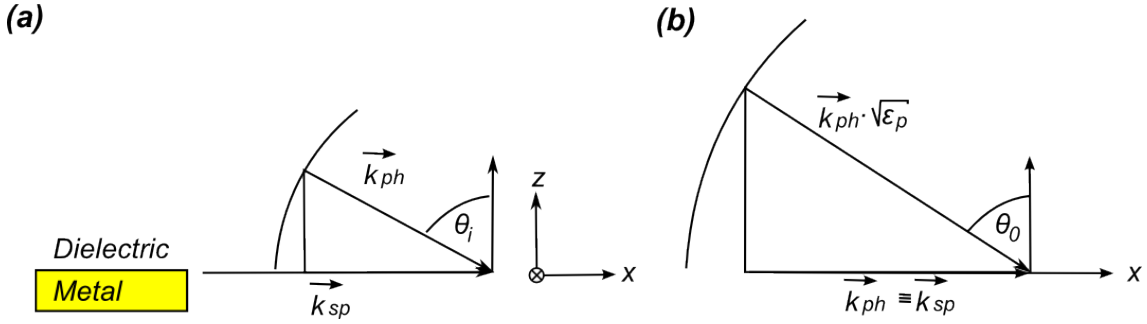

Figure 2.17: (a) Momentum relation between a surface plasmon, $\mathbf{k}_{sp}$, propagating along x and a photon, $\mathbf{k}_{ph}$, incident at the metal/dielectric interface at an angle θ. At any angles θ; $\mid \mathbf{k}_{ph} \mid < \mid \mathbf{k}_{sp} \mid$. (b) Wavevector matching condition for the resonant coupling of photons travelling in the prism: At the incident angle θ_0, the photon projection along the x-coordinate, $\mathbf{k}_{x,ph}$, matches the SP wavevector $\mathbf{k}_{sp}$. For details, see text.

2.3.1 Optical Excitation of Surface Plasmons

In order to excite SPs, the only relevant parameter is the photon wave vector projection to the x-direction. For a simple reflection of photons (with energy $\hbar\omega_L$,e.g. from a laser source) at a planar dielectric/metal interface, the variation of the angle of incidence causes a tuning of $\mathbf{k}_{x,ph} = \mathbf{k}_{ph} sin(\theta)$ from zero at normal incidence (point 0 in figure 2.23 (a)) to the full wave vector $\mathbf{k}_{ph}$ at glazing incidence (point 1 in figure 2.23 (a)).

Equation 2.46 and 2.47, however, tells us that this is not sufficient to fulfil the momentum-matching condition for resonant SP excitation because, for very low energies, the SP dispersion curve (figure 2.23 (a)) asymptotically reaches the light line, whereas for higher energies it approaches the cutoff angular frequency ω_{max} determined by the plasma frequency of the employed metal, ω_p:

$$\omega_{max} = \frac{\omega_p}{\sqrt{1 + n^2_{dielectric}}} \tag{2.49}$$

The employed dielectric function of gold is calculated according to the model of a free electron gas[44]:

$$\varepsilon_{Au} = (\omega) \approx 1 - \frac{\omega^2_{p,Au}}{\omega^2} \tag{2.50}$$

with the plasma frequency $\omega_{p,Au}$

$$\omega_{p,Au} = \sqrt{\frac{n_e e^2}{m_e \varepsilon_0}} = 13.7 \cdot 10^{15} rad/s \tag{2.51}$$

here n_e is the electron density, e the elementary charge, m_e the electron mass, and ε_0 the permittivity of free space.

For $\mathbf{k} \to \infty$ the dispersion relation approaches an upper bound:

$$\lim_{k \to \infty} \omega_{max} = \frac{\omega_p}{\sqrt{1 + \varepsilon_{dielectric}}} = \frac{\omega_p}{\sqrt{1 + n^2_{dielectric}}} \tag{2.52}$$

(equation 2.46 $\mathbf{k} \to \infty$ means $\varepsilon_{metal} \to -\varepsilon_{dielectric}$, $-\varepsilon_{dielectric}$ inserted in equation 2.50 yields equation 2.52)

Therefore, mostly metals such as gold, silver and aluminium are used for the excitation of SPs in the visible (Vis) and the near-infrared (NIR) part of the spectrum. The dispersion relation of SPs propagating on surface of these metals is shown in figure 2.18.

Experimental research on SPs started with electron beam excitation; in 1968, optical excitation was demonstrated by Otto[65] and Kretschmann and Raether[54]. An experimental setup introduced by Otto, accordingly called the Otto-configuration[65], allows the excitation of SP by not directly coupling photons to the metal/dielectric interface, but rather applying the evanescent field of light, after being totally internally reflected at the base of a high-index glass prism (with $n_{prism} > n_{dielectric}$). This evanescent light is characterised by a larger momentum [figure 2.23 (a), *solid line*] that for a certain spectral range can exceed

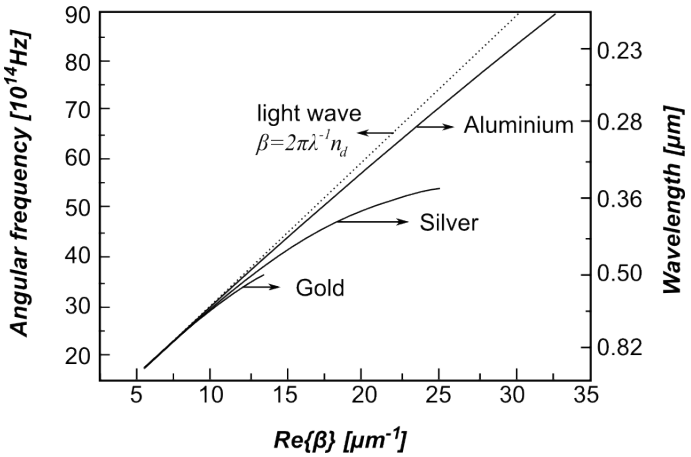

Figure 2.18: Dispersion relation of the SP at the interface between air ($n_{air} = 1$) and gold ($\tilde{n}_{Au} = 0.3 + i3.8$), silver ($\tilde{n}_{Ag} = 0.1 + i4.0$) and aluminium ($\tilde{n}_{Al} = 1.4 + i7.6$). [25]

the momentum of the SP to be excited at the metal surface. So, by choosing the appropriate angle of incidence θ_i [point 2 in figure 2.23 (a)], resonant coupling between evanescent photons and surface plasmons can be obtained. The corresponding momentum-matching condition is schematically given in figure 2.17 (b).

Figure 2.19 reveals the dispersion relation of a light wave in the dielectric and in the prism compared to that of SPs for the same materials as above. It can be seen that the dispersion relation of the light wave crosses that of SP for the angle of incidence $\theta = 51.5\ deg$ in the combination with a wavelength of $\lambda = 0.633 \mu m$. This finding appears to be identical to the value for which the matching condition (equation 2.46) is fulfilled and the minimum of SPR dip in figure 2.22 occurs.

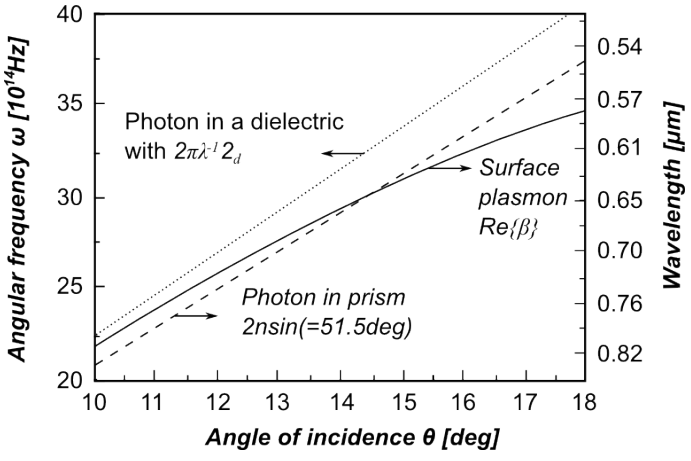

Figure 2.19: The comparison of the dispersion relation of a SP and photons in the prism and the dielectric for the same parameters. [25]

Experimentally, this resonant coupling is observed by monitoring, as a function of the incident angle, the laser light of energy $\hbar\omega_L$ that is reflected by the base of the prism, which shows a sharp minimum [see also figure 2.22]. The major technical drawback of this configuration is the need to get the metal surface close enough to the prism base, typically

to within $\sim 200nm$. Even a few dust particles can act as spacers, thus preventing efficient coupling. So, despite its potential importance for the optical analysis of polymer-coated bulk metal samples, this version of surface plasmon spectroscopy has not gained any practical importance[37].

By far the most widespread version of surface plasmon spectroscopy is based on the experimental configuration introduced by Kretschmann and Raether[54] [figure 2.20 (b)]. Conceptually, this scheme for exciting SPs is rather similar to the aforementioned technique, with the exception that this time the (high-momentum) photons in the prism couple through a very thin metal layer (typically, approximately $45 - 55nm$ thick, evaporated directly onto the base of the prism or onto a glass slide which is then index-matched to the base of the prism) to the SP states at the other side in contact with the dielectric medium.

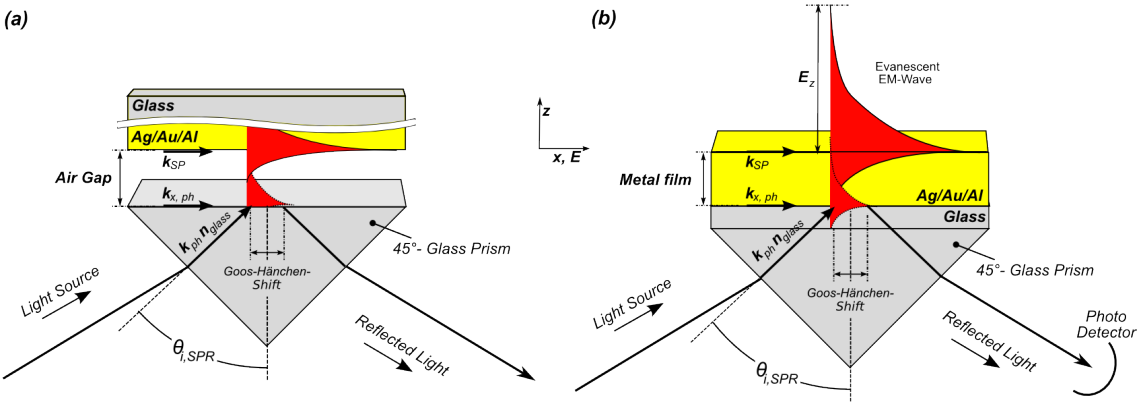

Figure 2.20: (a) The Otto configuration is based on TIR of a plane wave incident at an angle $\theta_{i,SPR}$ at the base of a prism. The evanescent tail of this inhomogeneous wave can excite SP states at an Au-dielectric interface, provided the coupling gap is sufficiently narrow (within the reach of the evanescent tail $d_{gap} \sim 200nm$). (b) Excitation of SP waves by internally reflected light in the Kretschmann-configuration. A gold coated ($d_{Au} \sim 50nm$) glass slide is optically coupled (index-matched) to a glass prism. At the resonance angle $\theta_{i,SPR}$ the projection of the light wave vector in glass, $\mathbf{k}_{x,ph}$, is equal to the wave vector of the surface plasmon wave $\mathbf{k}_{SP}$. The evanescent light field is penetrating the gold film and exciting the SP waves. Its exponentially decaying electric field $\mathbf{E}_z$ is also sketched (coloured in red). Since the SP waves are excited resonantly their electric field is enhanced (resonance amplification).

At the particular angle of incidence $\theta_{i,SPR}$ - the resonance angle - the SP waves are resonantly excited by the evanescent light field, because the resonance conditions are fulfilled: $\omega_{ph} = \omega_{SP}$ and $\mathbf{k}_{x,ph}(\theta_{i,SPR}) = \mathbf{k}_{SP}$. Although equation 2.46 must be modified for the Kretschmann-configuration[53,17], it holds as a good approximation, thus

$$\theta_{i,SPR} = arcsin\left(\frac{1}{n_{prism}}\sqrt{\frac{\varepsilon_{metal}\varepsilon_{dielectric}}{\varepsilon_{metal}+\varepsilon_{dielectric}}}\right) \tag{2.53}$$

Figure 2.21 shows the measured dispersion relation for the system BK7 glass/gold/water in comparison to dispersions relations calculated according to equations 2.46 and 2.47. The good accordance shows these equations can be used to describe the Kretschmann-

configuration.

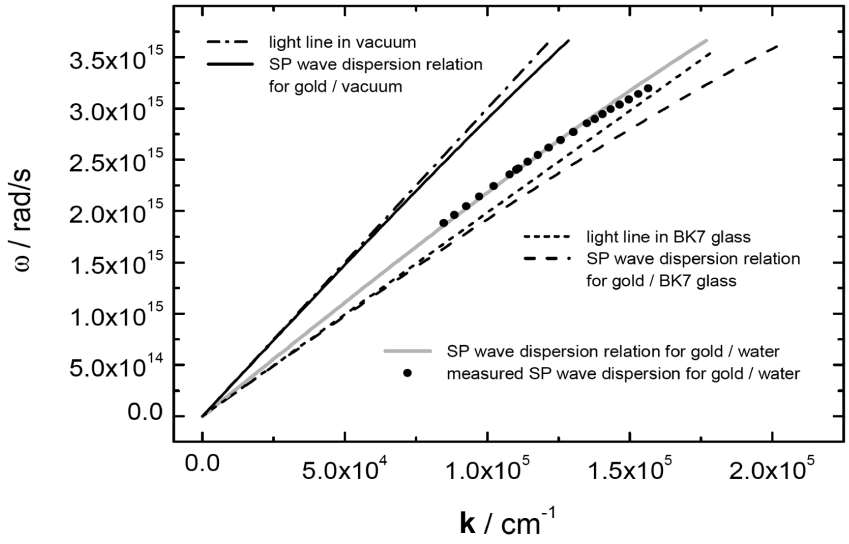

Figure 2.21: Calculated and measured dispersion relations of SP waves (compare with figure 2.19 and figure 2.23). The filled circles represent measurements between $\lambda = 590 - 1000nm$ in a multi-layer system consisting of BK7 glass / 50nm gold / water. The solid lines represent calculated dispersion relations according to equations 2.46 and 2.50 for different dielectrics. The broken lines represent the light lines in vacuum and BK7 glass. Since SP waves on a gold / BK7 interface have larger wave vectors than light in BK7, they can not be excited by light in BK7. Consequently there is no SP wave excitation on the interface glass / gold in the Kretschmann-configuration and $n_{dielectric}$ must be smaller than n_{prism} for SPR measurements. [25]

In case of resonant SP wave excitation the light energy is transferred into the SP waves; the reflected light intensity I_r decreases drastically. This can be observed as a characteristic minimum in I_r *versus* θ_i-plots (see figure 2.22). In the literature this minimum is sometimes referred to as 'plasmon', although this term is actually reserved to the quantum of plasma oscillations.

Qualitatively, the same consideration for energy- and momentum-matching apply as discussed for figure 2.20 (a) [see also figure 2.23 (a)]; however, quantitatively one has to take into account that the finite thickness of the metal layer causes some modifications of the dispersion behaviour of the SP modes. In particular, the possibility of coupling out some of the surface plasmon light through the thin metal layer and the prism opens a new, radiative-loss channel for SPs in addition to the intrinsic dissipation in the metal**?** . This means, that in the Kretschmann-configuration plasmons can decay into photons since a fraction of their electric field still penetrates into the glass prism. The imaginary $\mathbf{k}_z$ transforms into a real $\mathbf{k}_z$, and a propagating wave is generated leading to an increased $I_r(\theta_{i,SPR})$ - this effect is known as radiation damping, Γ_{rad}. The radiation damping can be decreased by larger gold film thickness, however, then the coupling of the evanescent light field to the SP waves becomes less efficient and $I_r(\theta_{i,SPR})$ increases also. Consequently, in order to minimise $I_r(\theta_{i,SPR})$, the gold film thickness needs to be optimised for each

wavelength, since the evanescent light field also possesses a wavelength dependent penetration depth. In case of optimal (gold) film thickness, $I_r(\theta_{i,SPR}) = 0$ is possible.

One then can describe the angular dependence of the reflectivity by solving Maxwell's or Fresnel's equations for this layer architecture of glass/Au-layer/dielectric. An example is given in figure 2.22, based on the known parameters n_{prism}, $n_{dielectric}$, and the values for $\tilde{n}_{metal} = (n_{metal} - i\kappa_{metal})$, and d_{Au}, the metal layer thickness. This figure also shows the dependence of SP coupling strength to the thickness of the metal layer. In the experiments presented in this work, the latter was adjusted to a gold layer thickness of $d_{Au} \approx 55nm$ for optimal coupling efficiencies for a material combination as stated above and by using a red light laser source at $\lambda = 632.8nm$. This thickness is a reasonable compromise for SPR experiments which the possibility to employ different wavelengths.

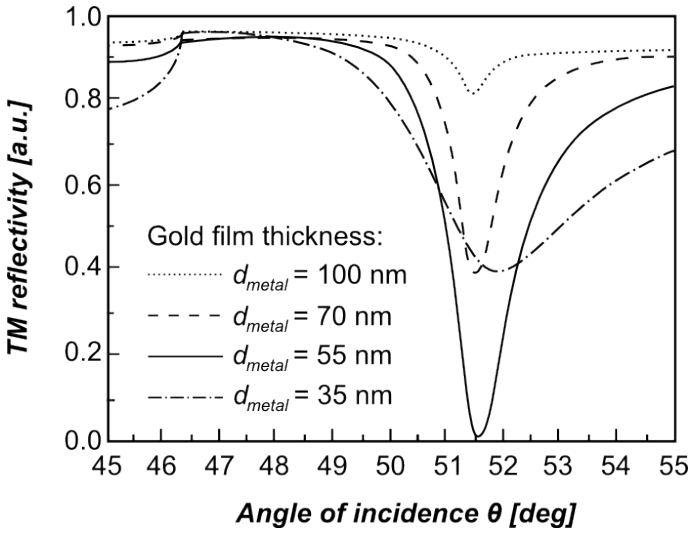

Figure 2.22: Angular reflectivity spectra for the excitation of SPs at the wavelength of $\lambda = 0.633\mu m$ the interface of gold ($\tilde{n}_{Au} = 0.3 + i3.8$) and water as the dielectric ($n_{H_2O} = 1.33$) using a prism coupler ($n_{LaSF9} = 1.845$) and a gold film with the thickness d_{Au} between 35 and 100 nm.[25]

One very important parameter, the angular dependence of the interfacial intensity at $(z = 0)$. One can see that assuming a perfect interface, i.e. describing the layer architecture that leads to the reflectivity curves of Figure 2.22, with perfectly flat interfaces exhibiting no roughness or other imperfections, enhancement factors of more than 80 for the surface plasmon light compared to the in-coupling laser light can be obtained. In real experimental situations the enhancement might be more moderate, but still exists[90,48]. This intensity enhancement is the source of the sensitivity gain that was found in many spectroscopic experiments with surface plasmon light, in particular, demonstrated for Brillouin- and Raman-spectroscopies[51], but also for fluorescence optical experiments using SP modes as the exciting field[5]. At this point, one should emphasise the resonance character of the excitation of a surface plasmon mode: As for any oscillator, the maximum amplitude and the width of the resonance curve depend on the degree of damping that exists

in the system. For the excitation of SP, the dissipation of energy in the metal is the relevant damping mechanism described in the Maxwell treatment by the imaginary (loss) part of the dielectric function, ε''_{metal} (or in terms of refractive index $2n\kappa$). For optical frequencies, Ag is the metal with the smallest ε''_{Ag}, followed by Au. Therefore, for a given laser wavelength λ, the SP reflectivity curve for a Ag/air interface has the smallest width, $\Delta\theta \simeq 0.5deg$ for $\lambda = 632.8nm$, and consequently shows the highest enhancement factor for the intensity. The resonance at an Au/air interface is $\Delta\theta \approx 2 - 3deg$ wide [depending on the homogeneity of the evaporated Au layer whose granular structure with the many grain boundaries gives rise to additional (scattering) loss mechanisms], and the enhancement is 'only' a factor of 20 (for $\lambda = 632.8nm$). Of course, the strong frequency dependence of $\tilde{\varepsilon}_{metal}(\omega) = \varepsilon'_{metal}(\omega) + \varepsilon''_{metal}(\omega)$ (or equivalently $\tilde{n}_{metal}(\omega) = n_{metal}(\omega) + i\kappa_{metal}(\omega)$) gives rise to a strong wavelength dependence of the width and the enhancement factor.

Furthermore, the dependence of the dispersion relation of SP waves from $\varepsilon_{dielectric}$ respectively $n_{dielectric}$ is the fundamental feature for the application of SPR. A change in the SP wave propagation characteristics means the occurrence of a change in $n_{dielectric}$.

2.3.2 Adlayer Sensing

In experiments aimed at characterising thin films, however, we modify the optical properties of only a narrow slice of the dielectric half-space that is probed by the evanescent SP field. For a qualitative picture only, we note that depositing an ultra-thin layer (with a thickness of $d_{adlayer} \ll \frac{2\pi}{\mathbf{k}_{zd}}$) of a material with an index of refraction $n_{adlayer} = \sqrt{\varepsilon_{adlayer}}$ larger than that of the ambient dielectric, e.g. air with $n_{air} = 1$, for a surface plasmon mode is equivalent to an increase of the overall RI integrated over the evanescent field. The net effect is a slight shift of the dispersion curve corresponding to an increase of $\mathbf{k}_{sp}$ for any given ω_L. This is depicted in figure 2.23 (a) ($dash - dotted\ curve$). As a consequence, the angle of incidence that determines the photon wave vector projection along the SP propagation direction has to be slightly increased [from θ_0, point 2 on the dazed SP curve in figure 2.23 (a) to θ_1, point 3 in figure 2.23 (a)] in order to again couple resonantly to SP modes[33].

Experimentally, the situation is relatively simple, a linearly p-polarised laser beam of wavelength λ, incident at an angle θ_i on the noble-metal-coated base of the prism (which is covered with the thin film of interest) is reflected, and the intensity of the reflected light is monitored with a detector as a function of θ. A typical reflectivity curve is given in figure 2.23 (b). The curve labelled a was taken in air on a bare Au-film evaporation-deposited onto the prism base. For $\theta_i < \theta_{critical}$ the reflectivity is rather high compared to the total

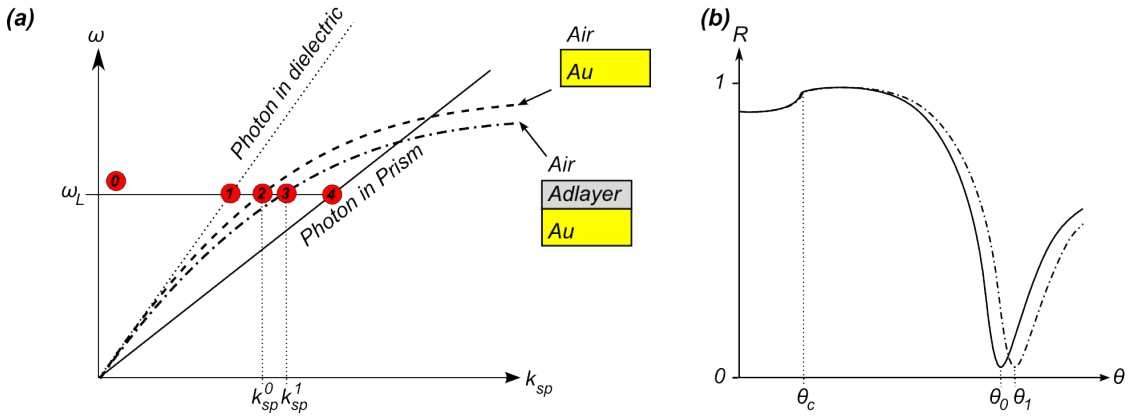

Figure 2.23: (a) Dispersion relation of a photon travelling as a plane wave in the dielectric medium, $\omega = c_{dielectric}\mathbf{k}_{ph}$, with $c_{dielectric} = \frac{c}{n_{dielectric}}$ the speed of light in the dielectric (solid line), and a photon propagating in the prism $\omega = c_{prism}\mathbf{k}_{ph}$, $c_{prism} = \frac{c}{n_{prism}}$ (dotted line). The dispersion relation, ω vs. $\mathbf{k}_{sp}$, of plasmon surface polariton at an Au-air interface (SP, dashed curve) and at an Au-dielectric coating-air interface (SP, dash − dotted curve). Laser light of energy $\hbar\omega_L$ couples at angles $\mathbf{k}^0_{sp}$ and $\mathbf{k}^1_{sp}$, respectively, given by the energy and momentum matching condition (see the intersection of the horizontal line at ω_L with the two dispersion curves). (b) Reflectivity curves obtained for a bare Au-film; solid curve, evaporated onto a glass prism; dash − dottedcurve , after adsorption of an ultra-thin adlayer ($n_{adlayer} = 1.45$, $d_{adlayer} = 3nm$) in air.

internal reflection discussed in section 2.2 because the evaporated metal layer acts as a mirror with little transmission. The deposition of an ultra-thin organic layer from solution to the Au-surface results in a shift of the dispersion curve for SP running along this modified interface and hence in a shift of the resonance angle (from θ_0 to θ_1, see Figure 2.23 (b)). The obtained reflectivity curve is labelled b in 2.23 (b). The critical angle $\theta_{critical}$ is unaffected by the presence of the adlayer, but only sensitive to the optical parameters of the multi-layer stack itself.

The dispersion relation and thus $\theta_{i,SPR}$ depend on the refractive index which is perceived by the surface plasmon waves within the penetration depth l_p of their electric field. The perceived refractive index can be constant within the penetration depth of the electric field of the surface plasmon waves or can be an effective, averaged refractive index N if the medium is not homogeneous within the penetration depth.

If l_p denotes the penetration depth of the surface plasmon waves defined by $\mathbf{E}_z = l_p = \frac{1}{e}\mathbf{E}_0(z = 0)$, the effective refractive index can be calculated according to Jung et al.[46]:

$$N = (\frac{2}{l_p}) \int_0^\infty n(z) e^{(-\frac{2z}{d_p})} dz \tag{2.54}$$

where $n(z)$ is the index of refraction at height z over the gold surface. The factor 2 in equation 2.54 considers the refractive index $n(z)$ to be probed by the intensity of the electric field of a surface plasmon wave, meaning squared electric field[56,46]. The penetration depth can thus be calculated by[46]:

$$l_p = \frac{\left(\frac{\lambda}{2\pi}\right)}{Re\left\{\sqrt{-\frac{n_{eff}^4}{(N^2+\varepsilon_{metal}(\omega))}}\right\}} \tag{2.55}$$

The penetration depth varies only weakly with N which justifies to assume a constant penetration depth for a certain wavelength. But, since the penetration depth is linearly dependent on the wavelength, it is possible to probe differently deep into the vicinity of the gold film with surface plasmon waves excited by different wavelengths. Figure 2.24 shows l_p as a function of the excitation wavelength and the variation of l_p with N.

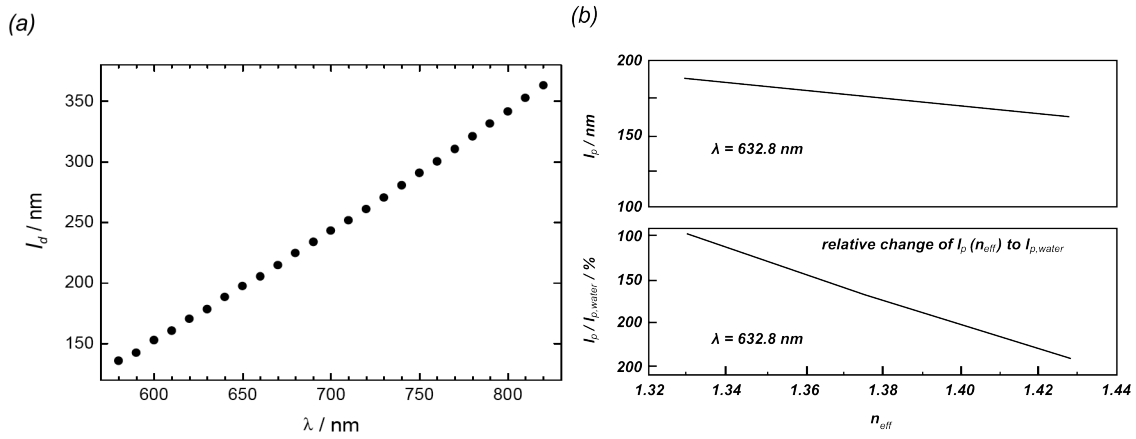

Figure 2.24: (a) The penetration depth l_p of surface plasmon waves in dependence of the excitation wavelength according to equation 2.55. (b) Upper graph: The variation of l_p with the effective perceived refractive index N, calculated for $\lambda = 600nm$. Lower graph: The relative change of l_p to $l_{p,water}$ in water.

For all practical purposes, the quantitative treatment of this problem is based on the Fresnel theory for calculating the overall transmission and reflection of a general multilayer assembly. The latter would, in the presented case, consist of the prism material, the metal layer, the adlayer(s), and the superstrate (dielectric half-space), typically air or a transparent liquid, e.g. water. Different algorithms based on either a matrix formalism or a recursion formula procedure for calculating the Fresnel coefficients of the i-th layer for s- and p-polarised light have been treated in the literature. The angular dependence of the overall reflectivity can be computed and compared with the measured curves [$dash - dotted\ curve$, figure 2.23 (b)]. The best fit then results in a set of parameters describing the Au reference layer and, more importantly, the optical thickness of the organic coating. If the refractive index of the material is known, the geometrical thickness can be determined, and *vice versa*. This ambiguity can be resolved if SPR curves are taken at different wavelengths[66] (with the ambiguity of the unknown dispersion behaviour of the refractive index of the coating), or in a contrast variation experiment[49] where the angular resonance shift is measured in two media of different refractive indices $n_{dielectric}$, e.g. in air and in contact to the solvent from which the adlayer was adsorbed. Since the angular

shift $\Delta\theta_{i,SPR}$ is a known function of d_{layer} and of the optical contrast to the surrounding medium, $(n_{layer} - n_{dielectric})$, i.e.

$$\Delta\theta_{i,SPR} = f(d_{layer}, (n_{layer} - n_{dielectric})) \tag{2.56}$$

one needs two independent measurements to separate ε_{layer} and d[13].

If the thickness of the coating is increased further, a new type of non radiative mode, guided optical waves, can be observed. The excitation of these modes of different order m can be seen again if the reflected intensity is recorded as a function of the angle of incidence, θ_i: narrow dips in the reflectivity curve above $\theta_{critical}$ indicate the existence of the various guided waves. In such a configuration the general principles of guiding light in transparent media with confined dimensions apply, and this multi-layer assembly becomes is referred to as waveguide.

2.4 Transfer matrix formalism

The reflection of light from a single interface between two media is described by the set of Fresnel's equations, and was already discussed in section 2.1.4. However, when there are multiple interfaces, such as in the above-mentioned multilayer system, the reflections themselves are also partially reflected. Depending on the exact path length, these reflections can interfere destructively or constructively due to their inherent wave character. Consequently, the overall reflection of a layer structure is the sum of an infinite number of reflections, which is cumbersome to calculate. The transfer matrix formalism is an extremely useful form of the steady-state solution to Maxwell's equations, subject to the boundary conditions, imposed by a multilayer stack and is reported extensively in the literature[38,45,71,18,19,73,79,72,84] A brief outline of the main features is given in this section.

The transfer-matrix method is based on the fact that, according to Maxwell's equations, there are simple continuity conditions for the electric field across boundaries from one medium to the next. If the field is known at the beginning of a layer, the field at the end of the layer can be derived from a simple matrix operation. A stack of layers can then be represented as a system matrix, which is the product of the individual layer matrices. The final step of the method involves converting the system matrix back into reflection and transmission coefficients.

The optical response of a coherent thin-film multilayer assembly can be calculated *via* different numerical mathematical methods, using either a recursion formula procedure or

a transfer matrix formalism (TMF). The first example, known as recursion procedure is based on the recursive calculation of the reflection coefficient starting from the last layer and progressing to the first one; a detailed explanation can be found elsewhere[9]. The latter approach, known as the TMF[12,47], is discussed here, because it forms the basis for the algorithm of the program "Winspall" used in this work for quantitative analysis of data from prism coupled ATR spectroscopy and to calculate reflectivity curves, as well as field distributions. It also provides the basic principles on which the simulation code for grating coupling was built.

The transfer-matrix method is a method often used in optics to analyse the propagation of EM waves through a stratified (layered) medium[12]. The optical response of a given coherent thin-film multi-layer system is therefore represented with Fresnel coefficients in a 2×2 matrix configuration. Accordingly, and due to the continuity of the tangential components of the wavevectors the complete electric and magnetic field within the multilayer system can be calculated by using only two partial waves propagating in positive (field amplitudes $\left(\mathbf{E}_j^+, \mathbf{H}_j^+\right)$) and negative (field amplitudes $\left(\mathbf{E}_j^-, \mathbf{H}_j^-\right)$) z-direction (for details see section 2.1.4: Fresnel's equations), as depicted in figure 2.25.

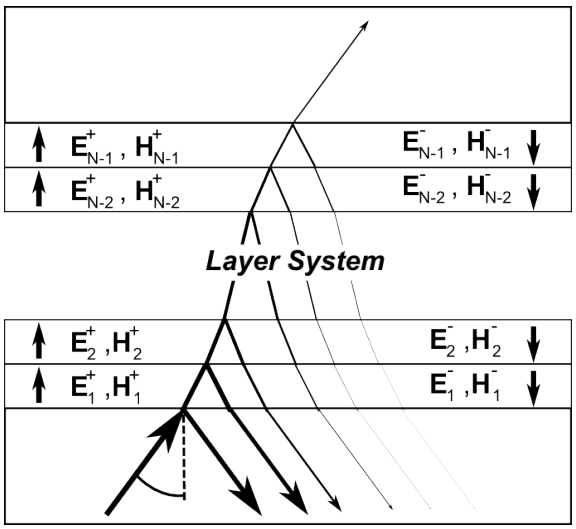

Figure 2.25: A multilayer system consisting of $N+1$ layers (the first and the last are omitted for cavity), each with individual properties (i.e. dielectric constant ε_j and a thickness d_j), is entered by a light beam with angle of incidence θ. Within these layers the electric and magnetic field may be described completely by two plane waves propagating in positive ($\mathbf{E}_j^+$, $\mathbf{H}_j^+$ field amplitudes) and negative ($\mathbf{E}_j^-$, $\mathbf{H}_j^-$) z-direction. The reflectivity can be calculated by considering the contribution of each interface and each layer by applying the 2×2 matrix formalism.

The translational symmetry accounts, again, for the possibility of separating the solutions into TM and TE modes, both being represented by the amplitude A. A general solution in z-direction of the above introduced system yields the following expression:

$$A_j(z) = A_j^+ \cdot e^{i\mathbf{k}_{j,z}z} + A_j^- \cdot e^{-i\mathbf{k}_{j,z}z} \tag{2.57}$$

Since the lateral momentum $\mathbf{k}_x = \mathbf{k}_0 \cdot sin(\theta_i)$ is constant throughout the whole system, the components of the wavevector $\mathbf{k}_{j,z}$ are expressed by:

$$\mathbf{k}_{j,z} = \sqrt{\varepsilon_j \left(\frac{\omega}{c}\right)^2 - \mathbf{k}_x^2} \tag{2.58}$$

Based on this, the propagation of a plane wave in one layer can be described by a matrix equation of the following form:

$$\begin{pmatrix} A_j^+(z_j) \\ A_j^-(z_j) \end{pmatrix}_{TM,TE} = \begin{pmatrix} p_j^{-1} & 0 \\ 0 & p_j \end{pmatrix} \begin{pmatrix} A_j^+(z_j + d_j) \\ A_j^-(z_j + d_j) \end{pmatrix}_{TM,TE} = \mathbf{P}_j \begin{pmatrix} A_j^+(z_j + d_j) \\ A_j^-(z_j + d_j) \end{pmatrix}_{TM,TE} \tag{2.59}$$

The left side of the equation describes the field at the upper edge of the layer j and is connected through the propagation matrix $\mathbf{P_j}$ to the field at the lower edge of the same layer. The quantity p_j is given by:

$$p_j = e^{i\mathbf{k}_{j,z} d_j} \tag{2.60}$$

Applying again the statement that the tangential components of the electric and magnetic field and the normal components of the dielectric displacement and the magnetic induction are continuous at an interface it follows that

$$\begin{pmatrix} A_j^+(z_j + d_j) \\ A_j^-(z_j + d_j) \end{pmatrix}_{TM,TE} = \frac{1}{2} \begin{pmatrix} 1 + \kappa_j^{TM,TE} & 1 - \kappa^{TM,TE} \\ 1 - \kappa_j^{TM,TE} & 1 + \kappa_j^{TM,TE} \end{pmatrix} \begin{pmatrix} A_{j+1}^+(z_{j+1}) \\ A_{j+1}^-(z_{j+1}) \end{pmatrix}_{TM,TE} = \mathbf{Q}_{\mathbf{j}\rightarrow\mathbf{j+1}}^{TM,TE} \begin{pmatrix} A_j^+ \\ A_j^- \end{pmatrix} \tag{2.61}$$

Here the matrix $\mathbf{Q_{j\rightarrow j+1}}$ is denoted Fresnel matrix and connects the amplitudes of the electric and magnetic fields on both sides of the interface. It completely describes the reflection and transmission processes at the material transition. The value of κ_j for both polarisation modes is given by:

$$\kappa_j^{TM} = \frac{\varepsilon_{j+1} + \mathbf{k}_j}{\varepsilon_j \mathbf{k}_{j+1}} \tag{2.62}$$

and

$$\kappa_j^{TE} = \frac{\mathbf{k}_j}{\mathbf{k}_{j+1}} \tag{2.63}$$

The transfer matrix $\mathbf{T}$ then summarises the different contributions of all the interfaces and acts as an intermediary between both infinite half-spaces with $j = 0$ and $j = N + 1$.

$$\begin{pmatrix} A_0^+(z_0) \\ A_0^-(z_0) \end{pmatrix}_{TM,TE} = \mathbf{Q}_{\mathbf{0}\rightarrow\mathbf{1}}^{TM,TE}\mathbf{P}_{\mathbf{1}}\mathbf{Q}_{\mathbf{1}}^{TM,TE}\dots\mathbf{Q}_{\mathbf{N-1}\rightarrow\mathbf{N}}^{TM,TE}\mathbf{P}_{\mathbf{N-1}\rightarrow\mathbf{N}}\begin{pmatrix} A_N^+(z_N) \\ A_N^-(z_N) \end{pmatrix}_{TM,TE} = \mathbf{T}^{TM,TE}\begin{pmatrix} A \\ A \end{pmatrix} \tag{2.64}$$

At any given refractive indices and thicknesses of the separate layers the transfer matrix is unambiguously determinable if the angle of incidence and the wavelength of the transmitting light are known. Therefore, a reflectivity *versus* angle of incidence curve can easily be calculated or fitted to experimental data, respectively. This is true even in the case of anisotropic media, where the dielectric constants have to be replaced by tensors. Since in the presented geometry no reflected beam in the lower half-space exists, the reflection coefficient r^{refl} is normalised to 1 and equation 2.64 simplifies to:

$$\begin{pmatrix} A_0^+(z_0) \\ A_0^-(z_0) \end{pmatrix}_{TM,TE} = \mathbf{T}^{TM,TE}(\omega, \mathbf{k}_x)\begin{pmatrix} 1 \\ 0 \end{pmatrix} \tag{2.65}$$

The reflectivity and transmission can be calculated accordingly by

$$R = \mid r^{refl} \mid^2 = \begin{pmatrix} A_0^+(z_0) \\ A_0^-(z_0) \end{pmatrix}^2 = \left(\frac{T_{2,1}}{T_{1,1}}\right)^2 \tag{2.66}$$

and

$$T = \mid r^{trans} \mid^2 = \begin{pmatrix} A_N^-(z_N) \\ A_0^+(z_0) \end{pmatrix}^2 = \left(\frac{1}{T_{1,1}}\right)^2 \tag{2.67}$$

2.5 Dielectric Slab Waveguide

Following the example stated above, and further increasing the film thickness of the adlayer on top of the gold film, a new type of non-radiative mode; spatially confined, guided optical waves, can be observed. This structure, capable of guiding light modes of different order m in a transparent medium above the gold film, with (spatially) confined dimensions is referred to as a special version of a multi-modal waveguide.

A waveguide in general is a physical structure that guides EM waves. Considering the optical spectrum of EM waves, such structures are accordingly called optical waveguides, in

contrast to acoustic waveguides or microwave-guides. Common types of optical waveguides include optical fibre and slab waveguides. As early as 1910, long before the invention of the laser, Hondros and Debye[40] theoretically examined the possibility of reducing the diffraction-induced divergence of light due to the total internal reflection — the phenomenon that gives rise to guided modes of EM radiation in dielectric waveguides. The field distribution in waveguides, however, was analysed by Carcuvitz in 1948 and also by Collin in 1960. Their solutions were subsequently used to study light-guiding phenomena in $p-n$-junctions[97]. Various aspects of simple planar waveguides were not, however, exhaustively investigated until the inception of integrated optics in the early 1970's.

An optical waveguide is most easily understood using the example of the simple dielectric slab waveguide[58], also called planar waveguide[58]. The slab waveguide consists in an ideal case of a homogeneous three-layer system separated by planar interfaces of infinite extent: A dielectric layer of high refractive index, and with a thickness on the same scale as the wavelength (typically $\leq 1\mu m$) is sandwiched between two half-spaces of lower index media, infinite in the directions parallel to their interfaces.

Figure 2.26 shows the typical three-layer configuration of a dielectric slab waveguide consisting not of infinite half-spaces of a subjacent substrate S , the waveguide film F and an overlying cover medium C , with n_S, n_F and n_C being the individual refractive indices of the substrate, the waveguiding film and the cover medium, respectively.

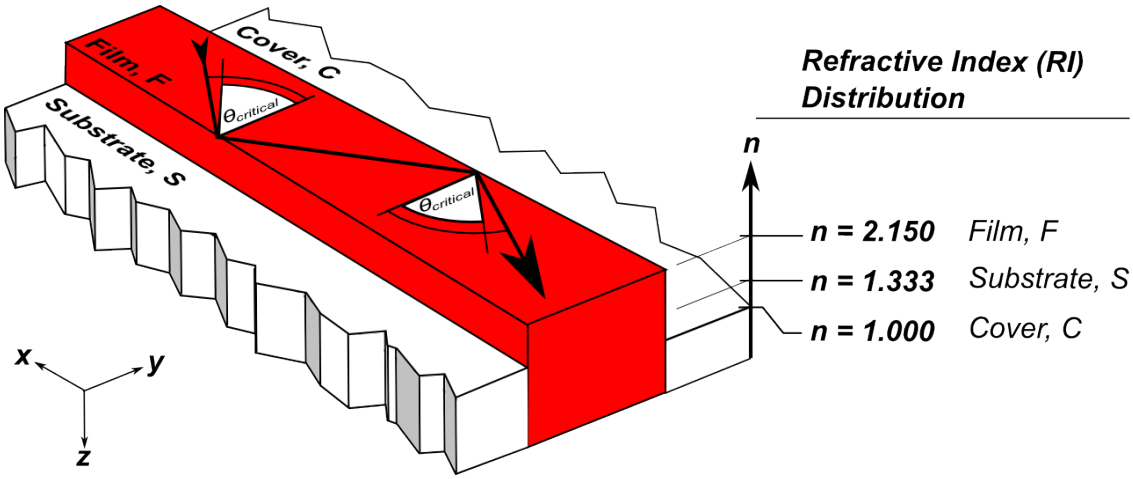

Figure 2.26: Basic waveguide structure with illustration of light guided in the waveguide film by total internal reflection (TIR) at the film boundaries. b) refractive index distribution along the multilayer structure.

In this fundamental configuration of three different dielectric media, with different refractive indices, where

$$n_F > max\left\{n_S, n_C\right\} \tag{2.68}$$

must be fulfilled in order to confine light and accordingly to make it possible for light to be guided inside the film layer F, as depicted in figure 2.26 b). In this approach all materials are assumed homogeneous, optically isotropic, and without scattering. For a more precise description, introduction of a non-zero component (as imaginary part) of the refractive index may include material absorption and miscellaneous loss-pathways due to material inhomogeneities[75]. In the above-described planar dielectric waveguide architecture, loss-less guiding of light within the film is made possible through total internal reflection (TIR) at the film/cover- and the film/substrate-boundary, respectively.

2.5.1 Total internal reflection

As discussed earlier, TIR is an optical phenomenon that occurs when a ray of light strikes a medium boundary at an angle of incidence θ larger than the critical angle $\theta_{critical}$ with respect to the normal to the surface. However, if θ > $\theta_{critical}$ then the light will change from being a normal propagating ray of light, crossing the boundary, to being totally reflected back internally. This can only be achieved for light propagating in a medium with a higher n towards one with a lower n, see figure 2.26 for illustration of reflection at the film/cover-boundary.

If $n_F > max\{n_S, n_C\}$ and the angle of incidence θ is large enough, so that $sin(\theta) > (\frac{n_F}{max\{n,n_C\}})$ (Snell's Law[93,94,68]) and the solution would give $sin(\theta) > 1$, then no light can pass through the interface, so effectively all of the light is totally internal reflected. The internally reflected ray is then at the same angle of incidence to the normal as the incident ray, and will therefore continuously undergo TIR, illustrated in Fig. 2.26.

The multiple internal reflections in the film give rise to interference effects at discrete angles of incidence. These angles are called waveguide mode angles or resonant angles θ_m. Since light in confined space can only exist upon constructive interference this means that, even though $\theta > \theta_{critical}$ is fulfilled, loss-less light guidance will only appear at discrete values of θ, *viz.* θ_m. Therefore, and unlike in free space, where light is propagating in every direction, optical waves in waveguides propagate only in a discrete set of states, the so-called (waveguide) modes.

2.5.2 Zigzag wave model

As described before the electric field distributions within a layer are the results of the linear combination of light waves propagating through the multilayer system, refers to 'zigzag' mode. Of course, one may set up an eigenvalue problem from Maxwell's equations,

and proceed to solve normal modes in the waveguide structure and the field distribution associated with each normal mode[20]. Still another approach is the use of ray optics, where a ray of light is considered to be reflected between the top and bottom surface of the film, following a zigzag path in the waveguide[89,86,88]. Even though this is not technically accurate, it provides an intuitive feel for how light propagates within a plane boundaries. Due to the fact that the slab waveguide involves plane geometry, the EM field distribution in it can be analysed as a superposition of two plane waves. Representing each plane wave by an optical ray, or a wave vector, normal to the wave front, the actual field problem can be converted to a problem of geometric optics.

In this section the most descriptive explanation of the wave guiding phenomenon is given by employing ray optics, hence applying the zigzag-wave model[87]. A plane wave is considered to propagate along the x-axis with inclination angle ϕ, as illustrated in fig. 2.27. The wavelength and the wavenumber in the film are $\frac{\lambda}{n_F}$ and $\mathbf{k} \cdot n_F (\mathbf{k} = \frac{2\pi}{\lambda})$, respectively, where λ is the wavelength of light in vacuum. The propagation constants along x and z (lateral direction) are expressed by $\beta = \mathbf{k} \cdot n_F \cdot cos(\phi)$ and $\kappa = \mathbf{k} \cdot n_F \cdot sin(\phi)$.

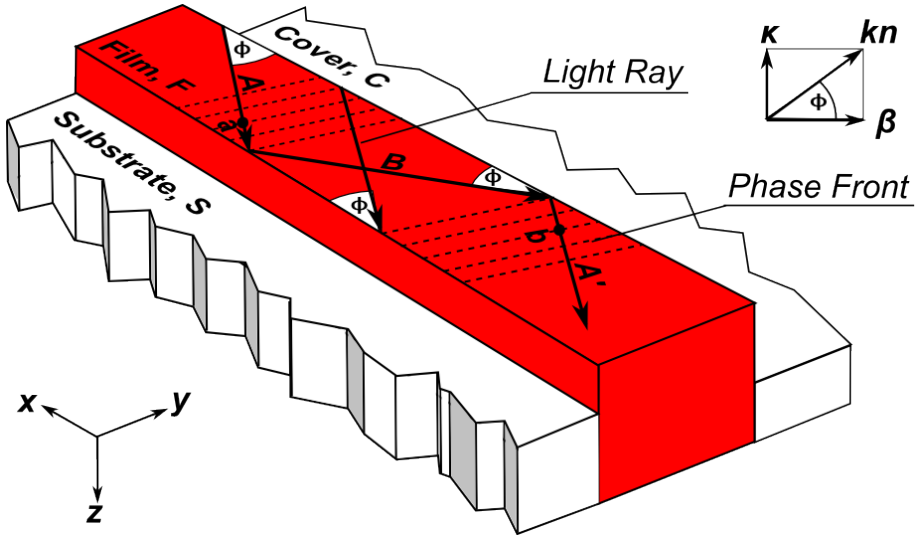

Figure 2.27: Zigzag wave representation of light propagation in a planar optical waveguide. (for details see text))

Based on the zigzag wave model, and treating the waveguide as a thin-film interferometer, the arising of a waveguide mode can be explained by constructive interference of reflected beams in the film upon experiencing reflections at both boundaries.

2.5.3 Waveguide modes

Constructive interference among the guided beams occurs if the wave fronts are in phase after reflection at both boundaries, which is illustrated for the two wave fronts in points a and b in figure 2.27. The total phase shift between point a and b should be an integral

multiple of 2π to obtain a waveguide mode. As the ray A is totally reflected into ray B at the film/substrate interface, the phase of the reflected light wave is advanced by $\phi_{F,S}$ at the point of reflection. The total reflection of ray B into ray A' at the film/cover interface, again, causes the phase of the reflected light wave to be advanced by $\phi_{F,C}$ at the point of reflection. The above-mentioned phase shift for the totally reflected light is called the Goos-Hänchen shift[58,83,32]. This phenomenon of total internal reflection is discussed in greater detail in[11].

The total phase shift between the two points comprises the change in phase due to the optical path difference between point a and b, $\phi_{\Delta S}$, and the phase shifts, $\phi_{F,S}$ and $\phi_{F,C}$ due to the reflections at the film boundaries. The criteria for a waveguide mode can thus be written as:

$$2\pi m = \phi_{\Delta S} + \phi_{F,S} + \phi_{S,C} \tag{2.69}$$

where $m = 0, 1, 2, \ldots$ is the mode order. The phase shift due to the travelled distance from point a to b depends primarily on the refractive index of the waveguide film and the film thickness d_F and is expressed by[87]:

$$\phi_{\Delta S} = 2d_F\sqrt{\mathbf{k}n_F^2 - N_m^2} \tag{2.70}$$

where $k = 2\pi/\lambda$ is the wave number in vacuum, with λ being the vacuum wavelength of the light used. N_m is the effective refractive index given by $n_F sin\theta$. Because the guided light mode has a transverse amplitude profile that covers all layers, the effective refractive index N_m of each individual mode m is a weighed sum of the refractive indices of all layers:

$$N_m = f_N(n_S, n_F, n_C, d_F, \lambda, m, \sigma) \tag{2.71}$$

Here, n_S, n_F, n_C are the refractive indices of the the substrate, film and cover medium, respectively. d_F is the effective thickness of the film. λ is the vacuum wavelength of the light used. $m = 0, 1, 2, \ldots$ is the mode order; and σ is the mode-type number that equals 0 for transverse electric (TE), or s-polarised, and 1 for transverse magnetic (TM), or p-polarised modes. The value of N further depends on the mode's power distribution (field) among all layers. The phase shifts due to TIR at the two boundaries are given by[87,85]:

$$\phi_{F,S} = -2arctan\left[\left(\frac{n_F}{n_S}\right)^{2\rho}\sqrt{\frac{N_m^2 - n_S^2}{n_F^2 - N_m^2}}\right] \tag{2.72}$$

$$\phi_{F,C} = -2arctan\left[\left(\frac{n_F}{n_C}\right)^{2\rho}\sqrt{\frac{N_m^2 - n_C^2}{n_F^2 - N_m^2}}\right] \tag{2.73}$$

where $\rho = 0, 1$ represents, again, the TE and TM polarised case, respectively.

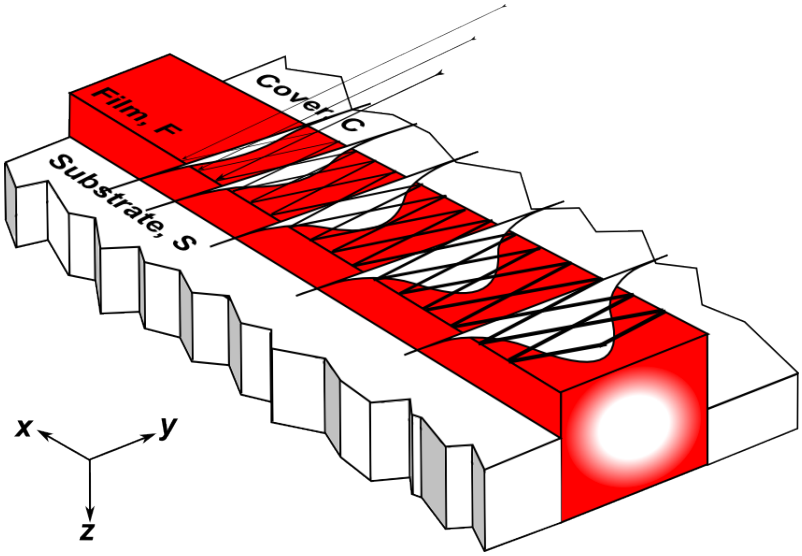

Figure 2.28: Fundamental mode (m = 0)

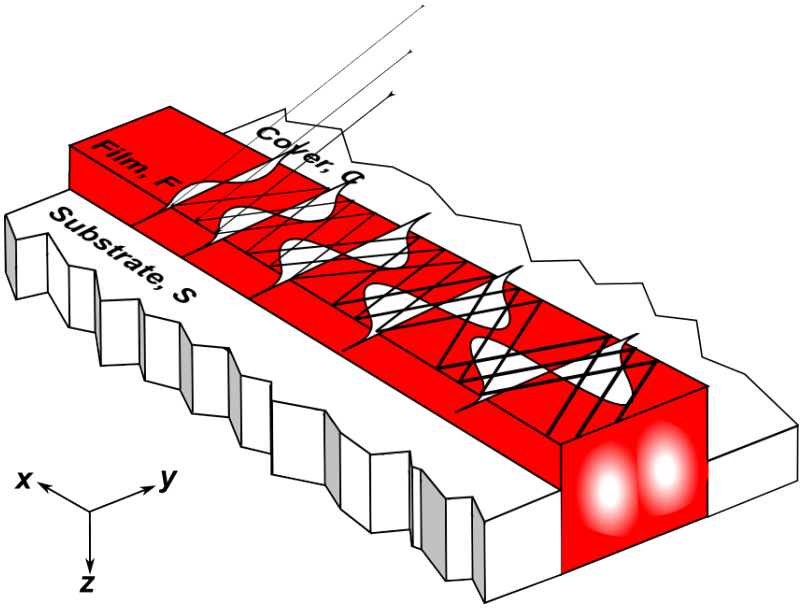

Figure 2.29: Higher order mode mode (m = 1)

Except for N_m, all parameters of the mode equation are known. However, N_m, which is a normalised wave vector component along x, is given by $\frac{\mathbf{k}_x}{\mathbf{k}}$. The expression 'effective refractive index' appears because the phase velocity along x in the waveguide is $v = \frac{c}{N_m}$. Now the solutions N_m for a given waveguide configuration can be calculated using the mode equation 2.69.

In figure 2.30 mode curves are shown in a mode map, where N_m is plotted vs. film thickness d_F for a representative waveguide structure. Here the solid and dashed curves

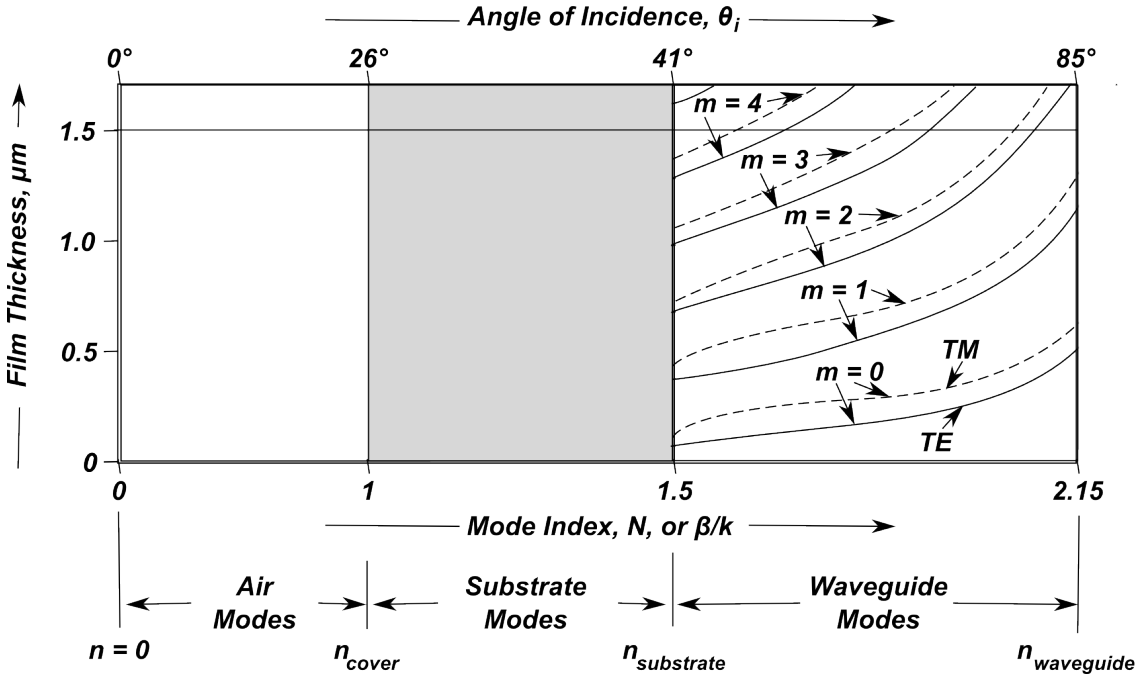

Figure 2.30: Schematic illustration of the properties of the normal modes using a solid $1.5\mu m$ thick $TiO_2/glass$ waveguide in air as the example. It shows that 'airspace', 'substrate', and 'waveguide' modes have mode indices between 0 and $n_{cover} = 1$, $n_{cover} = 1$ and $n_{substrate} = 1.5$, and $n_{substrate} = 1.5$ and $n_{waveguide} = 2.1$, respectively. On the right side of the figure mode curves are plotted. The dashed and solid curves are representing TM and TE waveguide modes, respectively.This shows the presence of five TM and five TE 'waveguide' modes. Each of the waveguide modes is the result of a 'zigzag wave'.

are for the TE and TM modes, respectively. Each curve represents one waveguide mode. All mode curves start, at the left, from $N_m = n_S$, and end, at the right, to $N_m = n_F$, and are monotonically increasing functions from left to right. In order to allow a waveguide mode to propagate, a minimum thickness must be obtained, as indicated by the mode curve at $N_m = n_S$. This specific thickness is called 'cutoff' thickness d_{cutoff}.

By gradually increasing the film thickness from this 'cutoff' film thickness it results in one to more supported guided modes of the same polarisation as the light, thus a single mode waveguide describes a waveguide in which one waveguide mode exists. In the case of a film that can support two or more supported waveguide modes of the same polarisation the waveguide is being referred to as multimode waveguide. For a multimode waveguide several cutoff thicknesses exists - one for each waveguide mode. These thicknesses are identified as the individual cutoff film thickness for a waveguide mode of mode order m. Referring to the examples in figure2.30 these cutoff thicknesses are approximately 95 nm, 400 nm and 695 nm for the $0th$, $1st$ and $2nd$ order modes, respectively.

Finally, at $N_1 = n_S, \theta$ is $arcsin(\frac{max\{n_C,n_S\}}{n_F}) = \theta_{critical,S,F}$, or the critical angle of the film/substrate interface. This figure shows that, for $\theta < \theta_{critical\{S,F\}}$, or $N_m = max\{n_S, n_C\}$, all waveguide modes are 'cutoff'. In this region only 'substrate' and 'air' modes can exist, see figure 2.31.

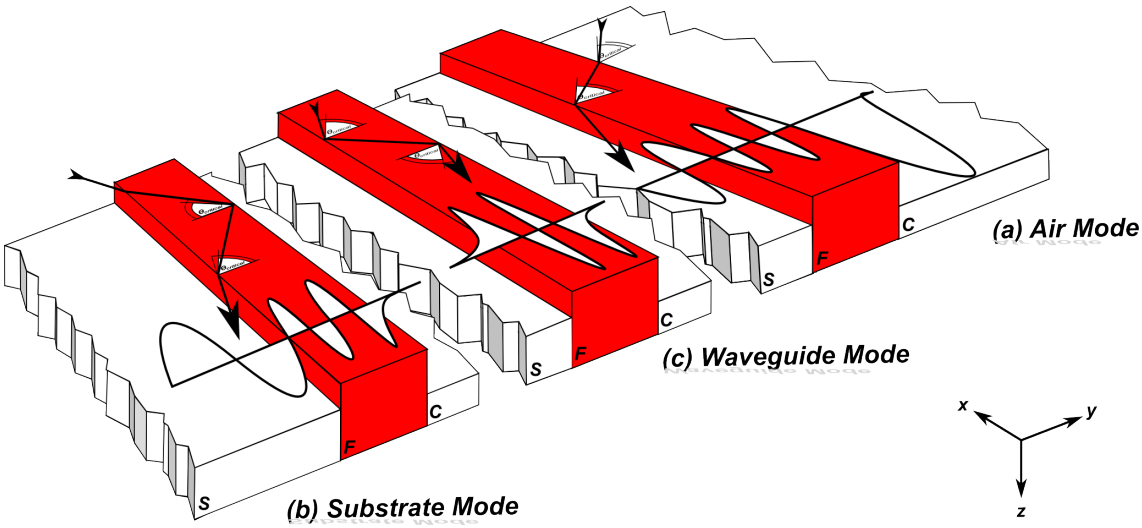

Figure 2.31: Shows various normal modes of the waveguide by considering a plane wave in the film. In (a), the incident angleθ_i is smaller than the critical angle $\theta_{critical}$ at the two interfaces. The light beam is refracted into both the substrate and the airspace forming an 'airspace' mode. As θ_i increases, it eventually becomes larger than the critical angle at the air-film interface. The light wave is then totally reflected at this interface forming a 'substrate' mode (b). Finally, a waveguide mode is formed as θ_i becomes larger than the critical angle at the film-substrate interface. In this case, the light beam appears as zigzag wave in the film (c).

In order to determine the value of the 'cutoff' film thickness for any given mode of order m the thickness can be calculated from equations 2.69, 2.4, 2.3 and 2.13 by setting $N = max\{n_S, n_C\}$.

$$d_{cutoff} = \frac{1}{\mathbf{k}\sqrt{n_F^2 - n_{max}^2}} \left\{ arctan \left[\left(\frac{n_F}{n_{min}} \right)^{2\rho} \sqrt{\frac{n_{max}^2 - n_{min}^2}{n_F^2 - n_{max}^2}} \right] + m\pi \right\} \tag{2.74}$$

with $n_{min} = min\{n_C, n_S\}$ and $n_{max} = max\{n_C, n_S\}$.

2.5.4 Excitation of Waveguide Modes

For coupling laser light into (and out of) the waveguide structure in order to excite waveguide-modes, basically two classical techniques are available: (1) coupling by matching the spatial distribution of the incoming light beam to that of the waveguide mode, and (2) methods which couple the light by matching the wave vector $\mathbf{k}$ of the incident light with the wave vector m of a waveguide mode. Since each guided mode has a characteristic wave vector m which is aligned parallel to the waveguide sheet and points into the propagation direction. The effective refractive index N_m for each mode is related to the wave vector by: $\beta_m = 2\pi N_m/\lambda$, with the wavelength λ of the propagating light. The need for coupling devices, i.g. prisms, for the excitation of these modes by laser light will be demonstrated in the following sections.

In the first technique, direct or transversal coupling, the light is coupled by focusing the

beam onto the polished endface of a waveguide to match the lateral field distribution. Here no simple experimental selectivity for specific modes is possible, because no experimental adjustment parameter is available. Therefore, this method is not of particular interest for multimode systems as those presented in this thesis.

However, the prism coupler, as already introduced in section 2.3.1and shown in Figure 2.20, is of great importance for applications with optical multilayer systems. It matches the wave vector of the incoming light with the guided mode wave vector β_m by increasing it with the help of the higher refractive index of the prism material n_p in comparison to air.

Another relevant representative of light-coupling devices is (discussed separately in chapter 8) the holographic grating. This particular method is wide-spread especially in integrated optical (IO) devices such as Lab-on-Chip platforms. The operation of a grating coupler is based on the matching of the wave vector β_m of the m-th mode by adding or subtracting integer multiples n of the grating vector G; the latter is oriented perpendicular to the grating lines and has a length $G = 2\pi/\Lambda$, with Λ the grating spacing. The experimentally available parameter to adjust for resonant coupling for both, the prism coupler and the holographic grating coupler, is then the angle of incidence θ_i.

As indicated above, prism coupling devices are mainly used to match the propagation constants of the impinging light $\mathbf{k}_x$ and waveguide-mode β_m, according to conservation of momentum. For a given angle of incidence the value of $\mathbf{k}_x$ is always proportional to the refractive index of the surrounding medium. Therefore, in order to excite all existing modes, the excitation has to occur from a region of refractive index not lower than the refractive index n_p of the waveguide itself, which, however, is inconsistent with the waveguiding condition (follows from equation 2.69).

$$\varphi > arcsin\left(\frac{max\left\{n_S, n_C\right\}}{n_F}\right) \tag{2.75}$$

This contradiction, however, can be avoided if the waveguide-mode is excited *via* the evanescent, exponentially decaying EM field. Equivalently to the procedure for the excitation of surface plasma waves, the evanescent field can be realised with a glass prism wherein a light beam is totally internal reflected at its base (see figures 2.13 and 2.20). This evanescent field, again, can now be utilised for evanescent field coupling of the incident light into the waveguide film to excite a mode of order m if the coupling condition

$$\mathbf{k}n_p sin(\theta) = \mathbf{k}n_F sin\varphi_m \tag{2.76}$$

is fulfilled. Under 'ordinary conditions' it is true that the creation of an evanescent wave

does not affect the conservation of energy, i.e. the evanescent wave transmits zero net energy. However, if a waveguide medium with a higher refractive index than the second medium is placed within less than several wavelengths distance from the interface between the first medium and the second medium, the evanescent wave will be different from the one under 'ordinary conditions' and it will pass energy across the second into the waveguiding medium (as shown in figure 2.13).

On account of the reversibility of the light path, it is clear that in-coupled light may also be coupled out in the exact same manner. Accordingly, if light has to be guided over long distances, as it is the case for waveguides in optical communication applications, one has to make sure that the coupling condition, once the light is coupled in, are fulfilled no more. In those cases, the coupling device may only adjoin the waveguide by an area as small as possible, and, therefore, not allow the guided light to leave the waveguide structure.

Two coupling configurations have been proposed to excite waveguide-modes optically by employing the evanescent field created by a laser beam which is reflected off the base of a high refractive index prism. (1) In the Otto-configuration2.32 (analogous to the Otto-configuration for excitation of SP[64] an air-gap ($n_{air}@STP = 1.0002926$)[35] with a thickness of the order of the employed laser wavelength is adjacent to the prism base. Located on the other side of the gap is a high refractive index layer of (theoretically) optically infinite thickness. TIR takes place for angles equal to or larger than the critical angle. Under the TIR condition, the evanescent field at the prism base can tunnel across the dielectric spacer and excite waveguide modes within the high refractive index film. The intensity of the reflected beam is monitored and, in the case of a multi-modal waveguide, each coupling condition appears as a minimum of the reflection intensity (see figures in 2.34). The reflected intensity is usually scaled by the incident intensity. This normalised quantity is called the reflectivity R ($R := \frac{I_i}{I_r}$).

The tunnelling process is very sensitive to changes in the thickness of the gap and the thickness has to be chosen in accordance with the dielectric constant of the gap material in order to yield a high coupling efficiency. Thus the Otto configuration requires the ability to build this three-component structure with high precision. For the study of adsorption processes, access to the dielectric layer is necessary in order to exchange material and introduce dielectric contrast. This demands an extremely thin flow cell construction that can be disassembled and reassembled. This, however, combined with the fact that the Otto configuration is very susceptible to thickness variations of the spacer layer introduced by dust particles *etc.* explains why the method is rather uncommon today.

(2) The Kretschmann configuration is the prevalent method today to couple light to

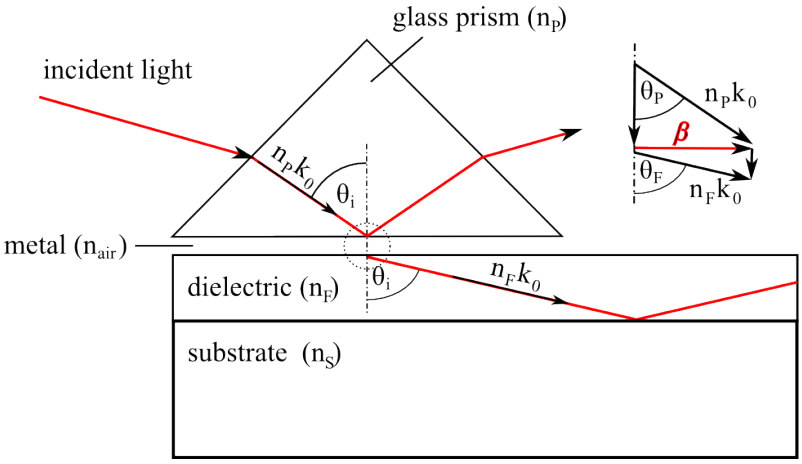

Figure 2.32: Otto configuration for light-coupling into a waveguide applies a prism with a thin metal air-gap between its base and the waveguide in order to totally reflect the laser light at the prism-base. During total internal reflection the light couples via evanescent wave into the waveguide given that the wave vectors match at angle θ_i, as illustrated on the right.

waveguide modes (and widely used for surface plasmon excitation as well) because of its relative simplicity and robustness. As illustrated in figure 2.33, a laser beam is reflected off the base of a high refractive index prism and the reflected intensity is measured.

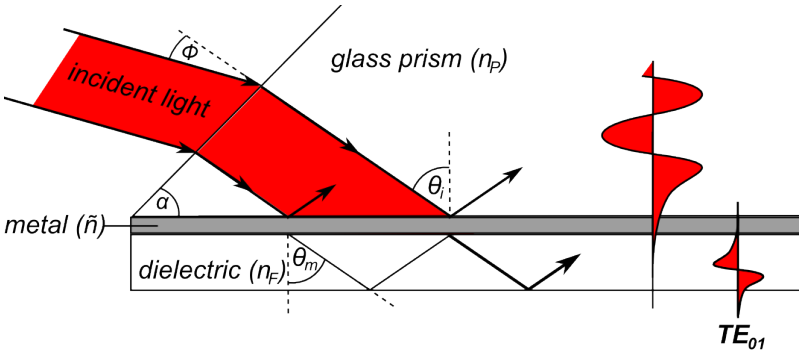

Figure 2.33: Kretschmann configuration for light-coupling into a waveguide utilises a prism with a thin metal layer (e.g. Au or Ag) between its base and the waveguide in order to totally reflect the laser light at the prism/metal interface. During total internal reflection the light couples via evanescent wave into the waveguide given that the wave vectors match at angle θ_i.

Metal and low refractive index dielectric layers swap roles compared to the previously described method but with the advantage that the dielectric phase is readily accessible in the Kretschmann configuration. A thin metal layer is located on the prism base, for example $\sim 50nm$ thickness for the combination of a gold film and a helium-neon laser ($\lambda_{HeNe} = 632.8nm$), followed by a high refractive index dielectric. The metal layer thickness needs to be precisely controlled in order to obtain the most efficient coupling to the excitation. If the metal layer is too thick and opaque to the EM field, it will not reach the interface on the opposite side. This system is essentially a mirror. Its reflectivity is high but below total ($R < 1$) because of bulk absorption. If the layer, again, is too thin, the interaction with the electrons can not fully develop, too much intensity will pass through

the metal and propagate freely as a transmitted or a reflected wave. In this case, the refractive index contrast between prism and medium determines the reflectivity curve.

The reflectivity is almost vanishing for angles smaller than the critical angle. It rises sharply at the critical edge located at $\theta_{critical}$, the onset of TIR. To excite the waveguide mode, i.e. to match the resonance condition, the layer needs to be thicker than this, but still thin enough for the field to penetrate the dielectric half-space. For the appropriate metal film thickness the resonances can be excited and the characteristic dips in the reflectivity scan appear if the power of the EM wave is nearly fully channelled into the waveguide-mode.

A big advantage of these attenuated total reflection (ATR) techniques is the relative simple theoretical descriptiveness, since solely the reflection of a light ray at a multilayer system is considered, which is fully described by the set of Fresnel's equations.

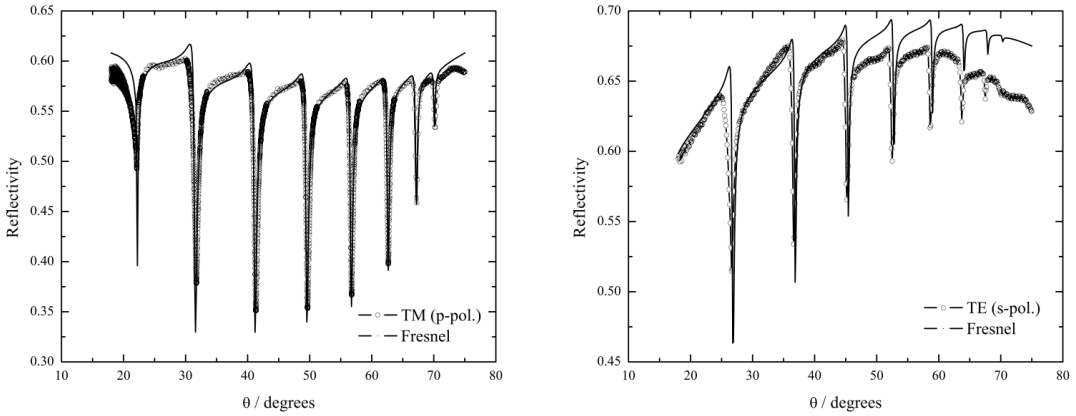

Figure 2.34: Angular dependent Kretschmann scan curves for a multi-mode waveguide. The the reflected intensity (i.e. reflectivity) of p-polarised light (left) and s-polarised light (right) with air as surrounding medium is fitted with a Fresnel simulation for reflections at multi-layer systems.

2.5.5 EM field profiles

A more accurate and complete understanding of the waveguiding phenomenon is provided by analysing light propagation in a waveguide in the form of normal modes with discrete field distributions. The characteristic EM fields for TE and TM modes are determined by the mode order and can be obtained by solving Maxwell's equations and the boundary conditions of the waveguide. Depending on the mode order, and based on the wave-nature of light these are eigensolutions of the wave equation. In the following, the eigenvalue equation will be ascertained starting from Maxwell's equations. For the wave-optical examination the guided mode in the x-direction is understood as a standing wave, therefore the time dependence can be neglected. As light is only guided in the film layer the

following formulation of the electric and magnetic fields, represented by their amplitude A, in the different layers will be made. The geometry, again, allows a separation into TE and TM modes in the form of

$$A_{1,y} = A_1 \cdot e^{-\mathbf{k}_{1,z}(z-d)} \qquad z \geq d \tag{2.77}$$

$$A_{2,y} = A_2^+ \cdot e^{i\mathbf{k}_{2,z}z} + A_2^- \cdot e^{-i\mathbf{k}_{2,z}z} \qquad 0 \leq z \leq d \tag{2.78}$$

$$A_{3,y} = A_3 \cdot e^{\mathbf{k}_{3,z}z} \qquad z \leq d \tag{2.79}$$

for A either being the electric field $\mathbf{E}$ or the magnetic field $\mathbf{H}$. $\mathbf{k}_{z1}$ and $\mathbf{k}_{z2}$ are the wave vectors along the z-axis and d represents the adlayer (i.e. waveguide) film thickness. The numbers 1, 2 and 3 are references to the media involved for $z \geq d$, $0 \leq z \leq d$ and $z \leq d$, respectively.

At this stage, the continuity relation for the tangential components of $\mathbf{E}$ and $\mathbf{H}$ have to be fulfilled, which gives for $z = 0$,

$$A_3 = A_2^+ + A_2^- \tag{2.80}$$

$$\kappa_{3,z}A_3 = \kappa_{2,z}\left(A_2^+ - A_2^-\right) \tag{2.81}$$

and for $z = d$

$$A_2^+ e^{i\mathbf{k}_{2,z}z} + A_2^- e^{-i\mathbf{k}_{2,z}z} = A_1 \tag{2.82}$$

$$-\kappa_{1,z}A_1 = i\mathbf{k}_{2,z}(A_2^+ e^{i\mathbf{k}_{2,z}} - A_2^- e^{-i\mathbf{k}_{2,z}z}) \tag{2.83}$$

κ is defined for a layer j as

$$\kappa_{j,z}^{TE} = \mathbf{k}_{j,z} \tag{2.84}$$

and

$$\kappa_{j,z}^{TM} = \frac{\mathbf{k}_{j,z}}{\varepsilon_{j,z}}. \tag{2.85}$$

Reflection coefficients r^{refl} are defined for both interfaces as the transversal field, reflected at the interface, divided by the one that is incident.

$$r_{2,3}^{refl} = \frac{A_2^+}{A_2^-} = \frac{i\kappa_{2,z} + i\kappa_{3,z}}{i\kappa_{2,z} - i\kappa_{3,z}} \tag{2.86}$$

$$r_{2,1}^{refl} = \frac{A_2^+}{A_2^-} = \frac{A_2^- e^{-i\mathbf{k}_{2,z}d}}{A_2^+ e^{i\mathbf{k}_{2,z}d}} = \frac{i\kappa_{2,z} + i\kappa_{1,z}}{i\kappa_{2,z} - i\kappa_{1,z}} \tag{2.87}$$

The boundary conditions for both polarisation modes result in the same condition for the excitation of guided modes in a film:

$$r_{2,1}^{refl} r_{2,3}^{refl} e^{i2\mathbf{k}_{2,z}d} = 1 \tag{2.88}$$

Since the magnitude of the reflected beam cannot be larger than that of the incident wave and both reflection coefficients have therefore absolute values, which can be written as $r^{refl} = e^{i\beta}$; $1 = e^{m2\pi i}$ with m being an integer referring to the mode number. This reshaping of the formula leads to the eigenvalue equation for waveguide modes of the order m for non-absorbing materials:

$$2\mathbf{k}_{2,z}d + \beta_{2,1} + \beta_{2,3} = m \cdot 2\pi \tag{2.89}$$

The meaning of above stated equation is that guided modes can only exist if the phase changes due to reflectance at the interfaces $\beta_{2,1}$ and $\beta_{2,3}$ and the phase shift $2\mathbf{k}_{2,z}d$, accumulated during travelling, add up to an integer multiple of 2π. For a given set of materials, and hence refractive index combinations, the only variable in the mode equation that is not fixed is the film thickness d. Thus, the number of eigenvalues, i.e. waveguide modes, only depends on the thickness of the waveguide layer. The characteristic wavevector of a guided mode is given by $\mathbf{k}_2 sin(\theta_i)$ indicating that only for discrete angles of incident light (of both polarisation modes) can be optically guided. A detailed analysis of Maxwell's equations also yields the optical field amplitudes for each eigenmode. However, if a metal layer is introduced in the multilayer system, an exceptional case of guided modes can be observed; the surface plasma wave (SP), or surface plasmon (SP). This resonance phenomenon is rooted in the excitation of plasma waves at the metal-dielectric interface [1] (for details referred to section 2.3).

2.5.6 Waveguide losses

Guidance of optical waves can always be achieved through material combinations where a higher refractive index waveguiding material is embedded in a lower refractive index medium. Nevertheless, it is essential for these systems to guide light with losses as low as possible. Attenuation of guided modes can always be explained by:

(1) Absorption losses in consequence of conversion of guided light intensity to another energy form (e.g. heat). Microscopic causes for adsorption losses include: (1a) Interband transitions, which appear if the energy of the light quantum is bigger than that of the energy gap between the valence and conduction band of the applied medium; in the case of ionic crystals the band gap is located at relatively high energies of several electron volts (eV), and this, again, leads to a so called UV-band edge. In these cases absorption starts not until the ultraviolet section of the light spectrum; in the case of oxide crystals mostly below $\lambda = 400nm$. (1b) Intraband transitions occur when impinging light leads to energy transitions within the energy band of a solid. This is of particular importance for semi conducting materials, where free charge carriers can absorb fractions of the light energy. (1c) Excitation of vibrational levels (phonons) of the lattice by light quanta in the infrared (IR) spectrum. (1d) Absorption by impurities and defects (colour centres); both lead to additional energy levels within the bandgap, thus result in adsorption bands caused by transition between these levels and therefrom into the conduction or valence band. Especially traces of transition metal ions with there adsorption bands, depending on the actual ion, distributed throughout the whole UV-VIS-NIR. Therefore it is of great importance to take special care of pure materials and careful preparation.

(2) Mode coupling losses as a result of coupling of the considered mode into another mode (e.g. into the spectrum of radiation modes) which includes scattering losses. It turns out to be reasonable to distinguish between volume- and surface-scattering. (2a) Volume-scattering occurs due to refractive index inhomogeneities in the waveguide, which can be ascribed to material inhomogeneities. Already a quite simple approach to describe the refractive index of such an inhomogeneous material with the Lorenz-Lorentz theory leads to:

$$\frac{\varepsilon' - 1}{\varepsilon' + 2} = \frac{n^2 - 1}{n^2 + 2} = \frac{1}{3\varepsilon_0} \sum_j \bar{N}_j \tilde{\alpha}_j \tag{2.90}$$

with the particle density $\bar{N}_j$ and the polarisability $\tilde{\alpha_j}$ of the component j of the solid. All fluctuations in the density cause $\bar{N}_j$, and in the composition additionally through $\tilde{\alpha_j}$, to refractive index fluctuations. Based on classical electrodynamics the scattering losses can be estimated by treating the refractive index fluctuations Δn in a small volume ΔV as

miniature dipoles. Applying the theory of Hertz's Dipols, and additionally summarising all scattering fractions, thus assuming Rayleigh-scattering, gives the value for the total losses. In general the volume-scattering losses can be minimised by choosing light of the optimal wavelength, according to the material dispersion. Surface-scattering appears due to excitation of radiation modes at surface and interface inhomogeneities, respectively. These losses are proportionally increasing to the square root of the surface (and interface) roughness over the square root of the wavelength of applied light.

Besides attenuation of the guided light intensity, volume- and surface-scattering influence (due to the scattered light) sensitivity, resolution and dynamic of most optical elements. As indicated above, absorption of light energy may happen in a variety of ways. In many cases these loss mechanisms are even dependent on the wavelength of the applied light source. According to the EM theory of guided waves it is possible to describe absorption losses by an imaginary part ε'' of the complex dielectric constant $\tilde{\varepsilon}$:

$$\tilde{\varepsilon} = \varepsilon' + i\varepsilon'' \tag{2.91}$$

For optical waveguides in general, material combinations are chosen with an imaginary part ε'' being as small as possible compared to the real part ε'. Thus the propagation properties are determined only by ε' or rather the real refractive index n. An exception of this are material combinations involving metals. In the case of metals (i.e. conductive materials), the contribution of the conductivity has to be taken into account:

$$\tilde{\varepsilon} = \varepsilon' + i\left(\varepsilon'' + \frac{\sigma}{\omega}\right) \tag{2.92}$$

where σ is the conductivity, ω is the angular frequency of the light.

Optical waveguides in the systems used in this thesis involve metal layers within a multilayer structure. In many cases thin gold films are applied as electric conductive layer or as self-assembly surface. A special problem involving metal films in optical systems is given if TM-polarised light is impinged upon the metal layer. Under certain conditions the SP resonance phenomenon can be observed, due to the interaction of the TM-polarised light wave with the free electrons in the metal. In this special case the light energy is coupled to the collective oscillation of the free electrons of the metal at the semi-infinite metal-dielectric interface.

Therefore, the following sections will go into more detail on this topic. Metals, however, possess a complex refractive index $\tilde{n} = n + i\kappa$. Here, n is the real refractive index indicating

the phase velocity, while κ is called the extinction coefficient, which indicates the amount of absorption losses when the EM wave propagates through the material.

Assuming a multilayer waveguide configuration with the dielectric constants for the individual layers being:

$$\tilde{\varepsilon}_j = (n_j + i\kappa_j)^2, \quad j = 1, 2, 3, ..., n \tag{2.93}$$

and therewith, because of $\tilde{\varepsilon}_j = \varepsilon'_j + i\varepsilon''_j$:

$$Re\, \varepsilon_j = \varepsilon'_j = n_j^2 - \kappa_j^2 \tag{2.94}$$

$$Im\, \varepsilon_j = \varepsilon''_j = 2n_j\kappa_j \tag{2.95}$$

2.5.7 Continuous refractive index profiles

Integrated optics methods frequently deals with continuous refractive index profiles in waveguide structures, caused by the production process itself and by reversible diffusion processes, respectively. These inhomogeneities only in the fewest cases correspond to step-like gradients, but more often form inhomogeneous gradients. Computation of the field distributions with the matrix-method is not restricted to homogeneous layers, but also possible for refractive index gradients within these layers. Therefore, the next section will discuss the possibility of monitoring continuous refractive index profiles. As illustrated before, the multilayer-matrix-formalism offers a numerical method to describe reflection- and transmission-coefficients as well as propagation-coefficients of guided waves within optical multilayer-systems. Therefore, a continuous refractive index profile $n(z)$ can be modelled precisely by assuming the gradient consisting of N individual fractions, i.e. N infinitely thin layers $N \to \infty$, each N with a constant refractive index. Accordingly, a variety of approximation methods have been developed, allowing the calculation of propagation-coefficients and field-distributions. However, most of these methods are based on the quantum theory-related WKB-method (Wentzel, Kramers, Brillouin)[59,22]. The matrix-formalism is also well-suited to be used to model a refractive index gradient. The fractionising of a given (exponential) refractive index gradient into $N = x$ layers is illustrated in Figure 2.35. For that reason, the following values are set for the waveguiding structure:

$$n(z) = \left\{ \begin{array}{c} 1 \\ n_S + \Delta n e^{\frac{-z}{a}} \end{array} \right\} \begin{array}{ll} , & z < 0 \\ , & z > 0 \end{array} \tag{2.96}$$

Where n_S is the refractive index of the waveguide substrate, Δn is the refractive index step on the surface and a is the penetration-depth of the profile into the substrate, sketched on the z-coordinate. The half-space $a < 0$ is set to be air with $n = 1$, while $x > 5a$ is the region of the waveguide substrate where $n(z) = n_S$.

$$\begin{aligned} n_i &= n(z_i) \\ z_i &= (i - 1/2)\Delta d \qquad (i = 1, 2, ..., N) \end{aligned} \tag{2.97}$$

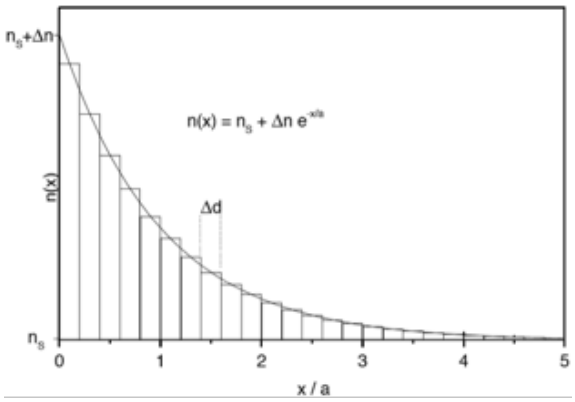

Figure 2.35: Illustration of a gradually decreasing refractive index gradient

In practise, the way of looking on this problem is inverse; from experimental data (mode-indices N_m) or reflection spectra the refractive index profile has to be determined.

Bibliography

[1] Adams, M. *An Introduction to Optical Waveguide* (John Wiley and Sons, Chichester, 1981).

[2] Aiello, A. & Woerdman, J. P. Role of beam propagation in goos-haenchen and imbert-fedorov shifts. *Opt. Lett.* **33**, 1437–1439 (2008).

[3] Antar, Y. M. & Boerner, W. M. Gaussian beam interaction with a planar dielectric interface. *Can. J. Phys.* **52**, 962–972 (1974).

[4] Ashcroft, N. W. & Mermin, N. D. *Solid State Physics* (International Thomson Publishing, 1976).

[5] Attridge, J. W., Daniels, P. B., Deacon, J. K., Robinson, G. A. & Davidson, G. P. *Biosens. Bioelectron.* **6**, 201–24 (1991).

[6] Aust, E., Ito, S., Sawodny, M. & Knoll, W. *Trends Polym. Sci.* **2**, 313–23 (1994).

[7] Barnes, W., Preist, T., Kitson, S. & Sambles, J. Physical origin of photonic energy gaps in the propagation of surface plasmons on gratings. *Phys. Rev. B* **9**, 6227–6244 (1996).

[8] Barnes, W. L. *et al.* Photonic gaps in the dispersion of surface plasmons on gratings. *Phys. Rev. B.* **51**, 11164–11167 (1995).

[9] Beckmann, P. & Spizzichino, A. *The Scattering of Electromagnetic Waves from Rough Surfaces* (Pergamon Press, Oxford, 1963).

[10] Born, M. & Wolf, E. *Principles of Optics, 7th ed.* (Cambridge University Press, Cambridge, England, 1999).

[11] Born, M. & Wolf, E. *Principles of Optics* (Oxford: Pergamon Press, 1970).

[12] Born, M. & Wolf, E. *Principles of optics: electromagnetic theory of propagation, interference and diffraction of light* (Pergamon Press, Oxford, 1964).

[13] Bunjes, N. *et al. Langmuir 13* **13**, 6188–94 (1997).

[14] Burstein, E., Chen, W. P., Chen, Y. J. & Hartstein, A. *J. Vac. Sci. Technol.* **11**, 1004.19 (1972).

[15] Chadwick, A. & Gal, M. An optical temperature sensor using surface plasmons. *Japanese Journal of Applied Physics* **32**, 2716–2717 (1993).

[16] Chan, C. C. & Tamir, C. Angular shift of a gaussian beam reflected near the brewster angle. *Opt. Lett.* **10**, 378–380 (1985).

[17] Chen, W. P. & Chen, J. M. Use of surface plasma waves for determination of the thickness and optical constants of thin metallic films. *J. Opt. Soc. Am.* **71**, 189–191 (1981).

[18] Chilwell, J. T. *Optical waveguiding in multilayer thin film stacks and the prism coupler: a matrix method.* Ph.D. thesis, University of Otago, Dunedin, New Zealand (1982).

[19] Chilwell, J. T. & Hodgkinson, I. J. Thin-film-matrix description of optical multilayer planar waveguides. *J. Opt. Soc. Am. A* **72**, 1821 (1982).

[20] Collin, R. E. *Field Theory of Guided Waves*, chap. 7 (McGraw-Hill, New York., 1960).

[21] Colombelli, R. *et al.* Quantum cascade surface-emitting photonic crystal laser. *Science* 1374–1377 (2003).

[22] Conwell, E. Optical waveguiding in graded-index layers. *Appl. Phys. Lett.* **25**, 40–42 (1974).

[23] Cross, G. H., Girling, I. R., Petterson, I. & Cade, N. A. *Electronics letters* **21**, 1111 (1986).

[24] Ditlbacher, H., J.R.Krenn, B.Lamprecht, A.Leitner & F.R.Aussenegg. Metal nanoparticles for spectrally coded optical data storage. *Optics & Photonics News* **11**, 43 (2000).

[25] Dostalek, J., Huang, C. J. & Knoll, W. *Surface Design - Application in Bioscience and Nanotechnology, Chapter 1.2 - Tutorial Review - Surface Plasmon Resonance-Based Biosensors* (Wiley-VCH, 2009).

[26] Drude, P. Zur elektronentheorie der metalle. *Annalen der Physik* **1**, 566–613 (1900).

[27] Drude, P. Zur elektronentheorie der metalle. *Annalen der Physik* **3**, 369–402 (1900).

[28] Fang, N., Lee, H., Sun, C. & Zhang, X. Sub-diffraction-limited optical imaging with a silver superlens. *Science* 534–537 (2005).

[29] Fisher, B., Fisher, T. & Knoll, W. Dispersion of surface plasmons on rectangular, sinusoidal and incoherent gratings, j. appl. phys, 75 (1994) 1577-1581. *J. Appl. Phys.* **75**, 1577–1581 (1994).

[30] Garces-Chavez, V., Dholakia, K. & Spalding, G. C. Extended-area optically induced organisation of micro-particles on a surface. *Appl. Phys. Lett.* **86** (2005).

[31] Girard, C. & Quidant, R. Near-field optical transmittance of metal particle chain waveguide. *Optics Express* **12**, 6141–6146 (2004).

[32] Goos, F. & Haenchen, H. Ein neuer und fundamentaler versuch zur totalreflexion. *Ann. Physik (Leipz.)* **7-8**, 333–346 (1947).

[33] Gordon, J. G. & Swalen, J. D. *Opt. Commun.* **22**, 374–78 (1977).

[34] Gotschy, W., Vonmetz, K., Leitner, A. & Aussenegg, F. R. Thin films by regular patterns of metal nanoparticles: tayloring the optical properties by nanodesign. *Appl. Phys. B* **63**, 381–384 (1996).

[35] Hecht, E. *Optics, Fourth Edition.* (Pearson Higher Education, 2003).

[36] Hecht, E. *Optics* (Pearson Addison Wesley, 2001).

[37] Hickel, W. *Entwicklung neuer Untersuchungsmethoden mit Oberflaechenplasmonen und Lichtleitermoden zur Charakterisierung ultraduenner Schichten.* Ph.D. thesis, ETH-Zuerich (1989).

[38] Hodgkinson, I. J. & Chilwell, J. T. Reflection of plane waves from a prism-loaded lossy multilayer waveguide. *J. Opt. Soc. Am.* **72**, 1744–1745 (1982).

[39] Homola, J. *et al.* A new optical fiber sensor for humidity measurement. *PhotonicsÕ 95, Prague, Czech Republic, August 1995, EOS Annual Meeting Digest Series* **2A**, 225–248 (1995).

[40] Hondros, D. & Debye, P. *Ann. Phys. (Leipzig)* **32**, 465 (1910).

[41] Hutley. *Diffraction gratings* (Academic Press, London, 1982).

[42] Hutley, M. & Mayster, F. The total absorption of light by a diffraction grating. *Optics communications* **19**, 431–436 (1976).

[43] Hutter, E. & Fendler, H. Exploitaion of localized surface plasmon resonance. *Adv. Mater* **16**, 1685–1706 (2004).

[44] Jackson, J. D. *Classical Electrodynamics* (New York, John Wiley & Sons, 1982).

[45] Jacobsson, R. *Inhomogeneous and coevaporated homogeneous films for optical applications* (Physics of Thin Films (Academic, New York, 1975), Vol. 8., 1975).

[46] Jung, L., Campbell, C. R., Chinowsky, T. M., Mar, M. N. & Yee, S. S. Quantitative interpretation of the response of surface plasmon resonance sensors to adsorbed films. *Langmuir* **14**, 5636–5648 (1998).

[47] Karthe, W. & Mueller, R. *Integrierte Optik* (Akad. Verlagsges. Geest & Portig, Leipzig, 1991).

[48] Knobloch, H., Brunner, H., Leitner, A., Aussenegg, F. & Knoll, W. *J. Chem. Phys.* **98**, 10093–95 (1993).

[49] Knoll, W. *Handbook of Optical Properties - Optics of Small Particles, Interfaces, and Surfaces* (Boca Raton, FL: CRC, 1997).

[50] Knoll, W. Interfaces and thin films as seen by boun electromagnetic waves. *Annual Review of Physical Chemistry* **49**, 569–638 (1998).

[51] Knoll, W. *Makromol. Chem.* **192**, 2827–56 (1991).

[52] Krenn, J. R. *et al.* Surface plasmon micro- and nano-optics. *J.Microsc.* **209**, 167 (2003).

[53] Kretschmann, E. The determination of the optical constants of metals by excitation of surface plasmons. *Z. Physik* **241**, 313–324 (1971).

[54] Kretschmann, E. & Raether, H. Radiative decay of nonradiative surface plasmons excited by light. *Z. Naturforsch. Teil A* **23**, 2135 (1968).

[55] Krishnan, A. *et al.* Evanescently coupled resonance in surface plasmon enhanced transmission. *Opt. Commun.* **200**, 1–7 (2001).

[56] Liedberg, B., Lundstroem, I. & Stenberg, E. Principles of biosensing with an extended coupling matrix and surface plasmon resonance. *Sens. Actuators B* **11**, 63–72 (1993).

[57] Liedberg, B., Nylander, C. & Lundstroem, I. Surface plasmon resonance for gas detection and biosensing. *Sensors and Actuators* **4**, 299–304 (1983).

[58] Marcuse, D. *Theory of dielectric optical waveguides* (Academic Press, New York, 1974).

[59] Marcuse, D. Te modes of graded-index slab waveguides. *IEEE J. Quantum Electron.* **9**, 1000–1006 (1973).

[60] Merano, M., Aiello, A., van Exter, M. P. & Woerdman, J. P. Observing angular deviations in the specular reflection of a light beam. *Nature Photonics* **3**, 337–340 (2009).

[61] Moerner, W. E. New directions in single-molecule imaging and analysis. *Proc. Natl. Acad. Sci. USA* **104**, 12596–12602 (2007).

[62] Moslehi, B., Foster, M. W. & Harvey, P. Optical magnetic and electric field sensors based on surface plasmon polariton resonance coupling. *Electronics Letters* **27**, 951–953 (1991).

[63] Nylander, C., B.Liedberg & Lindt, T. Gas detection by means of surface plasmon resonance. *Sensors and Actuators* **3**, 79–88 (1982/1983).

[64] Otto, A. *Spectroscopy of surface plasmons, Optical Properties of Solids*. (Seraphin Eds., Amsterdam, 1976).

[65] Otto, A. Excitation of nonradiative surface plasma waves in silver by the method of frustrated total reflection. *Zeitschrift fuer Physik A Hadrons and Nuclei* **216**, 398–410 (1968).

[66] Peterlinz, K. A., Georgiadis, R. M., Herne, T. M. & Tarlov, M. *J. Am. Chem. Soc.* **119**, 3401–2 (1997).

[67] Ra, J. W., Bertoni, H. L. & Felsen, L. B. Reflection and transmission of beams at a dielectric interface. *SIAM J. Appl. Math.* **24**, 396–413 (1973).

[68] Rashed, R. A pioneer in anaclastics: Ibn sahl on burning mirrors and lenses. *Isis* **81**, 464–491 (1990).

[69] Reather, H. Surface plasmons on smooth and rough surfaces and on gratings. *Springer tracks in modern physics, Springer Verlag, Berlin (1983)* **111** (1983).

[70] Reather, H. Surface plasmons on smooth and rough surfaces and on gratings (on roughness data). *Surf. Sci.* **125**, 621–634 (1983).

[71] Revelli, J. F. Enhancement of prism coupling efficiency in uniform optical waveguides: a correction. *J. Appl. Phys.* **52**, 3185–3189 (1981).

[72] Revelli, J. F. Mode analysis and prism coupling for multilayered optical waveguides. *Appl. Opt.* **20**, 3158–3167 (1981).

[73] Revelli, J. F. & Sarid, D. Prism coupling into clad uniform optical waveguides. *J. Appl. Phys.* **51**, 3566–3575 (1980).

[74] Ritchie, R., Arakawa, E., Cowan, J. & Hamm, R. Surface-plasmon resonance effect in grating diffraction. *Phys. Rev. Lett.* **21**, 1530–1533 (1968).

[75] Saleh, B. E. A. & Teich, M. C. *Fundamentals of Photonics*, chap. Appendix A: Fourier Transform, 918–927 (John Wiley & Sons, Inc., 1991).

[76] Salerno, M. *et al.* The optical near-field of gold nanoparticle chains. *Opt.Commun.* **248**, 543 (2005).

[77] Samples, J. R., Hibbins, A., Jory, M. & Azizbekyan, H. A surface plasmon study of the optical dielectric function of indium. *Journal of Modern Optics* **47**, 1227–1235 (2000).

[78] Schilling, A., O.Yavas, Bischof, J., Boneberg, J. & Leiderer, P. Absolute preasure measurement on nanosecond scale using surface plasmons. *Appl. Phys. Lett.* **69**, 4159–4161 (1996).

[79] Shakir, S. A. & Turner, A. F. Method of poles for multilayer thin-film waveguides. *Appl. Phys. A* **29**, 151–155 (1982).

[80] Siler, M., Cizmar, T., Sery, M. & Zemanek, P. Optical forces generated by evanescent standing waves and their usage for submicron particle delivery. *Appl. Phys. B* **84**, 157–165 (2006).

[81] Siler, M., Sery, M., Cizmar, T. & Zemanek, P. Sub-micron particle localization using evanescent field. *Proceedings of SPIE 5930, 0R1-0R9, 2005* **0R1-0R9**, 5930 (2005).

[82] Simon, H. J., Mitchelll, D. E. & Watson, J. G. *Phys. Rev. Lett.* **33**, pp 153 (1974).

[83] Tamir, T. *Integrated Optics, Topics in Applied Physics* ((Berlin : Springer-Verlag), 1975).

[84] Thelen, A. *Design of multilayer interference filters* (Physics of Thin Films (Academic, New York, 1969), Vol. 5., 1969).

[85] Tiefenthaler, K. & Lukosz, W. Sensitivity of grating couplers as integrated-optical chemical sensors. *J. Opt. Soc. Am. B* **6**, 209–220 (1989).

[86] Tien, P. & Ulrich, R. Theory of prism-film coupler and thin-film light guides. *J. Opt. Soc. Am.* **60**, 1325 (1970).

[87] Tien, P. K. Integrated optics and new wave phenomena in optical waveguides. *Rev. Mod. Phys.* **49**, 361–420 (1977).

[88] Tien, P. K. Light waves in thin films and integrated optics. *Appl. Opt.* **10**, 2395–2413 (1971).

[89] Tien, P. K., Ulrich, R. & Martin, R. J. Modes of propagating light waves in thin deposited semiconductor films. *Appl. Phys. Lett.* **14**, 291–294 (1969).

[90] Ushioda, S. & Sasaki, Y. *Phys. Rev. B* **27**, 1401–4 (1983).

[91] Warmack, R. & Humprey, S. Observation of two surface plasmon modes on gold nanoparticles. *Phys. Rev. B* **34**, 2246–2252 (1986).

[92] Welford, K. Surface plasmon-polaritons and their uses. *Optical Quantum Electronics* **23**, 1–27 (1991).

[93] Whewell, W. History of the inductive science from the earliest to the present times. *London: John H. Parker* (1837).

[94] Wolf, K. B. Geometry and dynamics in refracting systems. *European Journal of Physics 16: 14-20* **16**, 14–20 (1995).

[95] Wood, R. W. *Phil. Mag.* **4**, 396 (1902).

[96] Wysin, G. M., Simon, H. J. & Deck, R. T. Optical bistability with surface plasmons. *Optics letters* **6**, 30–33 (1981).

[97] Yariv, A. & Leite, R. C. C. Dielectric-waveguide mode of light propagation in p-n junctions. *Appl. Phys. Lett.* **2**, 55–57 (1963).

[98] Yeh, P. *Optical Waves in Layered Media Chap. 4-5* (Wiley, New York, 1988).

[99] Margheri, G., Mannoni, A. & Quercioli, F. (eds.). *A new high-resolution displacement sensor based on surface plasmon resonance, Proceeding of SPIE*, 2783 (1996).

[100] The dispersion relation of surface plasmons on rough surface, a comment.

[101] Thin-films field-transfer matrix theory of planar multilayer waveguides and reflection from prism-loaded waveguides, solutions for planar optical waveguide equations by selecting zero elements in a characteristic matrix.

Chapter 3
3 Experimental

Contents

3.1 General Reagents

• Cis-diisothiocyanato-bis(2,2'-bipyridyl-4,4'-dicarboxylato)ruthenium (II)bis-(tetrabutylammonium) (Solaronix, Ruthenium 535 bis-TBA), • titanium-(IV)-isopropoxide (Aldrich, 99.9%), • 2-propanol (Aldrich, anhydrous 99.8+%), • ethanol (Aldrich, anhydrous 99.8+%), • glacial acetic acid (BDH, 100%) • Carbowax (Riedel-de-Haen, Carbowax 2000), • I^-/I_3^- electrolyte solution, • primer silane (Microposit UN 2924, Rohm and Haas Electronic Materials), • thinner solution (Microposit EC-solvent, Shipley), • developer solution (ma-D 330, microresist), • 16-mercaptohexadecanoic acid (Aldrich).

All reagents were used as received without further purification.

3.2 Glass Substrates

The substrates ($25 \times 38 \times 2.5mm$) were chosen in order to fulfil the optical properties necessary to produce a multimode waveguide as described in the section before. Three different types of glass prisms and corresponding glass slides were used:

• fused silica: LITHOSIL-Q (*Schott*) with a low refractive index $n_{632.8} = 1.45699$ and high internal transmittance $\tau_i(25mm) = 0,999$ at $\lambda = 632.8nm$. Its dispersion is described with the following constants[3] ($B_1 = 6.7071081 \cdot 10^{-1}$, $B_2 = 4.33322857 \cdot 10^{-1}$, $B_3 = 8.77379057 \cdot 10^{-1}$, $C_1 = 4.49192312 \cdot 10^{-3}\mu m^2$, $C_1 = 1.32812976 \cdot 10^{-2}\mu m^2$, $C_1 = 9.58899878 \cdot 10^{1}\mu m^2$) by the Sellmeier equation.

• borosilicate crown glass: BK7 (*Schott*) with a low refractive index $n_{632.8} = 1.51509$, internal transmittance $\tau_i(25mm) = 0,994$ at $\lambda = 632.8nm$. Its dispersion is described with the following constants[3] ($B_1 = 1.38121836$, $B_2 = 1.96745645 \cdot 10^{-1}$, $B_3 = 8.86089205 \cdot 10^{-1}$, $C_1 = 7.06416337 \cdot 10^{-3}\mu m^2$, $C_1 = 2.33251345 \cdot 10^{-2}\mu m^2$, $C_1 = 9.74847345 \cdot 10^{1}\mu m^2$) by the Sellmeier equation.

• dense lanthanum flint: LaSFN9 (*Schott*) with a high refractive index $n_{632.8} = 1.84498$, internal transmittance $\tau_i(25mm) = 0,982$ at $\lambda = 632.8nm$. Its dispersion is described with the following constants[3] ($B_1 = 2.00029547$, $B_2 = 2.98926886 \cdot 10^{-1}$, $B_3 = 1.80691843$, $C_1 = 1.21426017 \cdot 10^{-2}\mu m^2$, $C_1 = 5.38736236 \cdot 10^{-2}\mu m^2$, $C_1 = 1.56530829 \cdot 10^{2}\mu m^2$) by the Sellmeier equation.

The Sellmeier equation is an empirical relationship between refractive index and wavelength for a particular transparent medium. The equation is used to determine the dispersion of light in the medium. It was first proposed in 1871 by W. Sellmeier, and was a development

of the work of Augustin Cauchy on Cauchy's equation for modelling dispersion. The usual form of the equation for glasses is:

$$n^2(\lambda) = 1 + \frac{B_1\lambda^2}{\lambda^2 - C_1} + \frac{B_2\lambda^2}{\lambda^2 - C_2} + \frac{B_3\lambda^2}{\lambda^2 - C_3} \tag{3.1}$$

where n is the refractive index, λ is the wavelength, and $B_{1,2,3}$ and $C_{1,2,3}$ are experimentally determined Sellmeier coefficients[3]. These coefficients are usually quoted for λ in micrometres.

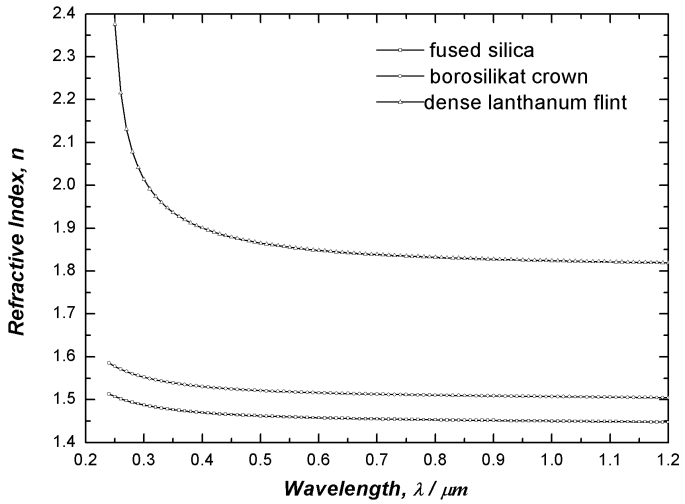

Figure 3.1: The Sellmeier equation gives the refractive index of transparent media with accuracy better than 10^{-5} for wavelengths ranging from $\lambda = 200 - 1200nm$. The plot shows the calculated RI values of glass material used in this thesis.

3.2.1 Cleaning

The glass components served as substrates for observation and measurement of interaction with light, therefore, to ensure high quality photometric measurements, great emphasis was placed on the cleanliness. The cleaning of all components was of great importance, as it required the complete removal of all contaminants without causing any damage to these delicate and high-quality optical components. On that account, a standardised cleaning procedure was developed. Most effective was the careful treatment with alkaline detergent solution (Hellmanex®, *Hellma*) (pH values at dilutions of 0.5%: 11.6 at 1.0%: 11.8 at 2.0%: 12.0), sufficient rinsing (15 repetitions), alternately in ultra pure water (Milli-Q®, $\rho \geq 18.2\ M\Omega\, cm^{-1}$ at 25 °C, Millipore) and ethanol. Ultrasound improved the cleaning process noticeably, especially at higher temperatures. However, powers that were too high or cleaning durations that were too long did result sometimes in damages by cavitation, especially if the glass was placed on the bottom of the cleaning bath. Finally, the glass was blown dry in a stream of nitrogen or heating at 90°C in a vacuum oven.

3.2.2 Plasma-Treatment

In order to obtain high quality multilayer systems it was essential to clean the glass slides carefully (according to 3.2.1). Therefore, the glass slides were further treated with O_2/Ar plasma using a Type 200-G plasma cleaner (*Technics Plasma GmbH*) with a maximum output power of $300W$ at pressures of approximately $50mbar$.

The non-equilibrium, high frequency plasma was generated with a gas mixture of 25% oxygen and 75% argon. Free electrons were accelerated to high velocities by an oscillating electromagnetic field (13.56 MHz) that excited gas atoms and created the plasma. Cleaning was carried out by reactive gas compounds formed by the plasma chemically reacting with organic material on the specimen and specimen holder. The plasma ions impinged upon the surface with energies of less than 12eV, which was below the sputtering threshold of the glass materials.

3.2.3 Thermal Evaporation of Metals

Subsequently after the plasma cleaning, the glass slides were mounted in a high vacuum coating plant (*Edwards*). The vacuum chamber was allowed to evacuate to $< 4 \cdot 10^{-6}$ mbar before the prim surface of the glass slides was coated with a ca. $50nm$ thick gold film by thermal evaporation of 1-2 gold beads. Optimal thickness of the gold film was achieved when $125mg$ or ca. $3.3cm$ of Au wire (99.9999%, $d = 0.5mm$) were put into the evaporation basket. In order to ensure sufficient adherence $2nm$ of chrome was evaporated between the glass and the gold as an adhesion layer. The evaporation rate for the first $10nm$ of gold was chosen to be as low as $0.1nm/s$ so as to assure enduring peel strength. Thereafter the evaporation rate was increased to $1nm/s$ in order to achieve a smooth metal surface[1]. After the evaporation procedure the samples were left in high vacuum for at least $25min$ allowing the fresh metal layer to cool to room temperature. Although the evaporated film thickness was monitored by a highly precise quartz crystal micro-balance, the final layer thickness on the substrates had slight variations due to the sample position in the holder. Therefore, the evaporation process was always terminated at an average value of $50nm$.

3.2.4 Annealing and Post-Treatment

To improve the optical properties of the gold films, annealing was performed for 90 seconds at $500°C$. Prior to surface functionalisation the slides were irradiated for $10min$ in heavy UV-light at RT. Finally, the slides are immerse for 10 minutes in $1mmol/L$ ethanolic solution of 16-mercaptohexadecanoic acid (*Aldrich*, 90%, $M = 288,5g/mol$).

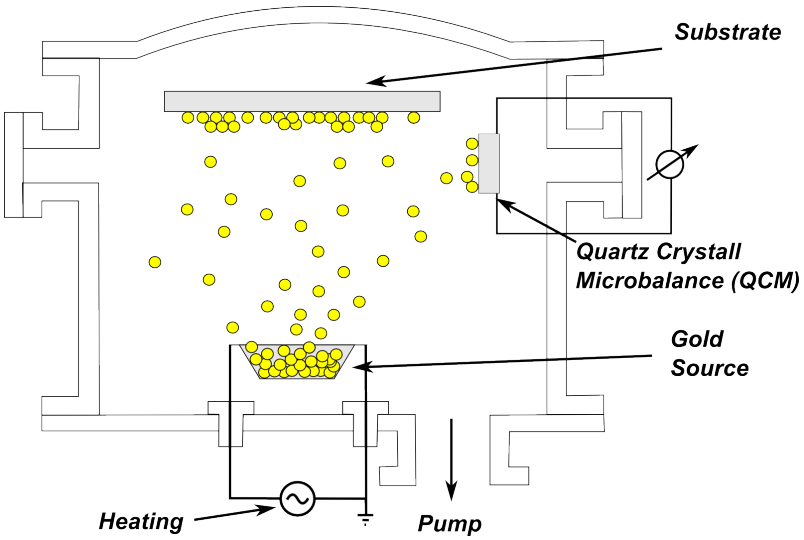

Figure 3.2: The cross-section of the high-vacuum apparatus illustrates the process of thermal evaporation of metallic gold. Gold is sublimated in the electrically heated source basket and evaporated onto the sample surface. The gold vapour spreads out uniformly in the whole volume of the chamber. The rate of evaporation and the total amount of deposited gold is measured by a quartz crystal micro-balance (QCM) and can therefore be terminated at the target layer thickness.

3.3 Preparation of Colloidal Nanocrystalline Titania

The general preparation protocol common to all the experiments involving colloidal nanocrystalline TiO_2 thin-film is outlined here. Other synthetic and preparative approaches for specific experiments are described separately in the corresponding section.

Aqueous based titanium dioxide colloidal sol was prepared by adding a mixture of 1 mL of 2-propanol (*Aldrich*, anhydrous $99.8+\%$) and $3.7mL$ of titanium-(IV)-isopropoxide (*Aldrich*, 99.9) drop wise over 30 min to $8mL$ of glacial acetic acid (*BDH*, 100%) and $25mL$ of deionised water in a conical flask at $0°C$. The solution was allowed to return to room temperature and stirred for 8 hours at $80°C$. The so obtained gel-like sol was then transferred to a PTFE lined titanium autoclave (*Parr*, General Purpose Acid Digestion Bomb, Model No. 4744) and heated at $230°C$ for 12 hours. When cool the sol was removed from the autoclave, sonicate for 15 minutes in a sonic bath (*KERRY*, $250W$ ultrasonicator). The solution was than concentrated to $150g/L$ on a rotary evaporator (*BUCHI*, R-114). Finally, $0.4g$ of Carbowax (Riedel-de-Haen, Carbowax 2000) was added and the mixture was allowed to stir for at least 12 hours before use.

3.3.1 Application of Titania Nanoparticle Films

In order to reduce contamination of the surface due to airborne dust film preparation was done, as far as possible, in a laminar-flow-box guaranteeing particle free environment during processing, preparation or storage.

The gold-coated slides were gently rinsed with ethanol, dried in a stream of nitrogen and fixed on a plane surface with two strips of tape (*Scotch*®, Magic TM Tape). This tape was chosen because it can easily be removed from the glass without leaving traces of adhesive materials. As illustrated in figure 3.3, a glass rod was used to rapidly spread the colloidal sol evenly across the gold surface, making a clean and transparent film. The film thickness was determined by the height of the tape that is used to fix the substrates, and, of course, the viscosity of the paste itself. A slow dry-out of the solvent and a subsequent sintering step was necessary to ensure optimal adhesion of the titanium dioxide layer onto the gold film.

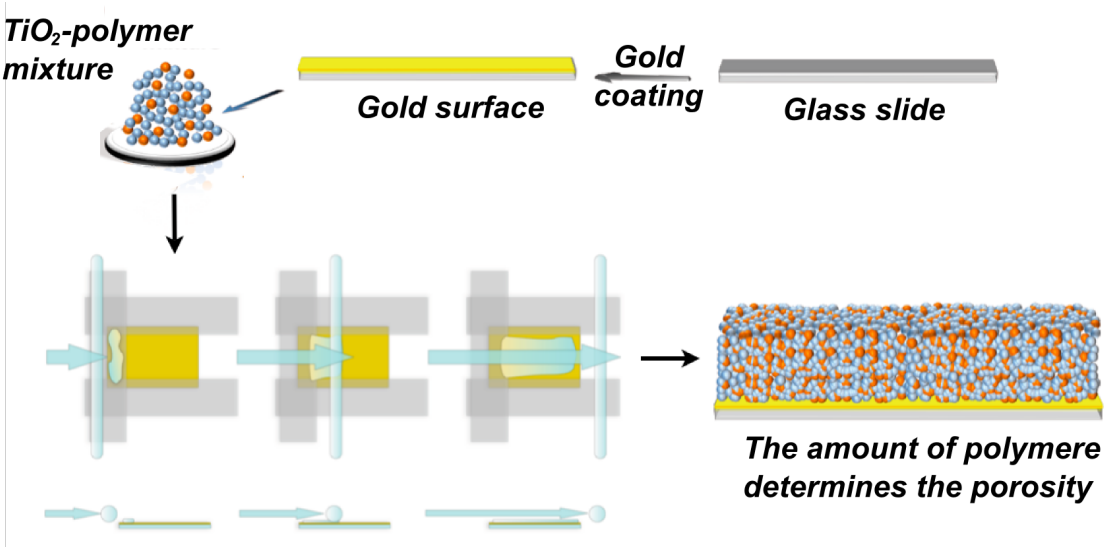

Figure 3.3: Application of TiO_2 thin-films

After complete evaporation of the solvent the colloids formed a smooth film which was than fired in the air jet of a hot-air gun at $500°C$ for 30 min, resulting in average film thicknesses from 1.2–$1.7\mu m$. This thermal treatment allowed the titanium dioxide nanocrystals to sinter partially together, in order to ensure electrical contact and mechanical adhesion on the glass. While heating up (e.g. rate: $\frac{100°C}{min}$), the films first turned brownish (sometimes they released fumes), and later turned yellowish-white due to the temperature dependent band-gap narrowing in the pure titanium dioxide (anatase). This indicated the sintering process being completed and the cooling rate was chosen (ca. $\frac{100°C}{min}$) to avoid cracking of the glass.

3.4 Preparation of Titania Nanotubes

3.4.1 Surface treatment

Titanium nanotube samples were prepared from 0.1mm thick titanium foils (99.6% purity, *Goodfellow*). Prior to any further steps the foils were degreased by sonicating in acetone, isopropanol, and methanol, then rinsed with deionised water and dried in a nitrogen stream. After this pre-treatment a three-step preparation procedure was applied to the titanium foils in order to mechanically polish the substrates to a mirror finish. The protocol is listed in table 3.1 below.

Step	Surface/Abrasive	RPM	Direction	Load (lbs.)	Time (min.)
1	Wet grind with 320 grit SiC paper	240	Comp.	6 (27N)	U.P.
2	Rough polish with 9µm METADI paste on an ULTRA-POL silk cloth*	120	Contra.	6	10
3	Final polish with MASTERMET 2 colloidal silica** on a MICROCLOTH pad	120	Contra	6	10

Notes:
Load - per specimen,
Comp. - head rotates in the same direction as the platen,
Contra. - head rotates in the direction opposite that of the platen,
U.P. - until surfaces are coplanar,
** METADI Fluid used as coolant/lubricant,*
*** For alpha titanium alloys and for pure titanium, add an attack polishing agent to the colloidal silica*
Table 3.1: Three-Step procedure applied to the titanium foils in order to mechanically polish the substrates to mirror finish.

The polished samples were then cleaned in three 5 min steps in ultrasonicated acetone, 2-propanol, and finally ultra-pure water and then dried in a flowing N_2 stream and used immediately for electrochemical treatment.

3.4.2 Electrochemical treatment

After cleaning and polishing, the titanium foil samples were pressed against an O-ring in an electrochemical cell (shown in figure 3.4), leaving $1cm^2$ exposed to the electrolyte. The electrochemical setup consisted of a conventional three-electrode configuration with a platinum gauze as a counter electrode and a Haber–Luggin capillary with Ag/AgCl (1M KCl) as reference.

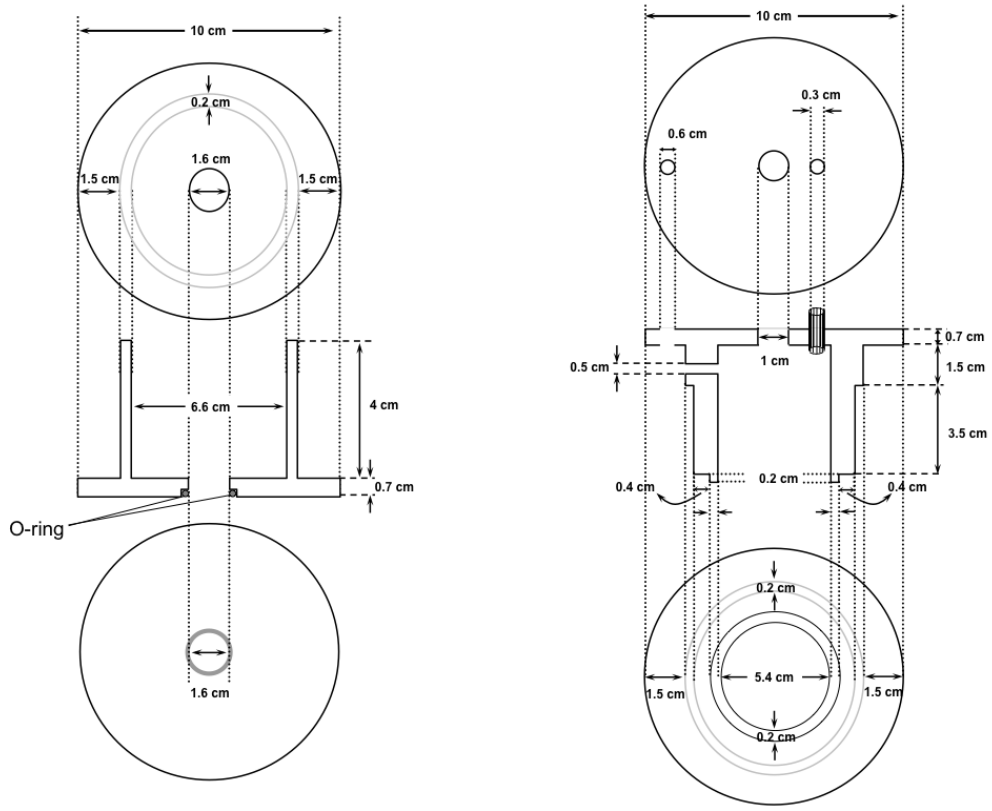

Figure 3.4: Proportional drawing which was made in order to produce the components for the anodisation cell. The left sketch shows the bottom part of the cell with the circular hole, which determines the area of the titanium foil exposed to the electrolyte solution. The right sketch displays the top part of the cell, which tightly fits the bottom part, providing a central circular opening for the stirrer and an opening allowing for the connection of the electrode. The components were milled from solid PTFE blocks. Not shown is a 1cm high copper block, which was used as the opposite electrode at he bottom of the cell.

Electrochemical experiments were carried out at room temperature using a high-voltage potentiometer Jaissle IMP 88. The electrolyte was 1M $(NH_4)_2SO_4$ with the addition of small amounts of NH_4F (0.5–5 wt.%). All electrolytes were prepared from reagent grade chemicals and deionised water. The electrochemical treatment consisted of a potential ramp from the open-circuit potential (OCP) to $20V$ with a different sweep rate followed by holding the applied potential at $20V$ for different times. For the purpose of precise control and reproducibility of the protocol a simple software was programmed.

After the electrochemical treatment the samples were rinsed with deionised water and blow-dried with nitrogen stream.

3.5 Structural Characterisation

3.5.1 Scanning Electron Microscopy (SEM)

In SEM, the electron beam is emitted from a heated filament or field emission tip. The electrons are accelerated by an electric potential in order of $1\text{–}400kV$. A condenser lens projects the beam from the source onto the condenser aperture. The beam is focused by an objective lens and raster-scanned by scanning coils over the sample. The spot size of the primary electron beam determines the resolution of the instrument. When the primary electrons hit the sample surface, they pass part of their energy to electrons in the sample, resulting in the emission of secondary electrons. This secondary electrons are collected by a detector and their intensity is displayed *versus* the position of the primary beam on the sample. The secondary electrons are viewed on a cathode-ray tube (CRT)[2].

SEM characterisation of all samples and titania films in this thesis was performed on a LEO 1530 Gemini field emission SEM. To avoid surface charging, the SEM was operated between $1\text{–}3kV$. Additionally, the samples needed to be made conductive, by connecting the titania film with the metal part of the sample holder. This was achieved with thin (ca. $2mm$) stripes of standard carbon conductive adhesive tabs with the total thickness of $125\mu m$. These tabs are solvent free and cause no parasitic out-gassing in the vacuum chamber.

3.5.2 Atomic Force Microscopy (AFM)

A Dimension 3100 AFM ((Digital Instruments/Veeco Metrology, USA)) with a nano-scope IV controller and a 15x15 µm scanner was used to investigate holographic gratings, periodic structures, either etched into glass slides or produced on polymeric substrates by means of hot-embossing. All images were acquired in Tapping Mode AFM in ambient environment.

Silicon Probes were used for tapping mode AFM applications, where the tip and the cantilever were an integrated assembly of a single crystal silicon, produced by etching techniques. Only one cantilever and tip was integrated with each substrate. The spring constant of the tips was $33.9\text{–}40.9N/m$ and the resonance frequency was $222.3\text{–}297.0$.

3.5.3 Profilometry

A computerised *Tencor* Alpha Step 200 profilometer was used to investigate the thickness and the surface morphology of the thin-films films. The P-10 is a stylus profilometer, which makes use of a sharp stylus (2 µm tip radius) to measure the surface topography

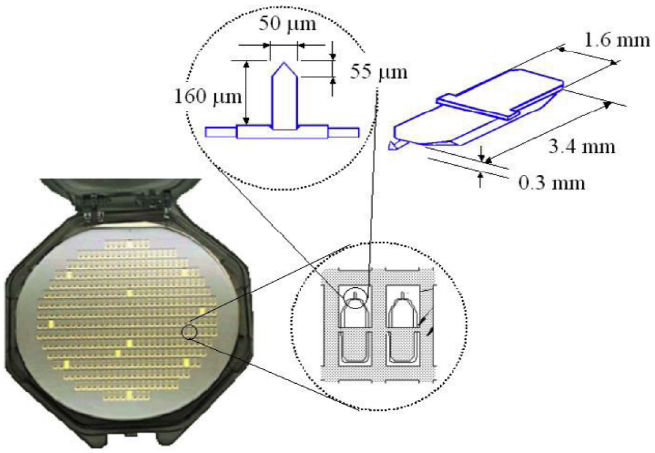

Figure 3.5: Tapping Mode AFM - Silicon Probes from single crystal silicon, produced by etching techniques.

precisely. The stylus was held at a fixed position, while the sample was scanned. The film thickness was determined by scanning the edges of several scratches, which were produced by moving a needle across the film while applying gentle pressure.

3.6 ATR Setup

The ATR-setup, developed and optimised in the course of this work, was designed to support both surface plasmon resonance spectroscopy (SPR) and optical waveguide-spectroscopy (OWS) in an 'easy-to-handle' design. Furthermore, it was built to support both, SPR and OWS measurements, either in the Kretschmann-configuration *via* evanescent coupling through attenuated total internal reflection or by means of a holographic grating coupler. Figure 3.6 shows a scheme and figure 3.7 a photograph of the experimental setup in its $\theta - 2\theta$ layout. In such an arrangement, the prism was rotated relative to a spatially fixed light beam in order to vary the angle of incidence. The detector, positioned to measure the reflected light intensity, thus has to move twice the rotation angle of the prism. The motorised and computer-operated two-goniometer alignment (figure 3.6) (*Huber*, Germany, One Circle Goniometer 410) managed the $\theta - 2\theta$ movement for both the prism and the detector. The setup was operated in reflection mode, in which the sample was illuminated from below, through the gold layer, while the reflected intensity was measured as a function of the angle of incidence θ. Measuring the reflectance resulted in a clear dip in the reflected intensity at an angle of incidence that matched the mode resonance angle ($\theta_{i,m}$). The typical time-resolution was $1s$, maximal $0.2s$. The repeat accuracy of the setup for the determination of $\theta_{i,m}$ amounts to $\pm 0.005°$ for the coupling angle (standard deviation for successive measurements) with a HeNe laser light source with *very high spectral purity*

and maximum power output of $5mW$ (*Uniphase*, model 1125, HeNe $\lambda = 632.8nm$). Two Glan-Thompson prisms were applied as polarising beam splitters in order to allow for an easy selection of TM or TE polarised light. All constituents of the setup were fixed to an optical table (Melles Griot, Cambridge, UK). The legs supporting the tabletop had air suspension mechanisms reducing practically all vibrations by two orders of magnitude and allowing for label-free low sensitivity measurements.

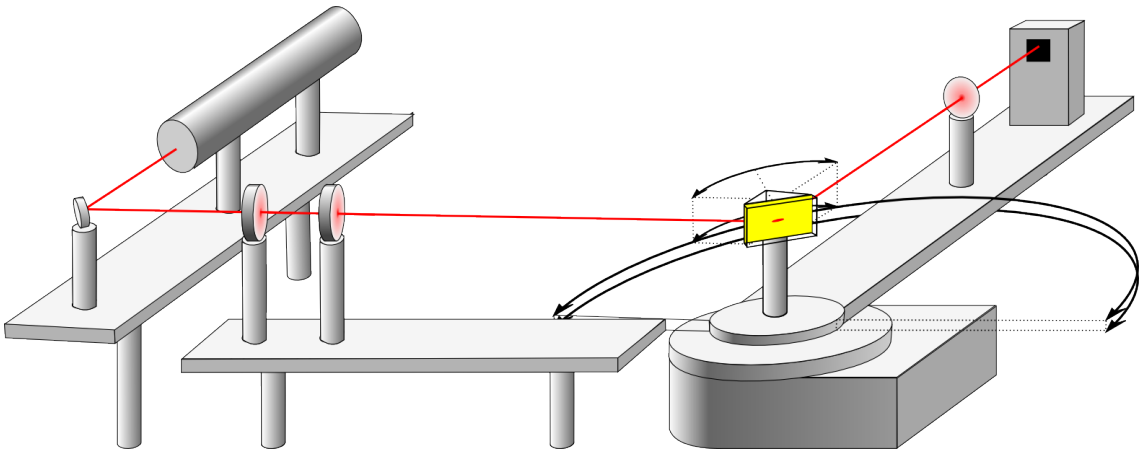

Figure 3.6: Schematic illustration of the experimental setup in its $\theta - 2\theta$ layout. The angular scan range is implied to give a visual understanding of the measurement principle.

3.6.1 General Description

In order to strike both the sample and the photo diode, the light path was constructed by diversion of the laser beam with a number of tilted mirrors. Rectangular intensity modulation was accomplished by a chopper *wheel (EG&G Instruments, model 651, Wokingham, UK, light chopper controller: EG&G Instruments, model 650)* (figure 3.7 CW), modulating the light at $1130Hz$ and providing a reference signal for the lock-in amplifier (*EG&G Instruments*, 7265 DSP) (figure 3.7 LI). The first polariser (figure 3.7 P1) was used to adjust the intensity of the incident light and the second one (figure 3.7 P2) to ensure that only light in the desired polarisation (i.e. TE or TM) reached the sample. The film of interest was formed on top of a ca. $50nm$ gold film deposited on the $LaSF9$ glass slide (*Schott Glass*, Germany) that was index-matched to the refractive index of the $LaSF9$ prism (*Hellma*, Germany) (figure 3.7 GP) by a thin layer of index matching fluid (*Cargille Laboratories Inc.*, $n = 1.700 \pm 0.0002$). For the actual measurement, immersion oil with approximately the same refractive index as the (glass-) substrate ($n_{BK7} = 1.5151$; $n_{LaSF9} = 1.8449$, etc.) was used. A small amount (1 drop) of the oil was applied on the bare side of the substrate, which was then brought into contact with the prism. Finally, after impinging onto the gold surface, the reflected light beam was focused by a collecting lens ($f = 50mm$) and the intensity was measured by a Si-photo diode ($200mm^2$ active area, dark current type.

5nA, *Hamamatsu*, Hamamatsu City, Japan) (figure 3.7 PD) as a function of the angle of incidence θ_i. The distance to the photo diode was chosen in a way that the reflected beam arrived on the diode surface at its focal point. This complete setup and the data acquisition were computer controlled (figure 3.7 PC).

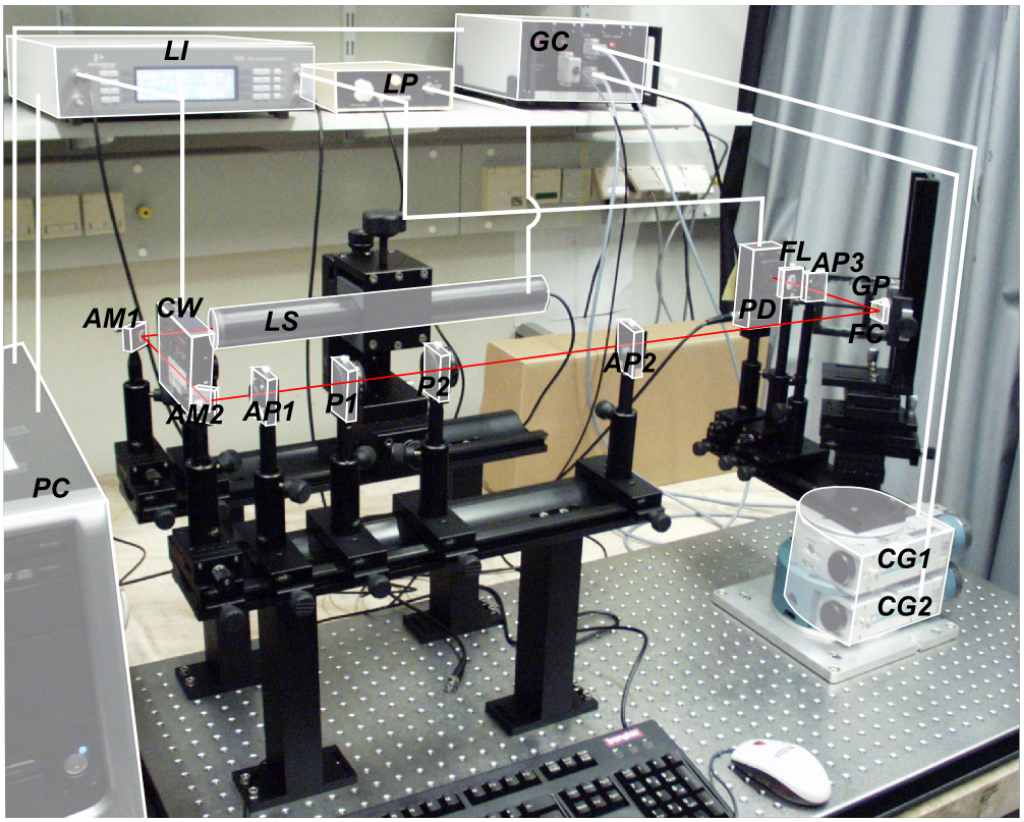

LS: laser source, **LP**: laser power supply, **CW**: chopper wheel, **MC**: monochromator, **AM1**: aligning mirror, **AM2**: aligning mirror, **AP1**: aperture plate, **P1**: polariser, **P2**: polariser, **AP2**: aperture plate, **GP**: glass prism, **FC**: flow chamber, **AP3**: aperture plate, **FL**: focusing lens, **PD**: photo detector, **LI**: lock-in amplifier, **CG1**: circle goniometer, **CG2**: circle goniometer, **GC**: computer operated goniometer control, **PC**: computer used to control the experiment and for the data acquisition.

Figure 3.7: Photograph of the experimental ATR setup. Detailed information about the setup is given in the text. For measurements of the reflected intensity as a function of the angle of incidence Θ the light beam from the monochromator M is used. The angle of incidence Θ is measured between the normal of the gold surface and the respective light beam.

3.6.2 Alignment

In order to align the system, first of all the light beam was adjusted by employment of two aperture plates (*Ovis*, iris diaphragm, $\varnothing = 25mm$). The laser beam was directed through the two apparatus so that it hit the axis of rotation of the goniometer.

After the light beam was aligned as described above, one aperture plate was taken off and positioned in close approximation to the photo diode, in order to align the beam path

after the laser beam has been reflected from the prism base to hit the active area of the photo diode throughout the whole angular range of movement. Therefore, the detector motor (2θ-goniometer) was rotated to parallel orientation to the incident laser beam, forming a $180°$-angle to it. Now, height and orientation of the photo diode was adjusted. Subsequently, the detector motor was moved perpendicular orientation to the incident laser beam, forming a $90°$-angle to it. Accordingly, the sample motor (θ-goniometer) was moved to form half the angle to the incident laser beam, i.e. $45°$-angle. At this position one face of the prism was orientated perpendicular to the laser light, reflecting a fraction back. This back-reflex had to be aligned to travel exactly at the incident light's axis.

The probing area, at the base of the prism, covered by the light beam amounted to several square millimetres at typical angles of incidence. Since the photo diode collect all reflected light from any beam the measurements represented an average over this area. If, however, during the rotation of the goniometer motors a movement of this spot was observed, then the prism stage has to be adjusted in its x-z-axis (in the plane of incidence).

Although the position of the light beam was once optimised for measurements, in general a slight readjustment for each individual experiment was necessary in order to compensate possible variances which may be caused by the mounting of the new sample.

3.7 Sample Mounting

The procedure presented in the following section was developed within the framework of this thesis to allow for an 'easy-to-handle' sample transfer without the need for reconstruction or readjustment of the whole setup. A multiple-cartridge mounting system was developed in the course of a diploma thesis which allowed the support of either prism- or grating-coupled probes for the excitation of resonance modes, using either the well-known Kretschmann prism coupling configuration or optionally a holographic grating coupling method. All samples discussed in the framework of this thesis were prepared according to this procedure.

3.7.1 Flow cell and Liquid Handling

Despite evidence that microfluidics- (e.g. Biacore sensor) and cuvette-based (e.g. IAsys sensor) optical detection systems provided basically equivalent opportunities for the detection and quantification of macromolecular interactions, the decision was made to still use a microfluidics flow cell for liquid sample delivery. Its distinctive function principle resulting in uniformly delivered analyte over the time, and according reduction of eventual

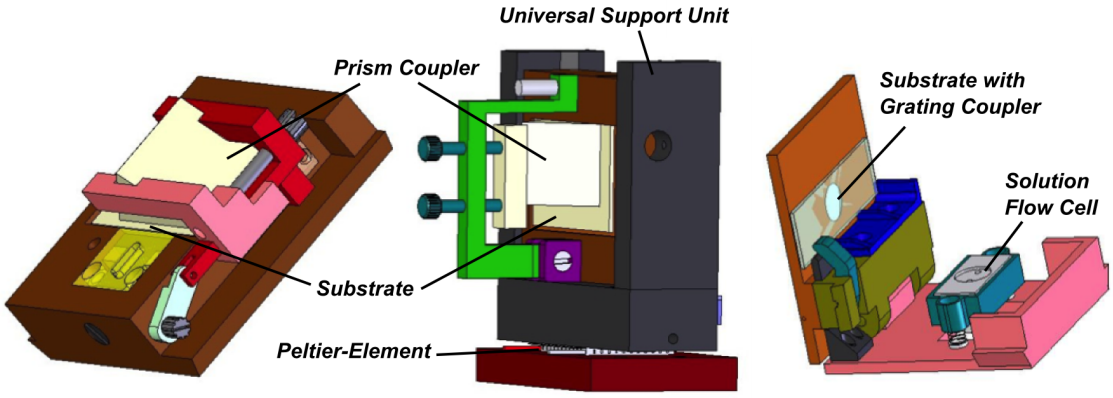

Figure 3.8: A cartridge, supporting the prism coupler for mode excitation in Kretschmann configuration (left). The scheme in the middle shows the universal support unit loaded with a cartridge for prism-based coupling (alternative design). The support unit is equipped with a Peltier-Element, allowing for computerised temperature control of the experiment. The illustration on the right shows the equivalent design of a cartridge foe substrates with grating coupler. The picture also gives an insight into the cartridge, showing the suspended support for the solution flow cell (common to all cartridge versions), which is tightly fit onto the sample when the cartridge is closed.

mass-transfer processes, and nevertheless the need for only small quantities of sample made it the system of choice.

In the early stage of this project, a simple fused silica flow cell with a volume of $85\mu L$ was used (see figure 3.9). The cell was connected with Tygon® tubings (R-3603 *Norton Ver*) with an inner diameter ($\varnothing = 0.76mm$) to a peristaltic pump (Rego Analog, Ismatec) allowed the flow rate to be adjusted. Before every experiment, the flow cell was washed thoroughly and then connected supplied with new Tygon® tubes in order to avoid sample contamination.

The actual sample was contained in an Eppendorf^{TM} tube ($1mL$) and two needle ends ($\varnothing = 1mm$) were inserted in its lid for injection. A representation of the flowing system is schematically illustrated in figure 3.9. The circulating volume was approximately $\sim 400\mu L$ of sample solution, with a circulation rate of $4\frac{mL}{min}$, ensuring optimised analyte delivery and minimising the sheer force above the sample, thus increasing mass transport. The flow cell was placed perpendicularly onto the substrate with its inlet at the bottom and the outlet on the top, in order to remove the miniscule stagnant air bubbles aggregating during extended measurements. The flow chamber was sealed with two Viton® O-rings against the substrate and the fused silica cover slide (Herasil, *Schott Glas*).

In a later stage of the project a new liquid handling system was designed and introduced. The flow cell was developed in cooperation with Hellma® to provide laminar flow and minimal consumption of the analyte solution, and furthermore, to fit the aforementioned multiple-cartridge mounting system. These flow cells were made of fused silica glass to ensure optimal optical properties in the UV/Vis spectral range (see section 3.2). Various

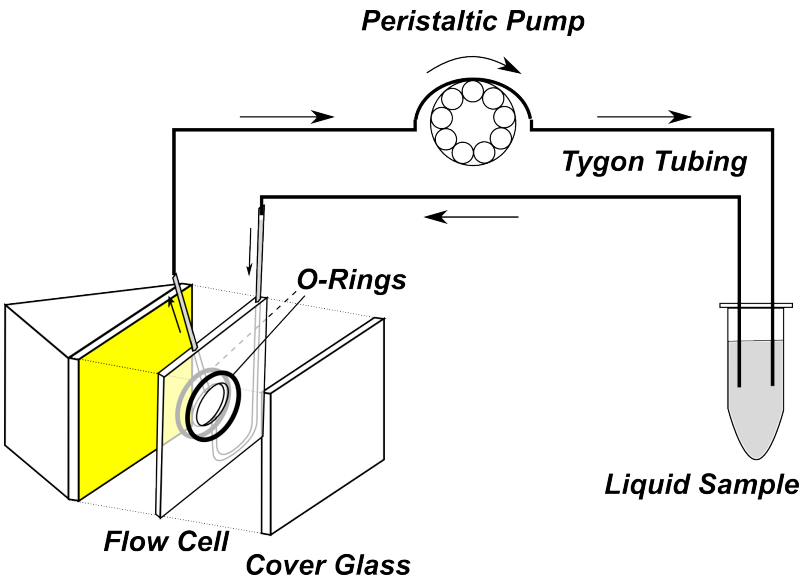

Figure 3.9: Schematic illustration of the early flow cell and the principle assembly of the liquid handling for sample delivery from solution.

flow cell volumes were available in a range from $2\mu L$ to $20\mu L$. In order to avoid (polymeric) sealing components to be in contact with either the sample or the analyte solution, the frame of the plane front side (facing the sample) of the fused silica cell was microscopically roughened and therefore self-sealing when pressed against the sample. Both, in- and outlet were located on the backside, and fit with $10cm$ long Teflon® tubings, glued to the fused silica. The tubing endings were equipped with standardised Omnifit® connectors.

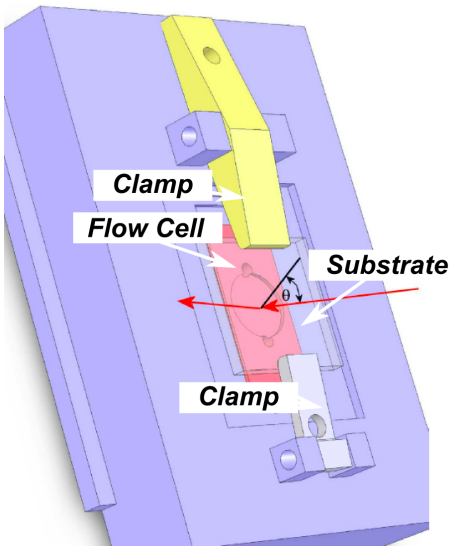

Figure 3.10: The new design of the flow cell, compatible with the developed multiple-cartridge system.

3.8 Measurement Procedure

In this section a detailed description of the measurement procedures used in this thesis is presented. The text is divided into (3.8.1) calibration and angular correction, (3.8.2)

Resonance scan curves, discussing SPR- and optical waveguide-spectroscopy, and (3.8.3) time-resolved measurement techniques, discussing the different modes provided by the control program to monitor kinetics.

3.8.1 Calibration and Angular Correction

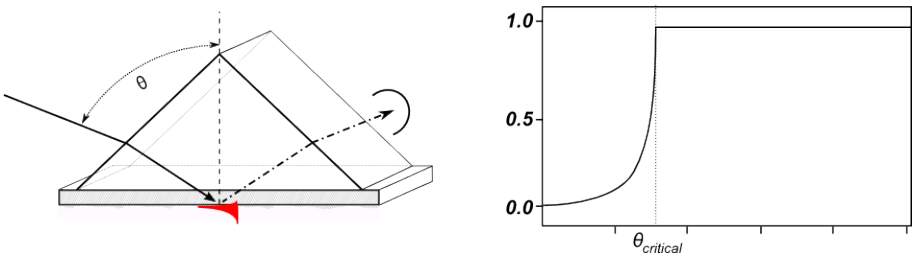

Figure 3.11: Measurement of the reflected intensity at an interfaces glass/air and glass/water in Kretschmann coupling geometry in dependence of the angle of incidence as determined by the goniometer reading. The steep increase in intensity indicates the transition to total reflection.

For reliable comparison of reflectivity measurements with Fresnel-calculation of a simulated layer system the angle of incidence had to be exactly known. For this reason, the setup was calibrated by means of the total internal reflection (TIR) occurring at the glass/air interface. The angle of TIR in air ($n_{air} = 1$) was calculated for the employed wavelength ($\lambda = 632.8nm$) and each individual glass with $n_{quartz} = 1.45699$, $n_{BK7} = 1.51509$, $n_{LaSF9} = 1.84498$, according to the Sellmeier equation3.1. Subsequently, the reflected intensity was measured with uncoated glass slides, optically coupled to the corresponding glass prism. Figure 3.12shows the measured intensity for TM and TE polarised light in dependence of the read angle of incidence from the goniometer.

The measured angles of TIR ($\theta_{TIR,read}$) were compared with calculated values for the different glasses. The goniometers had a vernier which allowed the position of the goniometer to be read with 0.005° accuracy. This experimentally measured angle of incidence $\theta_{i,read}$ between the impinging laser beam and the prism base was connected *via* Fresnel's equations with the the internal angle of incidence $\theta_{i,intern}$ according to the law of refraction, which describes the refraction of the impinging laser beam at the air/prism interface. In the case of the herein applied 90° prisms (see figure 3.11 inlet) this relation was given by:

$$n_{prism} \cdot sin(\theta_{intern} - 45°) = sin(\theta_{read} - 45°) \tag{3.2}$$

Calculated values for the three types of glass prism used in the course of this thesis are presented in figure 3.13 (left). As a consequence, the whole angular scan was 'squeezed

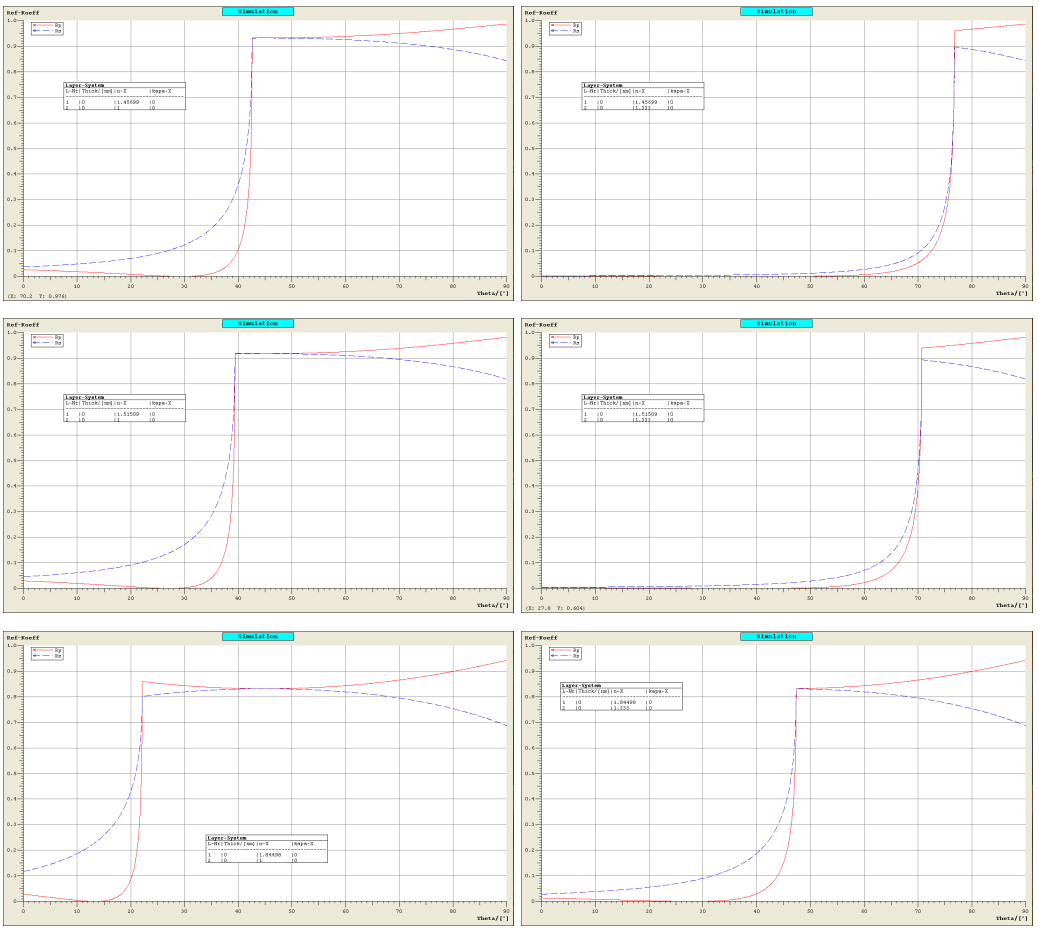

Figure 3.12: ATR scans of TE and TM polarised light in $n_{air} = 1.00000$ *(left side) and* $n_{water} = 1.33300$ *(right side) with three different prisms with a layer system* $d_{Au} = 50nm$, $n_{Au} = 0.312$, $k_{Au} = 3.823$ *and* $n_{prism} = 1.45699$ *(top),* $n_{prism} = 1.51509$ *(middle),* $n_{prism} = 1.84498$ *(bottom).*

together' from both directions with a factor proportional to the RI of the applied glass, Allowing for a broader angular range for high index prism materials. The range of the accessible angles was related with Snell's law and was important, since the resulting scan should cover the total internal reflection edge and (if present) all the resonance minimum.

The different heights of the curves reflect the material dependent intensities. Comparisons with the theoretical values for the TIR angle (θ_{TIR}) are shown in figure 3.13 (right). For further analysis of experimental values this correction was taken into account in order to get the correct angles of incidence. This correction has to be reconsidered for laser light of different wavelengths.

3.8.2 Resonance Scan Curves

After alignment of the setup and angle calibration the sample was mounted and a resonance spectrum was obtained by recording the reflected light intensity over an angular range from 20° to 80°. Subsequently, the polarisation plane of the laser light was rotated by 90° and a second scan was produced for the same sample but in a different polarisation.

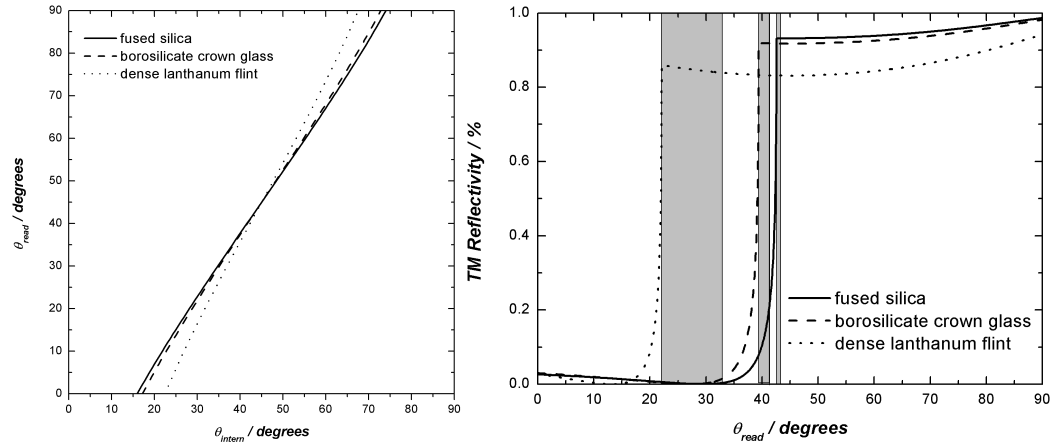

Figure 3.13: Connection between internal and external angle of incidence in the ATR-setup, calculated for a standard $90°$ *glass prism for (1) BK7 (*$n_{BK7} = 1.515$*) and (2) high refractive index LaSF9 (*$n_{LaSF9} = 1.845$*).*

A computer program (WASPLAS, designed in-house) was used to measure the magnitude of reflected light reaching the photo diode as a function of the incident angle, which was controlled by the goniometers. The control of the spectrometry was also done *via* WASPLAS software. All experimental values were recorded and processed by the this software, installed on personal computer.

Three different modes of operation are included with WASPLAS: (1) Scan Mode: Takes the complete angular scan. The scan acquisition time is typically in the range of a few minutes. (2) Kinetic Mode: Monitors the reflectivity as a function of time at a fixed angle of incidence with a time resolution $< 0,1s$. (3) Tracking Mode: Monitors the shift of the resonance dip in real time with a time resolution $< 4s$.

Analysis of the recorded raw data was carried out by adjustment of the Fresnel-simulation according to match the meta data by means of the transfer matrix method. Fitting parameters for this routine were the RIs with corresponding absorption coefficients or the complex dielectric constant, respectively, and the thickness of the individual layers.

The software can handle operation at arbitrary angles of incidence and s- and p-polarisation of the incident light, allowing anisotropy measurements and separation of optical constants n and d. The obtained spectra were fit using an iterative fitting program (WINSPALL, designed in-house), which calculated the reflectivity of an optical multilayer systems. The fitting software is based on the Fresnel equations and the matrix formalism. The typical result is usually the optical thickness [nm] and/or surface coverage [$\frac{ng}{cm^2}$] of a layer of interest.

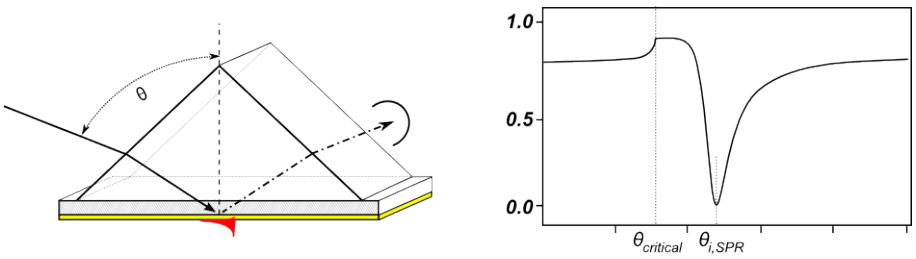

Figure 3.14: Measurement of the reflected intensity at an interfaces gold/air and gold/water in Kretschmann coupling geometry in dependence of the angle of incidence as determined by the goniometer reading. The steep decrease in intensity indicates the coupling of light intensity to the surface plasmon resonance (SPR) in dependence to the read angle of incidence. This angle is determined by the complex dielectric properties of the metal layer.

3.8.2.1 Surface Plasmon Resonance Scan

The accessible angular range varied depending on the materials chosen for the experiment, scans were, however, recorded from $20°$ to $80°$ of the read angle of the setup. The measurements produced and shown in this thesis were carried out either in air or in aqueous environment.

3.8.2.2 Waveguide Mode Resonance Scan

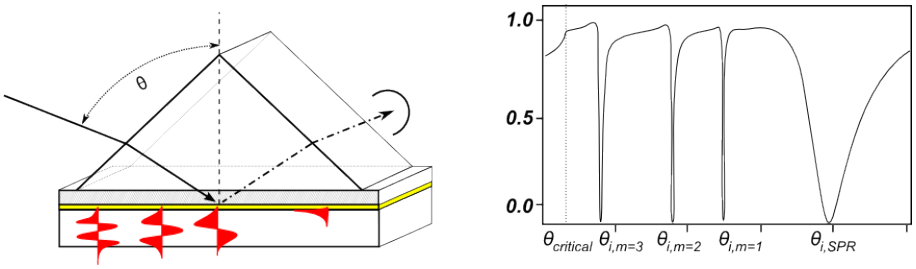

Figure 3.15: Measurement of the reflected intensity at an interfaces dielectric waveguide/air and dielectric waveguide/water in Kretschmann coupling geometry in dependence of the angle of incidence as determined by the goniometer reading. In this technique, light is coupled not only to the surface plasmon resonance (SPR) (broad dip at great angles of incidence at the right side of the scan) but also to a number of guided modes within the dielectric, adlayer in dependence to the read angle of incidence.

Planar waveguides were characterised with TM and TE polarised light. Each mode has a characteristic effective refractive index, N. In the case of films with a homogeneous refractive index distribution, the mode of order m is characterised by the real refractive index and the propagation angle in the film. The effective refractive indices of all modes were determined by selective excitation of each mode. Values for the effective refractive index of a mode, N_m, are always between the refractive index values of the waveguiding material and the lower index material adjacent to the waveguide, in the case shown below, either air or water. Since the gold layer is sandwiched between the glass support and the waveguide, it screens the waveguide film from the glass and allows guided modes with N_m

down to 1 in air and 1.333 in aqueous environment respectively.

The refractive index changes Δn of the surrounding cover medium were determined from changes of the incident angle at which the resonances occur. The refractive index N_m of each mode of the waveguide can be calculated from the incident angle, taking into account the optical properties of all applied materials. The fact that the light in the film is strongly attenuated over a short distance (in the µm-range) is mainly due to the absorption properties of the gold layer.

The position of the waveguide-modes directly depends on the thickness and the dielectric constants or refractive index of the multilayer system under investigation. A change in the optical density at any location within the system caused a change of the dispersion relation and shifts the resonance angles accordingly. This angular shift of the modes appeared, in first approximation, to be directly proportional to the change in optical thickness, i.e. proportional to the layer thickness. This effect was used for sensing purposes, because it is extreme sensitive and allows detection of adlayers and adlayer growth with a resolution of about $0.1nm$.

3.8.3 Time-Resolved Measurement Techniques

Besides the angle scan for SPR spectroscopy and waveguide mode spectroscopy, the setup also enabled time-resolved measurements in two different modes for monitoring time-dependent changes in resonance condition, and, consequently, a changes of the resonance angle. This could occur as a result of the adsorption of molecules from solution onto the waveguide structure. An angular shift of the resonances to higher angles may be followed by monitoring the reflected intensity R as a function of the angle of incidence $R(\theta_i)$ or the angular position of the resonance angle as a function of time. For this type of experiment the prism and attached sample were assembled with the liquid handling system (flow cell) as shown in figure 3.9 or alternatively, in later experiments with the new system depicted in figure 3.10.

3.8.3.1 Intensity Mode

In order to execute the intensity mode for tracking optical thickness changes of an adlayer the position of the angle θ_i has to be fixed at the left trailing edge of the resonance-dip (following the plotted line from left to right) (figure 3.16 top left). At this position the measurement of a time-dependent change of the optical density, and consequently, a shift of the resonance angle from θ_i to $\theta_{i,m}$, remains within the linear regime of the tailing edge

(figure 3.16 bottom left). The change in reflected intensity from R_1 to R_2 is then plotted against the time (figure 3.16 top right). Only if the shape of the mode remains unchanged this shift ΔR is directly proportional to the change in optical thickness, i.e. proportional to the layer thickness. However, if the mode is changed in its shape according to absorption and increased (or decreased) scattering or other mechanisms of attenuation, no correct assertion can be stated and another technique for time-dependent measurement has to be applied.

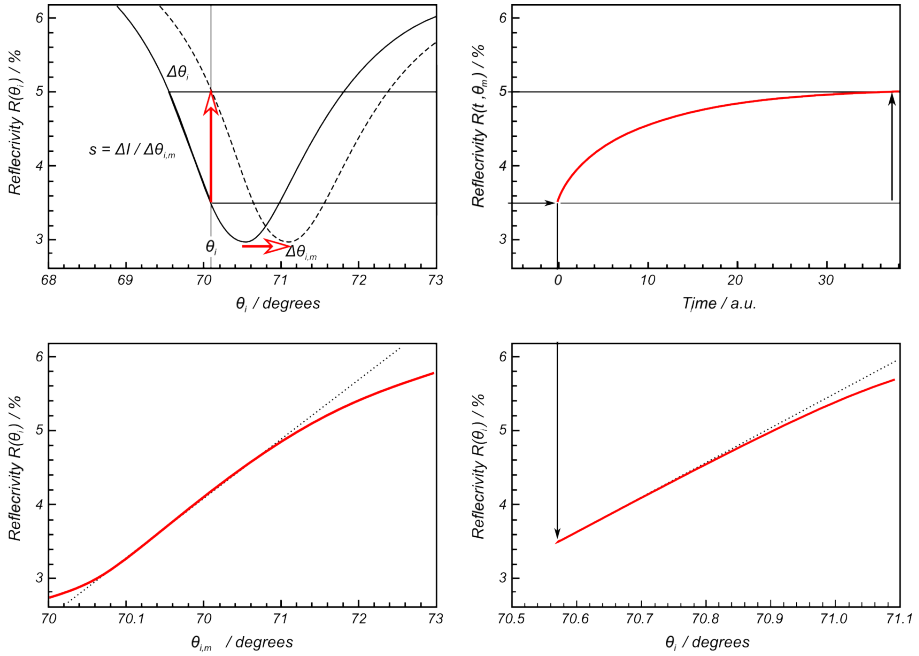

Figure 3.16: Principle of ATR-kinetic measurement at the trailing edge. The time-depending change of the optical density at an interface, causing a change in the resonance condition, and, consequently (top, left), a change of the resonance angle, can be detected as change in reflectivity ΔR at a fixed angle of incidence θ_k (top, right). In order to obtain significant results, a linear regime of the tailing edge must be chosen (bottom).

3.8.3.2 Angle Tracking Mode

An alternative experimental technique is given by tracing the angular shift of the reflectivity minimum from its start at θ_i to its end at $\theta_{i,m}$ (figure 3.16 top left), and providing time-dependant information of the change in optical density. In this mode, the software applies a three-point measurement at the resonance minimum with a pre-defined step-width, followed by an automatic parabolic fit of those three meta values, forming the base for the determination of the minimum position with good approximation. This parabolic fit gives, in addition, also a value for the full-width-at-half-maximum (FWHM) of the resonance dip. The disadvantage of the angle tracking mode is its time resolution, since the three-point fitting routine takes at least three times more than a single value measurement. Also the information exchange between the software and the lock-in amplifier and corresponding

goniometer control signals lies in the range of seconds.

This technique, however, may also be applied to reveal eventual change in reflected intensity ΔR additional to the angular shift of the intensity minimum, in order to determine the degree of optical losses due to absorption and scattering, occurring parallel to the changes of optical density (figure 3.16 bottom right).

Indeed, this method is by far not as sensitive to small changes as the aforementioned intensity measurement mode at the trailing edge, but its independence to changes in the shape of the mode makes this procedure much more versatile and extremely stable for long term measurements. Also greater changes in the optical density, i.e. thicker adlayer, may be monitored with this approach, not suffering from being restricted to a shift that does not leave the linear slope of the resonance plot.

Bibliography

[1] Hickel, W. *Entwicklung neuer Untersuchungsmethoden mit Oberflaechenplasmonen und Lichtleitermoden zur Charakterisierung ultraduenner Schichten*. Ph.D. thesis, ETH-Zuerich (1989).

[2] Lee, R. E. *Scanning electron microscopy and X-ray Microanalysis* (Prentice-Hall: NJ, 1993).

[3] *Schott glass catalogue, data sheets, 2009*.

Chapter 4

4 Optical Waveguide Spectroscopy with Mesoporous Titania Waveguides

Contents

Abstract

In this chapter, the highly sensitive gold-supported $meso-nc-TiO_2$ waveguide sensor in Kretschmann prism-coupling configuration is demonstrated. The impact of the thin metal layer, supporting the mesoporous titania thin-film waveguide, is shown in terms of its influence on resonance width and on the resulting detection sensitivity of this multi-layer assembly. It is demonstrated that the significant refractive index contrast, introduced by an optimum metal thickness of $40-50nm$, yields maximal confinement of the EM field distribution within the $meso-nc-TiO_2$ waveguide film, and hence allows for high sensitivity detection within the mesoporous structure. This optimised optical multi-layer configuration offers great potential for significant enhancement of sensing performance compared to state-of-the-art evanescent sensing schemes. In comparison to planar optical sensing techniques the porous waveguide layer has also the advantage that increased interaction of the analyte species with the highly confined EM field within the waveguide structure, and additionally the large adsorption area, that is extended to the interior surface area of the porous waveguide layer, can be exploited for significantly enhanced sensing performance. The overall sensing performance, again, is quantified according to first order perturbation theory and related to the degree of EM field confinement within the synthesised $meso-nc-TiO_2$ films according to their porosity and thus the effective refractive index of the multi-layer assembly.

4.1 Introduction

Optical waveguide spectroscopy (OWS) refers to the use of slab waveguides in the Kretschmann prism coupling configuration in general. Therefore, the waveguide on top of the semitransparent metal layer on a glass slide is optically matched to the prism. Thus, light is coupled through the prism/semitransparent metal film/glass assembly into the waveguide and confined within.

The presented waveguide format is a special version of the general principle of guiding light in a transparent medium with confined (optical) dimensions. Nevertheless, the operation principle of this optical waveguide (OWG) sensor is similar to a general slab-waveguide, where light is guided in the film of high refractive index. However, in contrast to the basic mechanism, where guided light experiences TIR at both (film/cover- and film/substrate-) interfaces the guided light in this metal supported waveguide is only totally internally reflected at the film/cover-boundary, while being normally reflected (NR) at the film/metal-boundary, whereat light is partly transmitted into the metal and (through it into) the

substrate and partly reflected back into the waveguide film at the film/metal interface see figure 4.1. A schematic sketch of this structure is shown in figure 4.1.

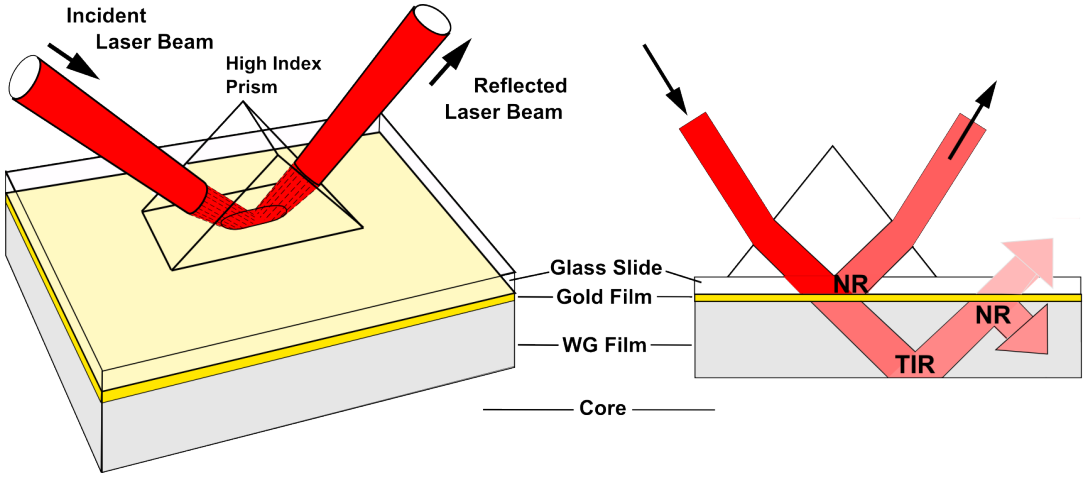

Figure 4.1: Sensing configuration and principle of light guidance of the metall supported waveguide sensor. (a) Basic mesoporous OW configuration with illustration of light guided in the waveguide film by total internal reflection (TIR) at the film/cover boundary and normal metallic reflection at the film/metal boundary. (b) Photograph of a fabricated mesoporous optical waveguides.

Constructive interference of these reflections forms guided modes. However, the operation principle is somehow different from the general slab-waveguide sensors, as a consequence of the metal film, and is therefore operated in reflection mode in the Kretschmann prism coupling configuration. Accordingly, the classical surface plasmon resonance (SPR) instrumentation was implemented and no significant changes were necessary.

In this configuration the prism (in combiation with the index-matched glass support) defines the momentum of the incident light, as well as the component parallel to the surface that can be adjusted by changing the incidence angle. Only at certain angles above the critical angle (θ_{TIR} or θ_{crit}) light is not reflected back from the back of the metal film, but rather coupled into the waveguide. These events are monitored by a photo diode, producing a dip in reflected intensity. Depending on the applied wavelength and the actual angle of incidence (in this configuration θ is scanned in a $\theta - 2\theta$ two-goniometer configuration as described for SPR), a match in momentum between the impinging light and a waveguide mode can be achieved. The resulting modes are referred to as the number of nodes in their inherent propagating electric field. Coupled light is guided in the waveguide film but also dumped by the metal layer, as it dissipates the energy into heat and little can be coupled back by the symmetrical prism. Therefore, propagation of the guided waves is strongly attenuated over a short distance. Additionally, by changing the polarisation of the incident light, different sets of waveguide mode spectra with according polarisations can be produced. Modes with the magnetic field component polarised in the plane of the film are transverse magnetic (TM) modes, while those with the electric

field component polarised in the plane of the film are transverse electric (TE) modes). In this thesis (if not stated explicitly different) all reported waveguide mode spectra are taken under illumination of a helium-neon red laser (HeNe) at $\lambda = 0.633\mu m$.

The reflectivity R vs. incident angle θ measurements are evaluated by comparing them to Fresnel calculations of the multilayer system, thus obtaining the thickness of an adlayer film and refractive index thereof. These results are solutions to the Maxwell equations for the multilayer system in Kretschmann configuration. In this context, the adsorbed species is treated as additional optical layer on top or in the case of the mesoporous WG as refractive index increase within the mesoporous film, or both if applicable. As a result of this change in the configuration, the waveguide mode coupling conditions are changed, thus shifted to higher angles of incidence for resonant mode coupling. The real-time monitoring of these shifts produces the actual sensing signal by following the angular minimum or recording the reflected intensity at an angle near the reflectivity minimum. The resulting spectrum can, again, be fitted to Fresnel calculations, hence the change due to analyte adsorption can be quantified in terms of thickness and refractive index.

4.2 Metal-Thickness and Resonance-Width

When designing the gold-supported $meso - nc - TiO_2$ waveguide sensor it is important to consider the application the sensor is aimed on; Either detection of a thin adlayer (e.g. growth monitoring) or the application as bulk refractometer (see introduction chapter). Moreover, the waveguide sensor is assembled of three different materials, the prism/glass substrate combination, the actual waveguiding film and the metal layer in between, whereas the refractive index of all three layers and additionally the thicknesses of the waveguiding film and the metal layer influence the optical properties and field distributions of the individual resonance phenomena. Therefore, in order to tailor the multi-layer structure for a specific sensing purpose various factors have to be considered for the desing of this device. In the following discussion the surface plasmon resonance is also included as TM_0 mode for comparison. In principal, several metals can be used for metal supported waveguide fabrication, however for this conceptual study the scope was limited on thin-films made of gold. Therefore, and for future reference, the metal applied for metal-supported optical waveguide spectroscopy in Kretschmann configuration will by default be gold.

The refractive index used for the calculation is the same as applied to all further simulations and discussions, if not stated explicitly different. The refractive index of the thin gold films

is $\tilde{n}_M = 0.312 + i3.823$, and by its nature as conductor, complex. In literature varying refractive indices are reported and for thin-film application again differen refractive indices can be found. The reason for the latter is the pronounced effect of the morphology at film thicknesses in the nanometre regime. Reasons therefore are mainly the highly increased surface-to-volume-ratio and associated surface effects. But not only the size effects alter the dielectric properties of the metal, also the history of a matirial (i.e. the way the material was processed) is another parameter which has effect on its (optical) properties. The gold films used in this thesis are all thermally evaporated thin-films from commercially available pure gold (see experimental chapter). Therefore, based on the thermal processing and the nanonetre size of the film-forming clusters, the value found for the refractive index of the gold films may deviate from the values reported in literature. Further it was observed, that this refractive index is not significantly changing for gold films with film thicknesses in the range of $5 - 80nm$.

However, by altering the gold layer thickness within this thickness regime, the properties for coupling to the field resonances change significantly. This behaviour becomes apparrent when, for example, resonant coupling to the TM_0 mode is calculated for different film thicknesses of the gold layer (see figure 4.2). The TM_0 mode or surface plasmon resonance appears in the absence of the $meso{-}nc{-}TiO_2$ waveguide, or in the theoretical extreme case were the waveguide thickness is assumed infinitesimally small. Also another theoretical extreme case allows the TM_0 mode to appear; If the refractive index of the waveguide is exactly matching the refractive index of the cover medium, in this case $n_C = 1.333$ for water.

If, on the other hand , a $1.2\mu m$ thick titania layer is applied on top of the gold film, then the TM_0 mode is shifted to high angles, too far to be detected within the accessible angular region of the setup. However, if the reflectance, R, over the angular range, θ, is measured for this configuration, other dips appear instead of the surface plasmon resonance and moreover, the reflected intensity decreases at these resonances are much steeper, the dip therefore much sharper (see figure 4.3). The angular position θ_m of a reflectance dip in the spectrum corresponds to the mode resonance calculated from the mode equation with the resulting value at the point where the function intersects with the x-axis (see appendix A). The solutions of the mode equation for $y = 0$ (see appendix A), are determined by the refractive index, which is effectively experienced by the guided EM field distribution within the multi-layer waveguide structure.

The effective refractive index for each individual mode, N_m, is often used to describe the sensing potential of a particular combination of refractive indices and film thicknesses of the

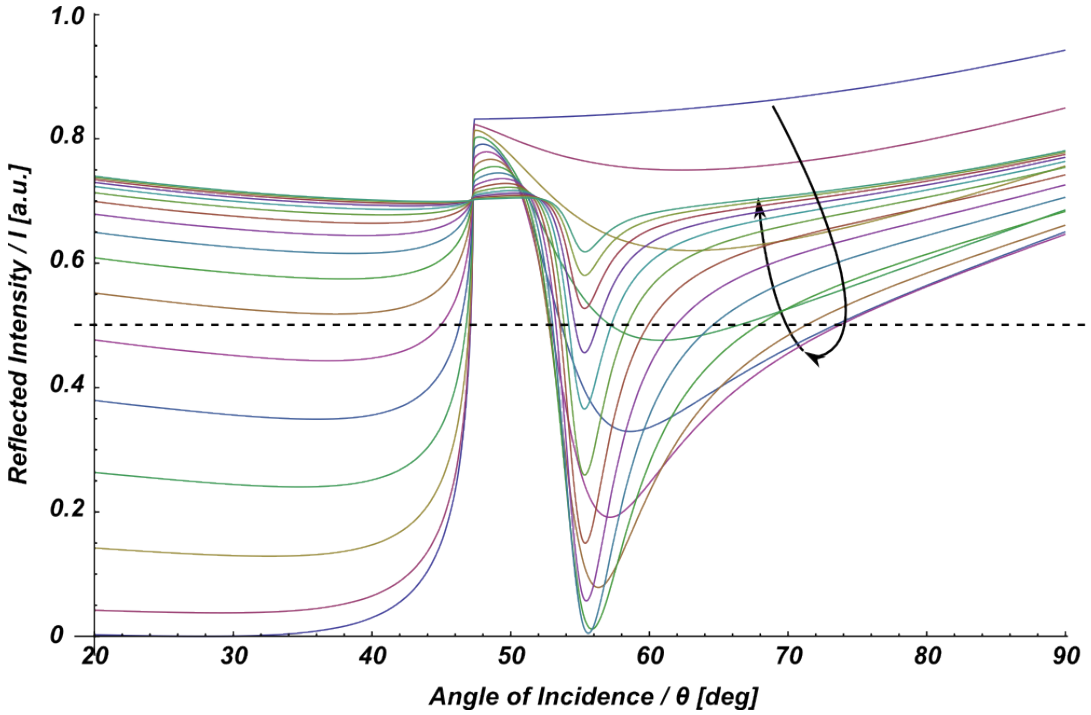

Figure 4.2: Calculated Fresnel reflectance for the TM_0 mode (surface plasmon resonance) with respect to increasing gold film thickness. This representative calculation was done for light at $\lambda_{HeNe} = 632.8nm$ impinging upon a prism/glass slide with $n_S = 1.84498$ with a gold layer on top with the refractive indices $\tilde{n}_M = 0.312 + i3.823$ and thicknesses varying from $0nm$ to $80nm$ in aqueous environment $n_C = 1.333$. The dashed horizontal line represents the plane of I=0.5 whereat the intersection points of each Fresnel curve were taken. The circumflexed arrow indicates the evolution of the curve as the gold film thickness increases.

individual constituents within a multi-layer waveguide assembly, thus it standardises the sensor performance and allows therefore for comparison between of systems. Especially in the field of integrated optics (IO) and sensors and actuators it is usual to express the reflected intensity *versus* N, where $N = n_S \, sin\theta_S$. The properties of N and its characteristic behaviour with regards to changes in the dielectric environment, hence in sensing applications, in terms of sensitivity of optical sensing systems has been thoroughly discussed in literature [7,17,13,5,19,2,18,6,20,21,4,11,14,3,12] (and references within), therefore here only the distinct properties of the mesoporous optical waveguide sensor in Kretschmann prism-coupling configuration will be highlighted.

As illustrated in figure 4.3, the gold layer thickness (though burried under the waveguide layer) also has a pronounced influence, not on the position of the resonance, but on its shape. Due to its complex optical properties the effect of the gold layer is not only described by linear attenuation and reduction of the guided light intensity, but rather it can be exploited in order to increase the sensitivity of the system when optimised to a certain thickness. Figure 4.3 shows the resonance dip of the TM_6 mode with a variation of the gold film layer thickness. Apparently, a gold film thickness of $\approx 50nm$ yields the optimal resonance feature with the largest aspect ratio.

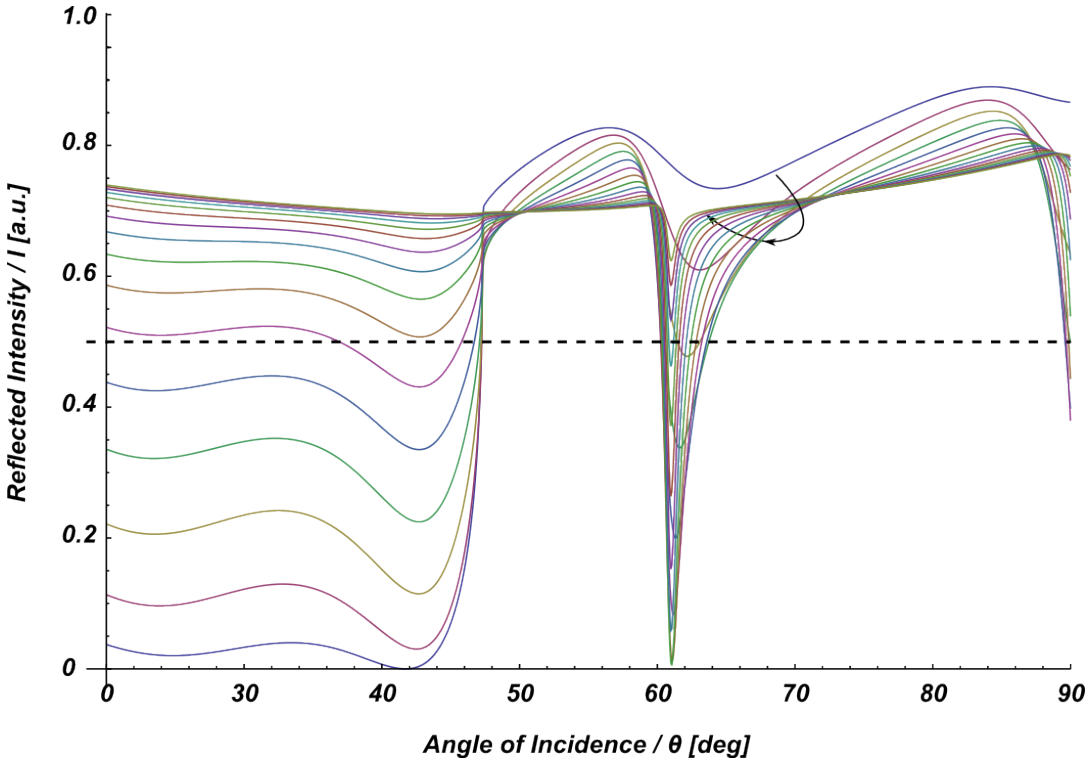

Figure 4.3: Calculated Fresnel reflectance for the TM_6 mode with respect to increasing gold film thickness. This calculation was done for the same optical parameters as shown in figure 4.2, but with the addition of a $1.2\mu m$ thick titania layer with $n_F = 2.1775$ on top of the gold film. The dashed horizontal line represents the plane of $I = 0.5$ whereat the intersection points of each Fresnel curve were taken. The circumflexed arrow indicates the evolution of the curve as the gold film thickness increases.

In order to systematically exploit the influence of thin metal layers on the optical properties of optical systems based on a combination of glass substrates ($n_S = 1.84498$) covered with thin gold films and $meso - nc - TiO_2$ waveguides on top of the metal, a series of contour plots of the reflected intensity *versus* angle of incidence and gold layer thickness was calculated for gradually changing porosities $P = 0.00, 0.10, 0.20, ..., 1.00$ (i.e. changes in composite refractive index $n_F = 1.333 \rightarrow 2.1775$) of the $meso - nc - TiO_2$ waveguide. The results are displayed in figure 4.4, for the operation in air $n_C = 1.00027$, and in figure 4.5, for the operation in aqueous environment $n_C = 1.333$.

The contour plots are calculated *via* transfer matrix approach from the total reflected intensity of the multilayer system with both TE and TM polarised laser light. The contour lines represent the values of reflectivity at at 50% intensity, $R = 0.5$ (depicted by the dashed lines in figures 4.2 and 4.3).

The left column in figure 4.4 and 4.5 represent the resonances appearing at illumination with TM polarised light, whereas the right columns illustrate the case for illumination with TE polarised light. The numbers at the left (y-axis) denote the metal layer thicknes ($d_M(Au)$), whereat the x-axis denotes the angular range of incidence. The individual rows represent the porosity of the $meso - nc - TiO_2$ waveguide, thereby the first row (bottom)

illustrates the contour spectrum for 100% porosity, which is equivalent to the surface plasmon resonance (SPR) configuration with no waveguide layer on top. For each following row above the first one the titania fraction is successively increased for 10%, accordingly in terms of porosity this represents a decreased by 10%.

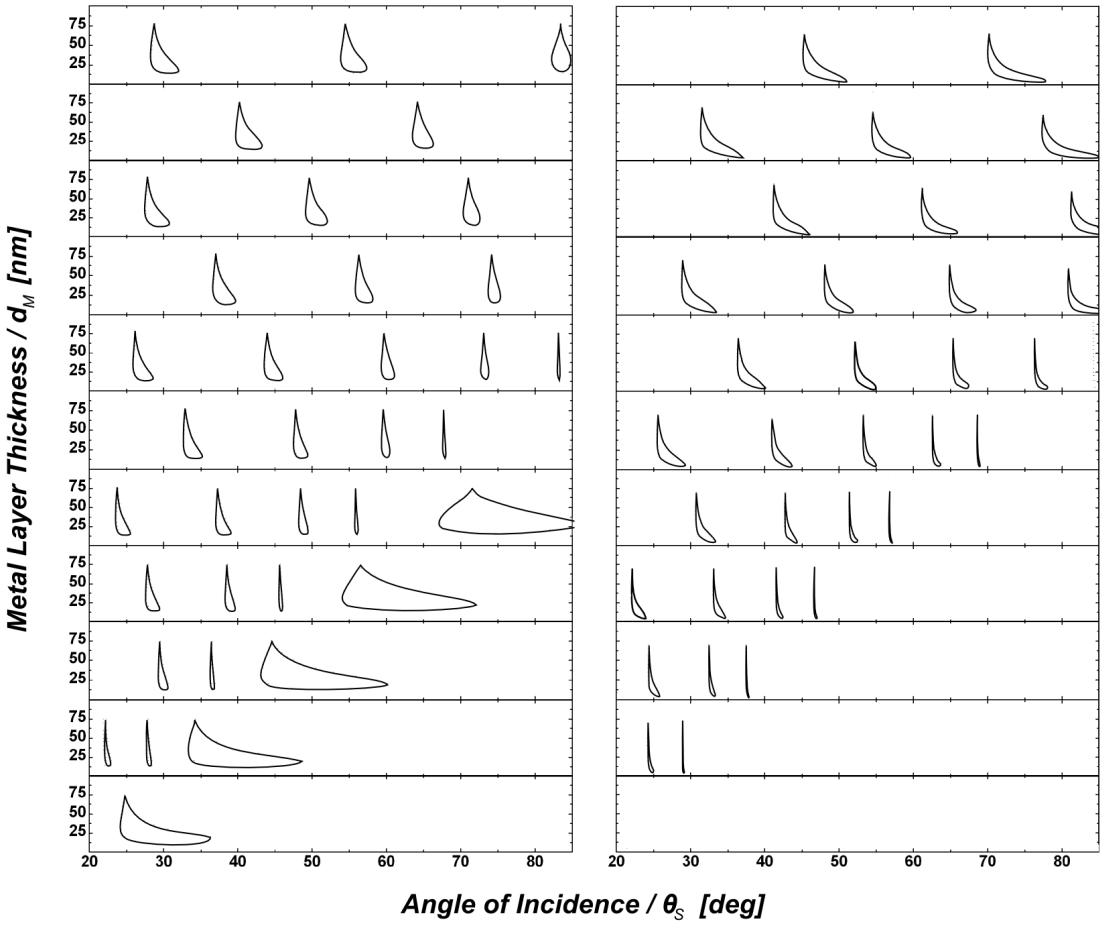

Figure 4.4: Contour plots of reflectance from gold-supported $meso-nc-TiO_2$ ($n_{meso-nc-TiO_2} = 1.6$), a glass substrate ($n_S = 1.84498$) and air as cover medium ($n_C = 1.00027$). The contour lines represent reflectance at 50% intensity, $R = 0.5$. The left column represents the resonances appearing at illumination with TM polarised light, whereas the right column illustrates the case for illumination with TE polarised light. The numbers at the left (y-axis) denote the metal layer thicknes ($d_M(Au)$), whereat the x-axis shows the angular range of incidence. The individual rows represent the porosity of the $meso - nc - TiO_2$ waveguide, thereby the fires row (bottom) illustrates the contour spectrum for 100% porosity, which is equivalent to the surface plasmon configuration with no waveguide layer on top. For each row above the first one successively are 10% increase in titania density simulated)

From figures 4.4 and 4.5 it can be observed that the angular position of the resonance dip(s) (corresponding each to a different mode) shifts nearly linearly with changes in porosity (i.e. changes in composite refractive index) from $n_F = 1.333 \rightarrow 2.1775$. Moreover, it proves that the gold layer thickness does not affect the angular position, but rather exhibits an optimum in terms of aspect ratio of the dip at around $45 - 50nm$ for both polarisation. In comparison, the contours plots, plotted for the TM_0 mode (i.e. surface plasmon resonance), present in the lower half of the TM plots at $n_F = 1.00027 - 1.471$ for calculations in air and $n_F = 1.333 - 1.502$ in aqueous environment, show very broad dips

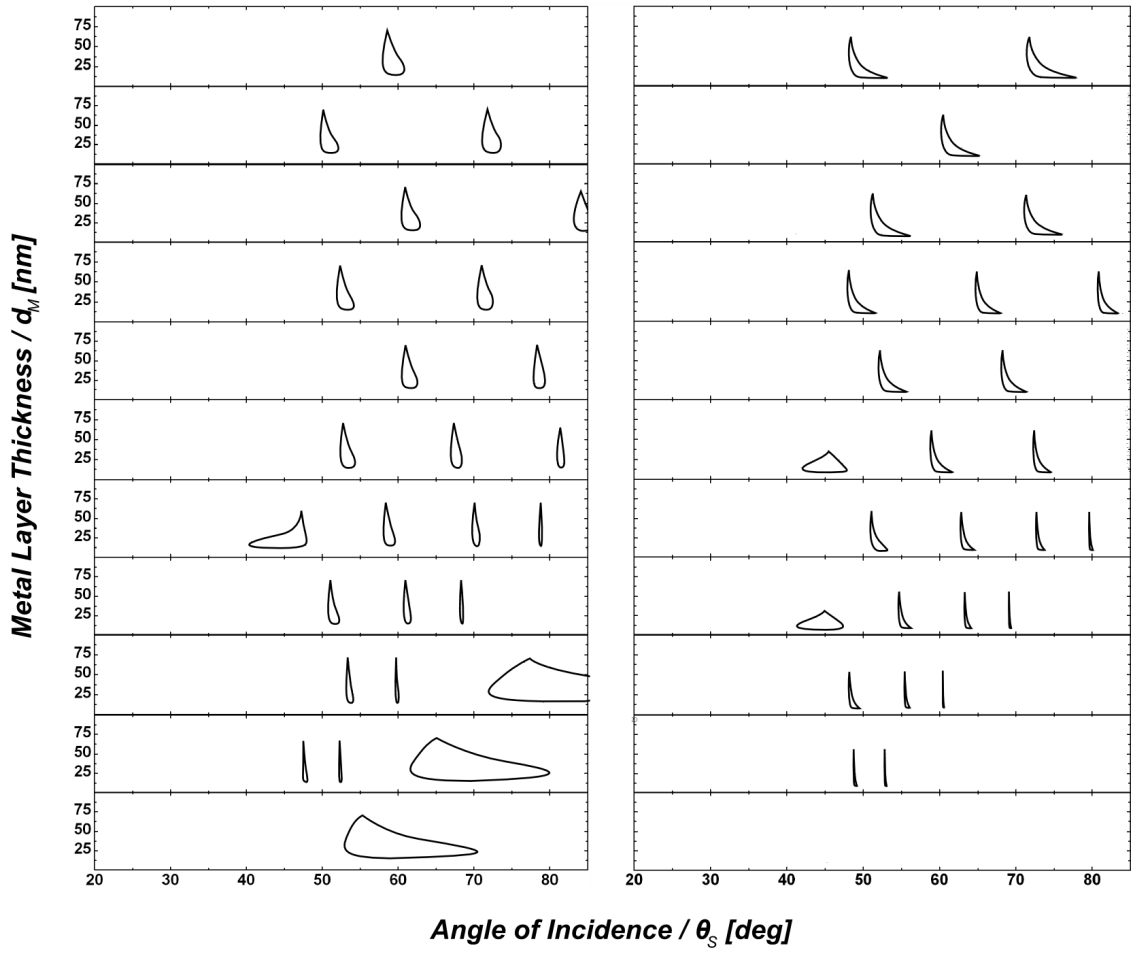

Figure 4.5: Contour plots of reflectance from gold-supported $meso-nc-TiO_2$ *(*$n_{meso-nc-TiO_2} = 1.6$*), a glass substrate (*$n_S = 1.84498$*) and water as cover medium (*$n_C = 1.333$*). for details see figure 4.4and text above.*

and reveal a very strong dependence on the value for $d_M(Au)$.

In general, all resonance features shift, with increasing metal layer thickness asymptotically towards the calculated value of N (using the mode equation), which corresponds to a Fresnel simulation with an infinitely thick gold layer [16]

However, it appears that once the gold thickness exceeds $\approx 40nm$, the solutions of Fresnel reflectivity calculations are identical with the values for N obtained *via* solution of the mode equation, which consequently means that the substrate has practically no influence on the electromagnetic field distribution in the waveguide once the gold layer has reached this thickness [16] [1].

Therefore, it can be concluded that an optimum metal thickness of $40 - 50nm$ yields maximal confinement of the EM field distribution within the $meso - nc - TiO_2$ waveguide film, and hence allowing optimal sensitivity within the mesoporous structure, due to the

[1] The glass substrate and accordingly the choice of the prism material have an influence on the experiment insofar as a high refractive index of the glass material allows for a broader angular range of angles to be acessible for the experiment (more details in the Experimental Chapter, Section:Calibration and Angular Correction).

refractive index contrast introduced by the thin gold layer. Accordingly, in the following the gold-supported $meso-nc-TiO_2$ waveguide films for prism-coupling in the Kretschmann configuration will be equipped with $45-50nm$ thick gold films.

4.3 Sensitivity Characterisation for Porous Waveguide Sensors

In this section the sensitivity characteristics of the porous titania thin-film waveguide sensor in Kretschmann configuration will be discussed. Also the significantly enhanced performance of the mesoporous titania waveguide compared to planar waveguides and surface plasmon resonance sensors, due to increased surface area and strong field confinement within the porous waveguide layer is demonstrated.

Since the sensing principle of this type of optical sensor roots in the refractive index change, induced by the presence of target molecules, it is crucial for being able to detect the molecules that the induced changes are sufficiently high to be within the resolution of the sensor. Mesoporous waveguides allow, due to their large available internal surface area for vast molecular binding and due to the large overal internal volume of nanoscale porespace for a greater number of molecules to interact with the confined power of the EM field and, again, to contribute to the change in refractive index experienced by the sensor.

As a consequence of the $meso-nc-TiO_2$ waveguide layer, this sensors profit from the ability of utilising largely enhanced access to interaction of guided modes with target molecules within the mesoporous interior of the actual waveguide film itself. Therefore, the transduction of the sensor response is greatly enhanced, in contrast to SPR sensors or conventional planer waveguides, that are restricted to an evanescent field-based detection approach. Comparable sensing approaches with gold-cladded porous alumina [10,9], and silicon [15,8] waveguides were reported recently.

Among porous materials, mesoporous titania is an excellent candidate, for sensing application, in part due to the large range of achievable nanoscale architectures (examples are shown in the Chapter:Synthesis of mesoporous titanium oxide thin films) and accordingly copious possibilities to vary the pore sizes and pore geometries, as well as the actual porosity (examples are shown in the Chapter:Synthesis of mesoporous titanium oxide thin films) and established protocols for oxide-surface functionalisation [1].

In this section the combination of characteristics for sensing application of metal-supported porous waveguides in the Kretschmann configuration is demonstrated on the example of $meso-nc-TiO_2$ materials. Therefore, theoretical analysis of the influence of various parameters of the multi-layer system on the detection sensitivity of these sensors is

provided. The calculations are based on light at a wavelength of $\lambda_{HeNe} = 632.8nm$ which is coupled into the mesoporous waveguide *via* Kretschmann prism-coupling configuration under angular modulation. Furthermore, both supported polarisation states, transverse-magnetic (TM or p-polarised) and transverse-electric (TE or s-polarised) are considered.

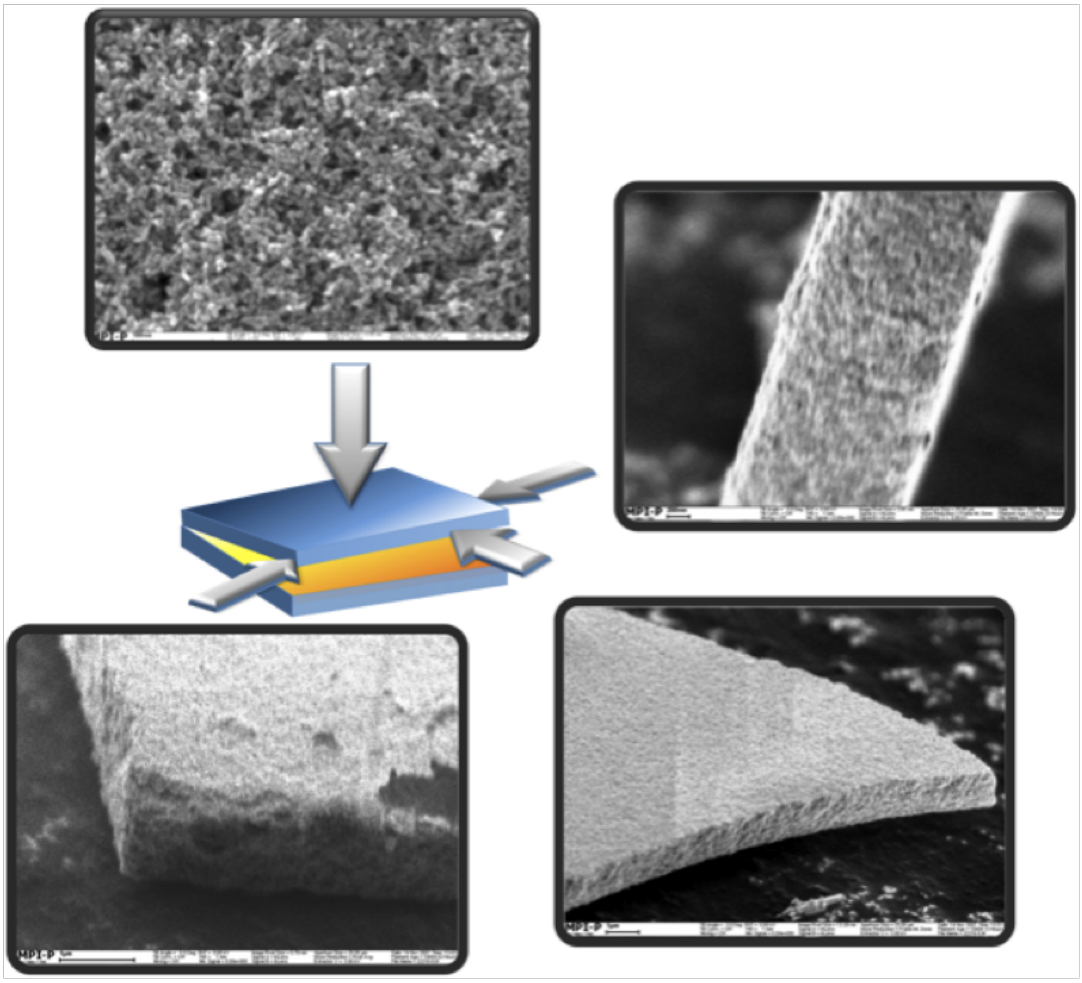

Figure 4.6: The SEM images clearly show that the meso-nc-TiO2 consist of a network of colloidal nanocrystals. The image shows a representative mesoporous titania film as used for the investigations described in the following chapters.

The theoretical capability of gold-supported $meso - nc - TiO_2$ waveguides, in the multi-layer assembly as shown in figure (4.6), for sensing application is demonstrated. Following the reported scheme[8] for application of first order perturbation theory for determination of the sensitivity of mesoporous waveguides to slight changes in the refractive index of their environment, triggered by the presence of small molecules within the nanoscale porespace of the intrior of the $meso - nc - TiO_2$ waveguide. As to the fact, that changes in the dielectric constant, $\Delta\varepsilon$, or the equivalent changes in refractive index, Δn, within the reach of the EM field of guided modes cause a corresponding change of the effective refractive index, ΔN. The change of the effective refractive index of the guided wave mode can be calculated by 4.1.

$$\Delta(N^2) = \frac{\int_{-\infty}^{\infty} \Delta\varepsilon \left[E(y)\right]^2 dy}{\int_{-\infty}^{\infty} \left[E(y)\right]^2 dy}. \tag{4.1}$$

The electric field in y-direction within each layer of the multi-layer system of the waveguide structure can be calculated by means of transfer matrix approach. Accordingly $\Delta\varepsilon(y) = 2n \cdot \Delta n$ and $\Delta(N^2) = 2N \cdot \Delta N$ can be rewritten in the above stated equation, giving

$$\frac{\Delta N}{\Delta n} = \frac{n_3}{N} \frac{P_{waveguide}}{P_{total}} \tag{4.2}$$

where the ratio, $P_{waveguide}/P_{total}$, quantifies the power confinement factor, which is defined as

$$\frac{P_{waveguide}}{P_{total}} = \frac{\int_{waveguide} \left[E(y)\right]^2 dy}{\int_{-\infty}^{\infty} \left[E(y)\right]^2 dy}. \tag{4.3}$$

This factor of power confinement represents the ratio of the power (of the EM field of guided mode) confined within the spatial distribution of the mesoporous waveguide layer in relation to the total power distribution throughout the entire multi-layer assembly of glass substrate, gold layer, waveguide film, and cover medium. For the application of $meso - nc - TiO_2$ waveguide sensors in the case of angular interrogation in Kretschmann configuration, the sensitivity can accordingly be defined as:

$$sensitivity = \frac{d\theta}{dn} = \frac{d\theta}{dN} \cdot \frac{dN}{dn}. \tag{4.4}$$

In order to give an analytical expression for the sensitivity of the $meso - nc - TiO_2$ waveguide, concidering that the tangential component of the incident light wave vector in the prism matches the wave number of the guided mode $N_m = n_1 sin\theta_m$, the following equation can be formed:

$$sensitivity = \frac{P_{waveguide}}{P_{total}} \cdot \frac{n_3}{N_m} \cdot \frac{1}{n_1 cos\theta_m}. \tag{4.5}$$

From the above stated equation it appears that the sensitivity is proportional to the power confinement factor and to the angle of incidence, but also inversely proportional to the effective refractive index, N_m, of the particular mode. In order to expose more clearly the relative contributions of the power confinement factor and the angle of incidence on the overal sensitivity, figure 4.7 displays the calculated mode resonance angles, power confinement factors, and sensitivities of gold-supported $meso - nc - TiO_2$ waveguides, at a laser wavelength of $\lambda_{HeNe} = 632.8nm$. The complex refractive index of the gold film at the applied wavelength is $\tilde{n}_{Au} = 0.312 + i3.823$.

Conclusion

The potential for highly sensitive sensing schemes with gold-supported $meso - nc - TiO_2$ waveguides in Kretschmann prism-coupling configuration is demonstrated. One great advantage, inherent to this new mesoporous sensing platform, compared to planar optical waveguides, is shown to arise from the significant refractive index contrast, introduced by an optimum metal thickness of $40 - 50nm$ beneath the waveguiding film. This strong confinement of the EM field is quantified by calculations based on first order perturbation theory, and expressed by the power confinement factor. Especially at higher angles of incidence it is possible to guide a high fraction (1.0 - 0.9) of the EM field power within the $meso - nc - TiO_2$ waveguide film. The large internal adsorption area, as intrinsic property of the mesoporous waveguide layer, additionally allowes to increased interaction of the analyte species with the highly confined EM field within the waveguide structure, thus results in significantly enhanced sensing performance. Under optimised conditions the overall sensing performance, again, is quantified according to first order perturbation theory and related to the degree of EM field confinement within the synthesised $meso - nc - TiO_2$ films according to their porosity, and thus the effective refractive index of the multi-layer assembly. In aqueous medium it is shown that operation with TE polarised light can lead to significantly enhanced sensitivity, compared to the case of TM light. This distinct advantage has its origin in more pronounced adsorption losses inherent to TM polarised light.

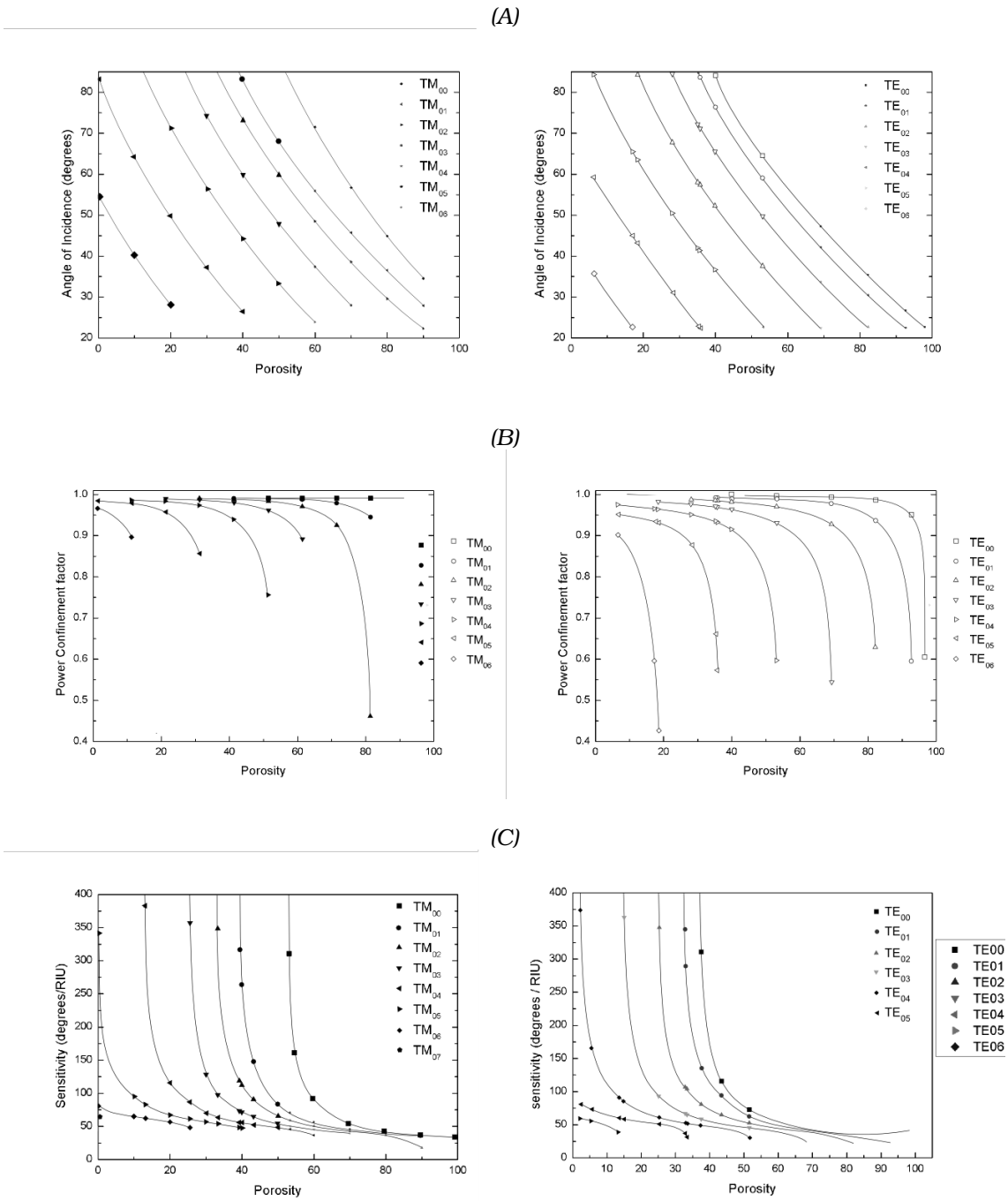

Figure 4.7: All graphs relate the displayed results to guided modes, excited in a $1.2\mu m$ thick gold-supported $meso-nc-TiO_2$ waveguide layer. Results are shown for calculations in air and for both cases, TM light (left column) and TE light (right column) at $\lambda_{HeNe} = 632.8nm$. (A) Resonant angles of incidence. (B) The power confinement factor. Apparently, the degree of power confinement for TM-light is assumed to be higher (compared to the TE light) due to the intrinsic interaction with the gold cladding. Thus the EM field confinement dacayes more appruptly for TM light compared to the case of TE light. (C) Calculated values for the sensitivity. The values calculated for sensitivities of TM and TE light are comparable for both polarisation states.

Bibliography

[1] Byrne, M. T. *et al.* Chemical functionalisation of titania nanotubes and their utilisation for the fabrication of reinforced polystyrene composites. *J. Mater. Chem.* **17**, 2351–2358 (2007).

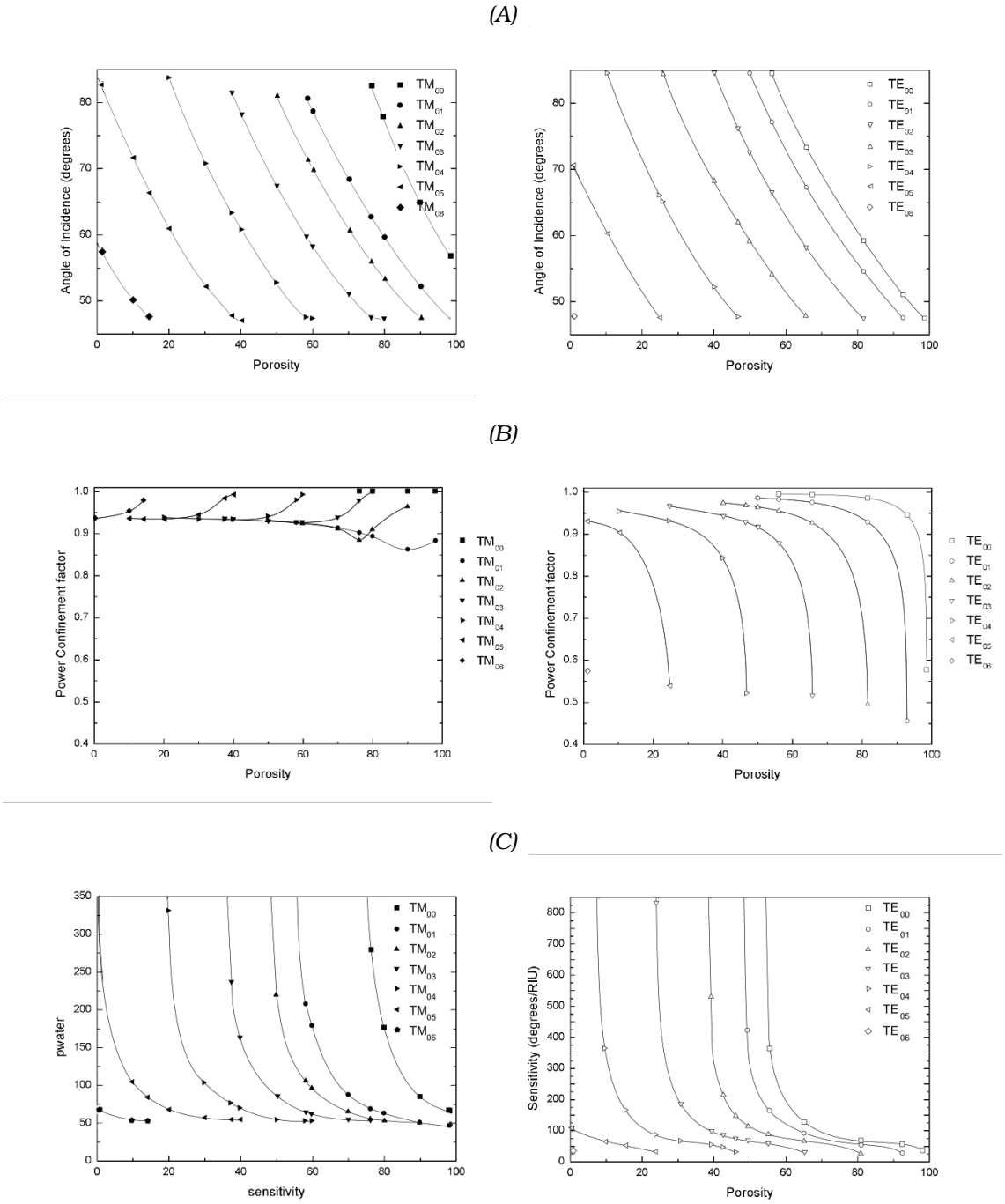

Figure 4.8: All graphs relate the displayed results to guided modes, excited in a $1.2\mu m$ thick gold-supported $meso - nc - TiO_2$ waveguide layer. Results are shown for calculations in aqueous environment and for both cases, TM light (left column) and TE light (right column) at $\lambda_{HeNe} = 632.8nm$. (A) Resonant angles of incidence. (B) The power confinement factor. Apparently, the degree of power confinement for TM-light is assumed to be higher (compared to the TE light) due to the intrinsic interaction with the gold cladding. (C) Calculated values for the sensitivity. The smaller values of TM modes, and accordingly the lower sensitivity is most probably due to the higher degree of interaction with the gold cladding (compared to the excited by TE light) which cause higher losses due to absorption in the metal.

[2] Chien, F.-C. & Chen, S. J. A sensitivity comparison of optical biosensors based on four different surface plasmon resonance modes. *Biosensors and Bioelectronics* **20**, 633–642 (2004).

[3] Clerc, D. & Lukosz, W. Integrated optical output grating coupler as refractometer (bio-) chemical sensor. *Sensors and Actuators B* **11**, 461–465 (1992).

[4] Duveneck, G. L., Abel, A. P., Bopp, M. A., Kresbach, G. M. & Ehrat, M. Planar waveguides for ultra-high sensitivity of the analysis of nucleic acids. *Analytica Chimica Acta* **469**, 49–61 (2002).

[5] Fujimaki, M. *et al.* Nanoscale pore fabrication for high sensitivity waveguide-mode biosensors. *Microelectronic Engineering* **84**, 1685–1689 (2007).

[6] Homola, J. On the sensitivity of surface piasmon resonance sensors with spectral interrogation. *Sensors and Actuators B* **41**, 207–211 (1997).

[7] Huber, W. *et al.* Direct optical immunosensing (sensitivity and selectivity). *Sensors and Actuators B* **6**, 122–126 (1992).

[8] Jiao, Y., Rong, G. & Weiss, S. M. Porous waveguide in the kretschmann configuration for small molecule detection. *Photonic Microdevices/Microstructures for Sensing* **7322**, 732205 (2009).

[9] Koutsioubas, A. G., Spiliopoulos, N., Anastassopoulos, D., Vradis, A. A. & Priftis, G. D. Nanoporous alumina enhanced surface plasmon resonance sensors. *JOURNAL OF APPLIED PHYSICS* **103** (2008).

[10] Lau, K. H. A., Tan, L., Tamada, K., Sander, M. S. & Knoll, W. Highly sensitive detection of processes occuring inside nanoporous anodic alumina templates: a waveguide optical study. *J. Phys. Cham. B* **108**, 10812–10818 (2004).

[11] Lukosz, W. Integrated optical chemical and direct biochemical sensors. *Sensors and Actuators B* **29**, 37–50 (1995).

[12] Lukosz, W. *Biosensors and Bioelectronics* **6**, 215–225 (1991).

[13] Lukosz, W. & Tiefenthaler, K. Sensitivity of integrated optical grating and prism couplers as (bio)chemical sensors. *Sensors and Actuators* **15**, 273 – 284 (1988).

[14] Nellen, P. M. & Lukoszt, W. Integrated optical input grating couplers as direct affinity sensors. *Biosensors & Bioelectronics* **8**, 129–147 (1993).

[15] Rong, G., Ryckman, J. D., Mernaugh, R. L. & Weiss, S. M. Label-free porous silicon membrane waveguide for dna sensing guoguang rong. *APPLIED PHYSICS LETTERS* **93**, 161109 (2008).

[16] Skivesen, N. *Metal-Clad Waveguide Sensors*. Ph.D. thesis, Riso, National Laboratory, Roskilde, Denmark (2005).

[17] Sotsky, A. . B. ., Primak, I. . U. . & Tomov, A. . V. . K. A. . V. . Sensitivity of integrated optical sensors based on a prism coupler. *Optical and Quantum Electronics* **31**, 191 – 200 (1999).

[18] Stoecker, P., Menges, B., Langbein, U. & Mittler, S. Multimode waveguide mode surface plasmon coupling: a sensitivity and device realizability study. *Sensors and Actuators A* **116**, 224–231 (2004).

[19] Taya, S. Enhancement of sensitivity in optical waveguide sensors using left-handed materials. *Opt. Int. J. Light Electron. Opt.* (2008).

[20] Veldhuis, G. J., Parriaux, O., Hoekstra, H. J. W. M. & Lambeck, P. V. Sensitivity enhancement in evanescent optical waveguide sensors. *Jornal of Lightwave Technology* **18** (2000).

[21] Vollmer, F. Label-free, high-sensitivity detection of biomolecules using optical resonance. *B.I.F. FUTURA* **20** (2005).

Chapter 5

5 Synthesis of Mesoporous Titanium Oxide Thin-Films

Contents

Abstract

Mesoporous nanocrystalline titanium oxide ($meso-nc-TiO_2$) thin-films are synthesised *ab-initio* from alkoxide precursors, which involves the chemical inhibition of premature precipitation of titanium oxide powder *via* acidic reaction conditions. Control over the oxide nanocrystal-assembly is gained through the use of different template assisted methods for controlled mesostructure formation, where triblock copolymeres play the role of structure directing agents which are finally removed upon calcination. P123 triblock copolymer and different titanium alkoxides as the initial reaction agents are subject to various solvent mixtures with the aim to produce interconnected pores throughout the whole film.

Furthermore, a non-scaffolded approach is introduced that utilises a top-down technique for the formation of mesopores; electrochemical anodisation of thin titanium foil in combination with supporting wet chemical processes. Contrary to the lamellar, tubular, hexagonal, cubic, and isotropic architectures from polymere templated synthesis, this method yields self-organised titania nanotube arrays which do not result in three-dimensional pore networks.

As an alternative to the fairly complex techniques of titania precursor-based block copolymer templating or the anodisation of metallic titanium in order to obtain mesoporous structures, feasible 3D-mesoporous films were also achieved by sintering nanoparticles (i.e. nanocolloids) together. The resulting films offer accessible interconnected pores throughout the whole film thickness, however, with the benefit of a simple one-pot synthesis protocol. More accurately, the nanocolloids were synthesised *via* sol-gel method, though films were also prepared directly from commercially available colloidal sols of titania nanoparticles and dry titania powder.

The effects of individual variation of synthesis parameters on the mesoscopic architecture, and finally on the thin-film optical waveguiding properties are discussed in detail on the base of scanning electron microscopy (SEM) and optical waveguide spectroscopy (OWS).

5.1 Introduction

Since the early 1990s, when the first synthesis routines for mesostructured and mesoporous materials were developed[58,9,40,35], a rapid growth in the field of nano- and mesostructured materials has been observed. This development is mainly rooted in the demand for unique structural and bulk properties, i.e. high specific surface area, large pore volume, narrow pore size distribution and rich surface chemistry. Although the core focus was put

on silica materials in the beginning, soon the range of elements utilised for mesostructure design expanded. Nowadays, the field of mesostructured materials research has evolved far beyond the original silica. The class of mesostructured materials has been extended to include many other compounds such as transition metal oxides[61,39,60,57], metals[4,5,6], semi metallic structures[48], carbon[59], and polymers[36]. Until today, roughly 50% of the metals and approximately 60% of transition metal in the periodic table of elements have been incorporated into a mesostructure, and roughly 50% of these mesostructures lead to mesoporous materials.

Extensive research was necessary to manufacture mesostructured materials with a high degree of structural control. The first steps in this direction were inspired by naturally occurring minerals like the zeolites with highly defined pore-structure of variable pore sizes ($0.5 - 2.0nm$)[12]. Traditionally microporous zeolites have been widely used as molecular sieves in the petroleum industry due to their inherently defined pore structure and their sharp size distribution. The relatively small pore sizes, however, restrict their application to small molecule separation.

The introduction of surfactant supramolecular templating approaches has led to a breakthrough in the extension of porous materials to the meso-scale, with relatively large, uniform and adjustable pore sizes. Since these characteristic properties of porous materials have been accessible for manipulation, a variety of new designs, and consequently new applications emerged and created a whole new field of science and technology. Especially the use of di- and triblock copolymers, as they are well-known to segregate at the molecular level and associate into various liquid crystal structures as they are mixed with solvents that have selective affinities to each block of the copolymer. This method has provided much synthetic freedom. One successfully utilised example of such block copolymers is the Pluronics family. These are triblock copolymers composed of poly(ethylene oxide) (EO) and poly(propylene oxide) (PO) block units that can elegantly be synthesised with a high degree of control in terms of molecular weight distribution according to the number of hydrophobic and hydrophilic block units, y and x respectively. The structural polymorphism, which is given by this class of triblock copolymers, was first recognised a decade ago[47,56,3], but nevertheless, today their associated properties such as phase behaviour (both theoretical behaviour[7] and experimental behaviour[2,29]) are well documented and can be used as a toolkit to predict and design mesoporous structures according to desired (optical) properties.

The aforementioned triblock polymers of the general architecture $EO_xPO_yEO_x$ are commercially available with various block sizes and are traded as nonionic surfactant by

BASF-Wyandotte and DOW Chemical Company. They are relatively low-cost, non-toxic and biodegradable; making them the structure directing agent of choice for the synthetic approaches presented in this thesis. The synthesis of mesoporous materials presented in this section was restricted to the use of Pluronics 123 ($MW = 5820g$) with 30% EO (x=20 and y= 70). The synthesis was undertaken under acidic conditions in aqueous solution[62,22] with variable volume fractions of polymer components, resulting in a range of mesoporous structures with large pore sizes (up to $20nm$).

The scope of this chapter will be limited to the synthesis of mesostructured titanium dioxide (titania) as material of choice. Titania is a well-known and widely used material with a wide range of commercial applications, ranging from the quite primitive use as an additive to mass-produced polymers, as a white pigment, and more recently in a highly-sophisticated manner in photovoltaics[28,27], photo catalysis[32], and battery applications[37]. Characteristic for titania is its wide band gap (3.2 eV), making it semiconducting with a range of accessible optical and electronic properties. However, it is still challenging to make mesoporous titania due to the extreme reactivity of titania precursors with water. Other difficulties are found during the templating step, e.g. incomplete condensation and crystallisation of the amorphous framework. Furthermore, the conservation of an intact mesostructure after removal of the organic template *via* calcination at temperatures above $400°C$ has to to be considered.

As well as synthesising mesoporous materials with different architectures using precursor solutions of titanium oxide and amphiphilic triblock copolymers, efficient control of the morphology, i.e. application of thin-films onto gold-coated glass substrates, had to be elaborated. Therefore, all these different aspects of mesoporous thin film synthesis are addressed in the following chapter. Starting with (1) the preparation and control of the titanium oxide precursor by the sol-gel method, followed by (2) the polymorphic behaviour of block copolymers in ternary solution, (3) suitable techniques for thin film application, followed by (4) the presentation of the waveguide properties of mesoporous thin films. The results are divided into individual sections in order to discuss experimental modifications and their consequences on the obtained mesoporous thin-films on the basis of electron microscopic imaging and optical waveguide spectroscopy.

5.2 Template Assisted Synthesis of Mesostructures

Synthetic approaches used in the framework of this thesis, in order to produce various amphiphilic block copolymer templated mesoporous morphologies of titania, have been

adapted from published literature([2,62,7,12,30,22,41]). Syntheses were modified to achieve good optical waveguiding properties of the resulting thin films. The nanostructured films had to be effectively optically homogeneous, with only limited scattering losses at visible wavelengths ($\lambda = 632.8nm$), in order to make them suitable as waveguide material. On the other hand, the pores had to be sufficiently big to support penetration of analyte species from solution. Therefore, effort was put into obtaining highly transparent films with thicknesses not more than $2\mu m$ for reduced sorption times, but also on realising sufficiently high refractive indices in order to be able to guide confined optical modes with low losses within these mesoporous waveguides in aqueous environments (i.e. $n_{film} > n_{water}$). In addition the pore size had to be greater than $15nm$ in average in order to allow adsorption of probe material into the pores.

5.2.1 Alkoxide Precursor

A general challenge concerning the synthesis of mesostructures of titanium oxide, and all transition metal oxides in general, is the pronounced reactivity of the transition metal complexes with water. The low electronegativity of titanium(IV) causes fast reaction rates for hydrolysis and condensation[13]. Actually, the alkoxides of transition metals are already hydrolysed by ambient water even at low humidity levels, which lets the liquid condense directly into the hydroxide, visible in form of a white powder. Under standard laboratory conditions, only the rate of this process may be slowed down (e.g. storage in ultra-dry condition). Alkoxides of titanium, in particular, are open to nucleophilic attack at the bond between the transition metal and the alkoxide (-OR) unit. The fact that transition metal ions are sometimes able to expand their coordination sphere makes it even more likely for them to be attacked by a nucleophile unit. Therefore, many different attempts at synthesising mesoporous titania have been made to overcome these problems and to produce materials with a wide variety of pore structures (2D-hexagonal, 3D-hexagonal, tubular) and different morphologies (powders, monoliths, thin films, thick films, fibres). A pioneering approach to the synthesis of ordered large pore materials was developed by *Stucky et al.*, wherein a simple and general protocol was described, based on an alcoholic solution of amphiphilic poly (alkyleneoxide) block copolymers under acidic conditions[61,60], which proved to result in mesostructures with good long range order.

5.2.2 Synthetic Approaches

A sol-gel synthesis of metal oxides can be performed *via* the hydrolysis and condensation of metal cations in aqueous solutions[31]. This inorganic route provides a cheap and reliable

way for industrial uses. The so-called Partial Charge Model (PCM)[51] provides a useful guide to describe and predict hydrolysis and condensation reactions in aqueous solutions. They can lead either to small solute condensed species (poly-anions or poly-cations) or to the formation of an infinite network (colloids, gels, or precipitates). The PCM is based on the electronegativity equalisation principle stated by R. T. Sanderson[51].

The strong susceptibility of titania precursors to nucleophilic attack, even at the isoelectric point of hydrolysed titanium(IV), which is at pH-values between 4 and 5, makes condensation kinetics so fast that they are effectively instantaneous, resulting in a white precipitate, which is formed immediately upon the addition of $pH4$ water to titanium alkoxide. Therefore, using the isoelectric point as a strategy to overcome this problem is not appropriate in this titania system (figure 5.1).

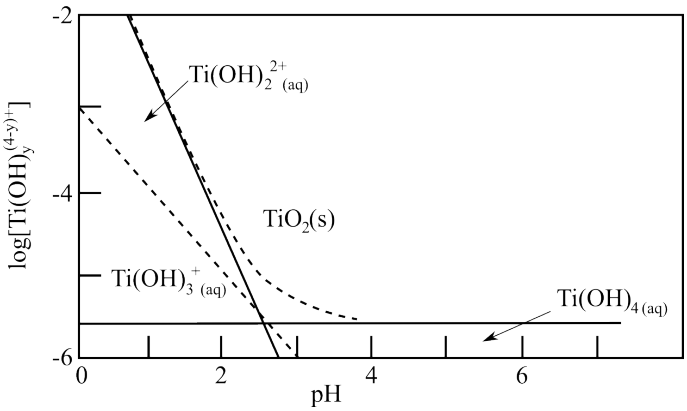

Figure 5.1: Hydrolysis phase diagram for titanium (IV)[22]

Accordingly, other hydrolysis conditions are required. One protocol[61], aims to slow down the hydrolysis process by not directly adding water to the reaction mixture. Instead, chloride salts of various metals are mixed with ethanol (containing azeotropic amounts of water) and ethoxychloride complexes of the metal are formed. These ethoxychloride complexes are then combined with nonionic surfactant and allowed to dry. As the film dries it hydrolyses under ambient hydrolytic conditions (i.e. relative humidity), and forms oxides in the presence of the amphiphilic structure directing copolymer. During evaporation of the solvent a liquid crystal-like structure is formed which is a good scaffold for the inorganic species. This method, however, was originally developed to make thick films and appeared not to be suitable for the production of crack-free thin films ($\sim 1\mu m$) with high optical quality.

Another synthetic approach[22], is condensation inhibition by doing the hydrolysis in highly acidic conditions in the presence of additional water as a means of stabilising the hydrolysed titania precursors by preventing their condensation (reaction scheme is depicted in figures 5.2 and 5.3).

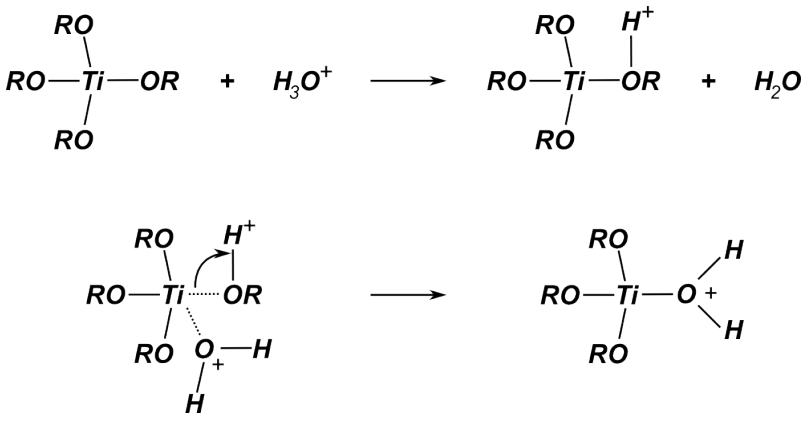

Figure 5.2: Acid catalysed hydrolysis Reaction of titania precursor titanium(IV)alkoxide.

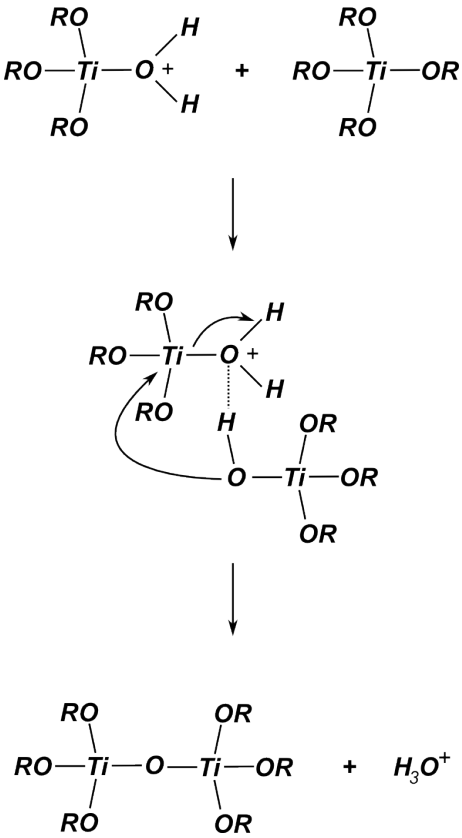

Figure 5.3: Condensation reaction of titania precursor titanium(IV)alkoxide.

In this context the hydrolysis phase diagram of titanium(IV) has been suggested[22] as a very useful guide to set the appropriate conditions for solubilising the titania(IV) species in aqueous conditions. Figure 5.4 shows the plotted diagram, depicting the concentration of titanium(IV) species present at a range of acidic pHs. With the help of this diagram the concentration of acid was chosen to solubilise the hydrolysed titanium(IV) species and to prevent the titania precursors from precipitating immediately during the hydrolysis reaction. The desired soluble species of titanium(IV) is present in the region to the left of the solid line (intersecting the x-axis at $pH \sim 2.7$ in figure 5.1). To meet these requirements extremely low pH, actually negative values are needed, since the high concentration of

acid acts as an ideal condensation inhibitor. (Depicted in the extrapolated regime of the hydrolysis phase diagram in figure 5.4.)

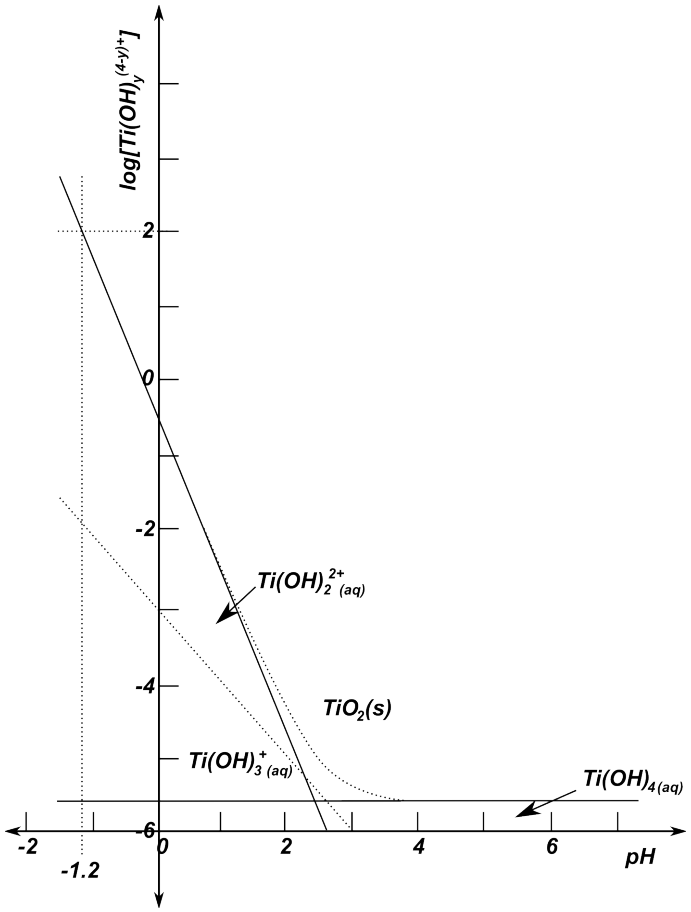

Figure 5.4: Extrapolated hydrolysis phase diagram

The choice of concentrated acidic environment leads to total hydrolysation of the titania and to the formation of very small nanosized clusters which are predicted to be oligomers of aquohydroxotitanium(IV) chlorides[22], solvated under highly acidic conditions, as depicted in figure 5.5[23,20]. The existence of these nanoclusters or nanoentities was verified by FT-Raman microspectroscopy[21].

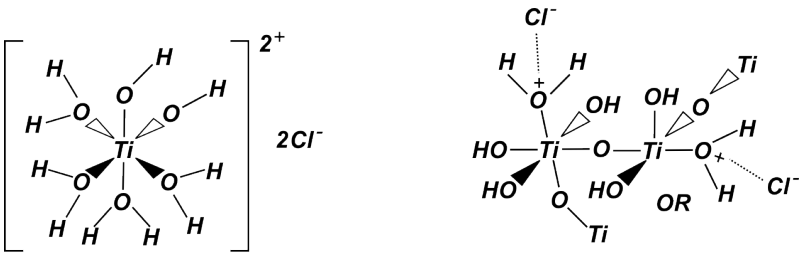

Figure 5.5: Solubilised titania species. Their appearance in highly acidic solution is expected to be in form of aquohydroxotitaniun(IV) chlorides, which form oligomers as shown on the right. ox-nanoentities.

At low pH, olation is the process by which metal ions form polymeric oxides in aqueous solution. Many metal ions exist in aqueous solution as aqua coordination complexes.

As the pH increases, water ligands ionise to form the hydroxo complex, the conjugate base of the parent hexa-aqua complex (illustrated in figure 5.5(left)). The hydroxo complex is poised to undergo olation, which is initiated by displacement of one water by a neighbouring complex, starting to form a cluster, a so-called oxo-dimer, as shown in figure 5.5(right). The remaining water and hydroxo ligands are highly acidic and the ionisation and condensation processes can continue. The formation of the oxo-dimer is a process called 'oxolation'.

One important factor that must be controlled during the nucleation and growth of the anatase structures of TiO_2 (rather than rutil structure) from aqueous solutions is the desoxolation reaction[31]. If it occurs before nucleation, condensation may be oriented towards cis-skewed chains characteristic of the anatase structure. If it occurs after nucleation, the trans-linear chain characteristic of the rutile structure is formed.

In order to produce thin films of these anatase nanocrystals on (gold-coated) glass substrates, a variety of different methods was available to chose from, e.g. spin-coating, dip-coating or doctor-blading. However, ultimately all these application techniques for thin films from solution are based on the principle of evaporation induced self assembly (EISA). For this purpose the water content had to be minimised to facilitate solvent evaporation, but still be of sufficient concentration to guarantee complete hydrolysis. A $Ti : H_2O$ ratio of $1 : 4$ was suggested as adequate[22] for complete hydrolysis, but in practise somewhat higher ratios (up to $Ti : H_2O$ ratio of $1 : 6$) were found to result in slightly more ordered material.

5.2.3 Control over the Mesostructure - Use of Structure Directing Agent

Templated materials arrived in 1992 with the first preparation of MCM-41[9], demonstrating that highly regular pore structures could be achieved on scales much larger than those present in zeolites. Developments in templating[25,4,14,33,15,55] and other micro-patterning technologies suggest the rational design of porous media for different applications is possible[15] and a wide variety of micro structures has been reported, including arrays of simple geometries, bi-continuous networks, and hierarchical structures[15].

As a first step towards block copolymer templating it was important to understand the aggregation and phase behaviour of the applied triblock copolymere (Pluronics P123) in solution before applying their segregation properties to form a suitable scaffold for the titania precursor in order to leave a mesoporous material after calcination. The P123 triblock copolymer is a surface active compound and accordingly it forms micelles and lyotropic liquid crystalline phases. The formation of these phases depends not only on the volume fractions of the mixture, but rather also to a high degree on the temperature

they are exposed to, referring to figure 5.6. This peculiarity is rooted in their critical micelle concentration, defined as the concentration of surfactants above which micelles are spontaneously formed. The cmc can shift several orders of magnitude with small temperature changes. It is of great importance to draw attention to this, since the main shift for this applied compound is found to occur in the temperature region between 20 and 50°, for example the $cmc(25°C) = 4 \cdot 10^{-3} wt\%$ and the $cmc(17°C) = 4.5 wt\%$[56].

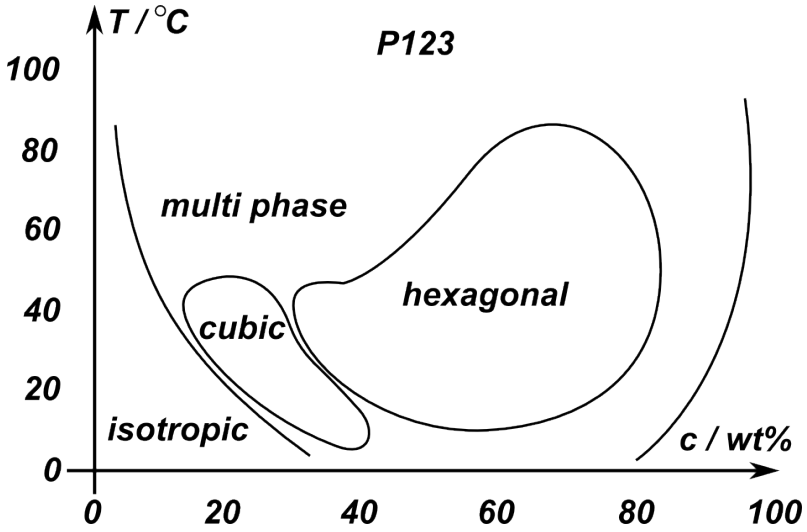

Figure 5.6: The phase diagram of the triblock copolymer P123 with the structure $EO_xPO_yEO_x$, $x = 20$, $y = 70$ in aqueous solution clearly shows the dependence of the system on temperature and composition.

The first attempt to gain control over the mesostructure and predictably produce ordered films used block copolymere-solvent-precursor mixtures in certain ratios, according to the phase diagram (figure 5.7). This ternary phase diagram allowed for the prediction of the resulting mesostructures according to the self-assembly behaviour of the copolymere in various concentrations. P123 block copolymers can form five different mesostructures. In the absence of the inorganic fraction, different liquid crystal structures are formed by the interaction of block copolymers and different amounts of water. The reason for this behaviour is given by the selective affinity of the hydrophilic part(s) of the polymer to water, which causes significant swelling of hydrophilic region(s) while the hydrophobic region(s) stay unchanged. The same is true for the hydrophobic part(s) when oil is added to the mixture, where, again, the hydrophilic part(s) stay unchanged. This selectively introduced swelling of different regions of the block copolymer allows the curvature of the hydrophilic/hydrophobic interface to be changed, and therefore, controls the type of micelles that are formed. For example, in the phase diagram of Pluronics P123, at small water content, spherical micelles develop and pack into a body centred cubic arrangement. The ternary phase diagram for water-butanol-P123 is shown in figure 5.7.

It is expected that addition of the inorganic species greatly modifies the phase diagram,

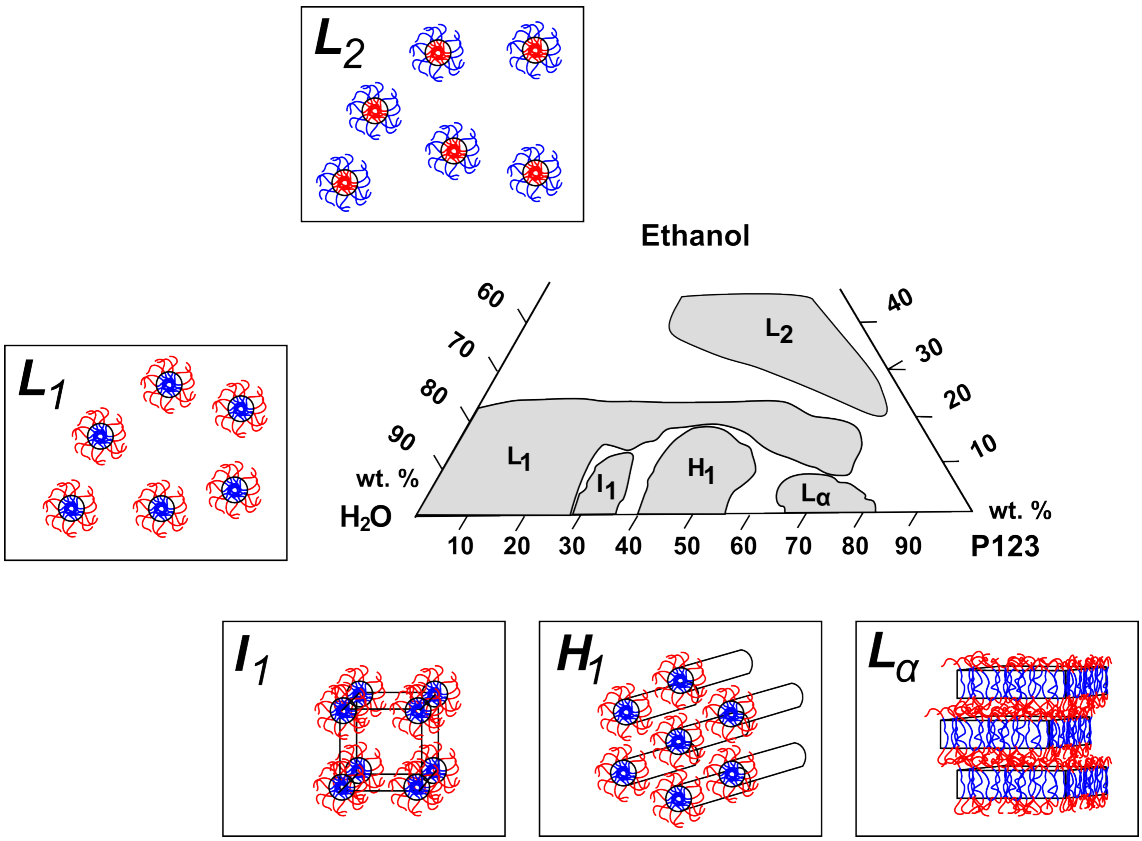

Figure 5.7: Ternary water-ethanol-polymer phase diagram for Pluronics P123. L represents a lamellar phase, H_1 a hexagonal phase and I_1 a cubic phase. The addition of titania species results in another dimension represented by an additional axis normal to the page.

by creating an additional domain in the phase space of the system. Nevertheless, several reports have been published[34] on the use of the ternary phase diagram (figure 5.7) as a good approach to predict and synthesise various phases of organic-inorganic mesostructured materials. Published methods include reports of the use of both non-ionic and ionic surfactants as well as several types of block copolymers and organic solvents[34,22].

The use of ionic surfactants, however, presents limited potential applications for mesostructured titania because of the strong surfactant interaction with the titania walls, which make it impossible to completely remove the surfactant by extraction procedures and in the collapse of the inorganic structure when post-synthetic thermal treatment is employed. Thus, nonionic surfactants were chosen as a potential alternative, as hydrogen bonding mediated the formation of the metal oxide-surfactant composites involved in the inorganic framework organisation. The attractive interactions between this nonionic block copolymer and the inorganic species (titania oxo-cluster), which are critical for the formation of the heterogeneous mesostructure, are relatively weak, and exhibit hydrogen-bonding/electrostatic characteristics[62,22].

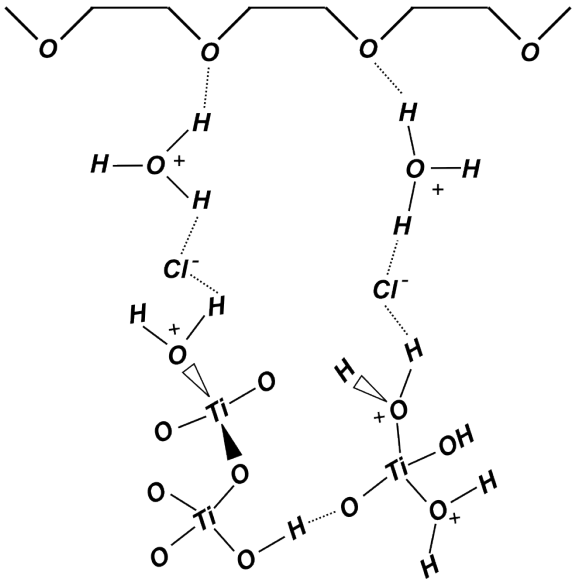

Figure 5.8: Illustration of the hydrogen bond/electrostatic interaction between the EOx block of P123 and the hydrolysed titania species.

5.2.3.1 Evaporation-Induced Self-Assembly (EISA)

The self-assembly process underlying the formation of mesostructured titania was facilitated by an home-made evaporation induced self-assembly (EISA) apparatus. The device was programmed to pull a (previously submerged) gold-coated glass slide out of the solution with a steady rate of $1mm\,s^{-1}$. Figure5.9 gives a schematic illustration of the processes occurring within the meniscus, which is formed at the gold/water interface during the pull-out process.

As non-ionic surfactants like the block copolymers of the Pluronics family do not form micelles in ethanol solution, both ethylene oxide as well as propylene oxide dissolve to approximately the same degree. Full phase separation occurs only upon evaporation of the solvent from the mixture. Therefore, the final film structure only depends on how the the structural arrangement is left after all the volatile components are evaporated.

Brinker *et al.* stated in a review article that self-assembly is "the spontaneous organisation of materials through non-covalent interactions (such as) hydrogen bonding, Van-der-Waals forces, electrostatic forces, π -π-interactions, etc. with no external intervention."

The process of spontaneous self-organisation was applied *via* dip coating the gold coated glass slides from an alcoholic surfactant solution, that was too dilute to contain micelles. As the dip coated films dry during the pull out process the volatile components (alcohol and water) evaporate from the film. Accordingly, the surfactant is concentrated in the presence of the titania oxo-clusters, titania precursors that are complexed by water and hydrochloric acid.

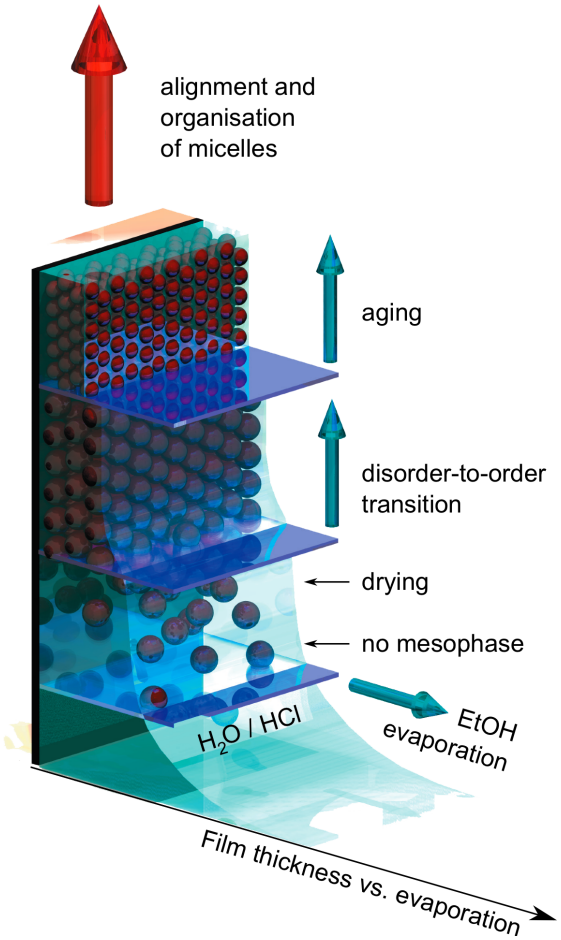

Figure 5.9: Preparation of the sensor was carried out by dip coating, implying evaporation induced self-assembly (EISA) of an ordered mesoporous titania thin film onto a gold-coated glass slide. EISA occurs upon pulling the films out from the titania precursor system.

Since, there are many possible variations how the two positive charges (according to the phase diagram in figure 5.6) are balanced (e.g. by closely associated chloride ions), and due to the uncertainty about the coordination number of titanium (IV) (between 4 - 6, which strongly depends on the type and size of the ligand(s)) it can only be approximated that 2 - 4 water molecules are associated with the titanium atoms. The interactions between the titania nanoentities and the block copolymer can be therefore assumed to be due to hydrogen bonding[61,23].

The titanium nano-cluster and associated chloride ions are representing the non-volatile hydrophilic domain around the Pluronics P123 micelles. The greater the ratio of this domain to the polymer, the greater the surface curvature in the final mesostructure. Depending on variations of this ratio it is possible to achieve at least three different possible liquid crystal structures. The equation can only be back calculated from empirical data.

In this thesis the synthesis of ordered mesoporous TiO_2 is approached by using the P123 triblock copolymer and titanium alkoxides as the initial reaction agents. The weak

surfactant-precursor interactions involved in the synthesis reactions made possible the effective elimination of the block copolymer by either solvent extraction or alternatively by a pre-calcination heating step.

5.2.4 Experimental

In order to produce 3D-mesoporous nc-titania thin films of a titanium(IV) precursor solution was prepared with the nonionic block copolymer (Pluronics P123) as the structure-directing agent. The process began with hydrolysis of titanium(IV) ethoxide (TEOH) in concentrated hydrochloric acid. The ratio of water (present in the acid solution) to Ti was held constant at $6:1$, which is equivalent to the stoichiometry of water and titanium cation in the hexaaquahydroxo-titanium(IV) complex. This ratio was expected to allow for the most complete hydrolysis possible in the solution, prior to making the films. The total amount of block copolymer was varied in order to find the optimum fraction to achieve highly porous structures and interconnected pores throughout the whole film structure. Therefore, the initial solution was made in two separate flasks; one containing the titania precursor with the general form of $Ti(OR)_4$ in highly acidic hydrochloride solution, the other one containing the structure directing amphiphilic block copolymer in alcoholic solution.

5.2.4.1 Ethanolic Solution

In the first series of experiments, pure ethanol was used as the alcoholic solvent and the titania source ($Ti(OR)_4$) was chosen to be titanium(IV) ethoxide with $R = C_2H_5$ ($TnEO$, Sigma-Aldrich). Subsequent experiments revealed that titanium(IV) isopropoxide with $R = C_3H_7$ (TiPO, Sigma-Aldrich) could also be used. Titanium isopropoxide is beneficial as it is more stable in air and less reactive towards ambient humidity, no significant change in synthesis conditions or resulting structure was observed. Although, the absolute amount of the precursor had to be adjusted accordingly to keep the ratio of water (present in the acid solution) to Ti constant at $6:1$. In the case of an absolute amount of $3.2g$ of hydrochloric acid ($12.1M$), which contained 62% water (i.e.$2g$ water), $1.6g$ TnEO and $2.0g$ PiPO were required to be added to the acid at a very slow rate, at a temperature of $0°$ and under vigorous stirring.

Meanwhile, in the second flask, an alcoholic solution of $1g$ $P123$ ($MW = 5800$, *Aldrich*) in $12g$ ethanol was prepared. After 20 minutes, the $EtOH/P123$ solution was carefully added (1 drop each 10 seconds) to the rigorously stirred mixture of $TnEO/HCl$ or

$TiPO/HCl$, respectively. The resulting sol was then aged at room temperature (RT) for $2-3$ hours under continuous stirring. Subsequently, uniform and transparent thin films were produced by dip-coating the gold coated glass substrates at a constant withdrawal rate of $1mm\,s^{-1}$ out of the freshly prepared solution. After the films had been aged for additional $24h$ at room temperature and a controlled relative humidity (RH) of 50% and 95%, respectively, the as-synthesised thin films were then calcined in an oven according to a temperature program at $450°C$ for $5h$ (ramp of $1°C\,min^{-1}$) in ambient atmosphere. This thermal treatment first gently removed the block copolymer completely, and as the temperature increased it allowed the titania precursor to cross-link, and finally, the inorganic structure (oxide) to crystallise and to leave an interconnected network of pores throughout the material. These films were subsequently characterised using scanning electron microscopy (SEM) and optical waveguide spectroscopy.

5.2.4.2 Butanolic Solution

During the course of experiments the initial solution mixture was modified and titanium(IV) n-butoxide (TnBO, Sigma-Aldrich) was used as titanium source. The $P123/TnBO$ system was used on the basis of its reported success in producing large-area crack-free and optically transparent meso-nc-titania thin films[19,41] with large pores. The alcoholic solvent for the amphiphilic block copolymer (P123) was also changed to $nBuOH$. A more detailed explanation is given in section5.2.3.1. The post-synthetic treatment was identical to the procedures described in 5.2.4.1 with no alterations. The experimental variations are summarised in table 5.2. These films were also subsequently characterised using scanning electron microscopy (SEM) and optical waveguide spectroscopy.

Precursor	**Alcoholic Solvent**	**Ageing Conditions**
TnEO / TiPO	EOH/iPO	RT/50% RH
	EOH/iPO	RT/95% RH
	nBOH	RT/50% RH
	nBOH	RT/95% RH
TnBO	EOH/iPO	RT/50% RH
	EOH/iPO	RT/95% RH
	nBOH	RT/50% RH
	nBOH	RT/95% RH

Table 5.2: Shows the experimental matrix of precursors and alcoholic solutions at different ageing conditions.

5.2.5 Results and Discussion

5.2.5.1 Chemistry

The hydrolysis of the titanium(IV) species in concentrated hydrochloric acid was successfully implemented. Moreover, the use of the acidic synthesis conditions outlined in section 5.2.2 provided appropriate conditions for the organisation of TiO_2 into a mesostructure having both a high surface area and pore walls formed by incipient anatase nanocrystals. Small amounts of precipitate were initially formed, but they were very quickly and effectively re-solubilised and no kind of permanent precipitate of bulk titania powder remained in the solution. This was attributed to the pH of < -1 in the solution, and the fact that at the concentrations used in these experiments water was able to solubilise titanium(IV) oxo-clusters (see figure 5.4 for details). Furthermore, it was advantageous to hydrolyse the titania species to this high degree as this greatly reduced the system's (parasitic) sensitivity to humidity through hydrolysis and condensation steps during the synthesis. Nevertheless, the ambient water still affected the condensation process in the titania films. Dry conditions tended to drive off water from the films and therefore increased the rate and degree of condensation, whereas very wet conditions in some cases led to the formation of condensed water droplets on the surface of the film or even washed the film completely off the gold-coated substrate surface.

Due to a small degree of condensation that appeared in the hydrolysis solution, the titania(IV) oxo-clusters appeared to continue growing during the time they were in the hydrolysis solution. The growth was proportionally determined by H/I, with the hydrolysis ratio $H = [H_2O]/[Ti]$ and the inhibitor ratio $I = [H^+]/[Ti]$. Accordingly, the growth of nanoentities was slowed down by dilution of the mixture with additional alcohol. Sufficiently small building blocks allowed for better structuring within the film. If, however, the nano oxo-clusters were allowed to grow further, it was only possible to achieve structures with lower curvature. In consequence of the acidic conditions, again, the titania entities seemed to be well-prevented from aggregating and precipitating out as white powder.

Once the titania oxo-clusters were incorporated into the liquid crystal architecture of the block copolymer and assembled into the mesostructure, they were not cross-linked into a rigid and interconnected network, therefore, the somewhat flexible structure had to be locked in by thermal treatment (calcination). The diagram in figure 5.10 shows schematically the Gibbs free energy for the formation process of the mesostructured films.

There were various pathways possible in order to manipulate the liquid crystal structure

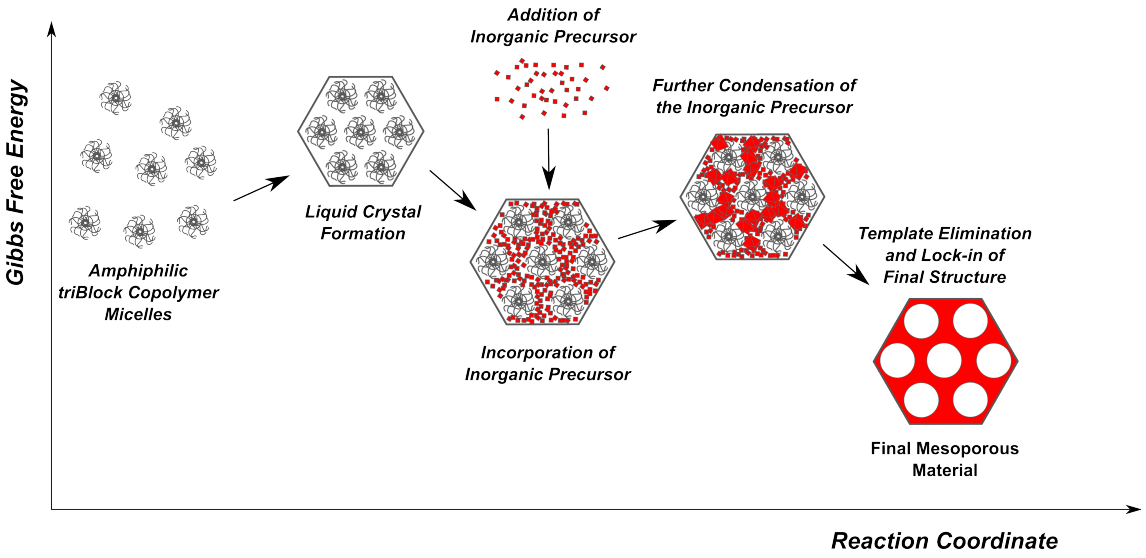

Figure 5.10: Titania nanoentities on free energy scale Schematic energy diagram for the synthesis of mesoporous titania films.

after the inorganic species was added (refer to figure 5.10). Obviously, the addition of the non-volatile fraction of inorganic nano-clusters itself, consisting of the titania oxo-complex and associated chloride ions, greatly altered the spatial distribution. More precisely, the amount of the inorganic fraction proportionally forced a higher curvature on the micellar architecture, which had to be considered when the volume fractions were chosen.

5.2.5.2 Equilibration Time

Although, the amount of water was fixed, other parameters were used to modify the mesostructure. For example, the time which the solution mixture was allowed to equilibrate. This equilibration time greatly influenced the degree of mesoscopic order in the final films. As the aim of this synthetic approach was to produce interconnected pores throughout the whole film, a mesostructure with a cage-like character was desired. Contrary to the lamellae and tubule which do not result in three-dimensional pore networks but ultimately collapse upon removal of the organic template during calcination, a (dense) spherical packing of micelles does fulfil this requirement, by leaving a cage-like imprint on the inorganic species.

In general, lamellar morphology (i.e. stratified sheets) can be created with high volume fractions of P123 to titania(IV) precursor, thus allowing for low curvature of the hydrophobic/hydrophilic interface of the micelles. With the synthetic approaches, presented within this thesis, no lamellar structure was observed after calcination at $> 400°C$, experiments aiming for such results produced crystalline bulk titania, likely due to a complete collapse of the meso phase upon template removal (see figure 5.11).

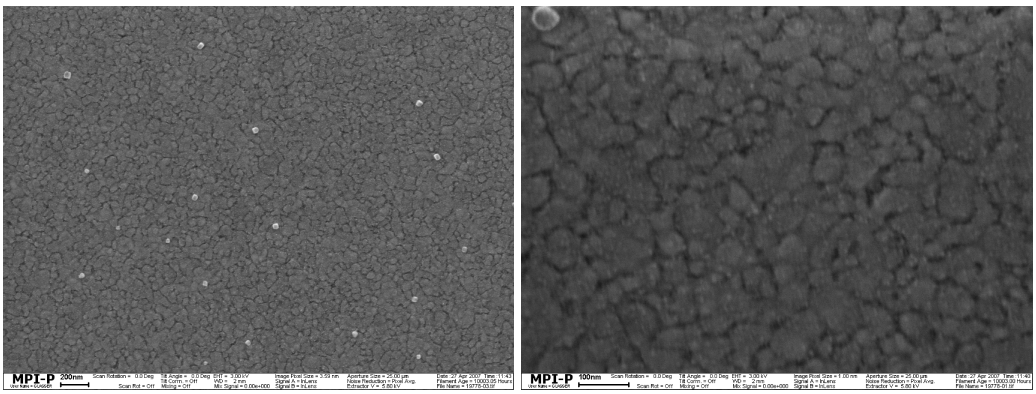

Figure 5.11: SEM images of the surface of collapsed lamellae which resulted in a thin layer of crystalline bulk titania after sintering the films

Therefore, in order to produce spherical packing of micelles throughout the mesophases, the size of the titanium(IV) poly-oxo-clusters had to be kept small to allow for highly curved micelles to exist, otherwise the mesophases transformed into tubule or lamellae. As well as the volume fraction of the surfactant and the inorganic in the hydrophilic phase, the time the mixture was sirred for also greatly controlled the mesophases. Since it appeared that the equilibration time was directly related to the oxo-cluster growth due to its polymerisation reaction rate, the stirring time was reduced to just $10 - 12$ minutes, in order to retain large, highly polymerised Ti(IV) oxo-cluster, which preferentially stabilised in less curved structures.

The short stirring time, however, did not allow the micelles to arrange properly and the SEM images of the first results revealed thin films with very poor structure templating success (see figure 5.12). The same was true for films if the solution was stirred for more than 30 minutes; no meso-phase ordering, and accordingly no kind of order was obtained in the calcined films.

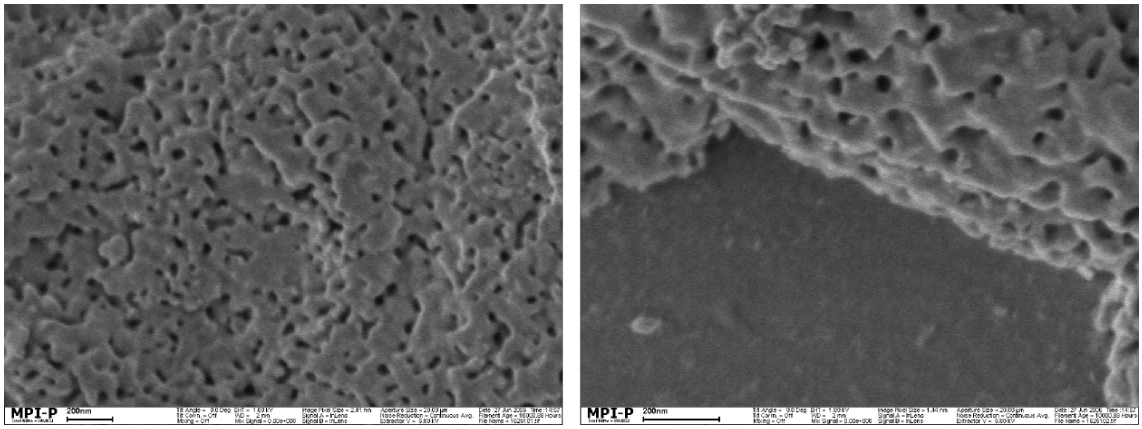

Figure 5.12: SEM images of the surface of mesostructured porous films after sintering and template polymer removal.

This problem was overcome by slowing down the polymerisation of the oxo-clusters with the addition of more alcoholic solvent during the equilibration period. The alcohol served

well as dilutant and also helped to control the final film thickness and homogeneity by adjusting the viscosity of the solution (while the dipping rate was kept constant), thus altering the ageing time and allowing for longer assembly duration. The SEM images taken of these films are shown in figures 5.13. The images clearly depict the sphere-like shape of the micelles, or rather the negative imprint of those, which is left after the calcination step when the polymer is decomposed and the nc-titania nanoentities sinter together in order to form a rigid network.

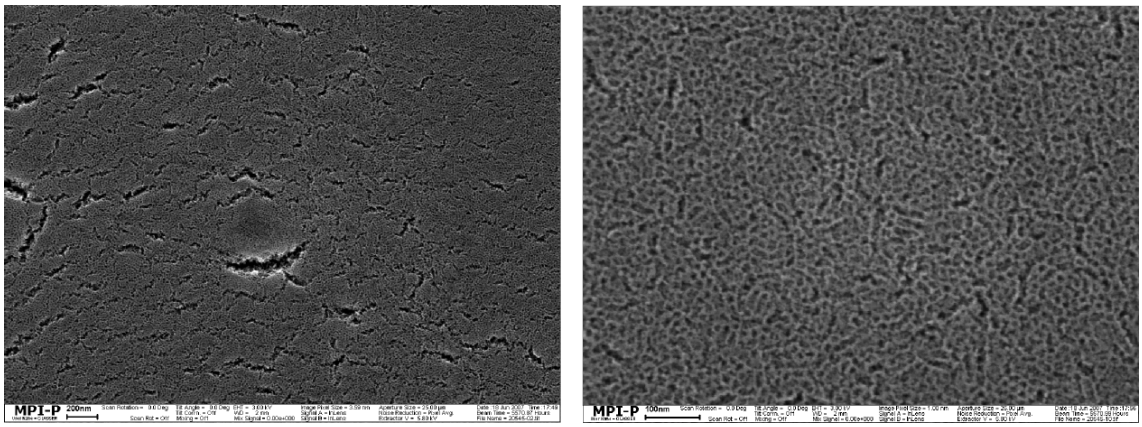

Figure 5.13: SEM images of the surface of mesostructured porous films produced at medium humidity levels.

These films, however, had many cracks, often in the range of micrometres, therefore the relative humidity (RH) was increased from 60% to 95% in order to extend the time available for self-assembly of the micelles during the dip-coating and ageing period. A representative SEM image of a meso-nc-titania film, obtained at 95% RH is shown in figure 5.14.

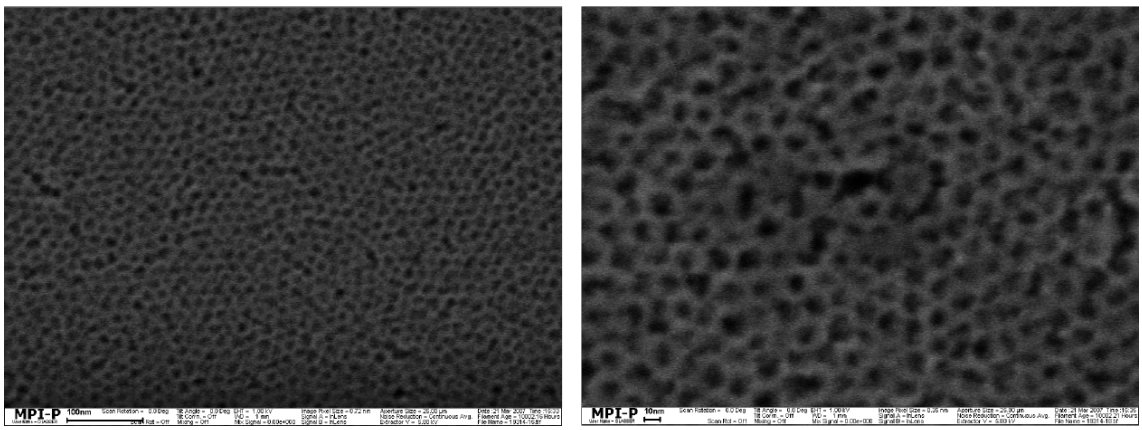

Figure 5.14: The increased level of ambient humidity resulted in more ordered structuring of the porous network and also in smooth crack-free surfaces as compared to 5.13.

Slightly increased order in pore arrangement was observed, compared to the films obtained at 60% RH; most likely in consequence to the extended time where sufficient mobility was allowed for the micelles to rearrange. Since the rapid evaporation rate of the ethanol mainly determined the mobility within the micellar arrangement and the ambient water

additionally supported condensation of the nanoentities, no drastic change was expected with high RH. Nevertheless, the films showed a much smoother surface and absence of larger cracks.

These smooth thin films were deposited onto a gold-coated glass slide and further characterised by means of optical waveguide spectroscopy (OWS). The angular scan spectra were taken both, in air and in an aqueous environment in order to determine the porosity of the films. As shown in figures 5.15 and 5.16, the experimental values were fit with a Fresnel simulation of the optical multilayer system, where the meso-nc-titania film served as the waveguiding layer. The simulations were fit to the measured data with the values listed in tables above the corresponding reflectivity scans.

	Thickness, d [nm]	Refractive Index, n [a.u.]	Extinction, κ [a.u.]
Prism/Substrate	∞	1.84498	0
Gold Film	48	0.312	3.823
meso-nc-Titania	1488	1.741	0.001
Superstrate	∞	1.000	0

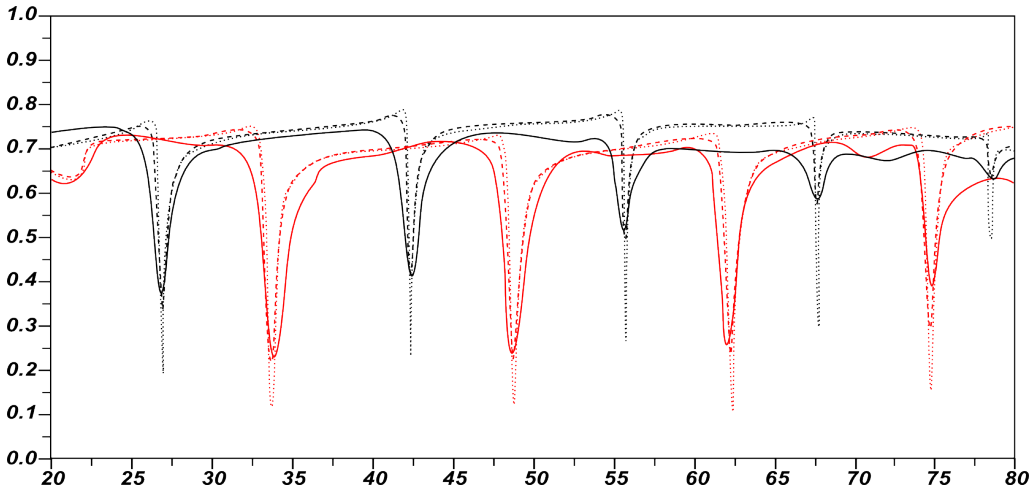

Figure 5.15: The OWS spectrum in air of mesoporous templated thin films at two different polarisations (red: TM, black: TE). Simulated Fresnel fits are shown as dotted curves for both polarisations in the corresponding colours. The simulation parameters for the fit are shown above.

The solid curves represent experimental data points (red: TM polarisation, black: TE polarisation) and the dashed curves illustrate the Fresnel simulation fit. The reflectivity spectra show significant, but still reasonable absorption coefficients within the meso-nc-titania waveguide film. Therefore the meso-nc-titania layer was considered to have a box-profile in its refractive index. For comparison the Fresnel simulation fit with zero extinction ($\kappa = 0$) is shown (dotted curves).

Both reflectivity scans (in air and water) show good accordance with the calculated values over the whole angular range, and the films can therefore be accepted as isotropic with respect to the laser wavelength ($\lambda_{HeNe} = 632.8nm$) applied for the measurement.

	Thickness, d [nm]	Refractive Index, n [a.u.]	Extinction, κ [a.u.]
Prism/Substrate	∞	1.84498	0
Gold Film	48	0.312	3.823
meso-nc-Titania	1488	1.880	0.001
Superstrate	∞	1.333	0

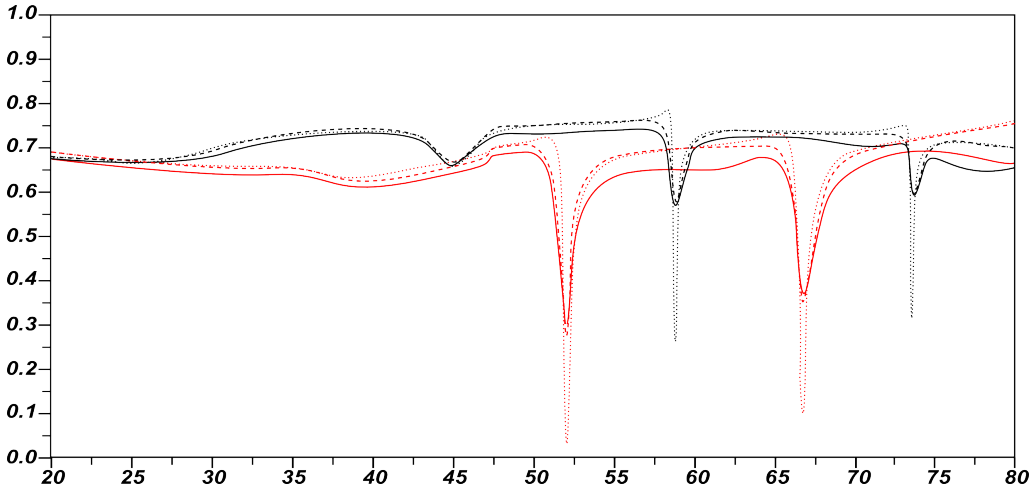

Figure 5.16: The OWS spectrum in air of mesoporous templated thin films at two different polarisations (red: TM, black: TE). Simulated Fresnel fits are shown as dotted curves for both polarisations in the corresponding colours. The simulation parameters for the fit are shown above.

The porosity was calculated for all mesoporous thin films according to the Bruggeman EMT. With the refractive index of the bulk anatase known ($n_{Ti,bulk}(anatase) = 2.1775$), the calculated porosity for the meso-nc-titania film, based on the measurements in air ($n_{air}(20°C) = 1.000$) and in aqueous medium ($n_{water}(20°C) = 1.333$) was 32.0% The porosity was homogeneously distributed within the meso-nc-titania film.

5.2.5.3 Titania Precursor

The liquid crystal structure was further manipulated by swelling (or collapsing) the hydrophobic core of the micelles to a certain extent, in order to achieve greater pore diameters. Therefore, titanium(IV) *n*-butoxide (TnBO) was introduced to serve as the titanium(IV) precursor, as it releases *n*-butanol *in-situ*.[41] This additional component acted as a swelling agent and assembled with its hydrophobic tail onto the hydrophobic polypropylene core of the surfactant micelle. Consequently, the diameter of the hydrophobic volume increased and resulted in greater pore diameters in the calcined mesostructured film. The principle is sketched in figure 5.17.

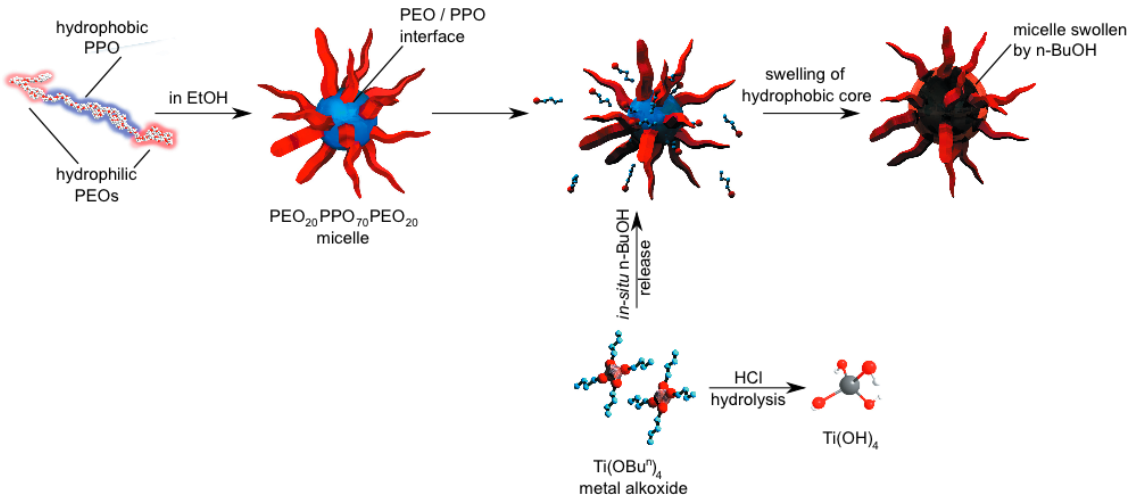

Figure 5.17: Schematic representation of the formation mechanism of the large-pore meso-nc-TiO2 films. I: original block copolymer micelle. II: micelle swelled by n-BuOH released in situ.

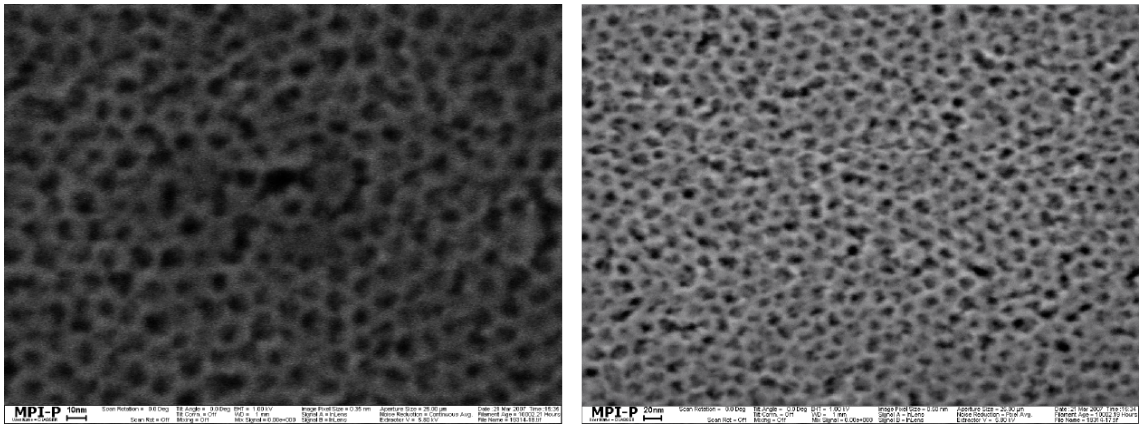

Figure 5.18: The left SEM image shows the pore sizes when TiPO is used as inorganic precursor ($\varnothing = 12 \pm 2nm$) (left). For comparison, the right SEM image of a mesoporous thin film depicts the increase in pore size ($\varnothing = 17 \pm 3nm$) due to in-situ released n-butanol and according swelling of the hydrophobic core of the micelles. Please pay attention to the scale bars at the bottom of the images. The scale bar in the left image shows 10nm, and 20nm in the right image.

The porosity was calculated by the Bruggeman EMT independently from both spectra (figure 5.19 and 5.20) to be 45.0% and 44.5% in air and water, respectively. By, comparing the SEM images and waveguide spectra of the original $TnEO/TiPO$ system and the $TnBO$ system micelles, an increase in pore diameter of ca. $5nm$ (ca. 40%) and accordingly an increase of the overall porosity (pore volume) from 32.0% to 45.0% was achieved by substitution of the Ti(IV) precursor. This effect was attributed to the ability of the *in-situ* release of *n*-butanol chains and according swelling of the hydrophobic core of the triblock copolymer micelles.

However, due to the increase in the fraction of hydrophobic components in the mixture, micelles had larger hydrophobic volumes, and therefore, lower surface curvature was created. The low curvature often resulted in undesired self-assembly to cylindrical hydrophobic domains of the triblock copolymer P123. Even though this architecture

	Thickness, d [nm]	Refractive Index, n [a.u.]	Extinction, κ [a.u.]
Prism/Substrate	∞	1.84498	0
Gold Film	48	0.312	3.823
meso-nc-Titania	2039	1.575	0.001
Superstrate	∞	1.333	0

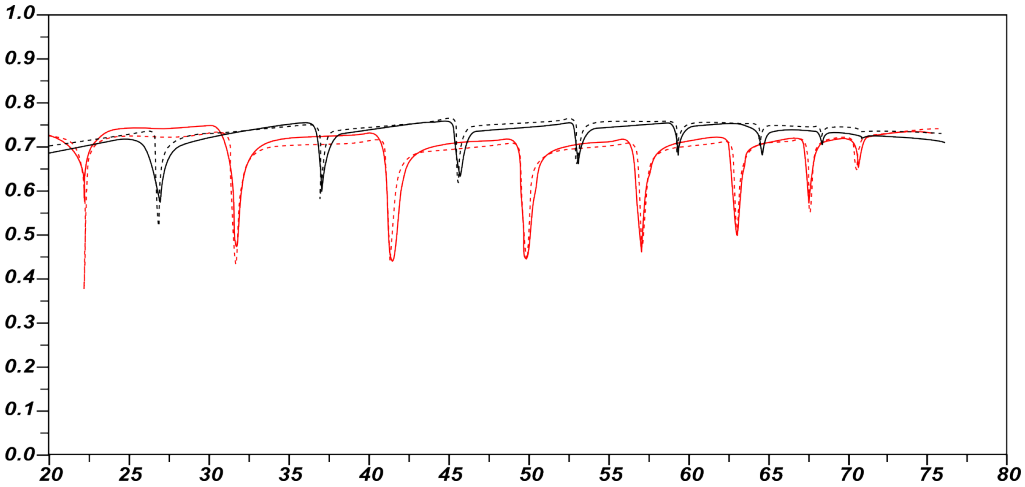

Figure 5.19: The OWS spectrum in air of mesoporous thin films of the imprint of swollen micelles and accordingly increased porosity pore structure at two different polarisations (red: TM, black: TE). Simulated Fresnel fits are shown as dotted curves for both polarisations in the corresponding colours. The simulation parameters for the fit are shown above.

	Thickness, d [nm]	Refractive Index, n [a.u.]	Extinction, κ [a.u.]
Prism/Substrate	∞	1.84498	0
Gold Film	48	0.312	3.823
meso-nc-Titania	2039	1.770	0.0006
Superstrate	∞	1.333	0

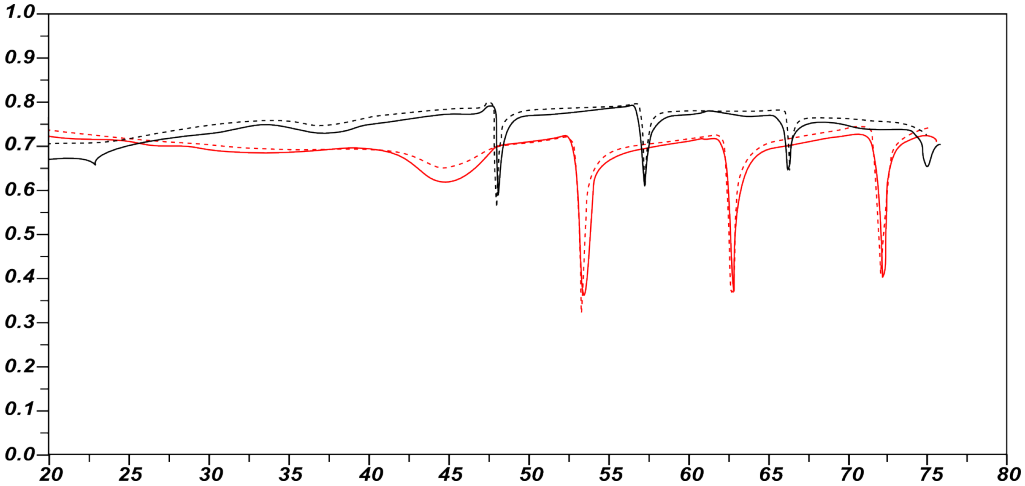

Figure 5.20: The OWS spectrum in water of mesoporous thin films of the imprint of swollen micelles and accordingly increased porosity pore structure at two different polarisations (red: TM, black: TE). Simulated Fresnel fits are shown as dotted curves for both polarisations in the corresponding colours. The simulation parameters for the fit are shown above.

also allows for mesoporous (titania) films with accessible open-pores, such films did not support an interconnected pore-network throughout the whole mesostructured material, but rather resulted in one-dimensional and isolated domains.

During calcination of films templated using cylindrical domains at temperatures $> 400°C$, the inorganic imprint of these rod-like micelles became unstable. Ultimately, the nanocrystalline titania network underwent structural breakdown and collapsed into a wormlike (vermicular) arrangement. Upright-standing, tube-like hexagonally mesostructured calcined films have not been observed within the framework of this thesis.

Experiments showed that the water and acid contents played an important role during self-assembly, yielding vermicular mesophases at low water concentrations (see figure 5.21, left column), but transforming to spherically packed mesostructure imprints at higher concentrations (see figure 5.21, middle and right column).

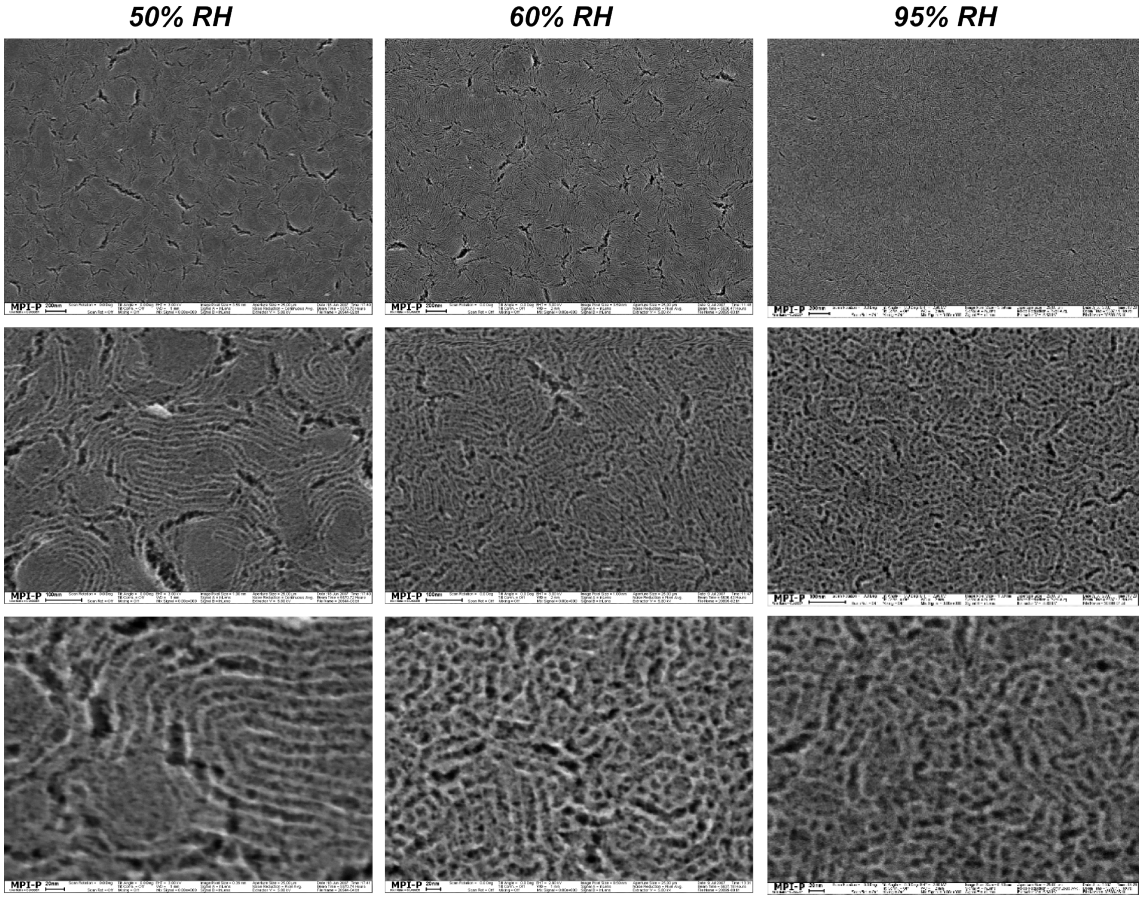

Figure 5.21: Vermicular structure observed at low water concentrations and 60% RH (left). high water concentrations and 60% RH (middle). high water concentrations and 95% RH (right). The scale bars of the SEM images in the top row shows 200nm, 100nm in the middle row, and 20nm in the bottom row.

In order to introduce high water content into the dip-coated film, the levels of external relative humidity (RH) were adjusted between 50% and 95%, respectively, during the $24h$ of ageing. As depicted in figure 5.21, depending on the presence and the amounts of available ambient water, the transformation to vermicular meso structures could be suppressed.

SEM images like the ones in figure 5.21 show the vermicular channels made by the hexagonally packed micelles. The fact that these hexagonal structures were not stable

upon removal of the surfactant implies that they may undergo a transformational phase change into lamellar or partially lamellar arrangements, which, again, collapse upon thermal treatment at temperatures $> 400°C$. These vermicular structured films can also be useful, but not for applications where highly connected networks of pores are needed.

OWS scans of the calcined vermicular meso-nc-titania film in air are shown below. In most cases, it was not possible to fit the Fresnel simulation to the measured data within the given parameter space. As one representative example the approximation with $n_{meso-nc-TiO_2} = 1.600$ is depicted in figure 5.23

	Thickness, d [nm]	Refractive Index, n [a.u.]	Extinction, κ [a.u.]
Prism/Substrate	∞	1.84498	0
Gold Film	48	0.312	3.823
meso-nc-Titania	1200	1.600	0
Superstrate	∞	1.000	0

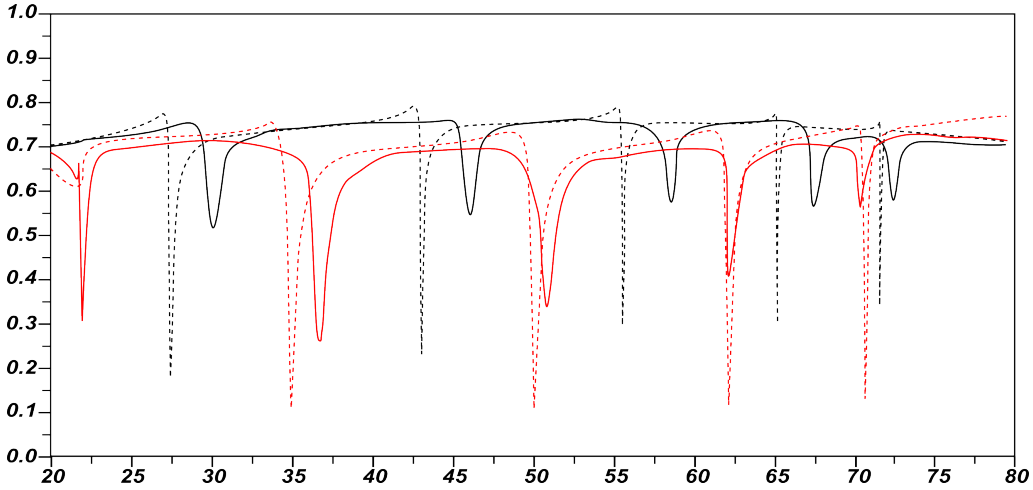

Figure 5.22: The OWS spectrum in air of mesoporous thin films of vermicular pore structure at two different polarisations (red: TM, black: TE). Fresnel simulation revealed inhomogeneous film density and were not able to fit the reflectivity scan with one homogeneous box profile. The simulations are shown as dotted curves for both polarisations in the corresponding colours. The initial simulation parameters are shown above.

Consequently, it was necessary to give up on the homogeneous-one-box-profile-layer simulation and increase the number of box-profile-layers with individual box-indices (still assuming homogeneity within each individual layer) until the simulation described the real vermicular meso-nc-titania film. It was sufficient to assume a four-layer system, as shown below in figure 5.23 and 5.24.

	Thickness, d [nm]	Refractive Index, n [a.u.]	Extinction, κ [a.u.]
Prism/Substrate	∞	1.84498	0
Gold Film	48	0.312	3.823
meso-nc-Titania	200	1.797	0.001
	50	1,402	0.003
	900	1,600	0.002
	60	1,510	0.004
Superstrate	∞	1.000	0

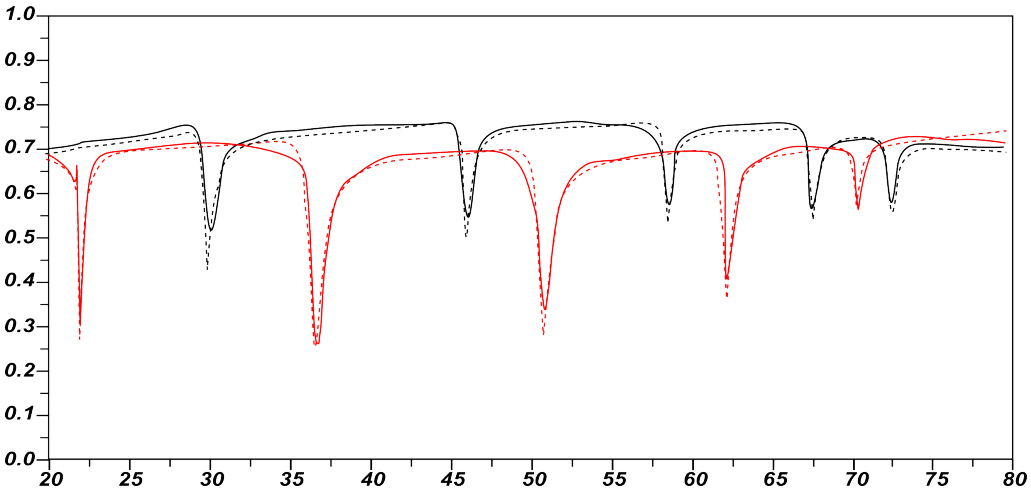

Figure 5.23: The OWS spectrum in air of mesoporous thin films of vermicular pore structure at two different polarisations (red: TM, black: TE). Fresnel simulation was extended to four sub-layers within the film in order to fit the inhomogeneous mesostructure density. The simulations are shown as dotted curves for both polarisations in the corresponding colours. The initial simulation parameters are shown above.

With the (arbitrarily) chosen four layer fragmentation of the meso-nc-titania film the Fresnel simulation of the multi-layer system was in good agreement with the measured data. Also the individual porosities of each of the four-layers, according to the Fresnel simulation, imply for both measurements (in air and in aqueous environment) only a very slight discrepancy of just 7% (less in the measurements with water as infiltrating medium), however, the deviation is monotonically represented in all four layers. This again legitimates the presumption that, even though the porosity is inhomogeneous (due to the collapse of the mesoscopic architecture), the pores are interconnected throughout the whole meso-nc-titania film and complete infiltration of the pores with water was carried out successfully.

This arbitrarily chosen fragmentation of the $meso-nc-TiO_2$ layer (in figure 5.23) allows to fit the experimentally obtained reflectivity curve but, however, does not necessarily describe the real RI profile of the structure. It might be possible to chose another number and/or combination of sub-layers with individual refractive indices to also fit the reflectivity curve. Therefore, this multi-box-profile can not be assumed as valid description until it does not describe also the reflectivity spectrum of the same $meso-nc-TiO_2$ film after a refractive index change, induced by the exchange of the cover medium (air to water) and

subsequent infiltration of the mesopores, still with the identical layer fragmentation (see figure 5.24).

	Thickness, d [nm]	Refractive Index, n [a.u.]	Extinction, κ [a.u.]
Prism/Substrate	∞	1.84498	0
Gold Film	48	0.312	3.823
meso-nc-Titania	200	1.985	0.001
	50	1,690	0.003
	900	1,848	0.002
	60	1,771	0.004
Superstrate	∞	1.333	0

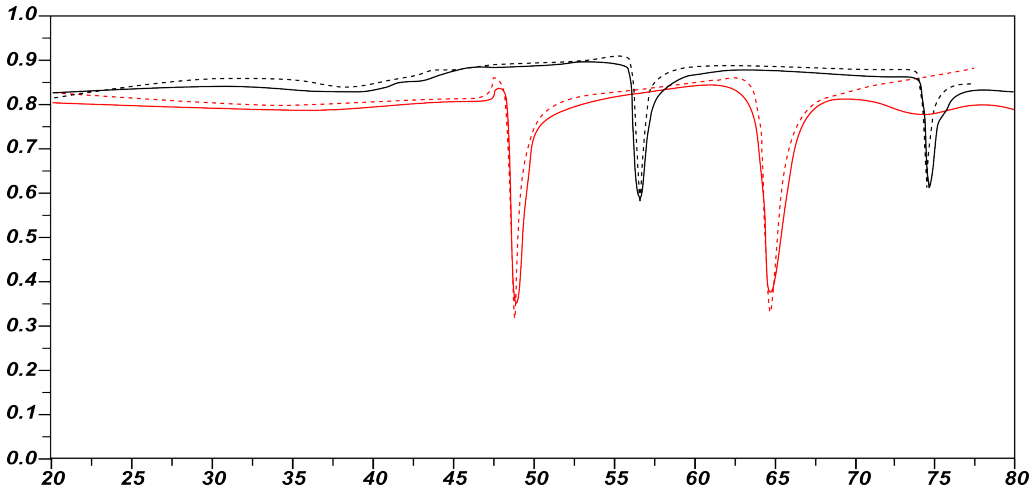

Figure 5.24: The OWS spectrum in water of the identical mesoporous thin film as shown above in figure 5.23 at two different polarisations (red: TM, black: TE). Simulated Fresnel fits are shown as dotted curves for both polarisations in the corresponding colours. The simulation parameters for the fit are shown above.

5.2.5.4 Solvent

The degree of self-assembly was also controlled by adjusting the solvent concentration and hence the conditions during the equilibration process (e.g. dilution, time, selective swelling/collapsing, temperature) of the mixture before films were dip coated. Of course, the amount of block copolymer had to be adjusted in order to meet the requirements to match each liquid crystal phase or rather the molar composition of the surfactant. Additional modification to the mesostructure was achieved by changing the alcoholic solvent, i.e. using n-butanol instead of ethanol for the solubilisation of the amphiphilic block copolymer, in order to obtain a more selective affinity to either the hydrophobic or the hydrophilic fractions. For this purpose *n*-butanol (also other long-chain alcohols) served very well without changing the parameter space greatly, however, they did reduce the critical micellar concentration (CMC) of the non-ionic surfactant in aqueous solution. The ternary phase diagram of the P123/n-BuOH/water system[34] (see figure 5.25) was used to predict phases in the hope of producing large-area, crack-free, optically transparent

mesoporous nc-titania films[19,18]. The starting ratios of the individual components were identical to those described in section **5.2.4** with the same aim of obtaining densely packed spherical micelles as the templating architecture.

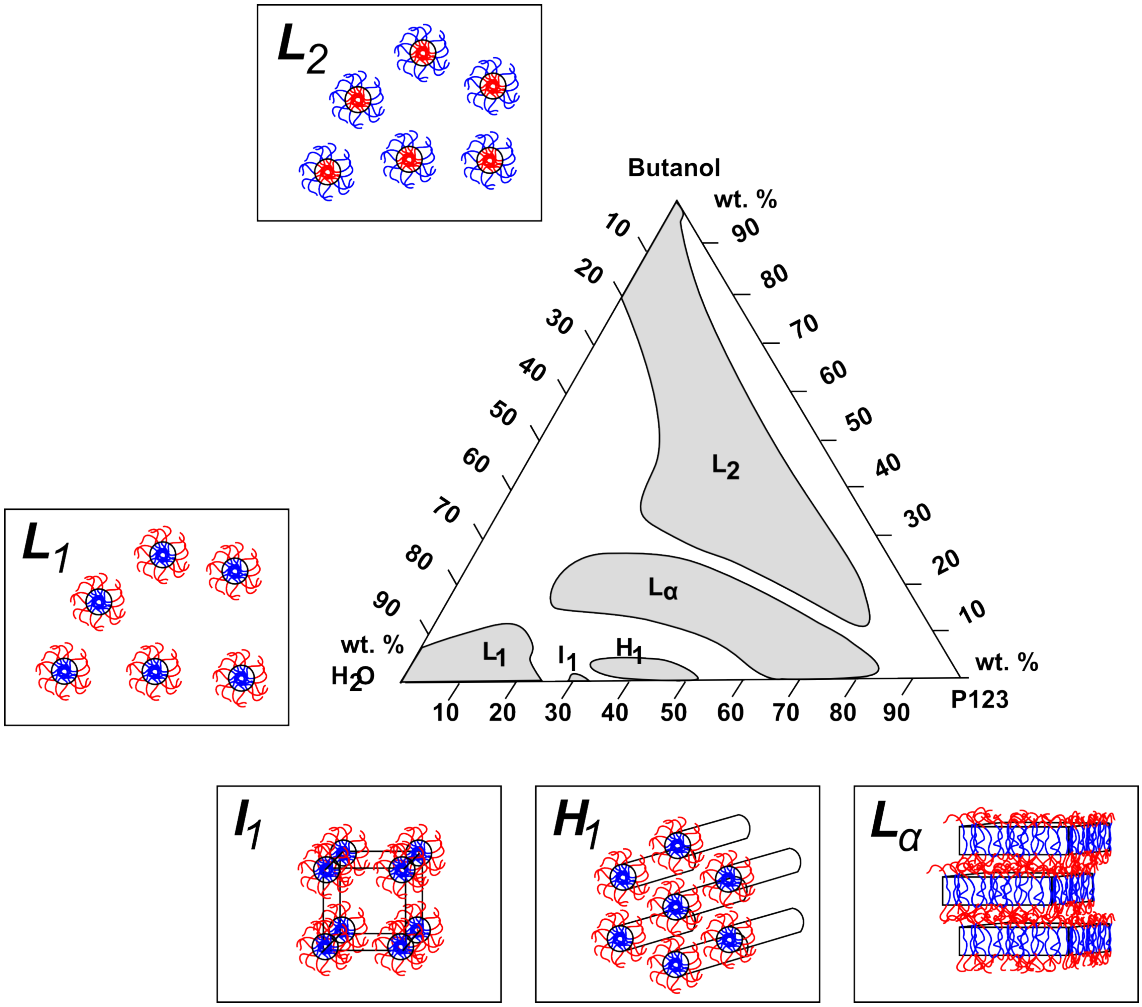

Figure 5.25: Ternary phase diagram of the P123/n-BuOH/water system.

The films obtained using the P123/butanol/water system (see figure 5.26) were highly porous and the mesostructure was interconnected throughout, giving films with desirable properties for sorption studies, but also for applications as optical waveguides. For optical applications as a waveguide, the mesostructure introduced (optical) density fluctuations which were (1) far below $\lambda_{HeNe} = 632.8nm$ and (2) homogeneous throughout the whole film due to the absence of extended long-range order. Also, since the pores were highly interconnected, this type of mesoporous material allowed for quick infiltration of the voids. Such mesostructured titania films were obtained after calcination at temperatures $> 400°C$. The thermal treatment allowed the inorganic entities (i.e. titania nano cluster) to partially crystallise into the anatase phase, making a semiconducting, optically and electrically active, mesoporous thin-film material. The formation of these comb-like mesostructures required the micelles of the highest curvature (spheres, rather than sheets

or rods), therefore, the solution ageing times had to be kept below 10 minutes. The short stirring time kept the degree of polymerisation of the titania precursors low, allowing them to associate with the highly curved hydrophobic volume of the spherical micelles.

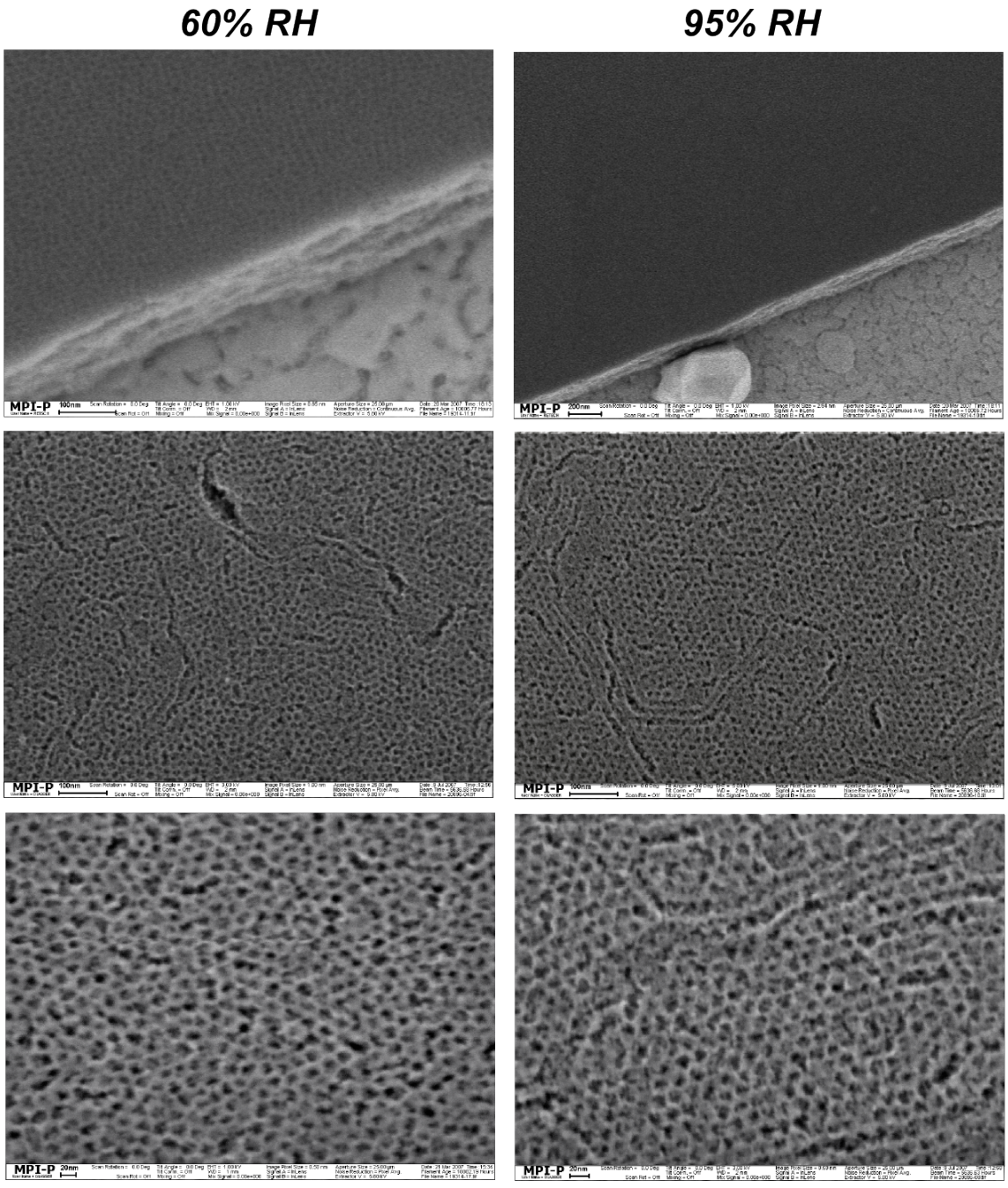

Figure 5.26: SEM images of the surface of mesostructured porous films after sintering and template polymer removal. The increased level of ambient humidity resulted in slightly more ordered structuring of the porous network. The scale bars of the SEM images in the top row shows 200nm, 100nm in the middle row, and 20nm in the bottom row.

Not only the solution equilibration times, but also the ambient conditions during film ageing had a profound effect on the mesostructure finally formed. The films were stored under ambient conditions ($20 - 25°C$, $1atm$) for several hours in order to allow micelles to assemble into 3D-hexagonal, rather than disordered spherical micellar structure. The phase diagram in figure 5.6 shows that phase transition from hexagonal to disordered

occurs at temperatures below $20°C$, at this particular polymer concentration.

No further effort was undertaken to achieve solely, cubic or hexagonal packing (referring to figure 5.6), therefore, the dip-coating process was always operated at $20°C$. However, in order to introduce high water content into the dip-coated film, levels of external relative humidity (RH) were adjusted to 50% and 95%, respectively, during the $24h$ of ageing. The films prepared at high humidity levels were more defined in their structural arrangement, forming slightly higher degrees of order and very homogeneous thicknesses with smooth surfaces.

	Thickness, d [nm]	Refractive Index, n [a.u.]	Extinction, κ [a.u.]
Prism/Substrate	∞	1.84498	0
Gold Film	48	0.312	3.823
meso-nc-Titania	1829	1.548	0.0012
Superstrate	∞	1.000	0

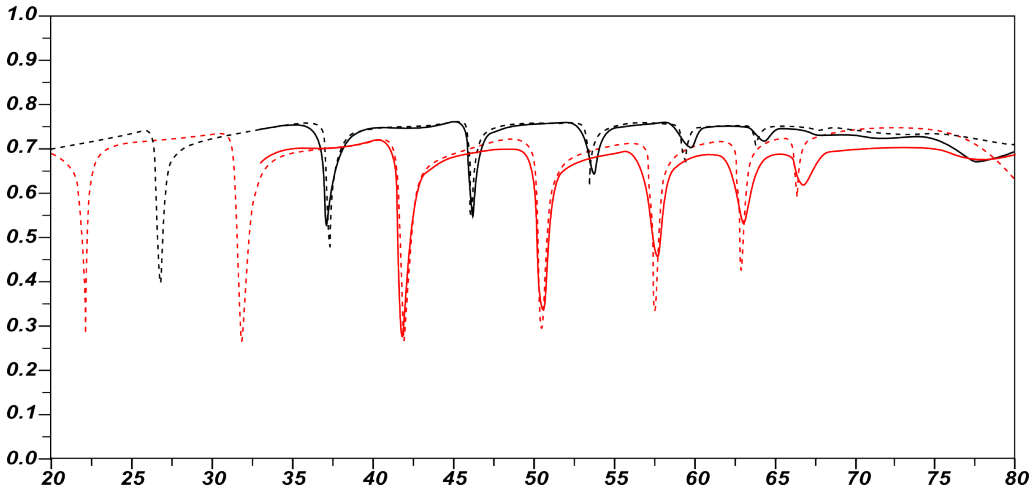

Figure 5.27: The OWS spectrum in air of dip-coated mesoporous thin films from templated titania precursor at two different polarisations (red: TM, black: TE). Fresnel fits were simulated are shown as dotted curves for both polarisations in the corresponding colours. The simulation parameters for the fit are shown above.

These final modifications to the solvents used in the self-assembly process of surfactant templated meso-nc-titania, resulted in the highest porosities achieved with this synthetic approach, as EMT calculations from OWS scans and respective Fresnel simulation fits of the scans yielded values as high as 47% of pore volume.

	Thickness, d [nm]	Refractive Index, n [a.u.]	Extinction, κ [a.u.]
Prism/Substrate	∞	1.84498	0
Gold Film	48	0.312	3.823
meso-nc-Titania	1829	1.751	0.001
Superstrate	∞	1.333	0

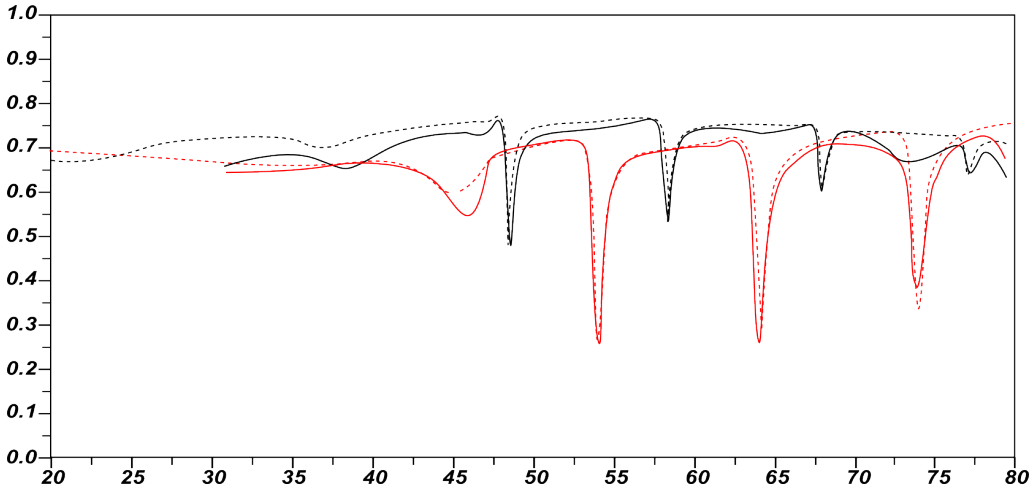

Figure 5.28: The OWS spectrum in water of dip-coated mesoporous thin films from templated titania precursor at two different polarisations (red: TM, black: TE). Fresnel fits were simulated are shown as dotted curves for both polarisations in the corresponding colours. The simulation parameters for the fit are shown above.

Also the calculated pore volumes for both (the scan in air and in water) were in good accordance to each other. Only a slight deviation between the experiment and the fit of as little as 0.5% was noticed. This fact gives rise to the statement that these highly interconnected pores formed a homogeneous network throughout the whole meso-nc-titania film and would allow for rapid and complete exchange of the void-filling medium. Furthermore, no significant anisotropy within the structure was observed (with $\lambda_{HeNe} = 632.8nm$) which substantiated the assumption of the films being homogeneous throughout the whole thickness.

5.3 Nanopores Formed by Anodisation

In the present section, the utilisation of a 'top-down' technique is introduced in order to obtain another type of titania mesostructure: self-organised titania nanotube arrays. The formation of these, perpendicular to the metal surface aligned, nanometre sized titania tubes was achieved *via* an electrochemical anodisation technique, which was combined with wet chemical processes.

Although, a great variety of nano- and mesostructured titania architectures have been successfully produced by classical approaches such as template based, and sol–gel methods, for example nano-wires, nano-rods and nanotubes[8,17], recent findings of the

self-ordering growth by anodic oxidation[63,26,10] have attracted rapidly growing interest in this field of research (see e.g.[43]). Since Zwilling and co-workers just one decade ago, in 1999, first grew self-ordered titania nanostructures[63] by anodising Titanium in a fluoride containing electrolyte (the obtained structures turned out to appear in a tubular shape), these tube-like titania structures were greatly optimised in their desired properties, i.e. length and shape[10,42,1].

In general, anodising is a process, applied to produce an oxide film or coating on certain metals – aluminium, niobium, tantalum, titanium, tungsten, zirconium – and alloys by electrolysis. Therefore, the metallic surface to be treated acts as the anode in an electrolytic cell and is therefore electrochemically oxidised. This electric field assisted oxidation step is fairly complex in its nature, since dissolution processes take place at the same time and the changing topology alters the complex field geometries. Nevertheless, once the parameter space is fixed it is an easily reproducible method. Highly sophisticated protocols are available for the anodisation of Titanium, and exactly describing the process conditions which help to control and promote the growth of an oxide layer.

Originally, anodisation has been carried out widely with the aim to improve certain surface properties, such as corrosion resistance, abrasion resistance, appearance, etc. Furthermore, since the oxide surface film is (highly) porous, it has been utilised for colouring of metals by the incorporation of pigments or dies into the pores of the oxide surface layer. In fact, nowadays it became this porous coating that is most often thought of as the actual product of anodising.

Within the framework of this thesis, the growth of (high aspect ratio) titania (i.e. Titanium(IV) oxide, TiO_2) nanotubes has been achieved by electrochemical anodisation in suitable (acidic) electrolytes (e.g. fluoride containing solutions). Mesoporous anodic titania assemblies are characterised by cylindrical pores of a high aspect ratio which run straight through the film thickness, whereas having a narrow size distribution of pore diameters. Under optimal processing conditions, the growth of this porous oxide is completely self-organised, however, leading into a variety of different structures. The specific properties of mesostructured titania, such as catalysis (self-cleaning), sensing, changes of wettability under UV illumination or solar energy conversion caused great interest for these materials within the last few years.

Essential, in order to obtain such oxide structures and to achieve highly defined tubes by simple anodisation is a controlled treatment of Titanium in fluoride containing solutions. Generally, the morphology of porous titania, and in particular of the tubular layers is affected strongly by the electrochemical anodisation conditions of the anode metal (i.e.

applied potential, electrolyte species, temperature, potential ramping speed, electrolyte pH, electrolyte viscosity, etc.). Accordingly, various different titanium oxide structures can be obtained, for example flat compact oxide films, randomly disordered porous layers, highly self-organised porous films, and of course the desirable highly self-organised nano-tubular layer (figure 5.29 schematically depicts the classification).

In published literature highly ordered and self-organised assemblies of titania nanotubes with lengths of several hundred nanometres have been reported. Most approaches grown the titania nanotubes on either thin titanium foils ($< 1mm$) or on sputtered Titanium thin-films ($\sim 0.1mm$). Depending on applied anodisation parameters, titania nanotubes with pore diameters ranging between $20nm$ and $200nm$, and typical wall thicknesses of $10nm$ to $25nm$ were achieved.

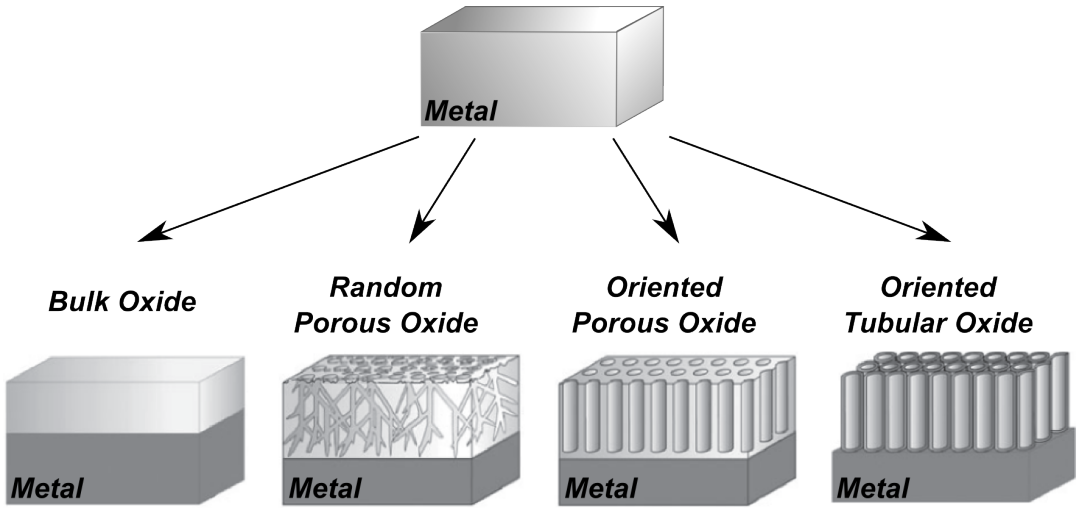

Figure 5.29: Morphologies which can be obtained by electrochemical anodisation of metallic titanium: a compact oxide film, a disordered random nanoporous layer, a self-ordered nanoporous or a self-ordered nanotube layer. (Reprinted from[24]).

As illustrated in figure 5.29, four different oxide morphologies may be obtained by anodising one identical starting material (see figure5.29b)). In general, the anodisation of most metals in most electrolytes results in a bulk oxide layer, referred to as barrier layer. Such dense oxide layers are formed *via* a so-called high field mechanism, which basically summarises a number of simultaneously occurring electrochemical processes (depicted in figure5.29a)) at the anode (i.e. Titanium surface facing the electrolyte solution) under sufficiently high voltage: (1) Metallic Titanium (Ti^0) is oxidised to its Ti^{4+} cation at the metal–oxide interface. While these Ti^{4+} ions migrate outwards (forced by the applied field), (2) Oxygen anions (O^{2-} ions) are dragged (under the applied field) towards the oxide surface, incorporated into the oxide layer, and forced to migrate towards the metal/oxide interface. Depending on the rate of this transfer within the oxide lattice with respect to O^{2-} *vs.* Ti^{4+} cation, the oxide film begins to form either at the outer oxide surface or at the inner metal/oxide

interface. Since the whole process is forced by a voltage, which is constantly applied, and the oxide layer is permanently increasing, the field strength within the oxide is successively reduced, and therefore the growth continuously slowed-down and finally self-limiting. As a result a flat layer of bulk titania oxide is produced with a final thickness proportional to the applied voltage.

Specific modification of this high-field process, however, can lead to different porous surface oxide morphologies. In particular, electrolyte and voltage conditions have to be optimally adjusted in order to selectively yield either random porous networks, organised pore assemblies, or aligned and ordered nano-tubular structures.

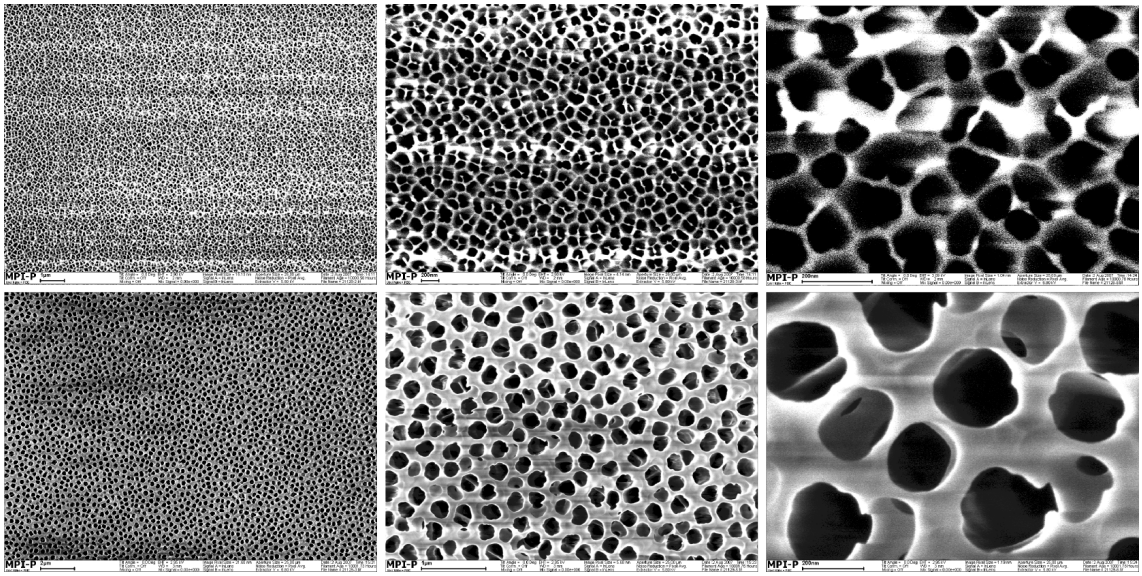

Figure 5.30: SEM images showing the oriented porous titania architecture as one accessible porous morphologies that can be produced by anodisation.

Deriving the oxide formation process[49,52,53,1,46] from the original protocol for anodisation of Aluminium (Al), where acidic electrolytes led to the formation of a porous oxide layer[38], whereas more neutral to alkaline conditions allowed a compact layer to grown, these known conditions were used as first approximation for the application on Titanium as anode material, in order to further optimise the system to achieve an almost ideal degree of self-organisation[45].

With regard to the origin of anodisation-induced self-ordering of pores in alumina, Parkhutik and Shershulskii[50] already considered the steps schematically represented in Fig. 5.32 in their pioneering work in the early nineties. They described the process of electrochemical oxidation as follows: At the beginning of electrochemical oxidation, the surface of aluminium is covered entirely with a compact, uniform anodic oxide (Fig. 5.32 a). The distribution of the electrical field in the oxide, however, is strongly correlated with the surface morphological fluctuations (more pronounced fluctuations lead to more local

focused electrical field, as shown in Fig. 5.32 b). As a result, field-enhanced dissolution in the anodic oxide takes place and the pores start to form (Fig. 5.32 c). Successively, the pore growth process reaches a steady-state and uniformly distributed pores are obtained (Fig. 5.32 d). Related to this sequence a current–time behaviour is obtained as in Fig. 5.32 e). The metal oxidation at the bottom of the pores takes place uniformly and simultaneously, and the material can only expand vertically, i.e. the existing pore walls are pushed upwards (Fig. 5.32 f). However, it is clear that for aluminium a pre-requisite for pore formation is a sufficiently acidic electrolyte (Fig. 5.32 g) or an electrolyte containing Al^{3+}-complexing ions to solvatise a certain amount of cations[54].

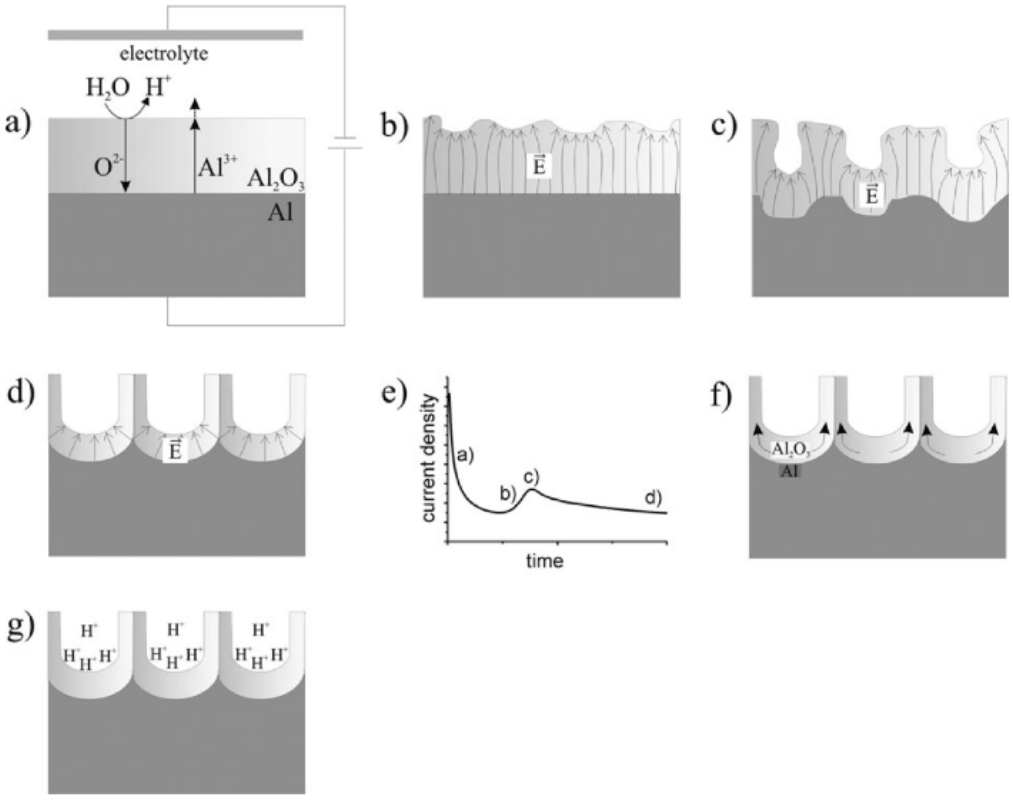

Figure 5.31: Schematic representation of alumina pore formation by electrochemical anodisation: (a) formation of the anodic oxide on aluminium; (b) local field distribution correlated to the surface morphological fluctuations; (c) initiation of the pore growth due to the field-enhanced dissolution; (d) pore growth in steady-state conditions; (e) represents the current transient recorded during anodisation of Al; (f) and (g) show the influence of the volume expansion and the local acidity on the alumina pore growth, respectively. (Reprinted from[24]).

Although, the above described processes describe the anodic oxide growth on metallic Aluminium, it was found that the same scheme, as depicted in figure 5.32a), suites the description of anodisation steps on other metals (such as Ti) as well.

As mentioned before, oxide growth is controlled by field-aided ion transport (O^{2-} and Ti^{4+} ions) through the growing oxide. Furthermore, the arriving cations need to be solvatised. For titanium, in contrast to aluminium, a low pH is not sufficient to create porous oxide layers (a low pH is normally not sufficient to solvatise Ti^{4+}, see section

5.2.2 for further details) and under almost all anodisation conditions compact oxide layers were obtained. An exceptional case is given in the presence of fluoride ions where the situation become different. The determining feature of fluoride ions is their ability to form water-soluble hexafluoro-titanium(IV) (TiF_6^{2-}) complexes. These complexes aid the prevention of Titanium-oxide layer formation at the tube bottom, and this also leads to mild but persistent chemical dissolution of formed TiO_2. Moreover, due to the small ionic radius inherent to fluorides, they are able to infiltrate the growing TiO_2 lattice and to be transported by the applied electric field through the oxide (competing with O^{2-} transport) to the metal–oxide interface[1]. All these three factors seem to be essential for tube formation. These processes are schematically represented in figure 5.32.

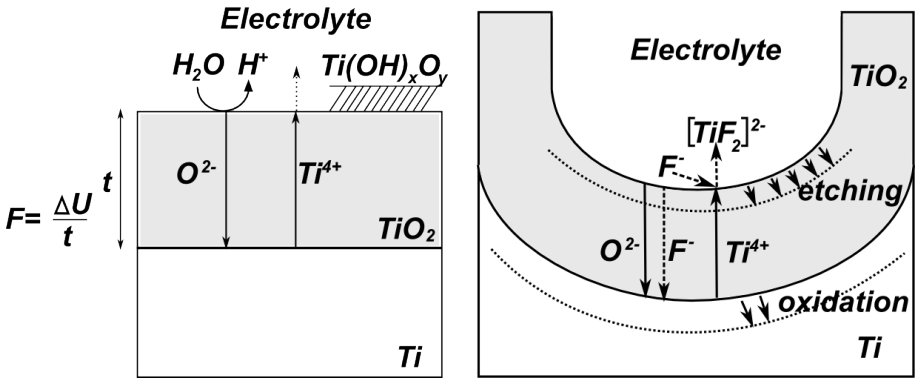

Figure 5.32: Schematic representation of the Ti anodisation (left) in absence of fluorides (results in flat layers), and (right) in presence of fluorides (results in the tube growth).

5.3.1 Experimental

The herein presented work was carried out in the course of a close cooperation with the group of Prof. Dr. P. Schmuki at Institute for Surface Science and Corrosion (LKO) (Friedrich-Alexander University in Erlangen, Germany) and accordingly the protocols for anodic oxidation of Titanium were only modified in order to suite the formation of mesoporous titania for optical thin film applications.

The Titanium samples (0.1-mm thick foils, 99.6% purity, *Goodfellow*) were degreased by sonicating in acetone, isopropanol, and methanol, then rinsed with deionised water and dried in a nitrogen stream. Thereafter, the foils were polished according to the procedure described in the experimental chapter.

In later stage of the project the experimental approach for the anodisation processes were therefore optimised in order to allow for the growth of nanotube arrays from thin Ti films[44,11] (for example evaporated or sputtered layers) on a (gold coated) glass substrate. The preparation of porous oxide films from thin Ti layers required that the initiation phase, where a disordered oxide is formed, was shortened, and accordingly, the chemical

dissolution rate to be minimised. Successful approaches were based on lowering the electrolyte temperature or by using optimised electrolytes[11].The actual electrochemical treatment of the metallic substrates and the composition of the electrolyte bath is described in the experimental chapter.

5.3.2 Results and Discussion

In spite of the successful and reproducible production of titania nanotube arrays with thicknesses ranging between $1.5\mu m$ and $2.5\mu m$, and aspect ratios of 25 to 50, it was not adequately possible to fit the Fresnel simulation to the experimental data. In figure 5.34 a representative example is depicted.

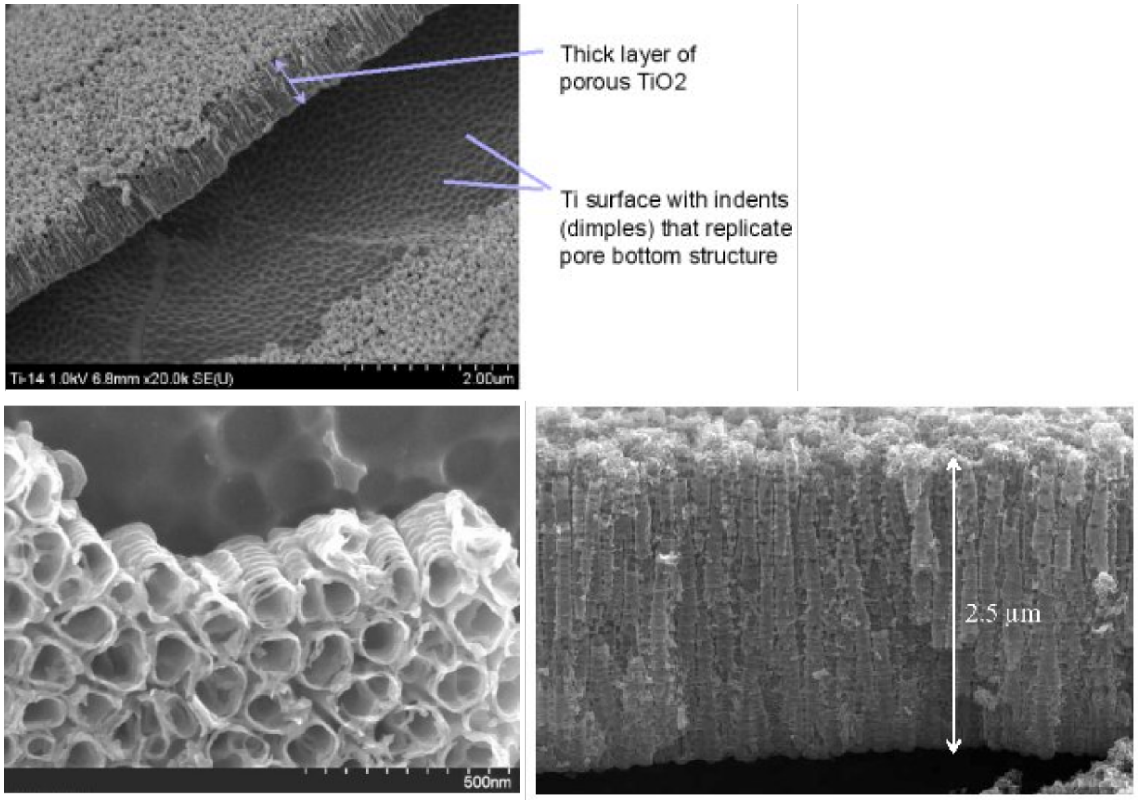

Figure 5.33: Electron microscopy images of titania nanotube array films with rough tube wall structure. ∪ Images provided by collaborators.

The main reason for the poor waveguide properties of the titania nanotube arrays was attributed to the surface roughness of these films and also to large amounts of scattered light caused by the periodic thickness irregularities of the crystalline side-walls of the individual tubes (compare figure 5.33).

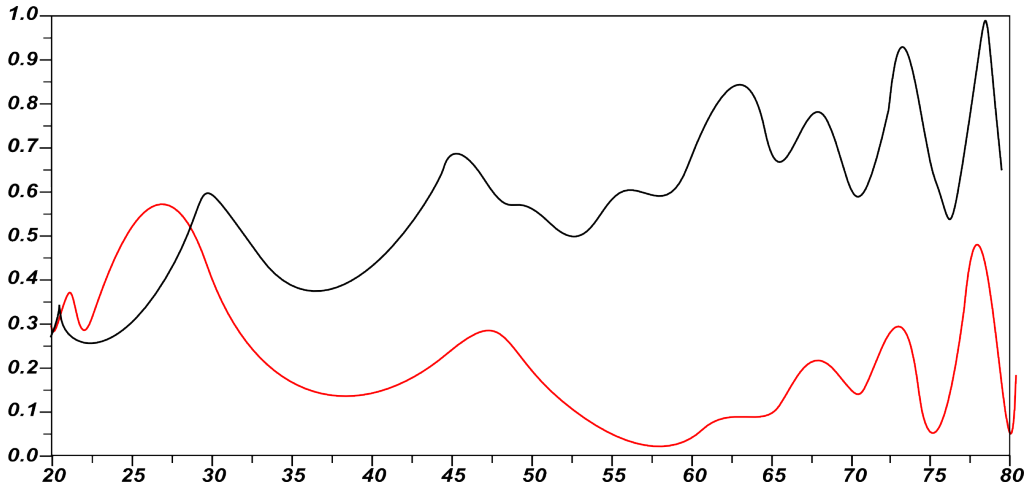

Figure 5.34: The OWS spectrum in air of thin films of nanotube arrays ƒ at two different polarisations (red: TM, black: TE). Fresnel simulations were not possible to fit the reflectivity scan, and are therefore not shown.

However, also the relatively large pore (tube) diameters of approximately $100nm$, with regards to the applied laser wavelength for OWS application were a point of concern. Accordingly, in the next step of the project, the aim was put onto the improvement of these characteristics. Therefore, new approaches were undertaken for the anodic formation of titania nanotube arrays, and our collaborators at the LKO made use of new findings regarding the influence if electrolyte composition and mainly its viscosity on the morphology of formed tubules[44]. The adjustment of the electrolyte viscosity, i.e. the application of highly viscous glycerol instead of water as electrolyte medium resulted in very smooth tubular structures, and also smaller pore diameter of approximately $50nm$ (refer to figure 5.35).

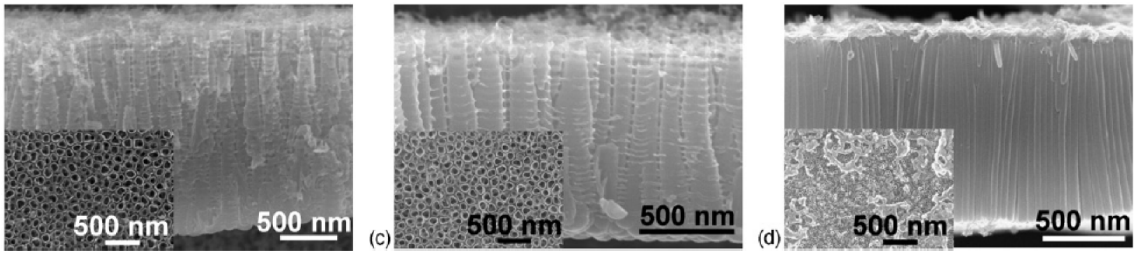

Figure 5.35: Side views of the titania nanotube arrays produced by anodisation depicting the optimised tube wall structures. Images provided by collaborators.

In addition, it was observed that variations in the operating temperature of the electrolyte bath showed profound impact on the tubular wall morphology. This was explained by the direct relation of operating temperature to the electrolyte viscosity, and accordingly the suppression of current oscillations during anodisation[42]. The OWS spectra taken of these improved titania nanotube arrays are presented in figure 5.36 and figure 5.37.

	Thickness, d [nm]	Refractive Index, n [a.u.]	Extinction, κ [a.u.]
Prism/Substrate	∞	1.84498	0
Gold Film	48	0.312	3.823
meso-nc-Titania (TE)	814	1.695	0.013
meso-nc-Titania (TM)	814	1.587	0.010
Superstrate	∞	1.000	0

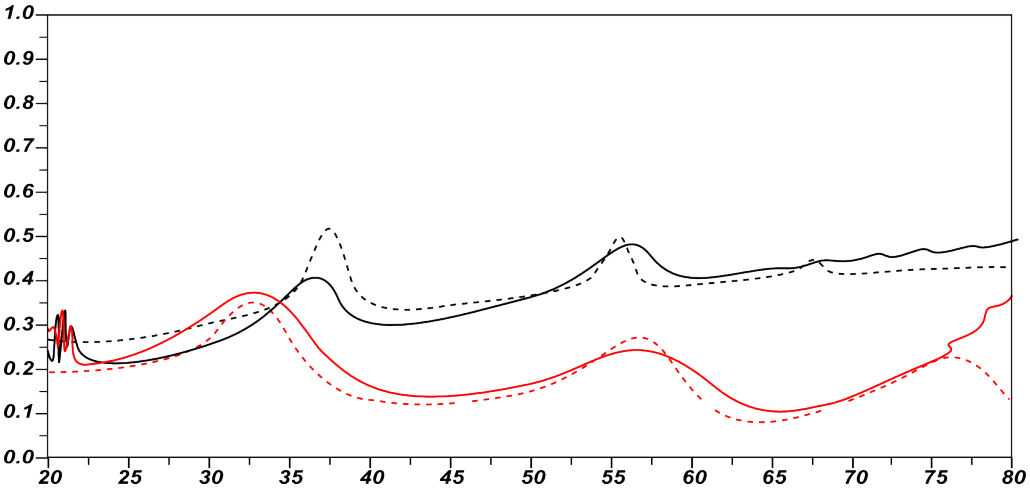

Figure 5.36: The OWS spectrum in air of thin films of nanotube arrays f at two different polarisations (red: TM, black: TE). Fresnel fits were simulated are shown as dotted curves for both polarisations in the corresponding colours. The simulation parameters for the fit are shown above.

The recorded angular reflectivity scans were improved (compared to the scans of the first generation of titania nanotube arrays, representative shown in figure 5.34), but still the Fresnel simulation could only be inadequately applied to fit the experimental data.

	Thickness, d [nm]	Refractive Index, n [a.u.]	Extinction, κ [a.u.]
Prism/Substrate	∞	1.84498	0
Gold Film	48	0.312	3.823
meso-nc-Titania (TM)	814	1.800	0.010
meso-nc-Titania (TE)	814	1.747	0.010
Superstrate	∞	1.333	0

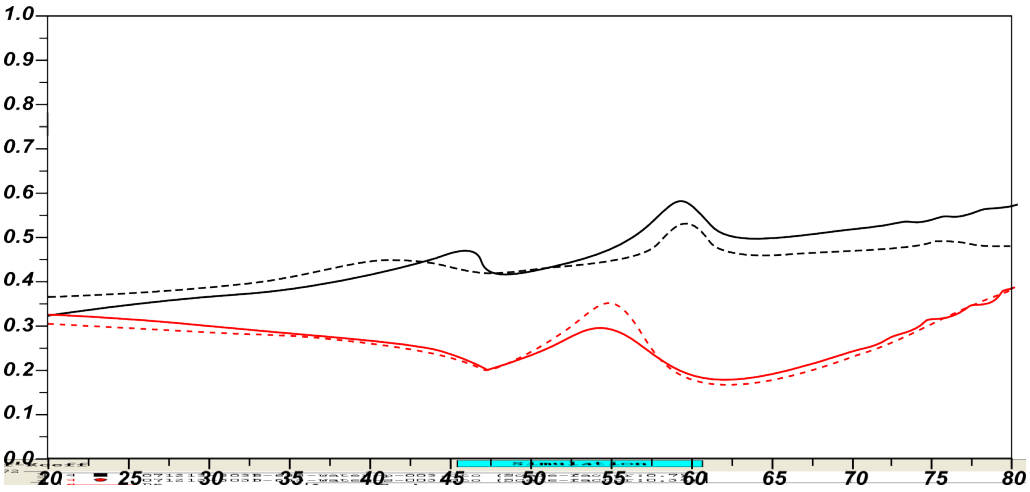

Figure 5.37: The OWS spectrum in water of thin films of nanotube arrays f at two different polarisations (red: TM, black: TE). Fresnel fits were simulated are shown as dotted curves for both polarisations in the corresponding colours. The simulation parameters for the fit are shown above.

Also the infiltration of the voids with water, whereby the refractive index contrast of pore space to matrix material was reduced, compared to the measurement in air, respectively, the theoretical description of the experiment remained to a high degree uncertain.

5.4 Mesoporous Films from Sintered Nanoparticles

5.4.1 Introduction

As an alternative to the fairly complex techniques of titania precursor-based block copolymer templating in order to obtain the mesoporous structure or the anodisation of metallic titanium, feasible 3D-mesoporous films were also achieved by sintering nanoparticles (i.e. nanocolloids) together.

The resulting films offered accessible interconnected pores throughout the whole film thickness, however, with the benefit of a simple one-pot synthesis protocol. More accurately, the nanocolloids were synthesised *via* sol-gel method, though films were also prepared directly from commercially available colloidal sols of titania nanoparticles (*Solaronix*, T/HT Colloids) and dry titania powder (BASF, P25). The preparation techniques are covered in section 5.4.2. In this section results and discussion based on SEM images as well as optical waveguide spectra of the produced thin-film materials will be presented.

The principle underlying this method for mesoporous thin film production is fairly straightforward and proved to be very reproducible. Basically, the titania nanocolloids were mixed with a sacrificial polymer, coated onto the glass-substrates and finally sintered in order to decompose the organic component and accordingly to leave a mesoporous and rigid titania architecture. A schematic illustration of the preparation steps is given in figure 5.38.

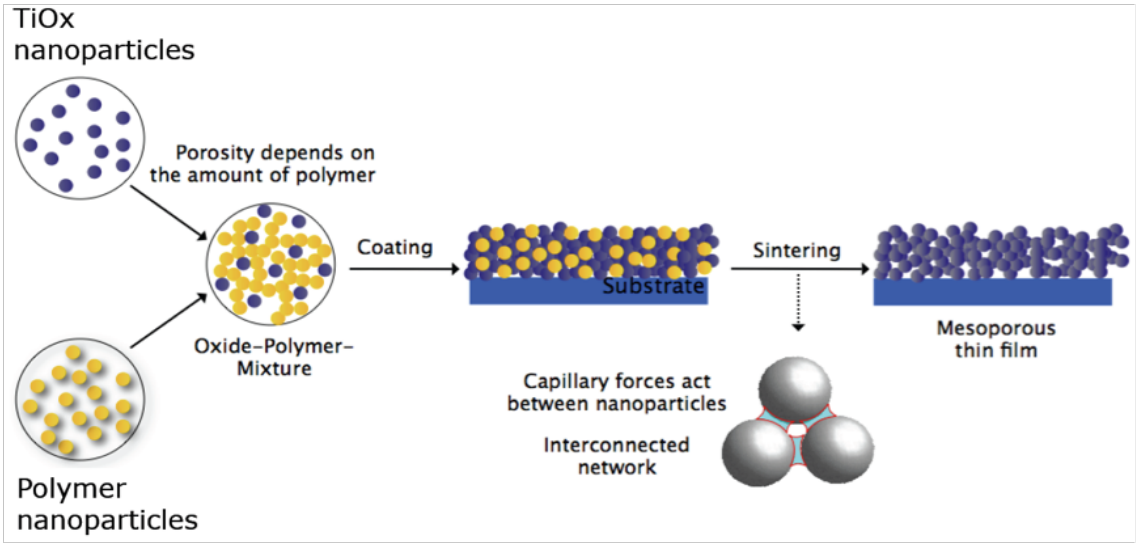

Figure 5.38: Schematic illustration of the reparation steps for the mesoporous thin-films from titania nanoparticle mixed with Carbowax M polymer entities.

The various nanoparticle of titania, which were applied in this approach were restricted in size to not exceed $25nm$ nanometre ($\ll \frac{\lambda_{HeNe}}{10}$), in order to assure good optical properties and only little scattering losses due to the refractive index fluctuations within the film architecture.

The synthesis of titania nanocrystals was achieved by means of elaborated wet chemistry, i.e. sol-gel chemistry. Hydrolysis and poly-condensation of titanium(IV) alkoxide of the general form of $Ti(OR)_4$ was performed in aqueous solution at acidic reaction conditions. The solution at low pH provided stabilisation of the ionic titania oxo-clusters formed in this medium (for further details see sections 5.2.1 and 5.2.2). The obtained oxo-cluster were organised in such manner to favour self-assembly into intermediate amorphous titania nanocrystals, which, in turn, self-assemble into anatase super-lattices, when undergoing autoclaving with the here presented reaction conditions. This process has been subject to a great deal of attention. Great theoretical work, particularly interesting to this work has been provided[31], which allowed to understand and predict inorganic polymerisation in the case of transition metal oxides and, in this particular work, in the case of titania. This fundamental developments have been exploited for the processing of anatase titania nanocrystals of homogeneous size and shape by adjusting the relative concentrations of titanium(IV) alkoxide and acid, the reaction temperature, and the pressure. The resulting nanocrystalline colloidal titania particles had a narrow size distribution, were non-aggregated and conform to a single anatase phase, according to published TEM and XRD analysis[16].

5.4.2 Experimental

The titanium dioxide colloidal sol was prepared by adding a mixture of $1mL$ of 2-propanol (*Aldrich*, anhydrous 99.8+%) and $3.7mL$ of titanium-(IV)-isopropoxide (*Aldrich*, 99.9%) drop wise over $30min$ to $8mL$ of glacial acetic acid (*DH*, 100%) and $25mL$ of de-ionised water in a conical flask at $0°C$. The solution was allowed to return to room temperature and was stirred for 8 hours at $80°C$. The so obtained gel-like sol was then transferred to a PTFE-lined titanium autoclave (*Parr General Purpose Acid Digestion Bomb*, Model No. 4744) and heated at $230°C$ for 12 hours. When cool the sol was removed from the autoclave, sonicate for 15 minutes in a sonic bath (*KERRY*, 250 W ultrasonicator). The solution was than concentrated to $150g/L$ on a rotary evaporator (*BUCHI*, R-114). Finally, $0.4g$ of Carbowax (*Riedel-de-Haen*, Carbowax 2000) was added and the mixture was allowed to stir for at least 12 hours before use.

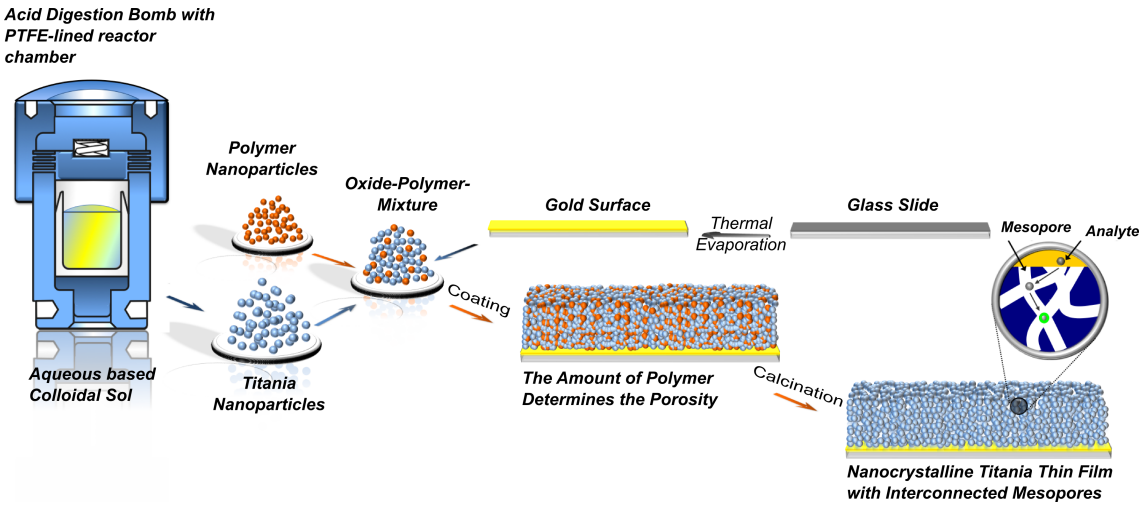

Figure 5.39: Schematic illustration of the production process in order to obtain mesoporous thin films of sintered titania nanocolloids.

A glass rod was used for spreading out the colloidal sol of nanocrystalline TiO_2 evenly across the hydrophilic functionalist gold surface, making a clean and transparent film, as illustrated in figure5.40. The film thickness was mainly determined by the viscosity of the paste itself and by the height of the tape (*Scotch*, Magic Tape) that was used to fix the substrates. This particular tape was chosen because it can be easily removed from the glass without leaving traces of adhesive materials, but in general every other tape might be app lid. In order to achieve film thickness of $1.5\text{–}2\mu m$, one layer of tape was required, although this depended on the paste concentration used. A slow dry-out of the solvent and a progressive heating was necessary to ensure optimal adhesion of the titanium dioxide layer onto the gold film.

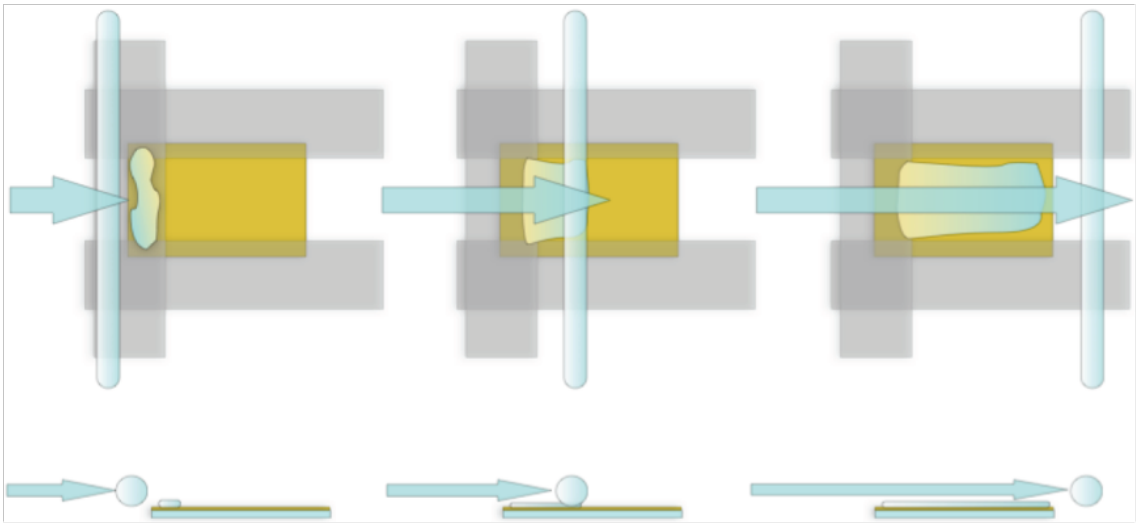

Figure 5.40: Illustration of the doctor blading (application) technique for spreading the nano-colloidal sol homogeneously on the substrates via an ordinary glass.

After complete evaporation of the solvent the titanium dioxide nanocolloids and Carbowax M mixture formed a smooth film which was than heated for 30 min at $450°C$. This

treatment allowed the titanium dioxide nanocrystals to sinter partially together, in order to ensure electrical contact and mechanical adhesion on the glass. While heating up (e.g. rate: $100°C/min$) the films, first turned brownish (sometimes fumes are release), and later they turned yellowish-white due to the temperature dependent band-gap narrowing in the pure titanium dioxide (anatase phase). This was the sign that the sintering process was completed. The cooling rate was chosen to avoid cracking of the glass (cool down from $450°C$ to $60 - 80°C$ in 3 minutes).

Alternatively, dip coating was also applied for film formation on gold-coated glass slides at constant dipping rates of $1\frac{mm}{s}$.

5.4.3 Results and discussion

The simplest method to produce mesoporous thin films by sintering titania nanoparticles together in order to form a randomly porous inorganic network was approached by three different protocols. The first one applied was based on commercially available P25 nanoparticles (Ø=25nm) dispersed in ethanol and mixed with a sacrificial polymer (Carbowax) as placeholder for the voids. One drop of the sol was equally spread on a gold coated glass substrate and accordingly characterised.

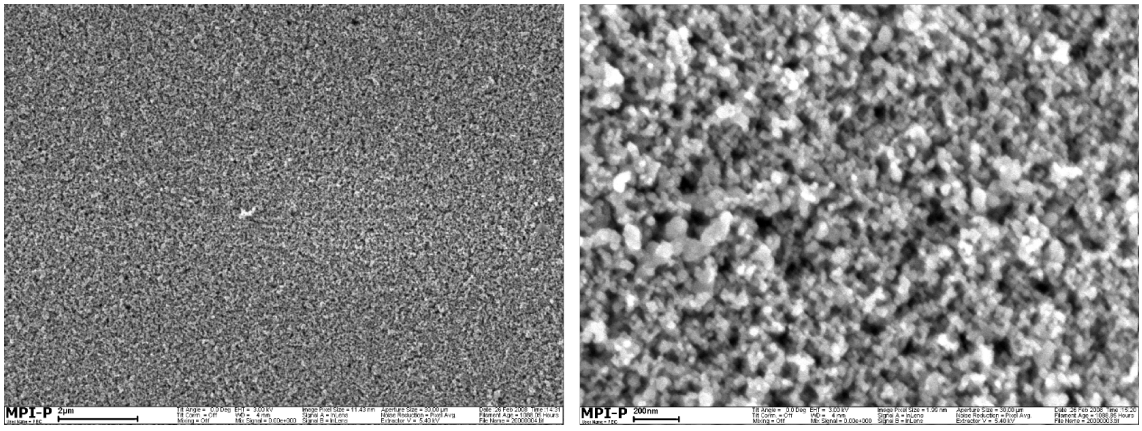

Figure 5.41: SEM images showing the surface of mesoporous thin films from sintered P25 colloids at two different magnifications.

The granular mesoporous structure is clearly visible in the above shown SEM image 5.41. The relatively big (Ø=25nm) titania crystals are expected to produce quite rough surfaces and also provoke relatively high internal scattering. As Illustrated in the OWS scan in 5.42, the obtained angular depending reflectivity could be fitted by the Fresnel simulation of the optical multi-layer system. However, as assumed the OWS scan revealed pronounced reflectivity losses which resulted in vehement variation to the Simulated curves. The OWS scan in figure 5.42 was representative for the whole series of mesoporous thin titania films which were formed *via* the powdery P25 nanoparticle source. The porosity of these

films was calculated on the basis of the obtained reflectivity spectra in air to be 36.5% in average.

	Thickness, d [nm]	Refractive Index, n [a.u.]	Extinction, κ [a.u.]
Prism/Substrate	∞	1.84498	0
Gold Film	48	0.312	3.823
meso-nc-Titania	2230	1.677	0.001
Superstrate	∞	1.000	0

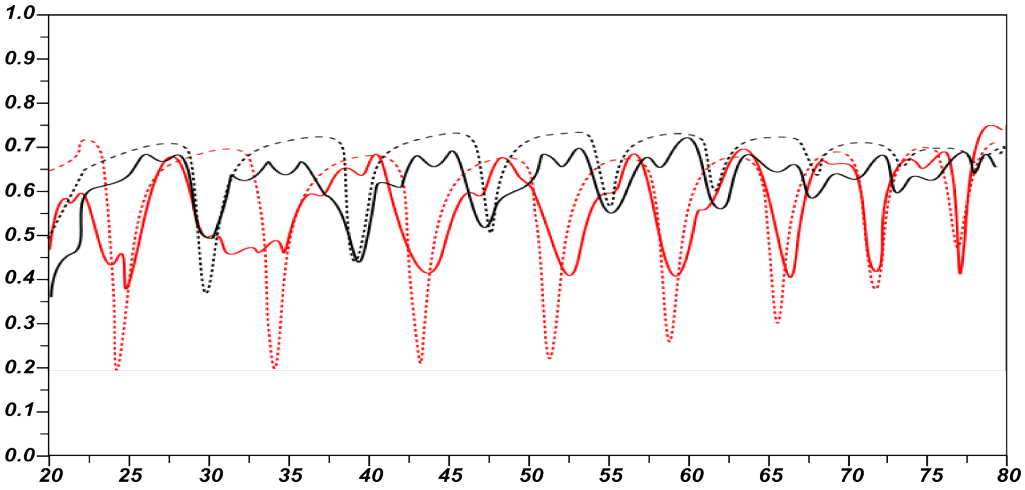

Figure 5.42: The OWS spectrum in air of mesoporous thin films from sintered P25 particles at two different polarisations (red: TM, black: TE). Fresnel fits were simulated are shown as dotted curves for both polarisations in the corresponding colours. The simulation parameters for the fit are shown above.

After the first series of experimental work on this approach it became apparent that the quality, provided by the commercially available powdery titania nanoparticles, was not sufficiently high to serve in optical application for the proposed mesoporous waveguide. Therefore, another commercially available source of titania nanoparticles was chosen, however, with smaller particle sizes this time (Ø=9nm). Ti-Nanoxide HT is a paste containing about 11% nanocrystalline titanium dioxide. This paste was specially designed by the manufacturer in order to fulfil the prerequisites for the formation of highly transparent (when sintered) photoelectrodes for dye sensitised solar cell application. The crystalline titania nanoparticles were delivered in form of a stabilised colloidal dispersion in a mixture of ethanol, water, and organic binders. One drop of the as-received sol was evenly spread onto a gold-coated glass slide and accordingly characterised.

The presented SEM photographs (refer to figure 5.43), again show the distinct granular character of the mesoporous nanocrystalline thin film, however, based on the smaller particle diameters much finer structures were formed in comparison with the powdery P25 nanoparticles. Therefore, the optical characteristics were expected to be also of higher quality.

The obtained angular reflectivity scans were fit in good accordance with the Fresnel

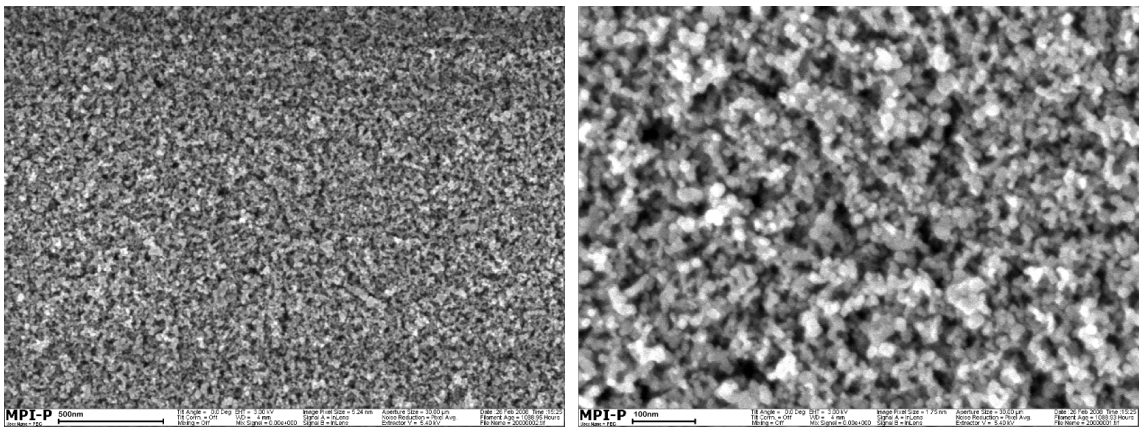

Figure 5.43: SEM images showing the surface of mesoporous thin films produced by sintering thin films applied from the commercially available HT paste at two different magnifications.

	Thickness, d [nm]	Refractive Index, n [a.u.]	Extinction, κ [a.u.]
Prism/Substrate	∞	1.84498	0
Gold Film	48	0.312	3.823
meso-nc-Titania (TE)	1004	1.740	0.003
meso-nc-Titania (TM)	1004	1.702	0.008
Superstrate	∞	1.000	0

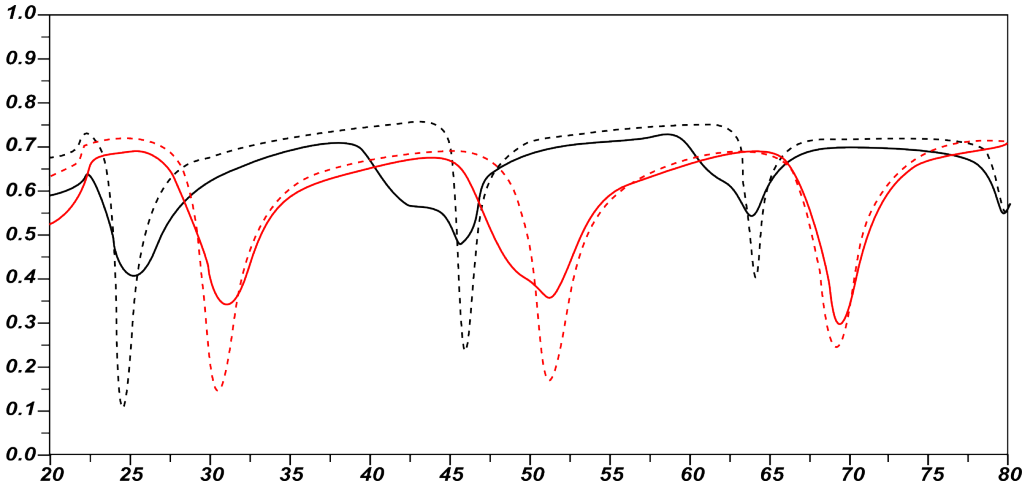

Figure 5.44: The OWS spectrum in air of mesoporous thin films from sintered HT paste at two different polarisations (red: TM, black: TE). Fresnel fits were simulated are shown as dotted curves for both polarisations in the corresponding colours. The simulation parameters for the fit are shown above.

Simulation of the optical multi-layer. However, for optimal fit of the OWS scan in air it was necessary to account for the anisotropy within the waveguiding thin film and to introduce two slightly different refractive indices for the two polarisations, TM and TE, respectively. Nevertheless, the scan curves showed still distinct features of various loss pathways within the mesoporous films and according variation to the calculated curves, which were mainly ascribed to the surface roughness caused by colloid agglomerates. The porosities of the films were calculated on the base of the taken OWS scans in air to be 35% (perpendicular through the film, measured by TM) and 32% (parallel through the film, measured by TE) and 36% in water for both polarisations, respectively.

	Thickness, d [nm]	Refractive Index, n [a.u.]	Extinction, κ [a.u.]
Prism/Substrate	∞	1.84498	0
Gold Film	48	0.312	3.823
meso-nc-Titania	1004	1.840	0.014
Superstrate	∞	1.333	0

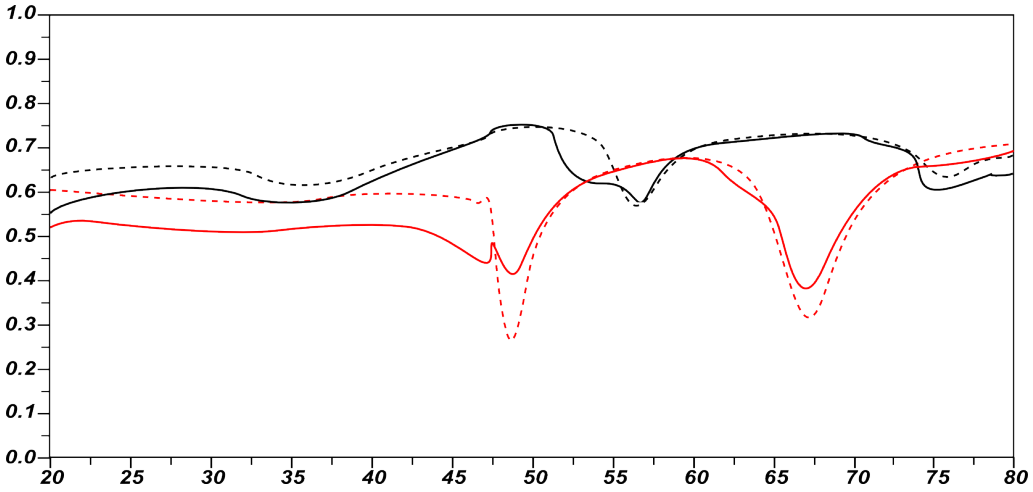

Figure 5.45: The OWS spectrum in water of mesoporous thin films from sintered HT paste at two different polarisations (red: TM, black: TE). Fresnel fits were simulated are shown as dotted curves for both polarisations in the corresponding colours. The simulation parameters for the fit are shown above.

As a consequence of the unsatisfying optical properties, inherent to the nano-granular films so far the attempt was made to synthesise the films *ab-initio* from molecular precursors (as described above in section 5.4.2) in order to gain control of each individual step of the film formation.

After successful synthesis of nanocrystalline titania colloids with a relatively homogeneous particle size of approximately $10nm$, it was repeatedly observed that sintered films tend to form cracks in the order of several micrometres throughout the whole film (of several square centimetre) as depicted in figure 5.46.

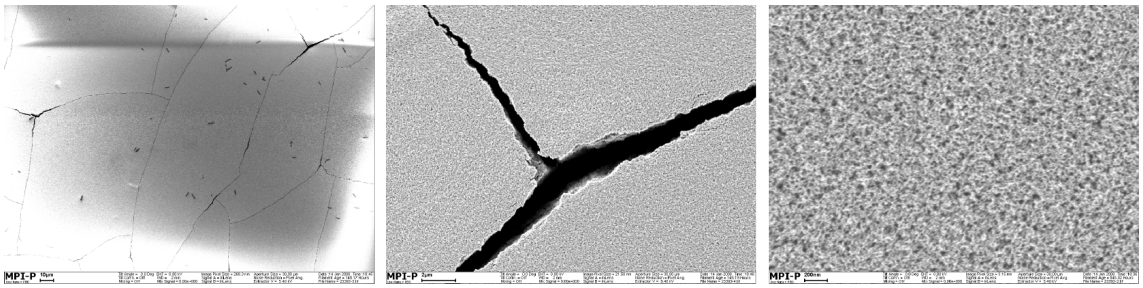

Figure 5.46: Micrometre sized cracks were observed in the films if the applied sol was to dilute.

This problem was overcome by adjusting the concentration of nanocrystals in the produced colloidal sol to $150\frac{g}{L}$ in a rotary evaporator. Colloidal sols of lower concentrations tended to produce large cracks, whereas more concentrated sols (i.e.$150\frac{g}{L}$) allowed for the formation of smooth and crack-free thin films of several square centimetre. Infrequently also the concentrated sol produced cracks, but, however, only locally restricted and of much smaller extensions. Figure 5.47 shows such an example of occasionally observed small cracks.

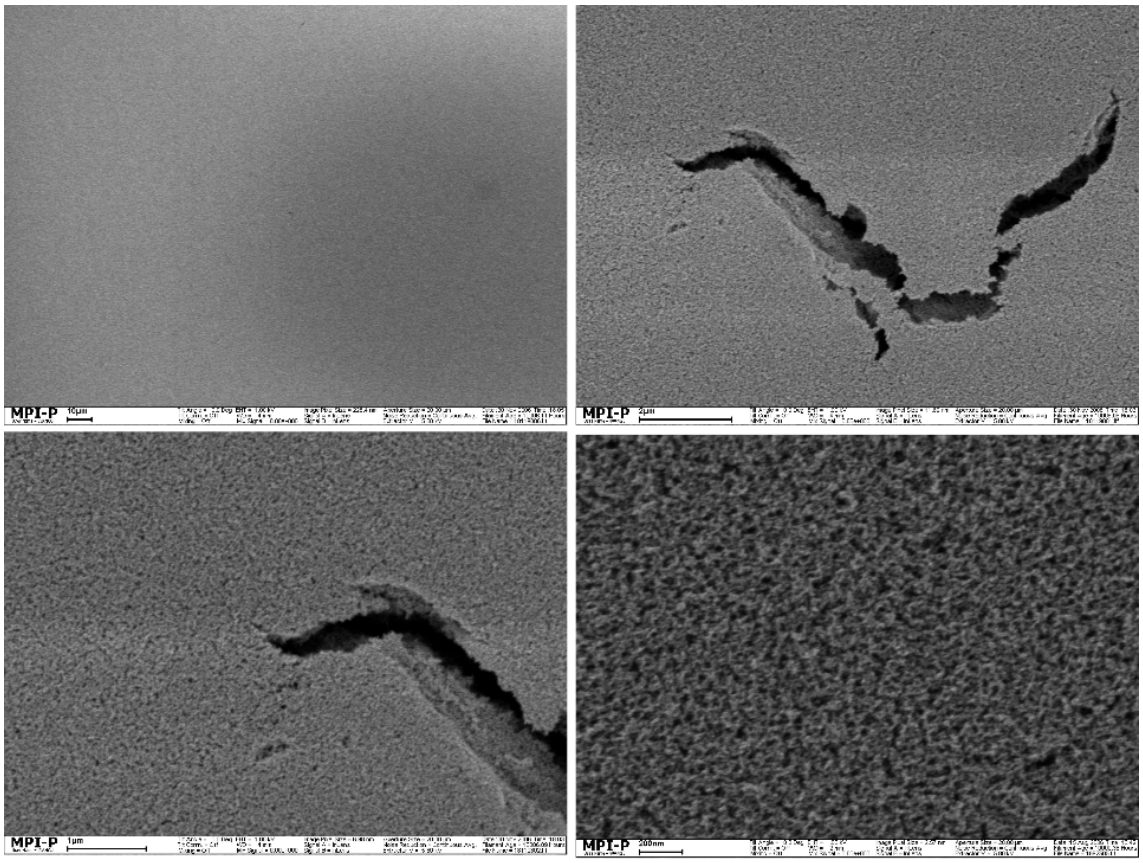

Figure 5.47: SEM images of the surface of mesoporous films after sintering of the concentrated sol. Cracks were rarely observed, however, being just very localised. The resulting 'nano canyon' allows for an insight into the film morphology, showing a homogeneously random architecture.

Certainly, this SEM images (in figure 5.47) and in particular the region of the crack in the film can be used to identify the homogeneously isotropic arrangement of the nanocrystals throughout the whole film thickness. The OWS scans taken of these mesoporous films are presented below in figures 5.48 and 5.49, for the case in air and in aqueous environment, respectively.

The angular reflectivity spectrum of the ab-initio controlled films showed reasonably good optical properties regarding the good consistence with calculated Fresnel simulations of the optical multi-layer assembly.

	Thickness, d [nm]	Refractive Index, n [a.u.]	Extinction, κ [a.u.]
Prism/Substrate	∞	1.84498	0
Gold Film	48	0.312	3.823
meso-nc-Titania	1201	1.4712	0.001
Superstrate	∞	1.000	0

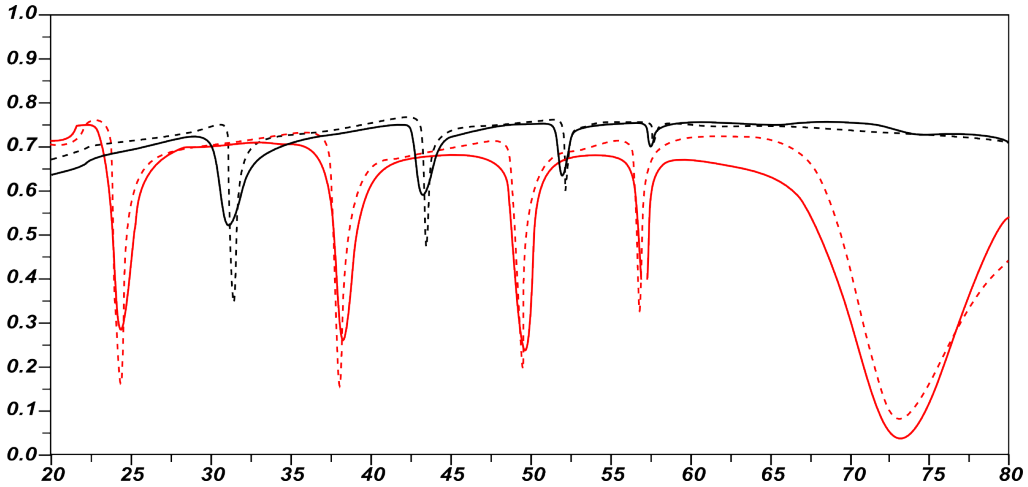

Figure 5.48: OWS spectrum in air of the ab-initio controlled thin films after sintering. Angular reflectivity scans are shown at two different polarisations (red: TM, black: TE). Fresnel fits were simulated are shown as dotted curves for both polarisations in the corresponding colours. The simulation parameters for the fit are shown above.

	Thickness, d [nm]	Refractive Index, n [a.u.]	Extinction, κ [a.u.]
Prism/Substrate	∞	1.84498	0
Gold Film	48	0.312	3.823
meso-nc-Titania	1201	1.6792	0.001
Superstrate	∞	1.333	0

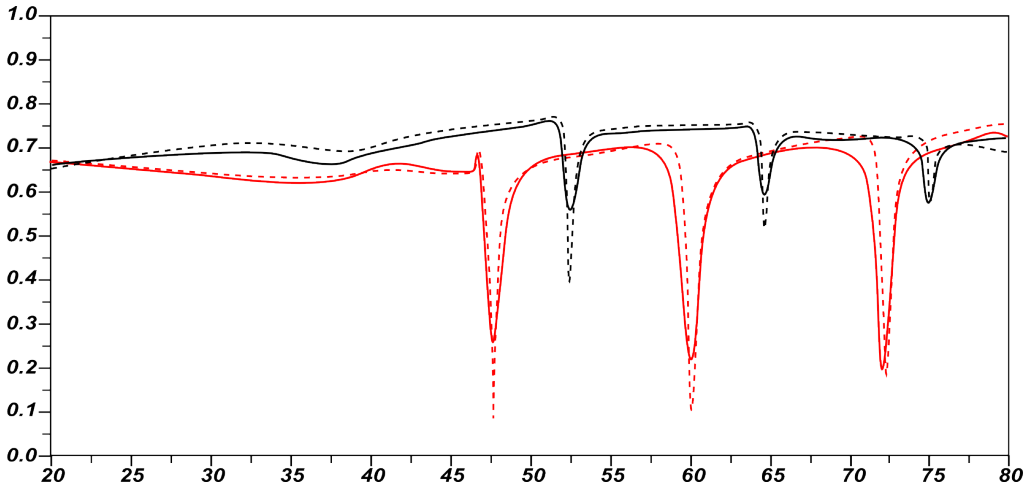

Figure 5.49: OWS spectrum in water of the identical film as above in figure 5.48. Angular reflectivity scans are shown at two different polarisations (red: TM, black: TE). Fresnel fits were simulated are shown as dotted curves for both polarisations in the corresponding colours. The simulation parameters for the fit are shown above.

Both spectra taken in air and in water, respectively, reveal a consistent porosity of 54.5%, being the highest obtained porosity with this approach until that point. These promising results and also the fact that the measurement in aqueous environment has verified the

complete infiltration of the porous network with the liquid medium, gave rise to more synthetic adjustments in order to further optimise the waveguiding properties of these mesoporous thin films while preserving or even increasing the porosity.

The first attempt to optimise the nano-granular mesoporous films was made by increasing the particle size of the nanocrystals in order to achieve a less dense packing of the titania around the sacrificial polymer and therefore, again, to increase the porosity. For that reason the autoclaving time of the sol was prolonged from 12 hours to be double, i.e. 24 hours. Resulting mesoporous films of these colloid assemblies are shown below in figure 5.50.

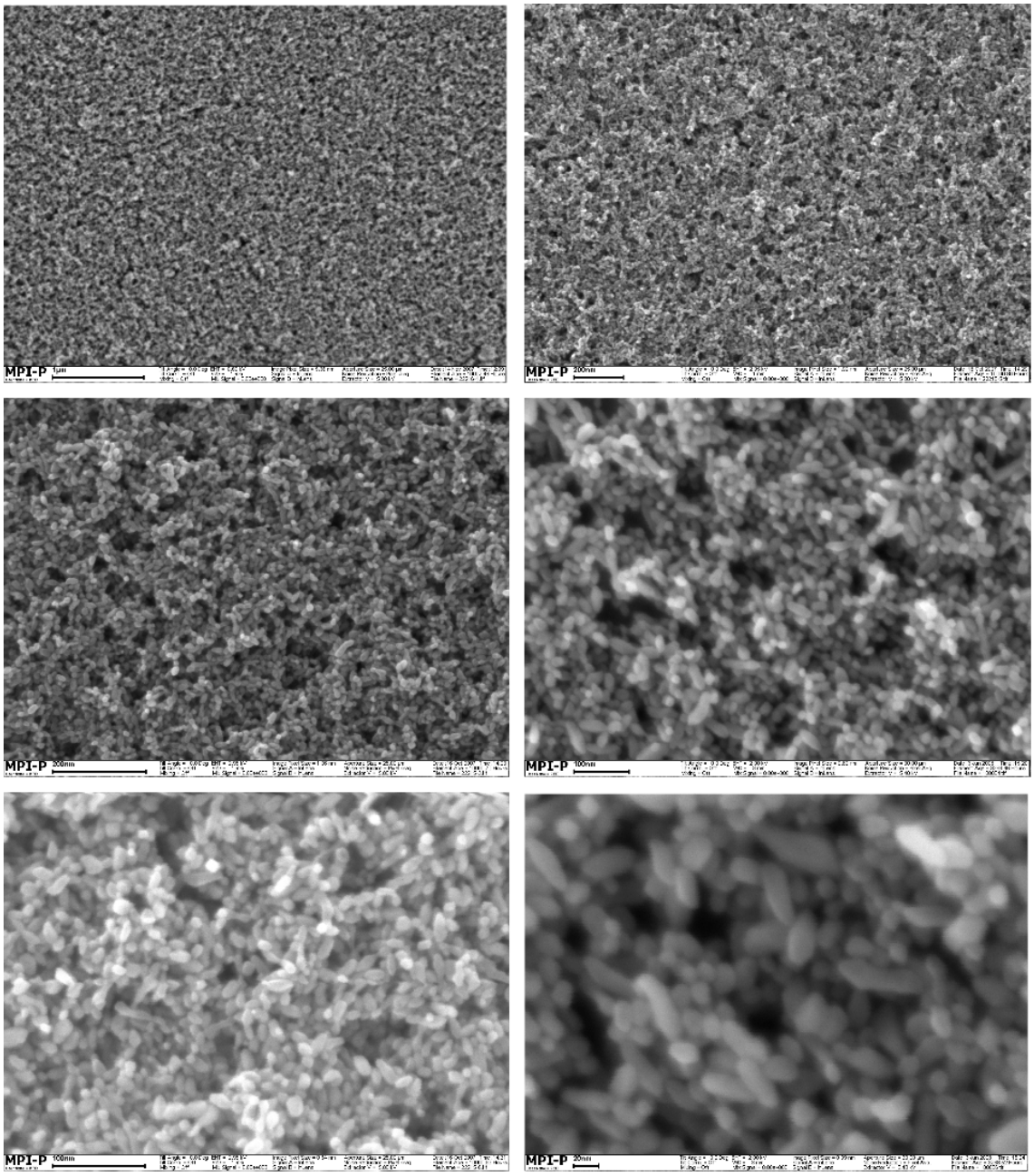

Figure 5.50: SEM images of the surface of mesoporous films after sintering of the nanocrystals of increased size (compare to figure 5.53). Cracks were not observed.

The increase in particle size to approximately $20nm$ (compared to the previous synthesis, depicted in figure 5.47) is clearly apparent from the SEM images in figure 5.50. In spite of the increased particle size of the nanocrystals, the OWS scans showed reasonably good accordance to the calculated Fresnel simulation. Nevertheless, a significant decrease in incoupled light intensity (depth of the dips at the resonant mode coupling angles) was observed (see figure 5.51). Also significant damping of the reflected intensity at high angles of incidence was observed, which strongly indicates distinctive surface scattering. The increased surface roughness was accounted to the larger particles used to assemble the film, whereas the decrease in ΔR at the resonance coupling conditions was most likely (also) due to the large grain sizes, but mainly caused by greater mono crystalline areas inherent to the larger crystals, as one possible loss-pathway.

	Thickness, d [nm]	Refractive Index, n [a.u.]	Extinction, κ [a.u.]
Prism/Substrate	∞	1.84498	0
Gold Film	48	0.312	3.823
meso-nc-Titania	1212	1.4642	0.009
Superstrate	∞	1.000	0

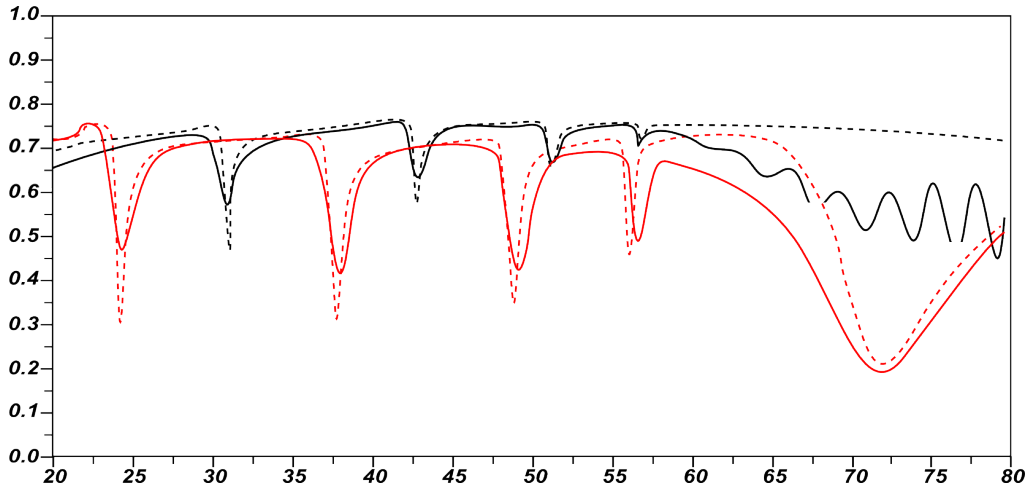

Figure 5.51: OWS spectrum in air of the mesoporous thin film after sintering the enlarged nano colloids together. Angular reflectivity scans are shown at two different polarisations (red: TM, black: TE). Fresnel fits were simulated are shown as dotted curves for both polarisations in the corresponding colours. The simulation parameters for the fit are shown above.

The equivalent losses were observed in the OWS scans in aqueous medium, however revealing a fully infiltratable and exchangeable pore volume of 54.5% of the whole film volume, which, surprisingly, meant no increase increase of porosity (compared to the previously shown results). Although, the results show that larger particles may be used for the assembly of these films, the films exhibited weaker overall performance as optical waveguide.

The final approach in order to increase the waveguiding properties of the nano-granular mesoporous thin films was undertaken by dip-coating the gold coated glass slides out of

	Thickness, d [nm]	Refractive Index, n [a.u.]	Extinction, κ [a.u.]
Prism/Substrate	∞	1.84498	0
Gold Film	48	0.312	3.823
meso-nc-Titania	1212	1.6842	0.009
Superstrate	∞	1.333	0

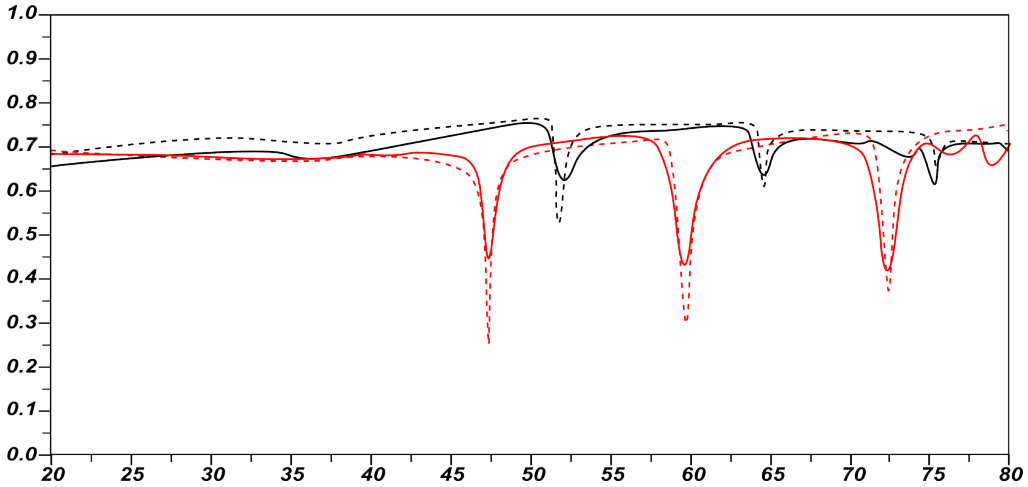

Figure 5.52: OWS spectrum in water of the identical film as above in figure 5.51. Angular reflectivity scans are shown at two different polarisations (red: TM, black: TE). Fresnel fits were simulated are shown as dotted curves for both polarisations in the corresponding colours. The simulation parameters for the fit are shown above.

the nanocrystalline colloidal sol (Ø $\sim 10nm$) at a withdrawal rate of $1\frac{mm}{s}$. In addition to the extended control of the film application, also the ambient humidity was increased to $95\%RH$ with the aim to allow the still-wet thin films for slower evaporation of the solvent and consequently more time to arrange into the final network. The SEM images of resulting films are shown in figure 5.53.

The obtained films were highly porous and homogeneously random assembled. The overall smooth surface was crack-free over a range of several square centimetre very homogeneous in thickness. The OWS scan show the angular reflectivity curve almost perfectly fitted by the Fresnel simulations, for both cases, in air and aqueous medium, respectively.

The porosity was calculated from obtained spectra to be 52.5% in both cases, proving the accessibility of the pore space by complete infiltration with the liquid medium.

5.5 Summary and Conclusion

A variety of approaches for the synthesis of mesoporous titania films was introduced. In the framework of the synthetic work the significant parameters for optimum optical and sorptive were determined and accordingly adjusted. The synthesis protocols were optimised as such, in order to obtain reproducible and homogeneous films with good optical proterties, thus high porosity and relatively large pore sise at the same time. The resulting

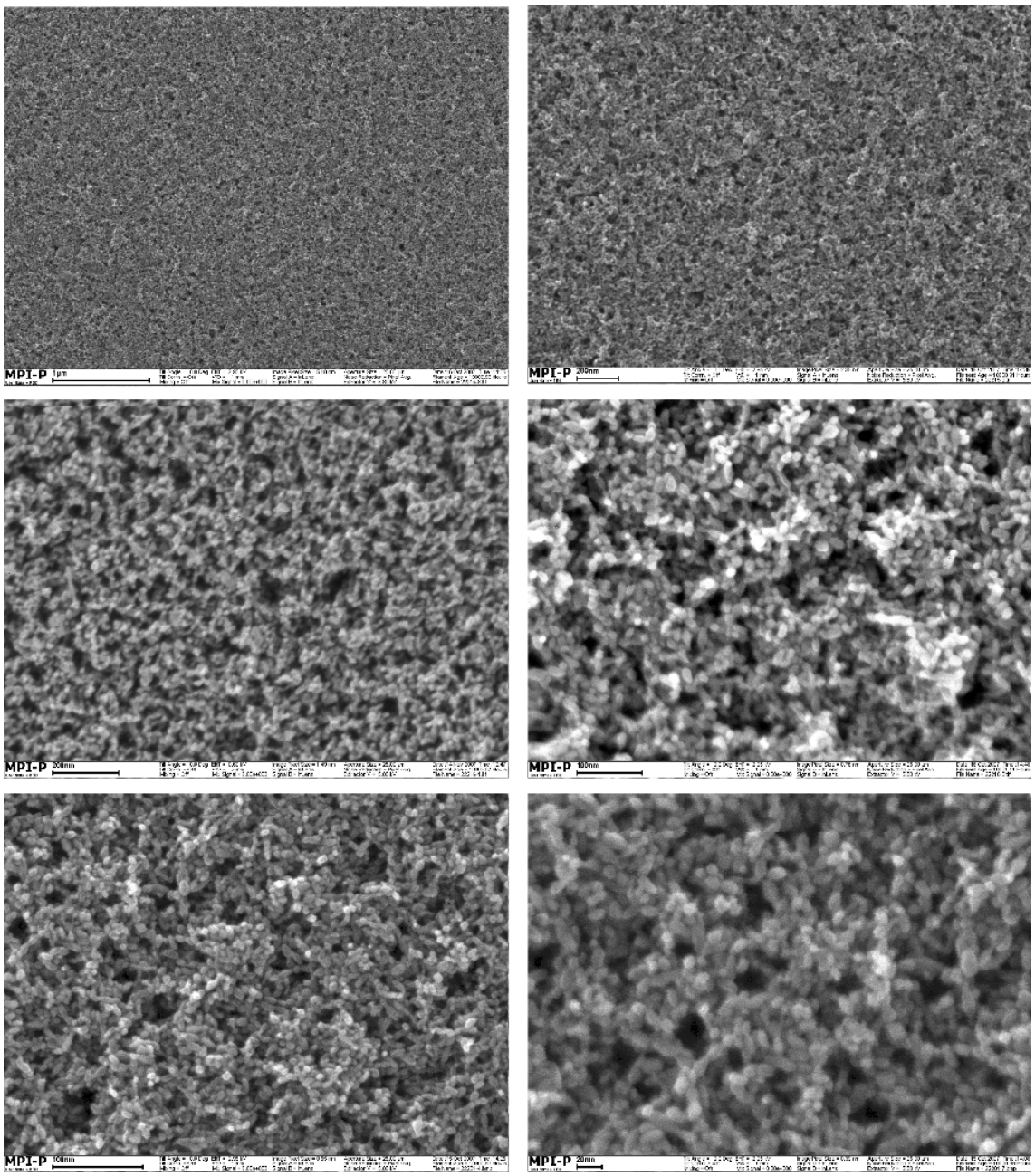

Figure 5.53: SEM images of the surface of dip-coated mesoporous films after sintering of the nanocrystals. Cracks were not observed.

films offer accessible interconnected pores throughout the whole film thickness, however, with the benefit of a simple one-pot synthesis protocol. These films were successfully used for optical waveguide spectroscopy.

	Thickness, d [nm]	Refractive Index, n [a.u.]	Extinction, κ [a.u.]
Prism/Substrate	∞	1.84498	0
Gold Film	40	0.187	3.48
meso-nc-Titania	1013	1.4968	0
Superstrate	∞	1.000	0

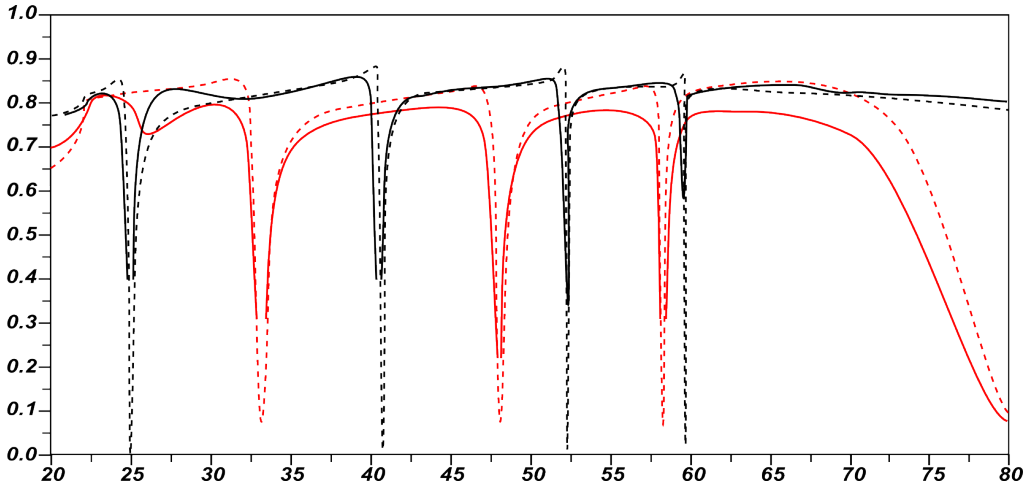

Figure 5.54: OWS spectrum in air of the dip-coated mesoporous thin film after sintering. Angular reflectivity scans are shown at two different polarisations (red: TM, black: TE). Fresnel fits were simulated are shown as dotted curves for both polarisations in the corresponding colours. The simulation parameters for the fit are shown above.

Bibliography

[1] Albu, S. P., Ghicov, A., Macak, J. M. & Schmuki, P. Long anodic tio2 nanotubes with hexagonal self-ordering. *Physica Status Solidi* **1**, 65 – 67 (2006).

[2] Alexandridis (1995).

[3] Alexandridis (1995).

[4] Attard, G. S., Coleman, N. R. B. & Elliott, J. M. The preparation of mesoporous metals from preformed surfactant assemblies. *Mesoporous Molecular Sieves* **117**, 89–94 (1998).

[5] Attard, G. S. *et al.* Liquid crystal phase templated mesoporous platinum alloy. *Microporous and Mesoporous Materials* **44-45**, 159–163 (2001).

[6] Attard, G. S. *et al.* Mesoporous pt-ru and pt-rh alloys from the hexagonal lyotropic liquid crystalline phase on a non-ionic surfactant. *Chem. Mater.* **13**, 1444–1446 (2001).

[7] Bates (1999).

[8] Bavykin, D. V., Friedrich, J. M. & Walsh, F. C. Protonated titanates and tio2 nanostructured materials - synthesis, properties, and applications. *Advanced Materials* **18**, 2807–2824 (2006).

[9] Beck, J. S. *et al.* A new family of mesoporous molecular sieves prepared with liquid crystal templates. *J. Am. Chem. Soc.* **114**, 10834–10843 (1992).

[10] Beranek, R., Hildebrand, H. & Schmuki, P. Self-organized porous titanium oxide prepared in h2so4-hf electrolytes. *Electrochem. Solid State Lett.* **6**, 12 (2003).

[11] Berger, S., Ghicov, A., Nah, Y. C. & Schmuki, P. Transparent tio2 nanotube electrodes via thin layer anodization - fabrication and use in electrochromic devices. *Langmuir* **25**, 4841–4844 (2009).

[12] Brinker, C. J., Lu, Y., Sellinger, A. & Fran, H. *Adv. Mater.* **11**, 579 (1999).

[13] Brinker, C. J. & Scherer, G. W. *Sol-Gel Science: The Physics and Chemistry of Sol-Gel Prcessing* (1990).

[14] Caruso, F., Caruso, R. A. & Moehwald, H. Nanoengineering of inorganic and hybrid hollow spheres by colloidal templating. *Science* **282**, 1111–1114 (1998).

[15] Caruso, R. A. & Antonietti, M. Sol-gel nanocoating: An approach to the preparation of structured materials. *Chem. Mater.* **13**, 3272–3283 (2001).

[16] Chemseddine, A. & Moritz, T. Nanostructuring titania - control over nanocrystal structure, size, shape, and organisation. *Eur. J. Inorg. Chem.* 235–245 (1999).

[17] Chen, X. & Mao, S. S. Titanium dioxide nanomaterials - synthesis, properties,

modifications, and applications. *Chem. Rev.* **107**, 2891–2959 (2006).

[18] Choi, S. Y. *et al.* 3d hexagonal (r-3m) mesostructured nanoctystalline titania thin films - synthesis and characterisation. *Adv. Funct. Mater.* **16**, 1731–1738 (2006).

[19] Choi, S. Y., Mamak, M., Coombs, N., Chopra, N. & Ozin, G. A. *Adv. Funct. Mater.* **14**, 335 (2004).

[20] Crepaldi, E. L., de A. A. Soler-Illia, G. J., Grosso, D. & Sanchez, C. Nanocrystallised titania and zirconia mesoporous thin films exhibiting enhanced thermal stability. *New J. Chem.* **27**, 9–13 (2003).

[21] Dag, O. *et al.* Solventless acid-free synthesis of mesostructured titania, nanovessels for metal complexes and metal nanoclusters. *Advanced Functional Materials* **13**, 30–36 (2003).

[22] Frindell, K. L. *Mesoporous Semiconducting Oxide Thin Films with Nanocrystalline Walls: Aynthesis, Characterization, and Application.* Ph.D. thesis, University of California, Santa Barbara (2003).

[23] G.J.deA.A.Soler-Illia, Louis, A. & Sanchez, C. *Chem. Mat.* **14**, 750–759 (2002).

[24] Ghicov, A. & Schmuki, P. *Chem. Commun.* **20**, 2791–2808 (2009).

[25] Goeltner, C. G. & Antonietti, M. Mesoporous materials by templating of liquid crystalline phases. *Adv. Mater.* **9**, 431–436 (1997).

[26] Gong, D. *et al. J. Mater. Res.* **16**, 3331–3334 (2001).

[27] Graetzel, M. *Pure Appl. Chem* **73**, 459–467 (2001).

[28] Hagfeldt, A. & Greatzel, M. *Acc. Chem. Res.* **33** (2000).

[29] Hamley (2001).

[30] Hamley, I. W., Mai, S., Ryan, A., Faircloughb, J. P. & Booth, C. Aqueous mesophases of block copolymers of ethylene oxide and 1,2-butylene oxide. *Phys. Chem. Chem. Phys.* **3**, 2972–2980 (2001).

[31] Henry, M., Jolivet, J. P. & Livage, J. Chemistry, spectroscopy and applications of sol-gel glasses, aqueous chemistry of metal cations: Hydrolysis, condensation and complexation. *Structure and Bonding* **77**, 153–206 (1992).

[32] Hoffmann, M. R., Martin, S. T., Choi, W. & Bahnemann, D. W. *Chem. Rev. (Washington, D. C.)* **95**, 69–96 (1995).

[33] Holland, B. T., Blanford, C. F. & Stein, A. Synthesis of macroporous minerals with highly ordered three-dimensional arrays of spheroidal voids. *Science* **281**, 538–540 (1998).

[34] Holmquist, P., Alexandridis, P. & Lindman, B. Modification of the microstructure in block copolymer-water-ÒoilÓ systems by varying the copolymer composition and the ÒoilÓ type: Small-angle x-ray scattering and deuterium-nmr investigation. *J. Phys. Chem. B* **102**, 1149–1158 (1998).

[35] Inagaki, S., Koiwai, A., Suzuki, N., Fukushima, Y. & K.Kuroda, K. *Bull. Chem. Soc. Japan* **69**, 1449–1457 (1996).

[36] Johnson, S. A., Ollivier, P. J. & Mallouk, T. E. Ordered mesoporous polymers of tunable pore size from colloidal silica templates. *Science* **283**, 963–965 (1999).

[37] Kavan, L., Attia, A. F., Lenzmann, F., Elder, S. H. & Gratzel, M. Lithium insertion into zirconia-stabilized mesoscopic tio2 (anatase). *J. Electrochem. Soc.* **147**, 2897–2902 (2000).

[38] Keller, F., Hunter, M. S. & Robinson, D. L. Structural features of oxide coatings on aluminium. *J. Electrochem. Soc.* **100**, 411–419 (1953).

[39] Khushalani, D., Ozin, G. A. & Kuperman, A. lycometallate surfactants. part 1: nonaqueous synthesis of mesoporous silica. *J. Mater. Chem.* **9**, 1483 (1999).

[40] Kresge, C. T., Leonowicz, M. E., Roth, W. J., Vartuli, J. C. & Beck, J. S. *Nature London* **359**, 710 (1992).

[41] Liu (2005).

[42] Macak, J., Tsuchiya, H., Taveira, L., Aldabergerova, S. & Schmuki, P. *Angew. Chem. Int. Ed.* **44**, 7463 (2005).

[43] Macak, J. M., Albu, S. P. & Schmuki, P. Towards ideal hexagonal self-ordering of tio2 nanotubes. *Physica Status Solidi* **1**, 181–183 (2007).

[44] Macak, J. M. & Schmuki, P. Anodic growth of self-organised anodic tio2 nanotubes in viscous electrolytes. *Electrochimica Acta* **52**, 1258–1264 (2006).

[45] Masuda, H. & Fukuda, K. Ordered metal nanohole arrays made by a two-step replication of honeycomb structures of anodic alumina. *Science* **268**, 1466–1468 (1995).

[46] Masuda, H., Nagae, M., Morikawa, T. & Nishio, K. Long-range-ordered anodic porous alumina with reduced hole interval

formed in highly concentrated sulfuric acid solution. *Jpn. J. Appl. Phys.* **45**, 406–408 (2006).

[47] Morensen (1992).

[48] Nandhakumar, I., Elliott, J. M. & Attard, G. S. Electrodeposition of nanostructured mesoporous selenium films. *Chem. Mater.* **13**, 3840–3842 (2001).

[49] O'Sullivan, J. P. & Wood, G. C. The morphology and mechanism of formation of porous anodic films on aluminium. *Proceedings of the Royal Society of London. Series A, Mathematical and Physical Sciences (1934-1990)* **317**, 511 (1970).

[50] Parkhutik, V. P. & Shershulsky, V. I. Theoretical modeling of porous oxide growth on aluminum. *J Phys D Appl Phys* **25**, 1258–1263 (1992).

[51] Sanderson (1951).

[52] Thompson, G. E. & Wood, G. C. Porous anodic film formation on aluminium. *Nature* **290**, 230 (1981).

[53] Thompson, G. E., Xu, Y. & Wood, G. C. Anodic oxidation of aluminium. *Philosophical Magazine B* **55**, 651 (1987).

[54] Tsuchiya, T. & Tsuchiya, J. High-pressure-temperature phase relations of mggeo3 - first-principles calculations. *Phys. Rev. B* **76**, 92105 (2007).

[55] Wakayama, H., Itahara, H., Tatsuda, N., Inagaki, S. & Fukushima, Y. Nanoporous metal oxides synthesized by the nanoscale casting process using supercritical fluids. *Chem. Mater.* **13**, 2392–2396 (2001).

[56] Wanka, H., Hoffmann, W. & Ulbricht, W. *Macromolecules* **27**, 4145 (1994).

[57] Wong, M. S., Jeng, E. S. & Ying, J. Y. Supramolecular templating of thermally stable crystalline mesoporous metal oxides using nanoparticulate precursors. *Nano Lett.* **1**, 637–647 (2001).

[58] Yanagisawa, T., Shimizu, T., Kuroda, K. & Kato, C. The preparation of alkyltrimethylammonium-kanemite complexes and their conversion to microporous materials. *Bulletin of the Chemical Society of Japan* **63**, 988–992 (1990).

[59] Yang, H. *et al.* Synthesis of ordered mesoporous carbon monoliths with bicontinous cubic pore structure of ia3d symmetry. *Chem. Commun.* **23**, 2842–2843 (2002).

[60] Yang, P., Zhao, D., Margolese, D., Chemlka, B. & Stucky, G. *Chem. Mater.* **11**, 2813–2826 (1999).

[61] Yang, P., Zhao, D., Margolese, D. I., Chmelka, B. F. & Stucky, G. D. *Nature London* **396**, 152 (1998).

[62] Zhao, D. *et al.* *Science* **279**, 548–552 (1998).

[63] Zwilling, V. *et al.* Structure and physicochemistry of anodic oxide films on titanium and ta6v alloy. *Surf. Interface Anal.* **27**, 629 (1999).

Chapter 6

6 Application of optical waveguides for the study of diffusion processes in Dye Sensitised Solar Cells

Contents

Abstract

Optical waveguide spectroscopy has been used to study the real-time diffusion of Ruthenium 535-bisTBA (N-719) dye into mesoporous nanocrystalline titanium dioxide films. The porous films were prepared on top of gold substrates and prism coupling was used to create guided waves in the nanocrystalline films. Dying was carried out by bringing the film into contact with a $3 \cdot 10^{-4} mol\, dm^{-3}$ dye solution and using optical waveguide spectroscopy to monitor the change in both the refractive index and the extinction coefficient of the mesoporous layer as dye diffused into the porous network. Dye uptake in a 1.27 µm film was slow with the refractive index of the film still increasing after 22 hours. The concentration of optically active dye molecules was $2.4 \cdot 10^{-4} mol\, cm^{-3}$ (as a function of total film volume) at equilibrium The diffusion coefficient of the dye in the film was estimated to be $6 \cdot 10^{-11} cm^2 s^{-1}$.

6.1 Introduction

Transport of adsorbate in porous materials is a topic of great interest and importance for science and technology. Transport in porous wide band gap semiconductor materials is of particular importance due to their wide-spread use in emerging nanotechnology applications. The need to understand diffusion phenomena on the nanometre scale is gaining more importance too. As one example the sensitisation of mesoporous titanium oxide with molecules capable of absorbing light in a broad range of the solar spectrum has led to the development of an effective photovoltaic device: the Dye Sensitised Nanocrystalline Solar Cell (DSSC). The basic concepts behind the DSSC will be introduced in this chapter, with particular focus on the effects of dye loading on the performance of the DSSC. As DSSCs go into commercial production, the controlled transport of molecules within nano-scaled systems has to be understood in greater detail. Particularly when wet-chemical processes at the liquid/solid interfaces are of major relevance to DSSC performance. But also from a more fundamental point of view, the variety of interactions which are possible when molecules have to diffuse through a liquid which is restricted by porous structures on the nanometre scale seems to be worth a deeper investigation. Therefore the second part of this chapter will outline the fundamentals of diffusion processes and relate their limitations to the characteristic properties of mesoporous titania films. The last part of this chapter will introduce the OWS-based methodology developed in the framework of this thesis in order to investigate diffusion processes in mesoporous films *in-situ*.

6.2 Dye Sensitised Solar Cell

One practical application of mesoporous nanocrystalline titanium oxide ($meso-nc-TiO_2$) is as the photoanode in the Dye Sensitised Nanocrystalline Solar Cell (DSSC), first reported by O'Regan and Grätzel in 1991. The fundamental idea behind DSSCs is the symbiotic interaction of dye molecules with a large band gap semiconductor electrode. In contrast to all-solid conventional semiconductor solar cells which use the combination of two doped crystals (n-type and p-type) to create an electric field in the depletion region near to the junction to transport electrons, the dye-sensitised solar cell is a photo-electrochemical solar cell. Special dyes have been developed and accordingly tuned to absorb the incoming photons in the desired region of the solar spectrum and with the ability to inject charges into the conduction band of the $meso-nc-TiO_2$. A distinct feature of these devices is the mesoscopic structure of the semiconductor. In combination with the electrolyte the composite system is commonly referred to as a 'bulk' or 3D junction (in contrast to 2D p-n-junctions, figure 6.1 (left)) due to the interpenetrating network of pores (see figure 6.1 (right)). The mesoscopic morphology produces an interface with a huge area (up to $100 m^2 g^{-1}$ and even more when templating techniques are applied), endowing these systems with intriguing optoelectronic properties.

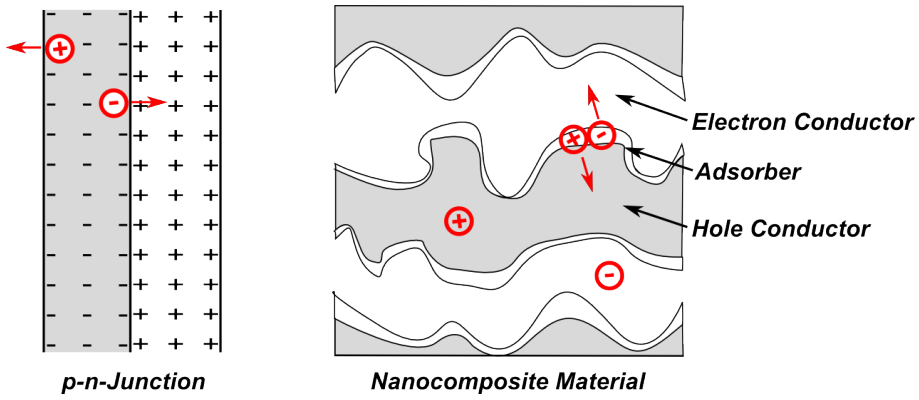

Figure 6.1: On the left a standard 2D p-n-junction is sketched and the principle of charge transport depicted. The right scheme highlights the highly increased area for the p-n-junction at the internal surface of the mesoporous material.

The light-to-electron conversion process in DSSCs differs fundamentally from the one in the conventional solar cells. Figure **6.2** shows a band diagram explaining the principle of operation of the DSSC, where the $meso-nc-TiO_2$ takes the centre stage. Electric contact is established between the nanocrystals by sintering them together. Electrons are injected into the conduction band of the semiconductor after photo-excitation of the dye which is attached to the nanocrystalline surface. The reduced dye is then regenerated by electron donation from the electrolyte, usually an organic solvent containing the iodide/tri-iodide (I/I_3^-) couple. The electrolyte itself is regenerated at the counter electrode by reduction of

the tri-iodide, the circuit being completed through the external load.

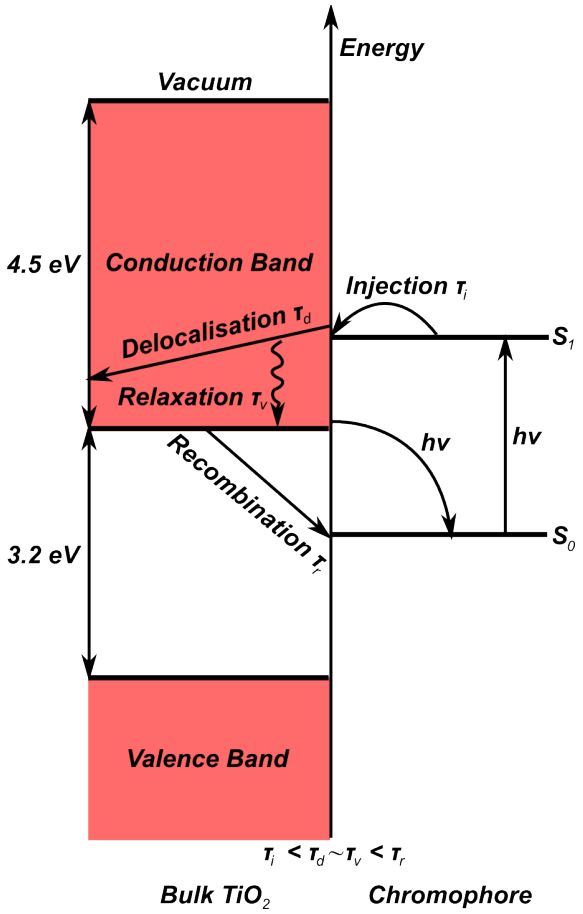

Figure 6.2: Energy diagram of the chromophore-$meso - nc - TiO_2$ interface. Electrons of the dye located in the semiconductor energy gap are promoted by absorbed photons from the ground state (S0) into an excited state (S1) that is in resonance with the conduction band (CB). Typically, the dye excited state is well inside the CB. Efficient electron injection into the edge of the CB avoids the energy and voltage loss by relaxation to the CB edge that is unavoidable if injection occurs deep into the CB. The injected electron delocalises from surface to bulk, simultaneously relaxing to the bottom of the CB owing to coupling to vibrations. If the electron returns to or remains trapped at the surface, it recombines with the positive charge residing on either the chromophore or the electrolyte mediator.

6.2.1 Titania Surface

The TiO_2 valence band (VB) is formed by oxygen orbitals. The conduction band (CB) is created by the d-orbitals of titanium atoms[12]. The band gap of bulk titania is 3.2 eV.

The close proximity to the surface induces lowering of the band gap energy substantially[4], however, saturation with dissociated water molecules brings back the value close to the bulk band gap energy. Typically (*as a n*-type semiconductor), titania traps electrons at its surface, resulting in a negatively charged surface while it is in contact with air or liquids. Consequently, an oppositely charged layer is induced at the surface of the nanocrystals in order to preserve overall electric neutrality. This, again, results in the characteristic 'bending up' of the energy band in close proximity to the surface. The bands can be moved

down again, for example in solutions with low pH as they support a large amount of positive charge carriers which accumulate at the surface.

6.2.2 Sensitiser Chromophore

The dye molecules harvesting light and are optimised to match the energy levels of $meso-nc-TiO_2$ but also to be thermally and photochemically stable[2]. Under illumination the dye forms a photo-excited state which is also the donor state for the interfacial charge transfer to the $meso-nc-TiO_2$ electrode. The rate at which charge transfer occurs is strongly determined by the energies of the dye-$meso-nc-TiO_2$ donor-acceptor states and how these interact with each other, i.e. how coupling is achieved[24]. Most generally applied sensitiser molecules chemisorb on the titania surface *via* oxygen containing substituents (e.g. hydroxyl, carboxyl, and phosphoric acid groups) in order to form a very strong bond, only separating the π-system of the dye from the surface by an oxygen atom and therefore resulting in very strong electronic coupling to the titania nanocrystals (see figure 6.3).

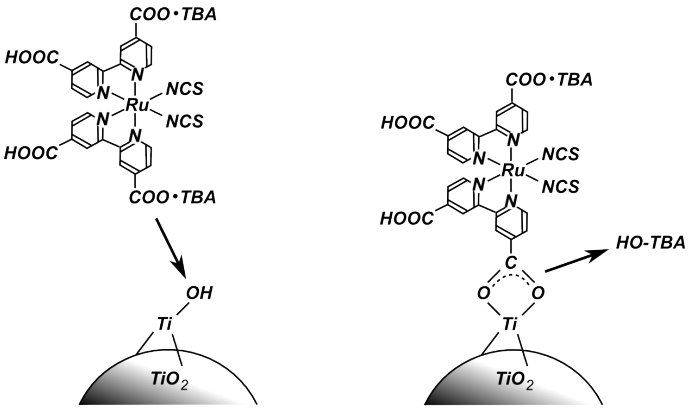

Figure 6.3: Schematic illustration of a binding geometry for the dye titania assembly.

Ruthenium based dyes, and more precisely the Ruthenium 535-bisTBA or "N-719" dye in particular, has emerged as the benchmark of sensitising species for $meso-nc-TiO_2$ based solar cells, mainly owing to its high efficiency and photochemical stability[16]. The dye molecules are adsorbed onto the internal surface of a several micron thick $nc-TiO_2$ film. The dyes absorb strongly in the visible spectrum and charge separation occurs when photo-excited electrons are injected from the dye into the $nc-TiO_2$. The dye is regenerated by donation of an electron from a redox mediator (usually solvated I_3^-) and the electrons in the $meso-nc-TiO_2$ film diffuse to a fluorine doped tin oxide (FTO) contact where they are measured as a photocurrent in the external circuit (detailed illustration in figure 6.4).

To date, the highest efficiency is over 11%, achieved by employing a Ru complex dye, TiO_2

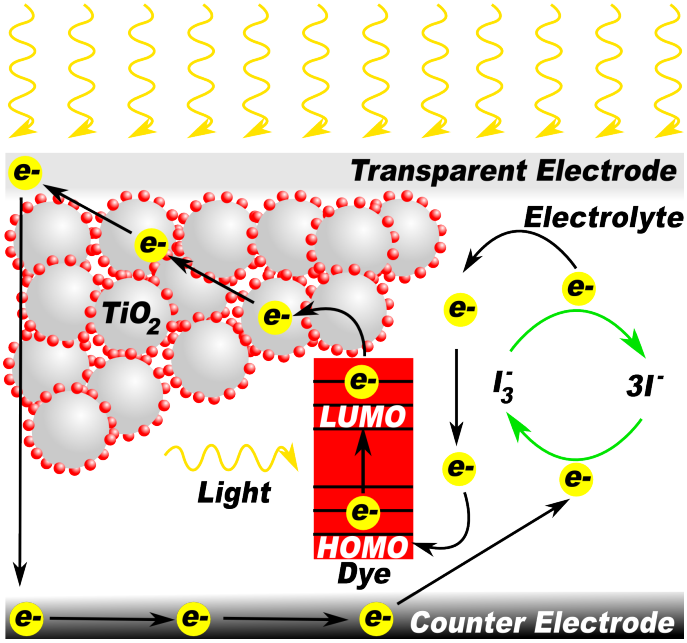

Figure 6.4: The working principle for DSSCs is illustrated, details are given in the test.

electrode, and I^-/I_3 - redox couple.[9], although the average efficiency of these systems is in the majority of cases $< 10\%$. Despite progress in the efficiency and stability of these solar cells, there are many fundamental aspects of their operation that are still unknown. The detailed structure of the dye/semiconductor interface is a central problem for which there is little information. Theoretical aspects of the binding of the favoured ruthenium complex sensitisers to the anatase surface have been discussed[31,30,32]. Another fundamental process, for which there is limited information, is the regeneration reaction between the photo-oxidised dye and the iodide ion that is commonly used to regenerate the adsorbed dye.

Therefore, several reasons can be considered for the low efficiencies (compared to Si-based devices), nevertheless, it seems apparent that the imperfect filling of the pores of the $meso-nc-TiO_2$ with the dye is the core of the problem. Accordingly, there is great motivation to understand and to control this process since it seems to be the key to assure optimal efficiency. In order to make DSSCs with reasonably high efficiencies it is crucial to optimise and control the adsorption behaviour of the molecules. Therefore, it is of extraordinary interest to investigate transport (and) diffusion processes in nanosized domains to better understand dye coverage. Accordingly, there is great demand for methodologies that allow for the *in-situ* measurement of diffusion occurring within mesoporous films.

6.3 Transport and Adsorption in Mesoporous Titania Thin-Films

The last 18 years have seen large improvements in the efficiencies of DSSCs. A variety of new nano- and mesoporous architectures and highly photo-stable sensitiser molecules[35] have been introduced. Despite the progress there remain some crucial details of DSSC operation for which limited information is available. One area is the study of dye diffusion, adsorption and surface coverage as well as the question as to whether the dye is homogeneously spread throughout the $meso-nc-TiO_2$ film. Typically, dying of the $meso-nc-TiO_2$ film is done by immersing the film in dye solution for approximately 12 hours. Dyes such as $cis-diisothiocyanato-bis(2,2-bipyridyl-4,4-dicarboxylato)ruthenium(II)bis(tetrabutylammonium)$ known as Ruthenium $535-bisTBA$ or "N-719" are commonly adsorbed from a $3\cdot10^{-4}M$ solution.

Dye adsorption from ethanol has been investigated as well as from a $50:50$ t-butanol:acetonitrile mixture. Recently a number of promising new dyes including $NaRu(4,4^{\prime}-bis(5-hexylthiophen-2-yl)-2,2^{\prime}-bipyridine)(4-carboxylicacid-4^{\prime}-carboxylate-2,2^{\prime}-bipyridine)(NCS)_2$ (C101) have been developed which show high molar extinction coefficients across the visible range[26]. There has also been research showing that the temperature at which self-assembly of the dye on the $meso-nc-TiO_2$ surface is carried out is an important parameter controlling dye packing and solar cell efficiency. The co-adsorption of small molecules such as deoxycholic acid have also been found to improve dye packing, to reduce recombination and improve efficiency[21]. Dying times can be drastically reduced by constant agitation of the dye bath, or by using constant flow or whirlpool methods.

Dye coverage and the mode of dye attachment are therefore crucial parameters in DSSC production but there are few methods for the $in-situ$ measurement of dye coverage. Dye uptake is commonly measured by one of two methods. The first method involves monitoring the falling concentration of dye in the solution above the $meso-nc-TiO_2$ film by UV-Vis spectroscopy. This method is most accurate when very low concentration dye baths are used and so does not give realistic information about dye uptake in normal highly concentrated dye-baths. In addition, information about the diffusion of dye into the film can only be inferred by the absence of dye in the bulk solution which gives no information about the diffusion front or the distribution of dye throughout the $meso-nc-TiO_2$ film.

A second method for measuring dye coverage is to completely desorb the dye from then $meso-nc-TiO_2$ film by submerging it in an aqueous or ethanolic solution of base and then measuring the desorbed dye concentration by UV-Vis spectrometry. This method gives the

total concentration of dye in the film, but again no information about adsorption/desorption kinetics or the homogeneity of the dye distribution.

Optical waveguide spectroscopy (OWS) has been shown to be a powerful technique for studying the adsorption of proteins and small molecules inside porous inorganic materials[3,27,22,8]. In this work OWS is used as a method for measuring the real time adsorption of Ruthenium 535-bisTBA dye molecules in $meso-nc-TiO_2$ films $in-situ$. In OWS the high refractive index $meso-nc-TiO_2$ film is used as a planar waveguide. The way in which light propagates through the $meso-nc-TiO_2$ film is highly dependent on the refractive index and thickness of the film as well as the refractive indices of the substrate and superstrate. In this case the substrate is gold and the superstrate is a $3 \cdot 10^{-4} M$ solution of Ruthenium 535-bisTBA dye in ethanol. As the dye diffuses into the $meso-nc-TiO_2$ network both the refractive index, n, and the extinction coefficient, k, of the film change and these changes are followed in real time by OWS. OWS is a particularly powerful technique as it is very sensitive to changes happening inside the mesoporous film and rather insensitive to changes that occur in the bulk solution. Using this method it has been possible to follow real time diffusion of dye into a $nc-TiO_2$ film without worrying about interference for the concentrated solution of dye above the film.

Here the $in-situ$ and real-time adsorption of Ruthenium 535-bisTBA is studied from ethanol. No attempt has been made, at this stage, to optimise dye adsorption by using solvent mixtures or co-adsorbates. As a first step the power of optical waveguide spectroscopy as a technique for measuring real time dye adsorption in nanoporous networks was investigated. Ethanol was chosen as a homogeneous solvent with a single well-defined refractive index which greatly simplified the fitting and modelling of the adsorption data. To the best of my knowledge, this is the first report describing the $in-situ$ monitoring of adsorption kinetics and diffusion properties of Ruthenium 535 bis-TBA within the mesoporous titania film.

6.4 Diffusion Sensing

Often diffusion processes are a controlling factor in the sensing of small molecules. Transduction of the signal, however, varies from method to method. In the case of an optical field intensity based sensor, the (time dependant) presence of analyte molecules and according changes in the refractive index within the EM fields are transduced into (reflected) intensity changes. The connection between refractive index change and change in analyte concentration is formed by the Lorenz-Lorentz equation as it relates the macroscopic

optical properties of a medium to its particle density N_j (i.e. the number of molecules per unit volume) and the intrinsic molecular polarisability α_j.

$$\frac{n^2-1}{n^2-2} = \frac{1}{3\varepsilon_0}\sum_j N_j\alpha_j \tag{6.1}$$

The value of ε_0 is defined by the formula $\varepsilon_0 = 1/\mu_0 c_0^2 = 8.85\,10^{-12} F\,m^{-1}$ where c_0 is the speed of light in vacuum and μ_0 is the magnetic constant or vacuum permeability.

Consequently, since the value of N_j is linearly related to the molecular concentration of the analyte, it can be related to the polarisability α_j in order to transduce an intensity change into a change in concentration. If, for example, analyte is added to the sensing environment described in equation 6.1 the equation is extended as follows:

$$\frac{(n+\Delta n)^2-1}{(n+\Delta n)^2-2} = \frac{1}{3\varepsilon_0}\sum_j N_j\alpha_j + \frac{1}{3\varepsilon_0}N_x\alpha_x = \frac{(n+\Delta n)^2-1}{(n+\Delta n)^2-2} = \frac{n^2-1}{n^2-2} + \frac{1}{3\varepsilon_0}N_x\alpha_x. \tag{6.2}$$

As long as the change in the refractive index $(\Delta n)^2 \ll 1$, the change in n can be related to the concentration *via* N_j:

$$\Delta n = \frac{n^2+2}{\frac{6n}{n^2+2} - 2n\frac{1}{3\varepsilon_0}N_x\alpha_x}\frac{1}{3\varepsilon_0}N_x\alpha_x \approx \frac{(n^2+2)^2}{6n}\frac{1}{3\varepsilon_0}N_x\alpha_x. \tag{6.3}$$

A refractive index change of $\Delta n = 0.0245$ is well in the linear regime of the function, and therefore allows for $\Delta n \sim N_x \equiv c_x$. This approximation is applicable as long as the polarisability α_j for the diffusive species remains constant, i.e. the dye does not interact with the matrix or any other species within the pores. Within these conditions, the optically accessible refractive index profile $\Delta n(x,t)$ truly describes the time and spatially dependent concentration profile $c(x,t)$ within the mesopores. On this basis a mathematical treatment of diffusion induced refractive index fluctuations $\Delta n(x,t)$ is possible by considering the starting and boundary conditions given by the diffusion equations.

Based on Brownian molecular motion, diffusion is driven according to the thermal energy ($T > 0$) inherent in a system. Though microscopically randomly directed, this molecular transport phenomenon is macroscopically always aimed to equilibrate concentration or pressure gradients within mixtures. In liquids the rate of this macroscopically directed mass transport is determined mainly by the density of the media (i.e. viscosity).

6.5 Diffusion

Mass transport through mesoporous is generally different to bulk mass transport. Adsorption/desorption kinetics in porous materials are generally controlled by mass transfer rather than by the intrinsic sorption kinetics which, at least for physical adsorption, are generally rapid. An understanding of these diffusion processes, especially the features associated with diffusion in mesopores, is therefore essential background for the study of sorption kinetics. This subject has been discussed in detail in a number of books and review articles [18,19,28,29]. The present section therefore provides only a brief introductory treatment at a level necessary to understand the principles of kinetic behaviour which has been observed in experimental studies.

In general, be it in the gas phase or in liquids, diffusion of molecules within nanosized environments comprises a well known and widely studied research topic [23,33,1]. Despite its highly complex nature, diffusion may be defined as the spreading of the molecules of one substance into the region initially occupied by another substance. At the same time as these molecules mingle with the other species in order to mix and form a concentration equilibrium throughout the whole accessible volume, the other species are moving as well.

There has been increasing interest in diffusion studies of molecules in mesopores since recent progress in the controlled synthesis of mesostructured porous materials has allowed for the study of tailored pore geometries. Transport in mesoporous structures is in general dominated by so called Knudsen diffusion. Experimentally two different diffusion problems can be considered: (i) Transport diffusion, where the particles diffuse in a non-equilibrium situation from one side of the system to the opposite side, subjected to the influence of the concentration gradient, and (ii) self-diffusion, which takes place under equilibrium conditions. Both problems are characterised by their intrinsic diffusion coefficients, D_t and D_s, respectively. Fick's first law defines D_t as the proportionality constant, relating the current density $\mathbf{j}$ and the concentration gradient $\partial c/\partial x$,

$$\mathbf{j} = -D_t \frac{\partial c}{\partial x} \tag{6.4}$$

whereas D_s is defined by the mean square displacement $\langle x^2(t) \rangle$ of a so-called 'random walker' [36] after time t, where d is the dimension of the pore.

$$\left\langle x^2(t) \right\rangle = 2dD_s t \tag{6.5}$$

Under the condition of Knudsen diffusion, both these coefficients are expected to coincide [18].

For the discussion of diffusion in this chapter therefore, the material specific diffusion coefficient D will be used, and no further differences between D_t and D_s is considered. D depends on the intrinsic properties of the diffusing particle and the surrounding medium it diffuses through, and is generally donated in units of $cm^2 s^{-1}$.

Combining Fick's first law with the continuity equation,

$$\frac{\partial c}{\partial t} = -\nabla \mathbf{j} \tag{6.6}$$

leads to Fick's second law, which describes the time and spatial dependent change of concentration and is therefore referred to as the 'diffusion equation'.

$$\frac{\partial c(\mathbf{r},t)}{\partial t} = \nabla \cdot [D(c,\mathbf{r})\nabla c(\mathbf{r},t)] \tag{6.7}$$

Diffusion into a pore can be described by a concentration gradient in one direction (i.e. from the solution into the mesoporous film). The diffusion equation can then be reduced to one dimension in the form of

$$\frac{\partial c(\mathbf{r},t)}{\partial t} = D\nabla^2 c(\mathbf{r},t) \tag{6.8}$$

also called the heat equation. Solving for $c(x,t)$ yields the time and spatially dependent concentration gradient which is accordingly generally referred to as the 'concentration profile' The simplest solution of equation 6.8 with defined starting values gives

$$c(x,t) = \frac{c_0}{2\sqrt{\pi D t}} exp(-\frac{(x-x')^2}{4Dt}), \tag{6.9}$$

where c_0 represents the total amount of substance present in the closed system:

$$c_0 = \int_{-\infty}^{\infty} c(x,t)dx \tag{6.10}$$

With the starting condition at $t \to 0$, equation 6.10 is introduced into the function of $c(x,t)$ to give a Delta-function:

$$\lim_{t\to 0} \frac{s}{2\sqrt{\pi D t}} exp(\frac{-(x-x')^2}{4Dt}) = s\delta(x-x') \tag{6.11}$$

Accordingly, this equation describes the starting condition for a diffusion process with the starting concentration at position $x = x'$ equal to the total amount of substance c_0 present

in the system, which is diffusing into space for $t > 0$. In the case of diffusion into a pore, the direction of diffusion is restricted to only $x > x'$ Since the solutions for both directions ($x > x'$ and $x < x'$) are symmetric at $x = x'$ and as the superposed solutions are identical in equation 6.9 a factor of 2 is added.

Solutions for the whole spatial distribution, based on the starting conditions outlined above, must fulfil the general condition

$$c(x, 0) = f(x) \tag{6.12}$$

in order to give

$$c(x, t) = \frac{1}{2\sqrt{\pi Dt}} \int_{-\infty}^{\infty} f(x') exp(\frac{-(x - x')^2}{4Dt}) dx' \tag{6.13}$$

where $t \to 0$ gives the starting condition.

A characteristic of this function is that the concentration is only related to the quotient $x/2\sqrt{Dt}$, which again implies that the distance, a certain concentration of diffusing species has travelled, is described by the square root of the diffusion time. Now assuming a constant concentration at $t = 0$ it leads to the following starting conditions:

$$t = 0 \begin{cases} c = c_0, x < 0 \\ c = 0, x > 0 \end{cases}$$

From insertion in equation 6.13 it follows that:

$$c(x, t) = \int_{-\infty}^{0} \frac{c_0}{2\sqrt{\pi Dt}} exp(\frac{-(x - x')^2}{4Dt}) dx' = \frac{c_0}{\sqrt{\pi}} [\int_{-\infty}^{0} exp(-\xi^2) d\xi - \int_{0}^{\frac{x}{2\sqrt{Dt}}} exp(-\xi^2) d\xi] \tag{6.14}$$

Commonly, integrals of the kind of

$$\frac{2}{\sqrt{\pi}} [\int_{0}^{x} exp(-\xi^2) d\xi = erfc(x) \tag{6.15}$$

are referred to as error functions erfc(x), which are related to each other as follows:

$$erfc(-x) = -erfc(x) \quad erfc(0) = 0 \quad erfc(\infty) = 1 \tag{6.16}$$

Accordingly, giving the well-known starting condition for a concentration profile that infinitely extends in one direction:

$$c(x,t) = \frac{c_0}{2}[erfc(\infty) - erfc(\frac{x}{2\sqrt{Dt}})] = \frac{c_0}{2}[1\text{-}erfc((\frac{x}{2\sqrt{Dt}})] \tag{6.17}$$

From this the solution for the right half space, $x > 0$ with constant values for $c(x,0)$ at all times is easily obtained, by simply substituting $c_0/2$ with c_0, thus yielding

$$c(x,t) = c_0 erfc(\frac{x}{2\sqrt{Dt}}) \tag{6.18}$$

This function expresses a diffusion profile, starting at $x = 0$ with direction along the x-axis into as long as $x < 0$ is set to be constant, which is well suited to describe an experiment with an unlimited and unchanging concentration of the diffusing species above the mesoporous film.

As diffusion processes in thin mesoporous films are the scope of this chapter, the above stated equations must also account for the finite film thickness of the material at $x > 0$ which is restricted by an impenetrable layer at $x = d$, here the gold substrate. Therefore the boundary condition relates the vanishing diffusion current at $x = d$ with the constant concentration c_0 at $x = 0$. Completing the conditions with:

$$t > 0 \begin{cases} c'(x = d, t) = 0 \\ c(x = 0, t) = c_0 \end{cases} \qquad c(x,0) = 0, \quad t = 0$$

and successive fulfilling of the boundary conditions results in an infinite series:

$$c(x,t) = c_0 \sum_{k=0}^{\infty} (-1)^k [erfc(\frac{2kd + x}{2\sqrt{Dt}})] + erfc((\frac{2(k+1)d - x}{2\sqrt{Dt}})] = c_0 f(x,t) \tag{6.19}$$

Though, infinite, this series converges quickly and therefore allows for a good approximation of the concentration gradient after calculation of just few terms. Figure 6.5 shows a 3D-plot of the progressing diffusion profile within the mesoporous film as a function of time. For details see caption.

6.6 Diffusion Limitation

The discussion of diffusion in this section will be restricted to diffusion in liquids, more precisely to diffusion in aqueous solutions. The focus will be on infiltration and diffusion

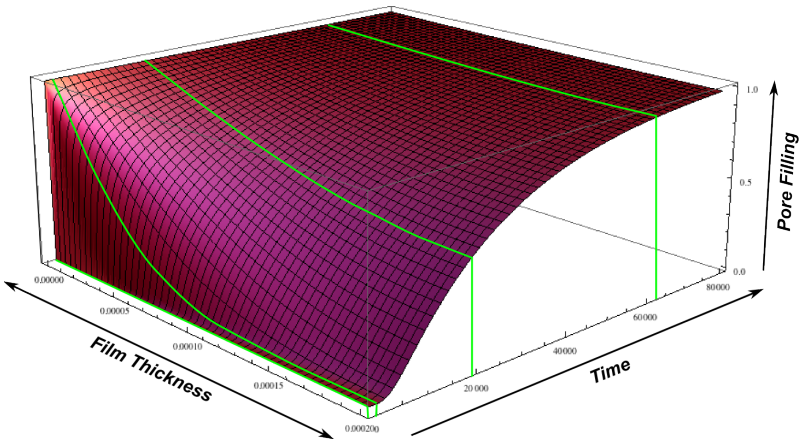

Figure 6.5: 3D-plot visualising equation 6.19. The progressing diffusion profile within the mesoporous film is plotted as a function of time. he green lines illustrate the progressing diffusion by indicating the concentration gradient through the mesoporous film at different points in time. Following the grid lines of the mesh above the time axis gives an idea of the variation of diffusion kinetics with dependence on the position within the film.

into and through the nano-scale environment of mesoporous titania films. The fundamental increase in entropy by the mixing of matter is well described by Fick's Laws of Diffusion. Fick's laws can be applied to both diffusion in bulk liquids and also diffusion within porous media and nanometre sized domains, however, with additional terms are added to account for pore geometries and roughness factors which cause surface trapping. In the case of porous materials, however, the diffusion constant D is substituted by the effective diffusion constant D_{eff}. Both quantities are related by:

$$D = \frac{D_{eff}}{p} \tag{6.20}$$

where p donates the fraction of porosity within the porous volume. Basically, three phenomena can influence the effective diffusion in (meso)porous networks:

(1) The particle flux, which is directly correlated with the cross sectional area perpendicular to the direction of diffusion. Since diffusion processes take place in a water-filled pore space, only a fraction of the total pore volume is available to support the transport process. The porosity $p = V_{pore}/V_{total}$ is used to relate the pore space to the total geometrical volume of a porous medium.

(2) In addition to the porosity, diffusion in porous materials are generally discussed in terms of tortuousity T_D, which is a measure for the effective diffusion path through the porous network. This effective diffusion path is often much longer than the film thickness (see figure 6.6).

More precisely, it is defined as the square of the quotient of the effective trajectory L_{eff} within the porous matter and the shortest, direct path L_s:

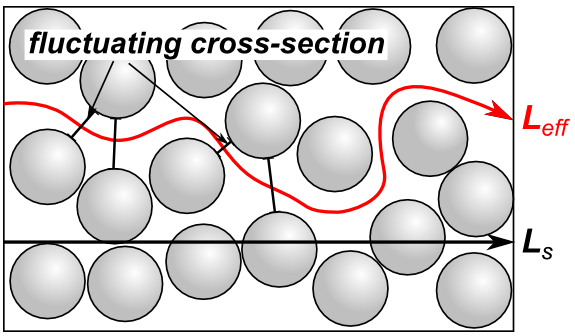

Figure 6.6: Diffusion through porous medium. The prolonged trajectory is described by the tortuousity T_D. Fluctuating cross-sections along the diffusion trajectory are quantified by the constrictivity δ.

$$T_D = \left(\frac{L_{eff}}{L_s}\right)^2 \tag{6.21}$$

(3) The constrictivity δ accounts for the fluctuations of these effective cross-sectional areas along the diffusion path. This aspect is especially important for randomly assembled structures like sintered nanocrystalline colloids discussed here, since these films feature large variation in the size of the interconnections within the pore structure (see figure 6.6). This characteristic feature of pore networks is described by:

$$\delta = \frac{D_{eff} T^2 D_b}{p} \tag{6.22}$$

where D_b is the diffusion constant in the pore-filling medium in its bulk volume. Whereas the influence of tortuousity is intuitive, it seems to be more difficult to grasp and quantify the measure of constrictivity (reported values range between $\delta = 0.3$ and $\delta = 1.8$[6]), therefore both coefficients can be merged in order to summarise the so-called matrix factor, q_m

$$q_m = \frac{T^2}{\delta} \tag{6.23}$$

This matrix factor gives a good measure for geometrical restrictions that influence the diffusion of molecules through porous networks. It is obvious that the matrix factor is also highly dependent.on the size (diameter and volume) of the diffusing species. Diffusion measurements of small molecules, for example the tri-iodide species in $meso - nc - TiO_2$ films, have been reported to have matrix factors as low as 1.37[20]. This is easily explained, since the size of the diffusing species determines the probability of finding a (relatively) straight diffusion path through the porous film. This probability, again, increases for small molecules and accordingly the matrix factor decreases, whereas large molecules suffer from high matrix factors. The diffusion coefficient of the Ruthenium dye used in

the studies describes here, is therefore expected to be considerably higher then the one reported for I/I_3^-. In the case of Ruthenium dyes mass transport is not only hindered by the pore diameter but also restricted by the small connections in the pore network, which force the dye molecules to take the tortuous path. Calculations and models are available for a wide range of porous structures based on approximations of random pore size distribution or varying pore sizes [15,34,17,13,5].

However, theory and model experiments predict matrix factors for a distribution of isotropic spheres of $1.25 - 1.8$ even for highly idealised systems[6]. These value were experimentally proven by measurements of helium diffusion through such architectures, however, the experiment was done in a gaseous environment and is not representative of the matrix factor in aqueous media.

6.7 Results and Discussion

In the experiments outlined here a $meso - nc - TiO_2$ film served as the waveguiding film. The substrate was a $\sim 50nm$ gold film and the superstrate was either air or ethanol. The incident laser light propagated along the $meso-nc-TiO_2$ film by total internal reflection at the layer interfaces. OWS measured the composite refractive index of the $meso-nc-TiO_2$ film and was therefore sensitive to any change in refractive index and extinction coefficient of the layer. Because of the high degree of field localisation within the $meso - nc - TiO_2$ film, very high sensitivity was observed for slight changes in refractive index. In the case of a mesoporous oxide, changes in refractive index were caused by the presence of any guest molecule within the mesoporous structure and the resulting modification of the wavevector. The composite refractive index, n_{xy}, of the film was found to change substantially when dye molecules diffused into the porous film. Changes in refractive index were monitored in real time and could be directly related to the concentration of dye inside the film.

In OWS the composite refractive index, n_{xy}, of the waveguide for both TE modes (excited by s-polarised light) and TM modes (excited by p-polarised light) was measured. In the case of a $meso - nc - TiO_2$ film, the composite refractive index was a combination of the dielectric properties of the nanocrystalline material and the refractive index of the air or solvent in the pores. If solvent molecules in the pores were replaced by a material with a higher refractive index, such as a ruthenium dye, the composite refractive index of the entire $meso - nc - TiO_2$ layer, and therefore also the effective refractive index of the whole optical system increased. This increase in refractive index of the $meso - nc - TiO_2$ film manifested as a parallel shift of the reflectivity minima to higher coupling angles.

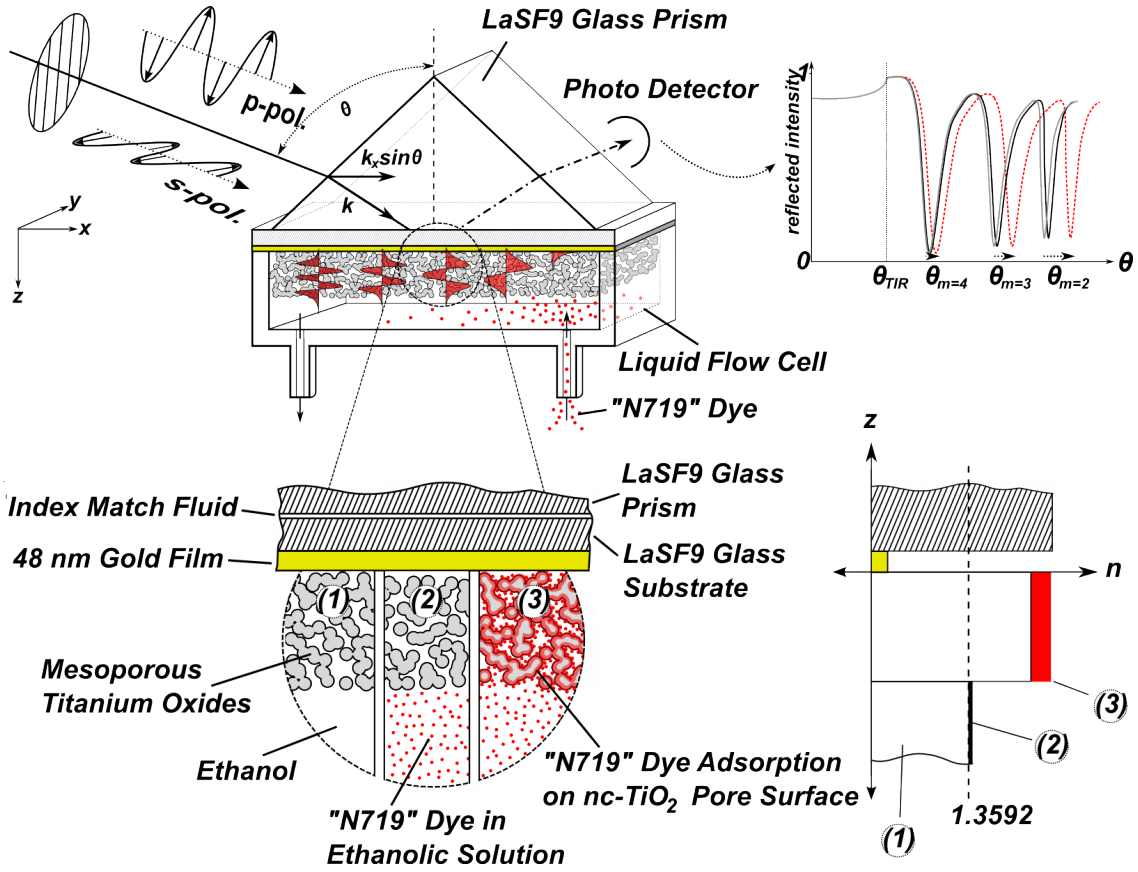

Figure 6.7: The experimental set-up showing coupling of laser light into the $meso-nc-TiO_2$ film using a prism and a 48nm gold layer. In OWS light was used to excite standing waves, 'modes', in a high refractive index material. The figure shows the first five TM waveguide modes. As the waveguiding layer was supported on a gold film, the first mode (m=0) was the surface plasmon resonance at the gold-TiO_2 interface. The waveguide spectrum was obtained by measuring the intensity of the reflected light as a function of incident angle. When the light excites a guided mode in the TiO_2 layer a sharp dip in reflectivity was observed.

The evanescent tail of the guided modes was generally sensitive to changes up to $200nm$ away from the surface of the $meso-nc-TiO_2$ film (see figure 6.7), for this reason OWS was suitable for monitoring processes that lead to changes in the optical density both inside and within ca. $200nm$ of the surface of the optical waveguide. One of the advantages of the technique is that it is easy to distinguish between small molecules attaching to the top surface of the film and small molecules diffusing into the film as only diffusion into the film causes parallel shifts in model reflectivity. In addition the internal area of the mesoporous film was so large in comparison to the geometric surface area of the film, the sensitivity to dye adsorption throughout the mesoporous network was much greater than to dye adsorption on the top surface. The most important point is that OWS is insensitive to very small changes occurring in the bulk solution of dye above the film, such as when diffusion of dye into the$meso-nc-TiO_2$ film occurs. If a large change in refractive index of the superstrate were to occur it would be immediately obvious by a shift in the critical angle at which total internal reflection occurs.

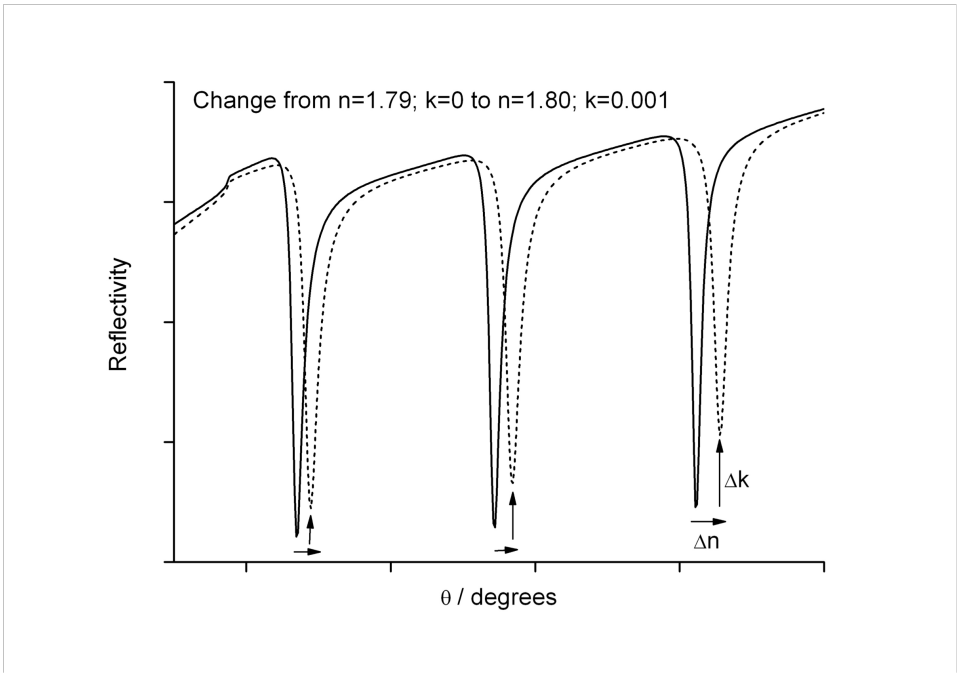

Figure 6.8: Simulated optical waveguide spectra (TM-modes) for a $1.4\mu m$ $nc-TiO_2$ *film on a* $48nm$ *gold substrate. The film was modelled with ethanol infiltrating the pores of the film as well as bulk ethanol above the film. The change in the waveguide spectrum for a small change in the composite refractive index of the film (*$n = 0.01$*) and the extinction coefficient (*$k = 0.001$*) was modelled. Changes in* n *are seen in the position of the minimum on the* x*-axis, changes in* κ *are seen in the position of the minimum on the* y*-axis.*

In order to extract information about dye adsorption inside the pores of the $meso-nc-TiO_2$ film it was necessary to use a model to describe how the composite refractive index of the mesoporous material (TiO_2 and pores) will change. It is assumed that the $meso-nc-TiO_2$ remained unchanged throughout the dying process and that the dielectric constant increased solely by dye displacing ethanol molecules in the pores. Equally it was possible to model the reverse situation where the dielectric properties of the $meso-nc-TiO_2$ were modified by dye adsorption and the volume of the pores simply shrinks. For simplicity the first case was assumed as both models will give the same overall dye coverage. The composite refractive index of the film was modelled using effective medium theory. The Bruggeman expression, also know as the effective medium approximation (EMA), describes the average or composite refractive index of a heterogeneous mixture (on the macro scale) of two different dielectric media (*A* and *B*)[7]. It assumes that inclusions of one dielectric material, *A*, are embedded in an averaged dielectric medium (*A*+*B*). It is particularly applicable when the volume fractions of *A* and *B* are similar such as in a mesoporous material. The EMA is discussed in more detail in the introduction, the central equation is recalled by equation 6.24, where ε_{xy} is the composite dielectric constant for the mixed nanocrystal/solvent layer, ε_{matrix} is the dielectric constant for the nanocrystalline particles, f_{matrix} is the volume fraction of nanocrystalline material, ε_{pore} is the dielectric constant for the pore-filling solvent and f_{pore} is the volume fraction of pore-filling solvent.

$$0 = f_{matrix}\frac{\varepsilon_{matrix} - \varepsilon_{xy}}{\varepsilon_{matrix} + 2\varepsilon_{xy}} + f_{pore}\frac{\varepsilon_{pore} - \varepsilon_{xy}}{\varepsilon_{pore} + 2\varepsilon_{xy}} \tag{6.24}$$

In the work presented here real time changes in ε_{xy} were measured. The porosity of the film and the dielectric constant of the $meso-nc-TiO_2$ particles were calculated by measuring waveguide spectra in air ($\varepsilon_{pore}(air) = 1.0016$) and in ethanol ($\varepsilon_{pore}(EtOH) = 1.79$). As $f_{pore} + f_{matrix} = 1$, the two equations could be used to solve for f_{pore} (porosity) and ε_{matrix}; this gives 0.45 porosity and ε_{matrix} and consequently $n_{matrix} = 2.1775$.

The dielectric constant, ε, is complex: $\varepsilon = \varepsilon'' + i\varepsilon'$. ε can be related to the frequency dependent refractive index $\varepsilon = \tilde{n}$. Where $\tilde{n}$ is defined as: $\tilde{n} = n + ik$. And n is the refractive index and k is the extinction coefficient of the material at the wavelength of excitation. If the dye absorbs at the wavelength of the exciting laser light then the extinction coefficient, k, measured for the film will also increase with increasing dye concentration. However, the laser wavelength was chosen so that it did not measure at spectral regions of very high dye absorption in order to reduce photo-bleaching of the dyes. The extinction coefficient is directly related to the absorption cross section, σ_a, and the number density of absorbers, N, in the sample. Where λ_0 is the wavelength of the incident light in free space.

$$\sigma_a N = \frac{4\pi k}{\lambda_0} \tag{6.25}$$

N and σ_a can be calculated directly from UV-Vis measurements using a variation of the Beer-Lambert law.

$$ln\frac{I}{I_0} = \sigma_a N l \tag{6.26}$$

Where l is the path length of light in the sample. OWS allows the composite refractive index, n_{xy}, and the extinction coefficient, k, of the films to be tracked separately with time. Both n_{xy} and k give information of the amount of dye within the film.

Kinetic measurements of dye uptake were measured by tracking the shift of the minimum of the TM_4 mode with time. The TM_4 mode was chosen as it was the highest order mode guided in the film, that could be resolved in the spectra (the TM_5 mode was at the stage of transition from a radiation mode to a guided mode) and as such gives the most accurate average value of the composite dielectric constant of the film. The modelled field intensity of the TM_4 mode in a $1.27\mu m$ film (identical to the film thickness used in this study) is shown in figure 6.9. It can be seen that the optical field is intense right at the surface of the film and as such is sensitive to changes as soon as dye molecules enter the pores.

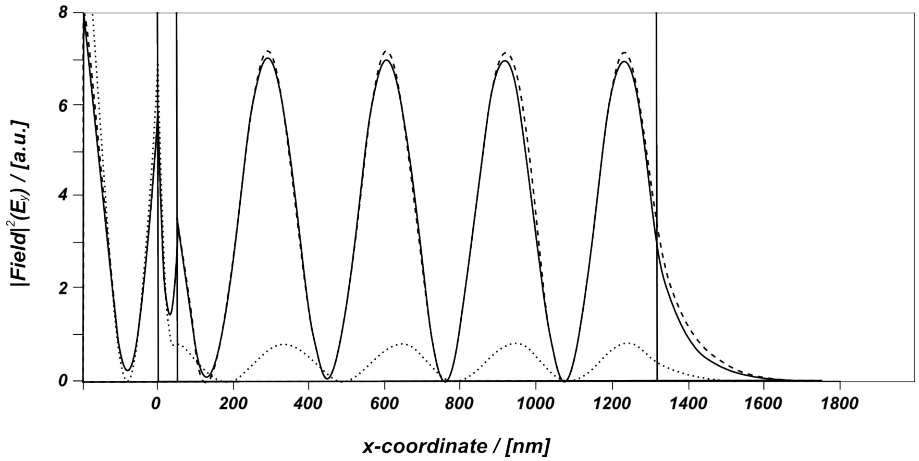

Figure 6.9: Field intensity for the TM_4 mode modelled in a$1.27\mu m$ film, the kinetic measurements show an average of the change in dye solution throughout the film.

6.7.1 Optical Waveguide Spectra

The $meso-nc-TiO_2$ films were made using identical methods to those typically employed to make the photoanode in a dye sensitised solar cell, so the results have direct relevance to DSSCs. A typical SEM image of a $meso-nc-TiO_2$ film used in this study and made by the acetic acid hydrolysis route is shown in figure 6.10 (left). Figure 6.10 (right) shows optical waveguide spectra taken with both p and s-polarised light for a $1.27\mu m$ $meso-nc-TiO_2$ on a gold substrate. In the first experiments the film was measured in air. A total of ten waveguide modes could be excited. The $meso-nc-TiO_2$ films were almost completely transparent and the mesoporous structure was on a length scale smaller than the wavelength of the light, as a result there was only a small broadening of the peaks and increase in the reflected intensity of the minimum position due to light scattering.

The $1.27\mu m$ $meso-nc-TiO_2$ film was used for dye uptake studies. The film was mounted as one side of a flow cell (figure 6.7) and dye uptake occurred over the $0.33cm^2$ area of the film defined by the o-ring. The film was first soaked in ethanol to ensure that it was stable and that no changes were seen in the absence of dye. In the second step a pump was used to rapidly replace the ethanol above the $meso-nc-TiO_2$ film with a $3\cdot10^{-4}mol\ dm^{-3}$ solution of ruthenium 535 bis-TBA dye in ethanol. Real time changes in the composite refractive index, n_{xy}, of the film at $632.8nm$ were measured by monitoring the angular position of the minimum angle of the TM_4 mode (seen in figure 6.11).

Real time changes in the extinction coefficient, k, at $632.8nm$ were measured by monitoring and fitting of the reflectivity at the resonance angle. Figure **6.12** shows optical waveguide spectra taken after the sample had been exposed to dye for 22 hours; for clarity the

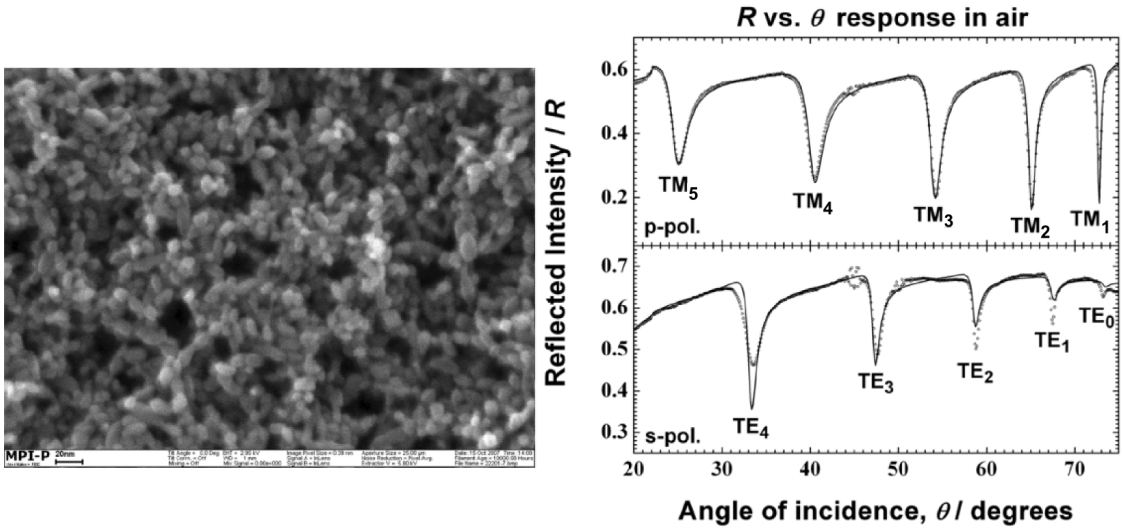

Figure 6.10: SEM image of a $nc-TiO_2$ film. The scale bar is $20nm$.(left) Optical waveguide spectra of a $1.27\mu m$ $nc-TiO_2$ film in air, waveguide modes were excited by both p-polarised light (above) and s-polarised light (below). The experimental data is given by the open diamonds and the fit is given by the solid line.(right)

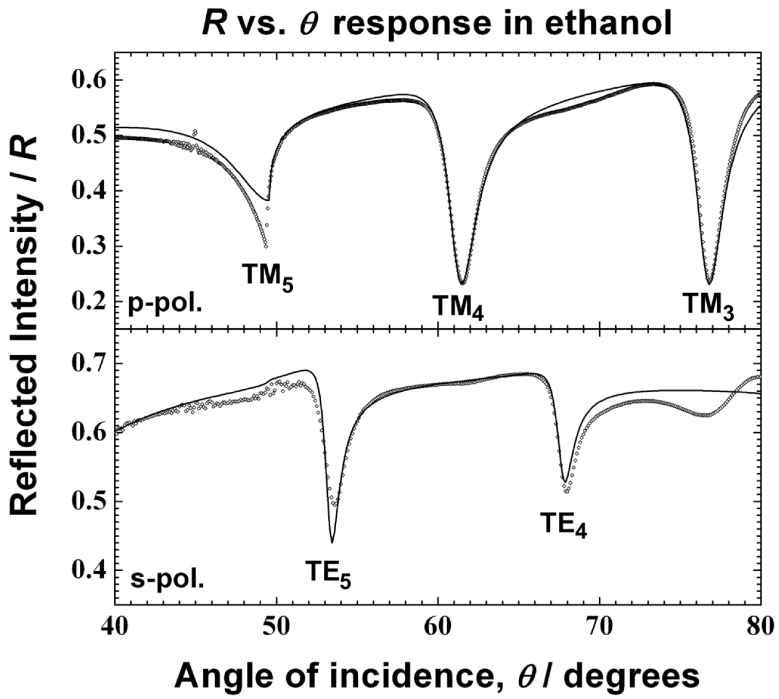

Figure 6.11: Optical waveguide spectra of the same film measured in figure 6.10, but in ethanol. Waveguide modes were excited by both p-polarised light (above) and s-polarised light (below) In ethanol the effective refractive index of the film is higher and this causes the modes to shift to higher angles. The critical angle increases from 21° in air to 50° in ethanol. The black diamonds show the experimental data and the fit is given by the solid black line.

waveguide spectra taken in ethanol before dye adsorption are shown in grey (dashed lines). A strong shift of the waveguide modes to higher coupling angles can be seen. In addition the reflectivity of the minimum angles decreased and the peaks broadened slightly due to the increase in the extinction coefficient as dye entered the film and was optically excited.

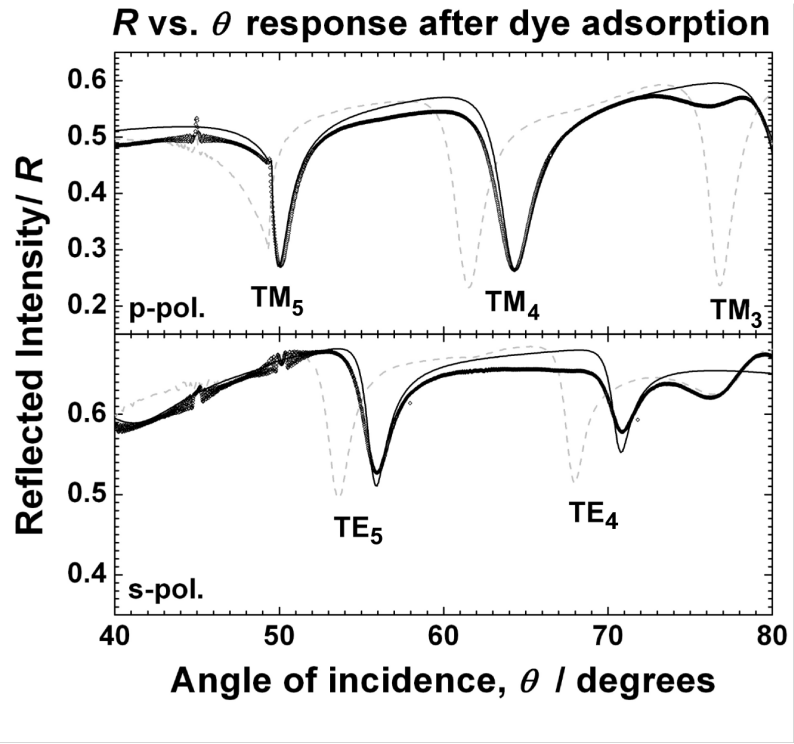

Figure 6.12: Optical waveguide spectra taken after (black circles) adsorption of dye into the $1.27nm$ $nc-TiO_2$. *The dashed grey line shows the experimental OWS spectra of the film in ethanol (from figure 6.11) for comparison.*

6.7.2 OWS Diffusion Kinetics Measurement

Figure **6.13** shows a kinetic measurement of the real time increase in refractive index and extinction coefficient obtained by tracking the minimum of the TM_4 mode throughout the experiment (inset shows shift in TM_4 mode). The position and shape of the TM_4 mode was fitted before and after dye adsorption using home-built fitting software based on the Fresnel equations of reflection and refraction at interfaces to model the behaviour of light in a multi layered system. In this case a four layer system was assumed, the fitting parameters are given in table 6.1. The fit is shown by the solid lines in figures 6.11 and 6.12.

	Layer	Thickness / nm	n	k
1	Prism	0	1.84498	0
2	Gold	35.824	0.312	3.8230
3a	TiO2 film[*1]	1269.89	1.7942	0.0055
3b	TiO2 film[*2]	1269.89	1.8192 Δn = 0.0245	0.0075 Δk = 0.0020
4	Ethanol	0	1.3592	0

Table 6.1: Layer model and fitting parameters used to fit the TM_4 *mode before and after dye adsorption. (*[*1] *before dye attachment,* [*2] *after dye attachment)*

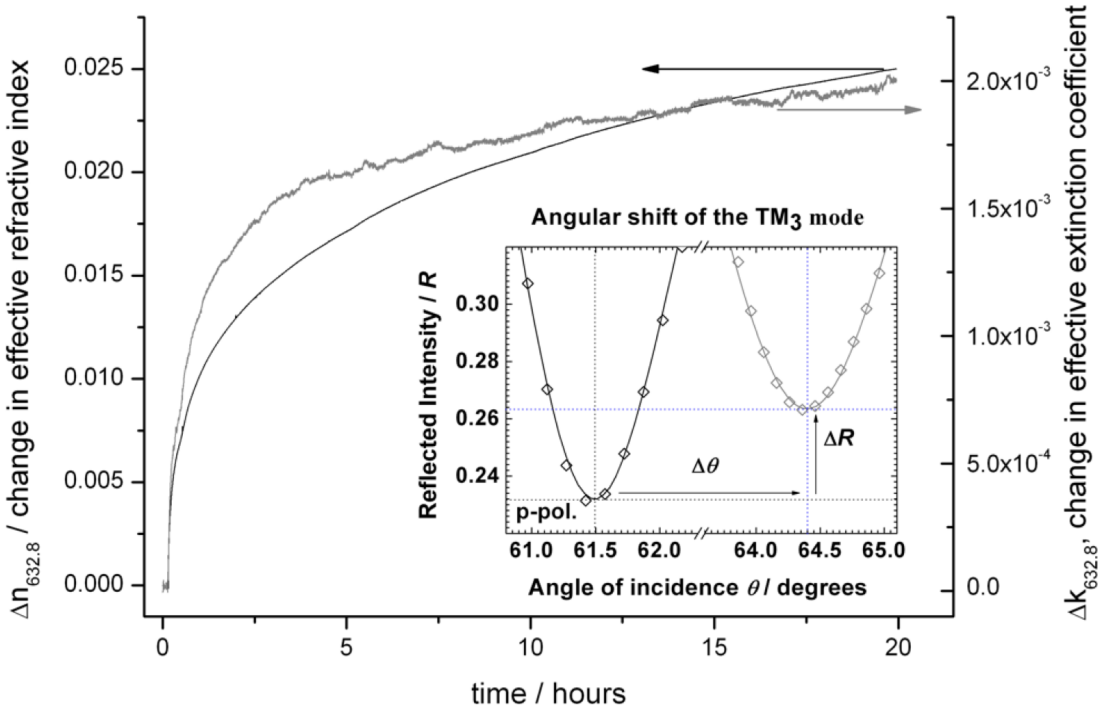

Figure 6.13: Kinetic plot showing the changes in both the composite refractive index, n_{xy}, and the extinction coefficient, k_{eff}, of the TM_4 mode with time. Inset shows the change in the TM_4 mode before and after dye adsorption.

In order to relate the OWS signal (i.e. change in angular position of the reflectivity minimum corresponding to the TM_4 mode) to the absolute amount of absorbed dye it was necessary to construct a calibration curve from a dilution series of the ruthenium 535 bis-TBA dye in $0.1mol\ dm^{-3}$ ethanolic KOH and also in pure ethanol. This allowed for both the quantification of total amount of dye desorbed by ethanolic KOH and also for increase in the extinction coefficient, k, in pure ethanol to be related to a dye concentration. In addition to measuring dye uptake by OWS *(A)*, a second sample *(B)* of identical $meso-nc-TiO_2$ film was immersed in a $3\cdot10^{-4}mol\,dm^{-3}$ solution of ruthenium 535 bis-TBA dye in ethanol. The dye was allowed to adsorb for the same period of time over which OWS was measured and then the dye was desorbed with ethanolic KOH and the dye concentration was quantified and directly compared to that measured by the OWS experiment.

Both films (see figure 6.14) were dyed for exactly the same amount of time, however, for one sample (in the OWS experiment) the dye solution was continuously cycled by a peristaltic pump whereas the second sample was left in dye solution with no stirring. In the case of this adsorption study the slides were both immediately dried after dye adsorption and the dye removed in $0.1mol\ dm^{-3}$ ethanolic KOH. Before the OWS measurement, UV/Vis absorbance spectra for various concentrations of N719 dye were obtained in pure ethanolic

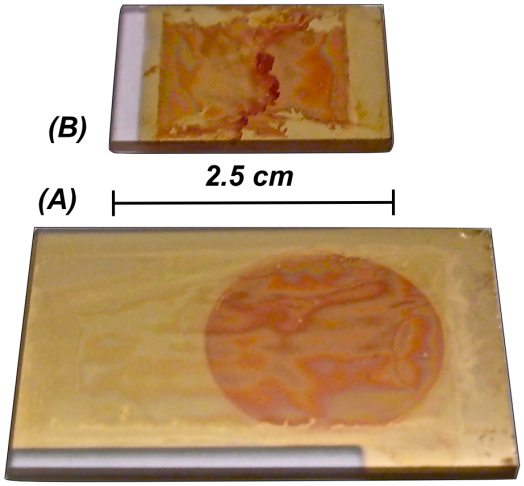

Figure 6.14: Photograph showing the two $meso - nc - TiO_2$ film on gold-coated glass samples after 20h exposure to a $3x10^{-4} mol\ dm^{-3}$ solution of ruthenium 535 bis-TBA dye in ethanol. (A) was homogeneously impregnated with dye molecules throughout the (circular) area which was in contact with the dye solution, whereas the cords in (B) are clearly visible with bare eye, indicating inhomogeneous dye sensitisation.

KOH, as a function of wavelength (figure 6.15 (left)).

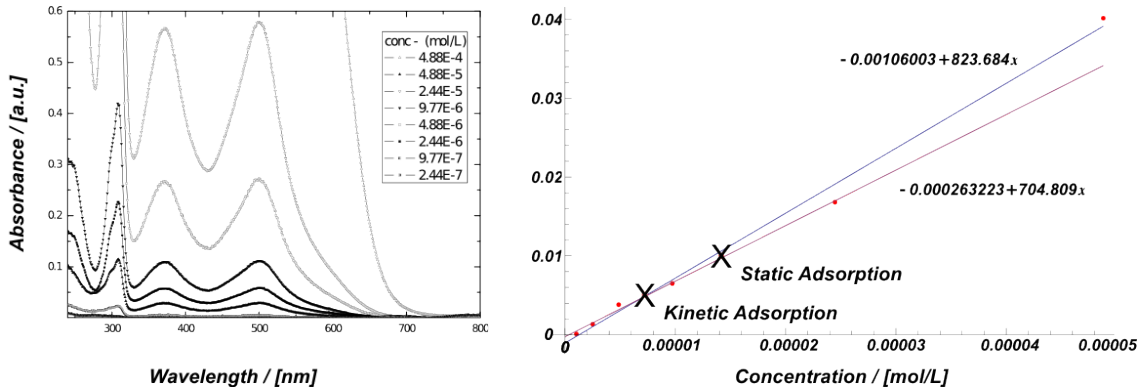

Figure 6.15: UV/Vis spectra of N719 dye in ethanolic solution at different concentrations served as reference. The absorption at $\lambda = 633nm$ is plotted against the different concentrations. The absorption values from the desorption measurements are marked with an X in the plot.

The absorbance at $632.8nm$ was plotted *versus* dye concentration (see 6.15 (right)) in order to determine the slope which gives the molar absorption coefficient, ϵ, in this solvent and for this wavelength (complex refractive index of dye is wavelength dependent) using the Beer-Lambert law[25]:

$$\epsilon = \frac{A}{lc} \tag{6.27}$$

where l is the path length of the light beam and c is the concentration of the dye. The molar absorption coefficient of ruthenium 535 bis-TBA dye in $0.1 mol\ dm^{-3}$ ethanolic KOH was measured to be $705 mol^{-1}\ dm^3\ cm^{-1}$ at $\lambda = 632.8nm$ from the reference meas-

urements in the same concentration region as samples *(A)* and *(B)* (see figure 6.16). The individually calculated molar absorption coefficients were $664 mol^{-1}\ dm^3\ cm^{-1}$for *(A)* and $684 mol^{-1}\ dm^3\ cm^{-1}$ for *(B)*. The total amount of dye desorbed from the films was $2.93{\cdot}10^{-8} moles$ for *(A) the* film used in the OWS kinetics experiment, and $5.72{\cdot}10^{-8} moles$ for *(B)* the film dyed in the non-stirred solution. These values correspond to $1.80 \cdot 10^{-4} mol\, cm^3$ and $3.51 \cdot 10^{-4} mol\ cm^3$ of the mesoporous film volume for the stirred and non-stirred adsorption, respectively. Relating these numbers to the pore space of the $meso-nc-TiO_2$ films, the concentration of dye after 20h within the pore space was calculated to be $0.18 mol\, dm^{-3}$ for *(A)* and $0.35 mol\, dm^{-3}$ for *(B)*, this, again, corresponds to a (internal) surface coverage (with an approximated value of $1.65 nm^2$ for the surface area of the N719 dye) of $3.41 \cdot 10^6 molecules\, cm^{-2}$ for *(A)* and $5.97 \cdot 10^6 molecules\, cm^{-2}$ for *(B)*, assuming that all dye present in the pore space was adsorbed to the $meso - nc - TiO_2$ walls. OWS measurements of the mesoporous films infiltrated with ethanol (before the adsorption experiments) determined the effective (i.e. accessible) pore volume to be identical to the total pore volume, this means that no isolated voids were present and that the EMA was still valid for the analysis of the adsorbed molecules. The total desorbed dye from sample *(A)* was used as a benchmark to check the accuracy of the total dye measured by waveguide spectroscopy.

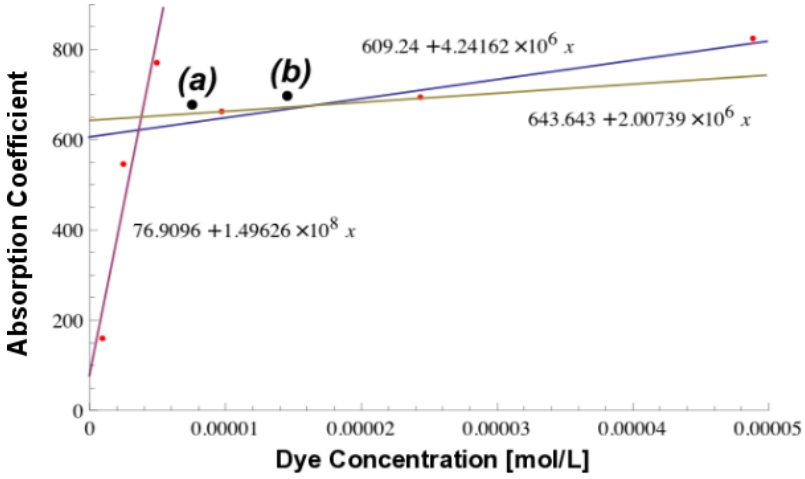

Figure 6.16: Interpretation of UV/Vis data for determination of the absorption coefficient of N719 dye in ethanol.

The total change in the effective extinction coefficient, $\Delta k = 0.002$ in sample *(A)*, was related to the total change in absorber density (and hence concentration) in the film using equations **6.25** and 6.26.

k defines how effectively a particular substance absorbs electromagnetic radiation. It can be characterised by the two interrelated optical properties, i.e. the absorption cross-section and the molar extinction coefficient. The value of k is experimentally obtained

via successive fitting of the Fresnel reflectivity to the recorded angular reflectivity as explained in more detail in the theory chapter. Molar absorption coefficient and absorption cross-sections are interrelated through

$$\sigma_a = \frac{2.303 \times 1000 \times \epsilon}{N_A} \tag{6.28}$$

where N_A is Avogadro's number. The absorption cross-section σ_a, calculated from UV-Vis measurements of the dye in ethanol, was $2.69 \times 10^{-18} cm^2$. With this a change in absorber density, N, of $1.56 \times 10^{20} cm^{-3}$ could be calculated, which relates (for sample *(C)*) to an increase in dye concentration of $4.2 \times 10^{-8} moles$ or $2.6 \times 10^{-4} mol\, cm^{-3}$ of the pore volume within the film. This value is in good agreement with the number obtained by desorbing the dye from films with KOH. *(A)* The kinetic OWS curves for dye attachment show that the extinction coefficient reached equilibrium more quickly than the increase in refractive index. This is likely to be due to quenching of the optical transition at higher dye coverages due to aggregation, so the change in extinction coefficient is measuring the active dye in the film.

The $\Delta n_{xy} = 0.025$ for the whole film can also be related to the dye concentration if the change in composite refractive index with dye concentration is known. A dn/dc measurement of 535 bis-TBA dye in ethanol was carried out and at low concentrations a linear increase in refractive index with dye concentration was observed.

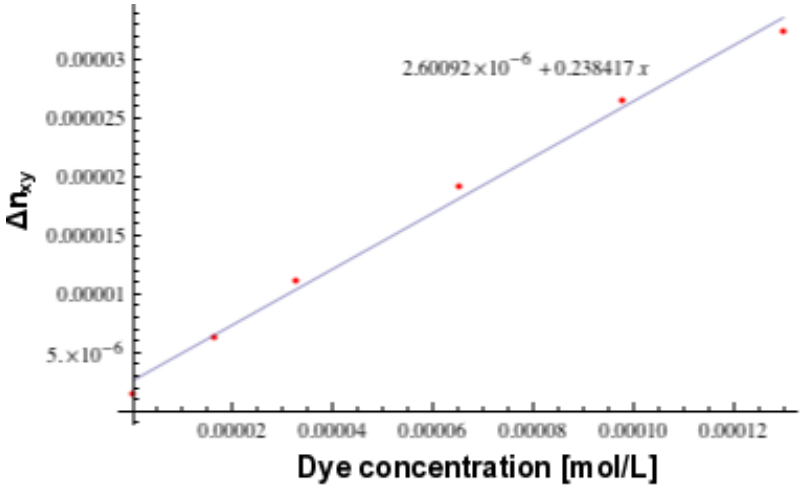

Figure 6.17: dn/dc measurement of low concentrations of 535 bis-TBA dye in ethanol shows linear increase in refractive index with dye concentration

If it is assumed that the same relationship applies at high dye concentrations the total dye in the film can be calculated to be $\sim 5 \cdot 10^{-9} moles$ or $\sim 2.98 \cdot 10^{-5} mol\, cm^{-3}$ of film volume. This is in reasonably good agreement with the total dye measured by KOH desorption. Unfortunately this method relies on the assumption that the linear relationship between

refractive index and concentration continues at high dye concentrations and when the dye is interacting with the surface of a porous oxide. This is extremely unlikely as 535 bis-TBA dye aggregates at relatively low concentrations leading to non-linear behaviour and it is unrealistic to think that the proximity of the titania in the pores can be ignored. It is therefore a relatively inaccurate way of calculating dye occupancy.

N719 Dye in Pores	**Total Amount** $[moles]$	**Concentration** $[mol\,cm^{-3}]$	**Surface Coverage** $[molecules\,cm^{-2}]$
(A) stirred KOH desorption	2.93×10^{-8}	1.80×10^{-4}	3.41×10^{6}
(B) non-stirred KOH desorption	5.72×10^{-8}	3.5×10^{-4}	5.97×10^{6}
(C) Δk	4.2×10^{-8}	2.6×10^{-4}	4.89×10^{6}
(D) dn/dc from Δn	$\sim 5 \times 10^{-9}$	$\sim 3 \times 10^{-5}$	-

Table 6.2: Overview of characteristic data of N719 dye adsorption experiments.

The total change in the effective refractive index of the film can be used to calculate a second, independent, value of the total amount of dye in the film. The Bruggeman expression is used to calculate the change in the dielectric constant of the pores before and after dye adsorption. It was assumed that the dielectric constant for the TiO_2, as well as the film porosity did not change throughout the experiment. It was therefore possible to calculate that the refractive index of the pores was $n_{pores} = 1.41$. The pore volume was $1.7 \cdot 10^{-5}\,cm^3$; assuming a refractive index of $n = 1.5$ for the dye this suggests that 16% of the pore volume was filled with dye after the 22 hours of the experiment.

One interesting observation is that the kinetics of dye uptake as measured by tracking n_{xy} and k are quite different. The extinction coefficient increases rapidly for five hours and then reaches equilibrium. In contrast, the refractive index of the film increases more slowly and is still increasing after 22 hours. One possible explanation is that after five hours the dye starts to aggregate and self-quench, whereas the refractive index is only dependent on the total amount of dye in the pores not just the optically active dye.

6.7.3 Fitting of OWS Diffusion Kinetics

The data obtained from desorption experiments (see table 6.2) allowed for quantitative fitting of equation 6.19 to OWS kinetics as shown in figure 6.18. A good fit of equation 6.19 to the signal progression during the *in-situ* monitoring of dye adsorption was only observed in the initial stage of the experiment, i.e. in the initial adsorption region of the $meso - nc - TiO_2$.

The differing time response of the experimentally obtained data, when compared to the simulation (which is rooted in the diffusion profile $c(x,t)/c_0$ of dye concentration inside the $meso - nc - TiO_2$ film and consequently also in the induced refractive index profile

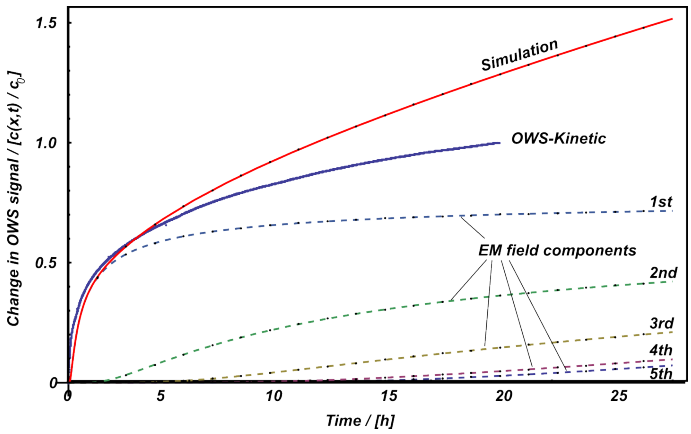

Figure 6.18: The sum of the solutions of equation 6.19 for x-values according to the location of peak intensities of the EM field within the mesoporous film. The dashed curves depict the diffusion profile as seen by the individual EM field portions. The numbering is according to time dependant signal contribution as a function of the diffusion rate, i.e. 1st = EM field at solution/film interface, 5th = EM field at film/substrate interface..

$\Delta n_{x,y}(x,t)/\Delta n$) was attributed to the profile of the EM field distribution as present at the TM_4 mode resonance which was used for the kinetic $\Delta n_{x,y}$ tracking. It is well-known that modes of different order, e.g. comparing a higher order waveguide mode to the surface-bound TM_0 mode (i.e. surface plasmon), exhibit a time- and therefore diffusion-dependant delay in their sensing signal. This intrinsic feature of EM field distributions can be applied for diffusion monitoring[8] as the TM_0 mode gives a distinct contribution to the signal when the diffusive species reaches the film/substrate interface. However, in order to utilise this phenomenon it is necessary to apply different spectroscopy techniques where more than one mode (including the TM_0 mode) is simultaneously observed or to restrict the experimentally obtained information to only the Diffusion time needed to reach the film/substrate interface by solely monitoring the surface bound TM_0.

Considering the diffusion profile described by equation 6.19, and given the diffusion is very slow ($D_{eff} \ll 10^{-6} cm^2\, s^{-1}$, which is a common value for diffusion constants of organic molecules in ethanol[37]), it was possible to resolve the refractive index distribution throughout the film thickness by monitoring only one waveguide mode.

The sensing signal of a single mode (here TM_4) does not exhibit linear response to locally restricted diffusion induced by $\Delta n_{x,y}(x,t)$, but rather from a periodic delay (due to the EM field intensity profile within the film) which is caused by diffusion. This characteristic, however, can be exploited to resolve the concentration gradient within the film caused by molecular transport processes. The great advantage of this technique compared to the above mentioned SP based measurements is the fact that the EM field of the waveguide modes is spread out through the whole film and therefore allows the tracking of diffusing species through the whole film. Also, due to the periodic intensity changes in the EM field

profile it is possible to extract spatial information and to determine $\Delta n_{x,y}(x,t)$.

Based on acknowledge of the theoretical distribution of the TM_4 mode it was possible to simulate the time response of reflectivity changes for the OWS *in-situ* kinetic measurements. Therefore, in order to gain information on the spatial distribution of dye within the mesoporous film at the end of the kinetic measurement, the sensing signal contributions were fractionised according to the modelled EM field intensity distribution (see figure 6.9) for the film under investigation.

Each intensity intensity peak of the EM field was ascribed to a position $x = d_{film}$ within the film and its contribution to the overall sensing of the diffusion profile was iteratively adjusted to match the diffusion profile as seen from the position of each individual intensity peak (dashed curves in figure 6.19) as well as the overall sensing signal (red curve in figure 6.19) as the sum of the fields. The diffusion constant resulting from this simulation was as low as $D_0 = 1.8 \times 10^{-13}$.

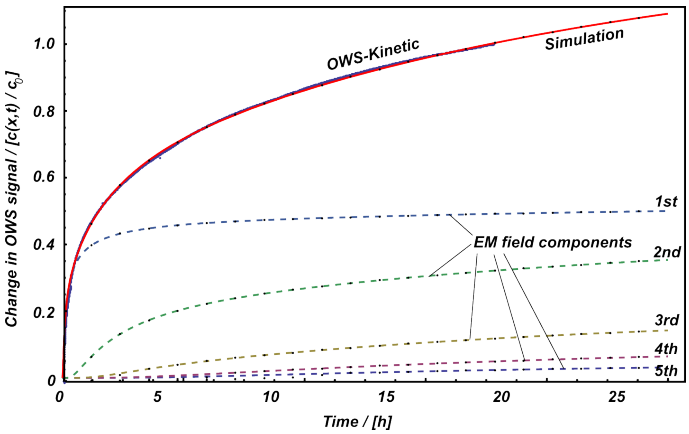

Figure 6.19: Modelled field intensities are shown in figure 6.9, accordingly the position x at each peak intensity was simulated and the diffusion profile seen from the position of each individual mode as well as the overall sensing signal (red line) as the sum of the fields. Fractionation, however, could also not fit the signal, not until the individual fractions were iteratively fitted to result in an overall signal that matches the kinetics signal by multiplying with

The iterative adjustment of equation 6.19 for each intensity peak of the electric component of the EM field, based on the function of the diffusion profile as seen by the EM field fragments is illustrated in figure 6.19. As a result a position-dependant signal contribution factor could be extracted. Interpolation between the points resulted in a characteristic profile of the dye distribution within the film at the time $t = 22h$ (shown in figure 6.20). This characteristic distribution profile indicated a strong influence of diffusion on the adsorption process.

Over the course of this study dye uptake in films of a variety of thickness and porosity was measured. Unsurprisingly the higher the film porosity, the more quickly equilibrium dye coverage was reached. Therefore, in order to allow comparison of mesoporous materials,

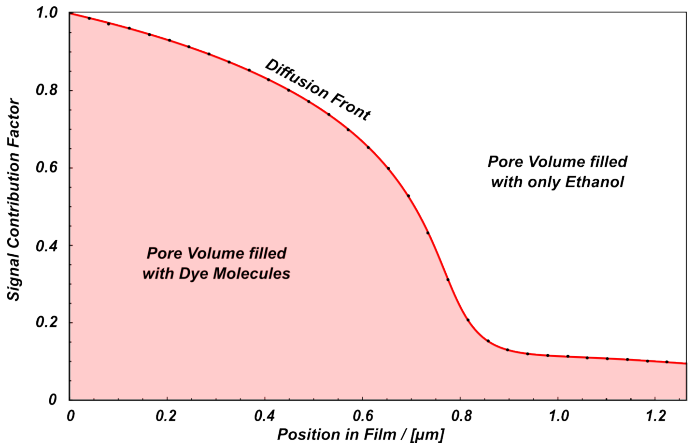

Figure 6.20: Signal Contribution as a function of EM field-position in the film, obtained from iterative fitting of the individual EM field components in the film

the values for the diffusion constant are given in terms of $D = D_{eff}/porosity$. The dye uptake seemed to be determined only by the rate of diffusion to the sites of adsorption, it is therefore plausible that the film thickness and dye concentration (constant and unlimited available during the sorption process) had no effect on the dyeing rates. All uptake curves were identical during the initial phase before approaching the plateau of saturation, which, together with the aforementioned findings strongly suggested that a mathematical model, describing diffusion limited adsorption, could be used to interpret the sorption kinetics.

Diffusion Limited Adsorption Model

In principle it was necessary to account for much faster adsorption of dye than its transport through the mesoporous film, and also that the region, after being passed by the diffusion front is totally covered with dye molecules and therefore no more adsorption take place, whereas the region in front of the diffusion front is not dyed at all and the concentration of the dye in this regime is zero. In such cases a linear diffusion gradient is mandatory to describe the dyeing process. As a consequence, this would cause a decrease in the rate of adsorption inversely proportional to the growth of dye-covered region as illustrated in figure 6.21. This simple model is characterised by the time dependence of the normalised dyed layer thickness:

$$\frac{x_0}{d} = \sqrt{\frac{2D_{eff}c_0}{\theta_0 d^2}}\sqrt{t} \tag{6.29}$$

where d is the layer thickness, t the time, c_0 the initial dye concentration, θ_0 is the maximum amount of dye molecules adsorbed per volume of porous. The amount of dye is assumed to be proportional to the position of the region of adsorption x_0.

The assumption that the total amount of absorbed dye in the mesoporous film is simply proportional to the to the position of the region of adsorption has already been applied for the description of dye sensitisation of mesoporous materials for solar cell application[11].

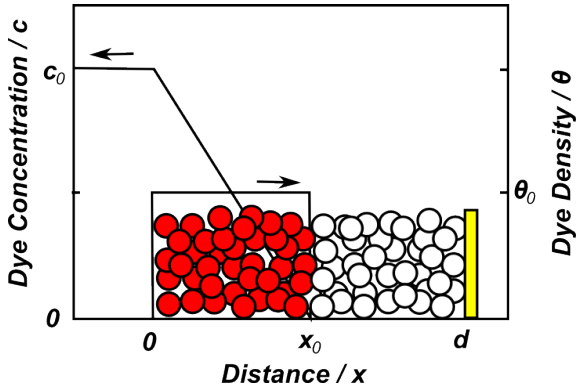

Figure 6.21: Representation of dye concentration in solution and dye coverage on the TiO_2 particles according to the suggested model. The dye concentration decreases linearly between c_0 at $x = 0$, the interface between porous layer and bulk solution, and zero at $x = x_0$, the region of adsorption. The amount of dye adsorbed is identical θ_0 in the region between $x = 0$ and $x = x_0$ and zero elsewhere. Inset: optical micrographs of cross sections of a $10\mu m$ thick film after 30 and $100min$ in dye solution. Bright at the right the glass substrate.model adapted from reference[11]

The model was applied to interpret the results obtained by *in-situ* monitoring of the adsorption process by OWS, however, this model did not fit the time dependant progression of the experimental data. Figure 6.22 shows the attempts to fit the model to the experimental values for the change in composite refractive index (6.22, left) and also for the change of the extinction coefficient. (6.22, left). The dashed lines represent theoretical kinetic progression, simulated for the dye concentrations obtained for samples *(B)* and *(C)*. Apparently, it was only possible to either fit the function to the initial regime of relatively fast rate of adsorption or to the long term behaviour with a much slower adsorption rate, however, only fitting of the complete kinetic scan curve could not be achieved with this method. Nevertheless, the simulation attempts showed that the two kinetic curves, for Δn and Δk, were characterised either by a fast or a slow process, whereat the kinetic progression for Δn was in good accordance to the slow rate, the kinetic curve for Δk was predominantly governed by the fast initial rate.

Sigmoid Sorption Model

The diffusion front in figure 6.20 can also be interpreted (within the accuracy of this assumed model) by a sigmoidal diffusion profile for the regime of mass transport, and therefore suggests the application of another version of the model for describing diffusion limited adsorption processes, which describes diffusion into a film of thickness d. This formula was originally outlined by Carslaw and Jaeger[10] for films which have two bound-

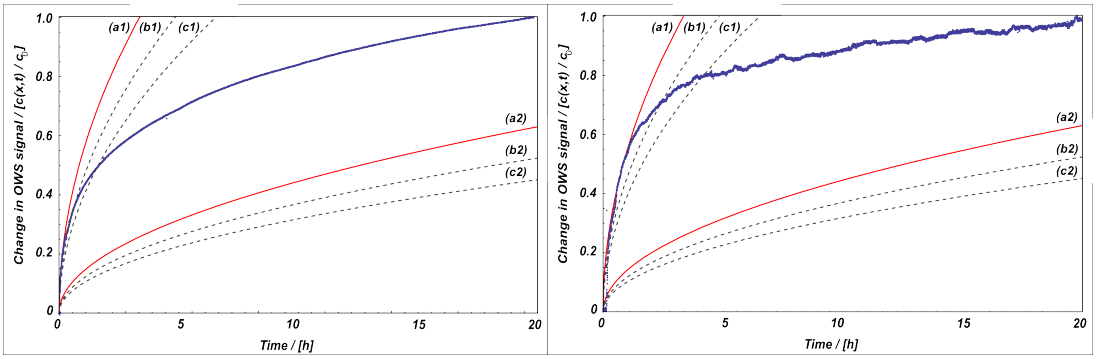

Figure 6.22: Two adsorption rate regimes were observer for both n and k changes, left and right, respectively. According to the model system, shown in figure, it was possible to fit equation 6.29 separately to either the fast initial region or to the much slower long term kinetics. The red curves illustrate the progression of the simulated sorption kinetics where (a1) for names the fit for the initial fast process and (a2) the slower long term process for both Δn and Δk, respectively.

aries, one at the substrate (in this case the gold layer) and one at the solution side. When dye is added to the solution side of the film it is assumed that the surface concentration, $\varphi(t)$, exponentially reaches a steady equilibrium value (equation 6.30).

$$\phi(t) = C_0\{1 - exp - (\beta t)\} \tag{6.30}$$

In practise this means that, as $\beta \rightarrow \infty$, the surface concentration rises instantaneously to C_0. The total amount of dye, $M(t)$, in the film at time t can then be related to the diffusion coefficient and film thickness by equation 6.31.

$$\frac{M(t)}{C_0} = 1 - exp - (\beta t)\sqrt{\frac{D}{\beta d^2}}tan(\sqrt{\frac{\beta d^2}{D}}) - \frac{8}{\pi^2}\sum_{n=0}^{n=\infty}\frac{exp\{-(2n+1)^2\pi^2 Dt/4d\}}{(2n+1)^2[1-(2n+1)^2\{D\pi^2/(4\beta d^2)\}]d} \tag{6.31}$$

Equation 6.31 was used to fit the absorption curve for the increase in refractive index with time, allowing the diffusion coefficient to be estimated. The constant β was set at 100, which assumed that the solution was injected rapidly into the cell and that the surface concentration did not effect the early kinetics. The film thickness d was taken from the fits for the OWS data. C_0 was the equilibrium dye concentration within the film. The only variable was the diffusion coefficient D. The fit was obtained for the adsorption curve during the first five hours of the Δn measurement and the diffusion coefficient was calculated to be $6 \cdot 10^{-11} cm^2\, s^{-1}$.

On the first attempts it was not possible to fit the model 6.31 to the whole range of experimentally obtained values, thus only approximations could be made that roughly fitted the kinetic plot. Nevertheless, upper and lower boundaries were established in order to set limits and to show the variance (figure 6.23) .

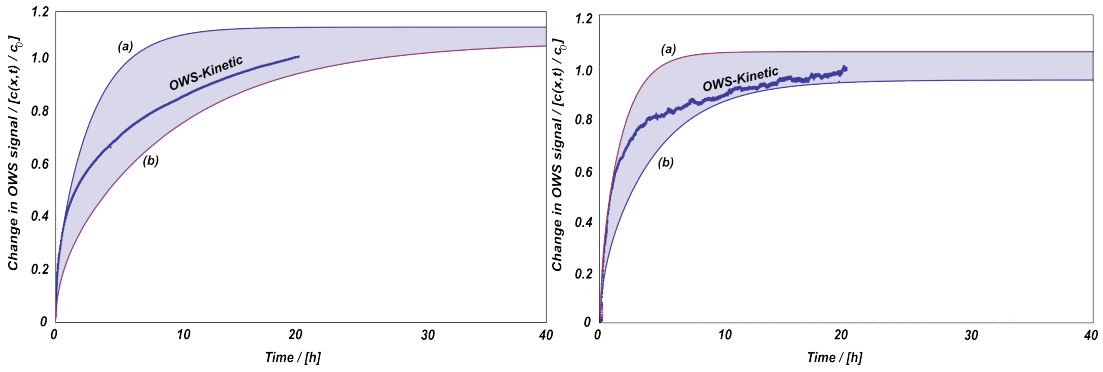

Figure 6.23: Simulated sorption-time curves approximating OWS-kinetic data with (a) diffusion coefficients fitted to the initial phase of absorption and (b) to the slower long time sorption regime.

It became apparent that the actual curve could not be fitted with one throughout constant diffusion coefficient, but can be described by the overlap of two simulated curves with different but constant rate coefficients at certain ratios, thus implying two superimposed diffusion/sorption processes to be simultaneously present during the dyeing process. In order to obtain non-trivial solutions, the two processes were assumed to occur in parallel and with constant and identical diffusion coefficients for both, Δn and Δk kinetics. It was assumed that both processes contributed to measurable changes in the refractive index and extinction coefficient of the dye within the film. Different optical properties (n and k) may arise due to the directional orientation of dye molecules with respect to the electric and magnetic field components of the incident light, or, more likely, due to close approximation to the surface of the $meso-nc-TiO_2$ and the consequently formed (chemical) interactions.

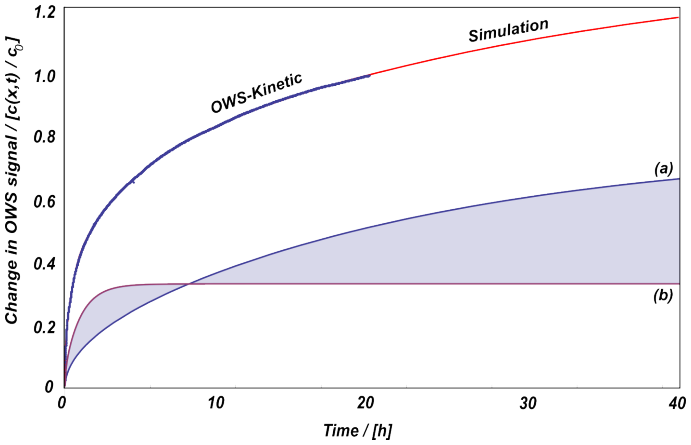

Figure 6.24: Fitting of kinetic OWS data for the change in refractive index due to dye adsorption in $meso-nc-TiO_2$ by superimposing two parallel transport processes. Both processes were simulated with equation 6.31, with $D = 1.86 \times 10^{-13}$ for curve (a) with a contribution of 0.70 to the total signal at equilibrium whereas a diffusion coefficient of $D = 3.78 \times 10^{-12}$ was obtained for curve (b) with a contribution of 0.30 to the total signal at equilibrium.

The assumption can be made that surface-bound molecules are able to inject electrons into the conduction band of the titania after they have been excited by absorbing portions

of the incident probing light. Electron transfer processes from the dye molecules, which are chemically adsorbed at the titania surface, and the nanocrystalline semiconductor could result in increased extinction coefficients. Provided that the ethanol acts as hole scavenger and the dyes are continuously regenerated, this could significantly alter the measured extinction coefficient, k, signal. The change in refractive index, n, on the other hand would just be a result of integration over the absolute amount of dye within the film, and would not distinguish between surface-bound and solubilised species within the pore volume.

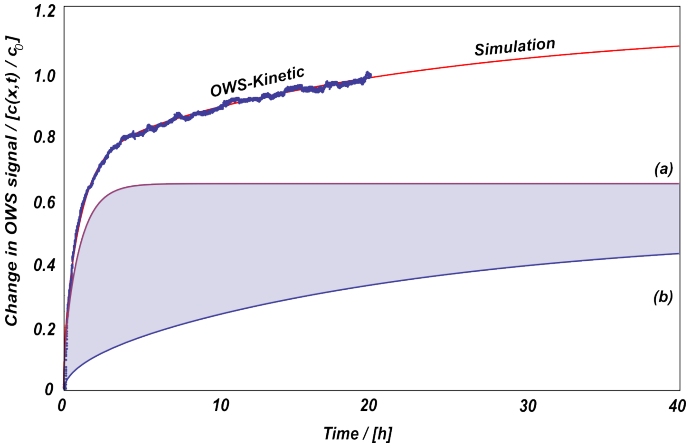

Figure 6.25: Fitting of kinetic OWS data for the change in extinction coefficient due to dye adsorption in $meso - nc - TiO_2$ by superimposing two parallel transport processes. Both processes were simulated with equation 6.31, with $D = 1.86 \times 10^{-13}$ for curve (a) with a contribution of 0.44 to the total signal at equilibrium whereas a diffusion coefficient of $D = 3.78 \times 10^{-12}$ was obtained for curve (b) with a contribution of 0.56 to the total signal at equilibrium.

If this theoretical assumption really is the reason for the variation of the adsorption kinetics measured by tracking n and k, the effect could be systematically investigated by variation of the excitation wavelength. This would change the fraction of the signal due to surface-bound molecules as they have the characteristic absorption maxima at certain wavelengths. Parallel to this experiment, it would be of great interest to combine this photo-excitation-based-loss experiment to *in-situ* measurement of the injected charges, i.e. monitoring the current produced by photoexcitation, and consequently correlate both rates to to each other.

6.8 Conclusion

OWS is introduced as a powerful analytical method to determine processes occurring within mesoporous films. This technique allows for monitoring molecular transport and adsorption in real time with high accuracy. One major goal in the manufacture of efficient dye sensitised solar cell devices is the optimising of dye sensitisation. As this step is one

of the key processes guaranteeing high overall efficiency of the cell very fast dye uptake leading to full-monolayer coverage is representing a high priority objective. Moreover, it is required to optimise the dye uptake leading to maximum amount of dye chemisorbed to the nano-crystalline titania surface, which again, allows for highly efficient light absorption.

It is important to take into account that the measured diffusion coefficients are effective diffusion coefficients which are an average for all the dye in the film. By now it is not possible to measure the local diffusion coefficient with the herein presented OWS technique. However, based on the homogeneously distributed pore space throughout the $meso-nc-TiO_2$ films this value can suit very well as a close estimate, thus help to predict optimal sorption times for DSSC fabrication. Nevertheless, the values are also afflicted with a quite large error since the sigmoid sorption model does not represent a porous film but rather a volume into which molecules diffuse in a linear fashion. In addition there may be uncertainty as to the accurate refractive index of the dye species, as well as the impact of matrix-interaction on its change.

Baering in mind the above mentioned inaccuracity, OWS was applied to monitor adsorption of ruthenium dye molecules out of ethanolic solution onto $meso-nc-TiO_2$ in real time. These measurements show transport to be mostly diffusion limited. The observed kinetic behaviour for time-dependant Δn and Δk suggests at least two processes taking part in the total mass transport. The difference between the Δn and Δk adsorption isotherm is consistent with reported data for comparable systems[14]. Accordingly, the absolute mass transport through the mesoporous structure was attributed to two parallel occurring processes with individual but constant diffusion coefficients of $D_1 = 1.86 \cdot 10^{-13} cm^2\, s^{-1}$ and $D_2 = 3.78 \cdot 10^{-12} cm^2\, s^{-1}$, which could be ascribed to surface-bound and solubilised dye species.

In summary, however, it is shown that the adsorption of dye molecules through the porous network is mostly diffusion limited with diffusion constants found to be, compared to the behaviour in pure solvent (ethanol $D_b \approx 10^{-6} cm^2\, s^{-1}$) six to seven orders of magnitude lower as measured for D_1 and D_2, respectively. The slowing down is related to the mesostructured architecture of the material by factors describing porosity, pore-size, constrictivity and tortuousity. These characteristic features were summarised in the matrix factor $q_m \approx 10^6 - 10^7$. Further work needs to be done to clarify the exact mechanism for these effects.

Bibliography

[1] Adler, P. M. *Porous Media - Geometry and Transports* (Butterworth-Heinemann, 1992).

[2] Argazzi, R., Iha, N. Y. M., Zabri, H., Odobel, F. & Bignozzi, C. A. Design of molecular dyes for application in photoelectrochemical and electrochromic devices based on nanocrystalline metal oxide semiconductors. *Coord. Chem. Rev. 248:1299Ð316* **248**, 1299–316 (2004).

[3] Awazu, K. *et al.* High sensitivity sensors of perforated waveguides. *Opt. Express* **15**, 2592–2597 (2007).

[4] BA., G. Interfacial processes in the dye-sensitized solar cell. *Coord. Chem. Rev.* **248**, 1215–24 (2004).

[5] Beekman, J. W. & Froment, G. F. *Ind. Eng. Chem. Fundam.* **21**, 243 (1982).

[6] van Brakel, J. & Heertjes, P. M. *Intl. J. Heat Mass Transfer* **17**, 1093 (1974).

[7] Bruggeman, D. A. G. Berechnung verschiedener physikalischer konstanten von heterogenen substanzen. i. dielektrizitaetskonstanten und leitfaehigkeiten der mischkoerper aus isotropen substanzen. *Annalen der Physik* **416**, 636–664 (1935).

[8] Cameron, P. J. *et al.* Optical waveguide spectroscopy study of the transport and binding of cytochrome c in mesoporous titanium dioxide electrodes. *J. Mater. Chem.* **18**, 4304–4310 (2008).

[9] Chiba, Y. *et al. Jpn. J. Appl. Phys.* **45**, 638 (2006).

[10] Crank, J. *The Mathematics of Diffusion, Second Edition* (Oxford University Press, 1986).

[11] Duerr, M., Schmid, A., Obermaier, M., Yasuda, A. & Nelles, G. Diffusion properties of dye molecules in nanoporous tio2 networks. *J. Phys. Chem. A* **109**, 3967–3970 (2005).

[12] Duncan, W. R. & Prezhdo, O. V. Theoretical studies of photoinduced electron transfer in dye-sensitized tio2,. *Annu. Rev. Phys. Chem.* **58**, 143–84 (2007).

[13] Feng, C. F. & Stewart, W. E. *Ind. Eng. Chem. Fundam.* **12**, 143 (1973).

[14] Fillinger, A. & Parkinson, B. A. The adsorption behavior of a ruthenium-based sensitizing dye to nanocrystalline tio2 coverage effects on the external and internal sensitization quantum yields. *Journal of The Electrochemical Society* **146**, 4559–4564 (1999).

[15] G. F. Froment, K. B. B. *Chemical Reactor Analysis and Design* (John Wiley & Sons, New York, 1979).

[16] Hagfeldt, A. & Greatzel, M. *Acc. Chem. Res.* **33** (2000).

[17] Johnson, M. L. F. & Stewart, W. E. *J. Catal.* **4**, 248 (1965).

[18] Kaerger, J. & M.Ruthven, D. *Diffusion in Zeolites and Other Microporous Solids* (Wiley & Sons, New York, 1992).

[19] Kaerger, J. & Ruthven, D. M. *Diffusion and Adsorption in Porous Solids in Handbook of Porous Solids* (Wiley-VCH Weinheim, Germany., 2002).

[20] Kron, G. *Electrochem. Sol. State Lett.* **6**, E11 (2003).

[21] Kuang, D. *et al.* High molar extinction coefficient ion-coordinating ruthenium sensitizer for efficient and stable mesoscopic dye-sensitized solar cells. *Adv. Funct. Mater.* **17**, 154–160 (2007).

[22] Lau, K. H. A., Tan, L., Tamada, K., Sander, M. S. & Knoll, W. Highly sensitive detection of processes occuring inside nanoporous anodic alumina templates: a waveguide optical study. *J. Phys. Cham. B* **108**, 10812–10818 (2004).

[23] Lu, G. Q. & Zhao, X. S. *Nanoporous Materials - Science and Engineering* (Imperial College Press, 2004).

[24] Memming, R. *Semiconductor Electrochemistry* (Weinheim, Germ.: Wiley-VCH, 2001).

[25] Nazeeruddin, M. *et al. J. Am. Chem. Soc.* **115**, 6382 (1993).

[26] Nazeeruddin, M. K. *et al.* A high molar extinction coefficient charge transfer sensitizer and its application in dye-sensitized solar cell. *Journal of Photochemistry and Photobiology A - Chemistry* **185**, 331–337 (2007).

[27] Qi, Z. M., Honma, I. & Zhou, H. Nanoporous leaky waveguide based chemical and biological sensors with broadband spectroscopy. *Appl. Phys. Lett.* **90**, 11102 (2007).

[28] Ruthven, D. M. *Physical Adsorption: Experiment, Theory and Applications* (Kluwer Academic Publishers, Dordrecht., 1997).

[29] Ruthven, D. M. & Post, M. *Introduction to Zeolite Science and Technology* (Elsevier, Amsterdam., 2001).

[30] Shklover, V. *et al. J. Solid State Chem., 132,* **60**, 132 (1997).

[31] Shklover, V. *et al. Chem. Mater.* **9**, 430 (1997).

[32] Shklover, V., Ovchinnikov, Y. E., Braginsky, L. S., Zakeeruddin, S. M. & Graetzel, M. *Chem. Mater.* **10**, 2533 (1998).

[33] Szymanski, J., Patkowski, A., Wilk, A., Garstecki, P. & Holyst, R. Diffusion and viscosity in a crowded environment: from nano- to macroscale. *J Phys Chem B.* **110**, 25593–7 (2006).

[34] Wakao, N. & Smith, J. M. *Chem. Eng. Sci.* **17**, 825 (1962).

[35] Wang, P. *et al.* Stable new sensitizer with improved light harvesting for nanocrystalline dye-sensitized solar cells **16**, 1806–1811 (2004).

[36] Zschiegner, Russ, S., Bunde, A. & Kaerger, J. Pore opening effects and transport diffusion in the knudsen regime in comparison to self- and (or tracer-) diffusion. *EPL* **78**, 20001 (2007).

[37] Lide, D. R. (ed.) *CRC handbook of chemistry and physics* (CRC Press, 2009).

Chapter 7

7 Grating-Coupled Optical Waveguide Spectroscopy of Mesoporous films

Contents

Abstract

With the aim of facilitating *in-situ* experiments on operating DSSCs, a holographic grating-coupler element was implemented with the $meso-nc-TiO_2$ waveguide. With this step not only the Kretschmann multi-layer configuration (i.e. prism/beam-alignment, index-matching, evaporation of thin gold layer) could be avoided, but also the fundamental problem of destructive chemical interaction of the I^-/I_3^- electrolyte solution with the gold layer was resolved. The highly reduced experimental complexity of this improved technique and the resulting advantage for integration with various other techniques and applications are discussed. Also changes to the sensing system, its capabilities and limitations are described.

In order to investigate the kinetics of dye adsorption onto $meso-nc-TiO_2$ pore walls with grating-coupled OWS, the amount of absorbed dye was monitored (*via* resonance angle shift due to a change of the composite refractive index of $meso-nc-TiO_2$) as a function of time. Accordingly, the experiment was run in kinetic tracking mode in order to monitor these changes. Differences between the kinetic response of n and k towards N719 dye adsorption were observed to be very pronounced, especially in the initial phase of the diffusion process. These preliminary results, clearly show the different sensitivities of the two probing techniques (Δn and Δk) related to diffusion and adsorption processes of dye molecules into and within $meso-nc-TiO_2$ waveguide films. Preliminary results of simulations and experimental data on refractive index and extinction measurements, as well as adsorption monitoring, and time-dependent kinetics scans are presented.

7.1 Integration with Dye-Sensitised Solar Cells

Optical waveguide spectroscopy gives the possibility for *in-situ* monitoring of processes on the nanometre scale within mesoporous films, thus opening up a range of application in science and technology. The majority of laboratory evanescent sensing systems, as well as commercial products, rely on prism coupling as the method employed to match photons for excitation of resonance phenomena in order to utilise modes of light.

One fundamental problem for the $meso-nc-TiO_2$ waveguide sensor, as introduced in the previous chepter, to be integrated with a DSSC is basically the fact that the electrolyte solution in the DSSC consists mainly of the I_3^-/I^- redox couple. Of all the halides, iodine exhibits the widest range of oxidation and pH conditions for the stabilisation of gold complexes. At $[Au] = 10^{-5}M$ and $= 10^{-2}M$, AuI_2^- is stable between $0.51V$ and $0.69V$

and at $pH < 12$. Gold iodide complexes are the most stable of all metal-halide complexes in aqueous solutions.

Iodine also exhibits the ability to exist as a polyhalide. The formation of the triiodide ion is shown in the following chemical reaction:

$$I_{2(aq)} + I^- = I_3^-$$

The formation of I_3^- allows for high solubility of iodine in solutions containing the iodide ion. Thus, I_3^- can actually serve as an oxidant for gold according to this half-cell reactions:

$$\text{(Anodic) } Au + 2I^- = AuI_2^- + e^-$$

$$\text{(Cathodic) } I_3^- + 2e^- = 3I^-$$

$$\text{(Net Reaction) } 2Au + I_3^- + I^- = 2AuI_2^-$$

$$\text{This again } 2Au + I_3^- + I^- => 2[AuI_2]^-.$$

The destructive interaction of the I_3^-/I^- species with the thin gold film at the $meso-nc-TiO_2$ film/substrate interface eliminates the possibility of using prism coupling in the Kretschmann configuration for in-situ monitoring of operating DSSCs. Therefore, it was necessary to develop the $meso-nc-TiO_2$ waveguide sensor further in order to allow full integration with an operating DSSC.

In this chapter the technologies and processes will be introduced to fabricate a $meso-nc-TiO_2$ waveguide system, which is capable of operating in an environment that contains the I_3^-/I^- redox couple. The operation of grating-coupled systems will be introduced and spectroscopic data will be discussed in detail.

7.2 Coupling Light to Waveguide Modes *via* Gratings

While prism couplers in the Kretschmann configuration are extremely versatile and very useful for studying thicker films in the range of up to several micrometres, they fundamentally rely on a thin metal (here $50nm$ of gold) coupling-film which interfaces the waveguide. The use of gold-coupling films may be avoided for prism coupling in the Otto-configuration (7.1*(a)*), but the practical operation of this technique (with the several nanometres wide air-gap between the prism base and the waveguide film) is not only

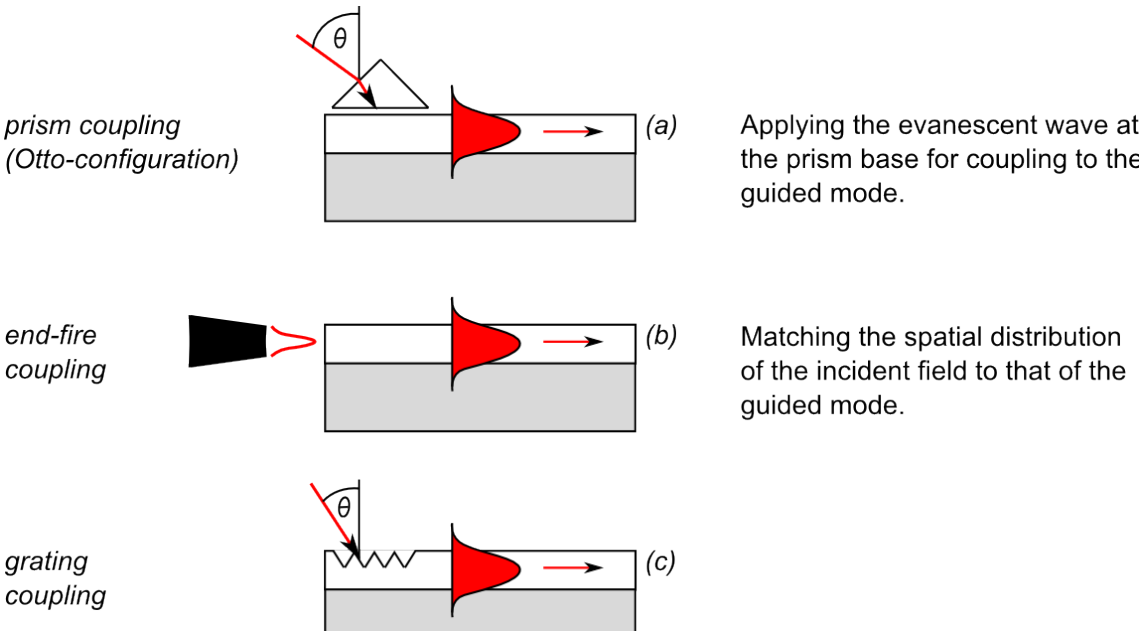

Figure 7.1: The three classical coupling techniques: (a) prism coupling, (b) grating coupling, (c) end-fire coupling.

extremely cumbersome, but also inadequate for the integration with operating DSSC devices where both sides of the multi-layer arrangement have to be accessible.

Alternatively, light can be coupled directly into the end face of the waveguide (7.1*(b)*). This co-called 'end-fire coupling' matches the spatial distribution of the incident field to that of the guided mode and is often applied to optical fibres and in communication applications. This technique needs highly precise adjustment of all components in order to achieve effective coupling of light into the waveguide and is therefore difficult to handle in combination with non-static operation (i.e. angular variation of incident light) of the waveguide.

Accordingly, in order to avoid using a gold film but also to allow stable and robust handling of the system, grating coupling was considered as the methode of choice (7.1*(c)*). The placement of structures with periodic density fluctuation between interfaces of optical multi-layer waveguides allows effective coupling of light to guided modes. Optical gratings are well-known elements in the field of integrated optics and can be fabricated by various techniques with high precision (e.g. optical and electron lithography, holography, and ion-etching). The simplest theoretical grating is of sinusoidal shape[1]. Characteristic for a grating are its periodicity or grating constant Λ and its groove depth. The groove depth is more often described (having a sinusoidal curve in mind) as the amplitude seen at half the profile depth.

The application of diffraction gratings as coupling element allows for the excitation of

[1] Gratings can have several grating constants and amplitudes that are not necessarily collinear and hence the grating can be two or even three-dimensional. This work focuses exclusively on one-dimensional gratings.

waveguide modes without the use of a gold layer, furthermore, the excitation can be incident from the top as well as from the back-side of the device, which, again, allows for an experimental platform with very versatile possibilities for application.

As was the case for prism coupling, a condition for waveguiding is phase-matching between the incident and the guided wave which has to be fulfilled. Also the refractive index of the waveguiding layer has to be higher than the refractive indices of the surrounding materials to ensure total internal reflection (TIR) on both interfaces of the waveguide layer and consequently for light guidance within the film. In order to depict this coupling platform, a ray optical model is applied in which a plane wave-field is incident at angle θ_i onto a grating with a grating period constant Λ on top of a waveguide structure (see figure 7.2).

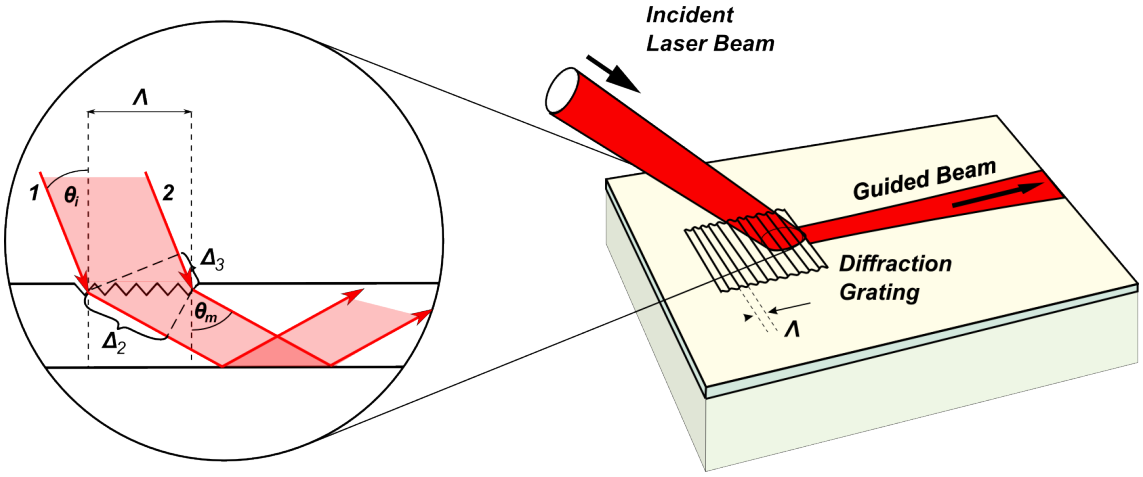

Figure 7.2: Illustration of the principle of light coupling to and from an optical waveguide via a grating coupler (right). Weights of the various diffraction orders depend on the groove shape. The coupling is adjustable by the grating amplitude as well as the groove shape. For in-coupling the mode m can be selected by adjustment of the angle θ_i (left). The guided light is detected at the end-face. [10]

A fraction of the light ray is, as a consequence of refraction, transmitted into the waveguide and continues to propagate within this structure with a propagation angle θ_m, based on TIR at both interfaces. In order to achieve constructive interference in the direction of propagation, the optical path difference of parallel light-rays has to be a multiple of λ, therefore

$$n_2\Delta_2 - n_3\Delta_3 = m\lambda, \quad m = 0, \pm 1, \pm 2 \tag{7.1}$$

The geometrical paths Δ_3 and Δ_2 can be expressed by the grating constant and the incident angle, the propagation angle:

$$n_2 sin\theta_i - n_3 sin\theta_m = m\frac{\lambda}{\Lambda} \tag{7.2}$$

There are specific resonance conditions where coupling of the incident light to a waveguide mode occurs, thus light guiding takes place. Each coupling condition allows one waveguide mode to be excited. These resonances can be accessed in two perpendicular planes of polarisation, TE-modes for s-polarised light and TM-modes for p-polarised light. Each individual mode has therefore its own propagation constant, β, or effective refractive index, N, which can be determined by measuring the resonant coupling angle, θ_m, for each mode and inserting it into the mode equation for N.

$$N = n_3 sin\theta_m + m\frac{\lambda}{\Lambda} \tag{7.3}$$

The effective refractive index, N, will change depending on the composite refractive index of the $meso - nc - TiO_2$ waveguide; hence it also depends on the concentration of molecules in a sample (placed within the pore space). The measurement of coupling angles, as in the case of the prism-coupling configuration, allows for an accurate determination of N.

An incoming light wave experiences the periodic structure, given by the grooves of the grating, as an array of scattering centres. After light undergoes scattering at the grating, the total field of the incoming light can accordingly be reconstructed in different diffraction orders from the portions of individual constructive interferences. These reconstructed waves can, if their in-plane components of the wavevector (of a given order) match the wavevector of the resonantly guided wave, excite guided optical modes.

Given a grating constant, Λ, the grating vector can be described with the magnitude:

$$|\mathbf{G}| = \frac{2\pi}{\Lambda} \tag{7.4}$$

with its orientation in the plane of the corrugated surface and perpendicular to the grating grooves. Accordingly, multiples of m can be added to the wavevector of the reflected field ($m = 0$), which is located in the $x - y$-plane, thus

$$\mathbf{k}_{diffracted} = \mathbf{k}_{photon} + m\mathbf{G} = \begin{pmatrix} k_x \\ 0 \\ k_z \end{pmatrix} + \begin{pmatrix} m\frac{2\pi}{\Lambda} \\ 0 \\ 0 \end{pmatrix} \tag{7.5}$$

where m is an integer, that indicates the diffraction order of the wavevector. Only those

combinations persist that conserve the magnitude of the wavevector and thus lie on a circle in reciprocal space[2]

7.3 Rayleigh Approximation

The reflection of light on multi-layer systems with periodically modulated surfaces has been the subject of considerable research, resulting in several mathematical models[2,14], developed for the theoretical treatment of grating structures. The Rayleigh approximation, however, is the most commonly applied. Another approach to this problem was introduced by Chandezon[5,4]. In order to describe a curved structure with Maxwell's equation, coordinate transformation is applied; hence the grating is flattened and so are the related boundary conditions which can then be described with a set of Maxwell equations.

In this chapter, mathematical treatment of grating coupled waveguide modes and simulation of the same, were done using 'Mathematica 7' by Wolfram Research. The code based on calculations of corrugated geometries under the assumption of the Rayleigh approximation allowed simulation of the reflectivity of gratings, calculation of the field distributions and analysis of experimental data. The code is still under development in order to include further features.

The Rayleigh expansion under assumption of a harmonic time dependence and the according expansion of the transfer matrix formalism (explained in the theory chapter) will be just outlined here. Additional information about the algorithm can be found in the literature[12,7]. The rapid convergence of this method at high numerical stability is a substantial advantage and the main reason for the use of this method. Its application, however, is restricted to shallow gratings with an aspect ratio < 0.1[9] (amplitude divided by grating constant).

The surface profile of the grating was monitored by AFM and accordingly simulated with 'Wingitter'. Solutions to Maxwell's equations feature the same translational symmetry as the grating profile. Application of EM fields had to satisfy the Floquet-Bloch theorem which transforms the periodic system into a traditional linear system with constant, real coefficients. In solid-state physics, the analogous result (generalised to three dimensions) is known as Bloch's theorem, where the periodic potential of the (crystal) lattice results in application of Schrödinger's wave functions[1]. Under the assumption of a harmonic

[2] This approach is similar to the Ewald construction in reciprocal space used in solid state physics to describe the elastic scattering of x-rays by a three-dimensional atomic lattice[1]. While this concept is very pictorial and hence easy to understand, in the treatment of grating coupling this advantage is lost since imaginary components of the wavevector are present that can not be shown in real space drawings.

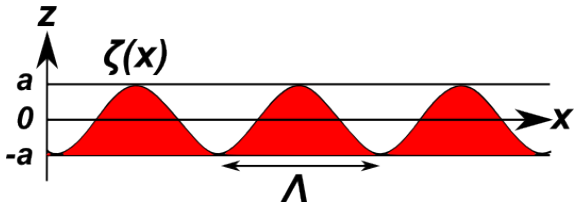

Figure 7.3: The Rayleigh approximation as applied to periodically modulated surfaces. The Rayleigh approximation extends the application of the transfer matrix method to the region containing the corrugation ($-a \leq z \leq a$). All references to the height above the grating are based on the central line at $z = 0$. This can be displaced from the middle of a and $-a$ by an amount of $1/\Lambda \int_0^{\Lambda} \zeta(x)\, dx$ if the profile curve $\zeta(x)$ encloses more area in the $z < 0$ half-space than in the $z > 0$ region, or vice versa

time dependence in the shape of $e^{(-i\omega t)}$ it is possible to expand the fields according to the Rayleigh expansion in the interval $0 < x < \Lambda$ into a superposition of plane and evanescent waves. Accordingly, the field can adopt the form:

$$\mathbf{E}_{j,x}(x,z) = l \sum_{l=-\infty}^{-\infty} (\mathbf{E}_{j,x}^{+(l)} e^{(i[k_x^{(l)} x + k_{j,z}^{(l)} z - \omega t])} + \mathbf{E}_{j,x}^{+(l)} e^{(i[k_x^{(l)} x + k_{j,z}^{(l)} z - \omega t])}) \tag{7.6}$$

with

$$k_x^{(l)} = k_x + l\mathbf{G} \tag{7.7}$$

and

$$k_{j,z}^{(l)} = \sqrt{\left(\frac{\omega}{c}\right)^2 \varepsilon_j - k_x^{(l)2}}. \tag{7.8}$$

As long as the space $|z| > a$ is considered (see figure 7.3) this expansion is valid. However, in the grating regime, ($-a \leq z \leq a$), where the two media interdigitate, this homogeneity can not be assumed, and the Rayleigh hypothesis takes effect by extending equation 7.6 into the modulation zone. This approach is extensively thoroughly discussed in the literature[8,3]. The continuity conditions at the interface determine the coefficient fields $E_{x,i}^{\pm(l)}$. Therefore the Cartesian components of the EM fields can be expressed by expanding the transfer matrix formalism, since the translational symmetry accounts, again, for the possibility of separating the solutions into $E_{x,i}^{\pm(l)}$ and $E_{y,i}^{\pm(l)}$ for TM or TE polarisation, respectively:

TM polarisation

$$E_{j,z}^{\pm(l)} = \mp \frac{k_x^{(l)}}{k_{j,z}^{(l)}} E_{j,x}^{\pm(l)} \tag{7.9}$$

$$H_{y,i}^{\pm(l)} = \pm \frac{\omega \varepsilon_i}{c k_{z,i}^{(l)}} E_{x,i}^{\pm(l)} \tag{7.10}$$

TE polarisation

$$H_{j,x}^{\pm(l)} = \mp \frac{c}{\omega} k_{j,z}^{(l)} E_{j,y}^{\pm(l)} \tag{7.11}$$

$$H_{j,z}^{\pm(l)} = \mp\frac{c}{\omega} k_x^{(l)} E_{j,y}^{\pm(l)}. \tag{7.12}$$

In a similar approach to that of prism coupling to a multi-layer system (see theory chapter), the electric field components in the *0th* and *Nth* layer were related *via* the transfer matrix for this multi-layer system, with the difference that one or more of the interfaces are periodically modulated and exhibit an identical surface profile $\zeta(x)$. As an example for the case where $j/j+1$ is modulated, the relation can be extracted from

$$\begin{pmatrix} \vdots \\ E_0^{+(l)} \\ E_0^{-(l)} \\ \vdots \\ E_0^{+(0)} \\ E_0^{-(0)} \\ \vdots \\ E_0^{+(-l)} \\ E_0^{-(-l)} \\ \vdots \end{pmatrix}_{TM,TE} = \mathbf{Q}_{0,1}^{TM,TE} \mathbf{P}_1 \cdots \mathbf{P}_j \mathbf{Q}_{j,j+1}^{TM,TE}(\{\zeta(x)\}) \mathbf{P}_{j+1} \cdots \mathbf{P}_{N-1} \mathbf{Q}_{N-1,N}^{TM,TE} \begin{pmatrix} \vdots \\ E_N^{+(l)} \\ E_N^{-(l)} \\ \vdots \\ E_N^{+(0)} \\ E_N^{-(0)} \\ \vdots \\ E_N^{+(-l)} \\ E_N^{-(-l)} \\ \vdots \end{pmatrix}_{TM,TE} \tag{7.13}$$

with

$$\mathbf{P}_i = \begin{pmatrix} \ddots & & & & & & \\ & \mathbf{P}_i^{(l)p,s} & & & & & \\ & & \ddots & & & & \\ & & & \mathbf{P}_i^{(0)} & & & \\ & & & & \ddots & & \\ & & & & & \mathbf{P}_i^{(-l)} & \\ & & & & & & \ddots \end{pmatrix} \tag{7.14}$$

and

$$\mathbf{Q}_{i,i+1}^{TM,TE} = \begin{pmatrix} \ddots & & & & & & \\ & \mathbf{Q}_{i,i+1}^{(l)TM,TE} & & & & & \\ & & \ddots & & & & \\ & & & \mathbf{Q}_{i,i+1}^{(0)TM,TE} & & & \\ & & & & \ddots & & \\ & & & & & \mathbf{Q}_{i,i+1}^{(-l)TM,TE} & \\ & & & & & & \ddots \end{pmatrix} \tag{7.15}$$

for the case when $i \neq j$. Here $\mathbf{P}_i$ and $\mathbf{Q}_{i,i+1}^{TM,TE}$ are matrices of type $2(2L+1) \times 2(2L+1)$ with the grating Fourier order of 1, thus running from $-L$ to L. Whereas the $\mathbf{Q}_i^{(l)}$ and $\mathbf{Q}_{i,i+1}^{(l)TM,TE}$ are matrices of type 2×2 and represent (for $i \neq j$) the propagating components (both layer and interface components) for the smooth interface layers with the wavevector $k_{i,z}$.

The interfacial propagator $\mathbf{Q}_{i,i+1}^{TM,TE}$ contains all information about the profile of the modulated interface $j/j+1$. The tangential components of the electric field amplitudes $E_j^{\pm(l)}$ can therefore be found, and arranged into

$$\sum_l = \mathbf{M}_{j+1}^{TM,TE} \begin{pmatrix} E_{j+1}^{+(l)} \\ E_{j+1}^{-(l)} \end{pmatrix}_{TM,TE} = \sum_l = \mathbf{M}_j^{TM,TE} \begin{pmatrix} E_j^{+(l)} \\ E_j^{-(l)} \end{pmatrix}_{TM,TE} \tag{7.16}$$

The program 'Mathematica' was applied in order to numerically evaluate the matrix equation, or alternatively 'Wingitter' was used to simulate experimental data.

7.4 Grating fabrication

In the following section the methodology applied for the fabrication and evaluation of grating couplers will be outlined.

Historically, diffraction gratings have been manufactured mechanically. In some cases this is still done today. The grating grooves are lined by diamond into glass substrates *via* vibration damped machines in a process that is very sensitive to environmental factors like changes in temperature and atmospheric pressure[13]. The ruling cycle can last from one day to six weeks.

Alternatively, and much quicker, gratings can be manufactured *via* the combination of the methods of photo-lithography and reactive ion beam etching in a clean room environment within a time span of two days, following the five step procedure, which is outlined in

subsection 7.4.2-7.4.6. Initially, the grating structure is formed by holographic techniques into a photoresist film. The pattern is then transferred into the substrate material by reactive ion beam etching in order to obtain a spatially identical imprint in the glass substrate.

7.4.1 Basics for Holographic Gratings Fabrication

In the case where two sets of coherent equally polarised monochromatic optical plane waves of equal intensity intersect each other, a pattern of standing waves will form in the region of intersection. The intensities combine and form, according to the combined intensity distribution, a set of straight equally-spaced fringes at the surface they impinge on.

These fringes are separated by a distance, i.e. the grating constant Λ, where

$$\Lambda = \frac{\lambda}{2sin\theta} \tag{7.17}$$

and θ is the angle between the beams (see figure 7.4). A small angle between the beams will produce a widely spaced fringe pattern (large Λ), whereas a larger angle will produce a fine fringe pattern. The lower limit for Λ is given by $\lambda/2$, so for visible recording light, thousands of fringes per millimetre may be formed within this restriction.

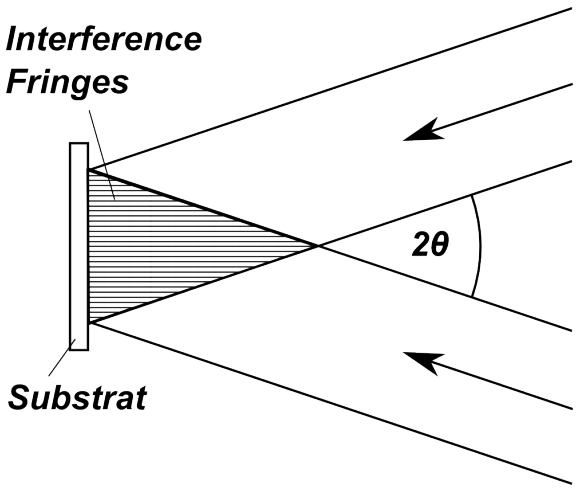

Figure 7.4: Two collimated beams of wavelength λ form an interference pattern composed of straight equally spaced planes of intensity maxima (shown as the horizontal lines). A sinusoidally varying interference pattern is found at the surface of a substrate placed perpendicular to these planes.

7.4.2 Substrate cleaning

Glass substrates used for holographic grating manufacture included fused silica (LITHOSIL-Q, Schott) and borosilicate crown glass (BK7, Schott) microscopic glass slides, which were

generally dimensioned to a standard size of $2.5 \times 2.5cm$.

Prior to any fabrication steps, the substrates were subject to the cleaning procedure for glassware, which was described in the experimental chapter.

After cleaning, the substrates were put on a hotplate at 120°C for 10 minutes to remove adsorbed water from the glass surface. Alternatively, a furnace can be used at same temperature for 30 min.

7.4.3 Photoresist deposition

In order to avoid redeposition of water on the surface the substrates were processed immediately after cooling down. The adhesion of the photoresist material onto the glass surface was improved by treating the microscopic slides with a primer silane (Microposit UN 2924, Rohm and Haas Electronic Materials). Therefore, the glass surface was covered with the primer solution and left at rest to interact for 30 s. Excess solution was spun-off the glass sample (1 minute at 3000 rounds per minute (rpm)) after the period of 30s elapsed, in order to terminate the process.

The actual photoresist solution was diluted with a thinner solution (Microposit EC-solvent, Shipley) in order to adjust the viscosity for the spin-coating process. Therefore the photoresist was mixed with an equal volume of thinner and the spin-coater was accordingly adjusted to spin the substrate at 3500 rpm for one minute. Thereafter, remaining solvent was removed by a by 'softbaking' the resist at 100°C for 50 s on the hot-plate (when using a furnace, 95°C for 12 min are suggested, but it was found that hotplate baking gave better results).

After the soft-bake process was finished, a resist film thickness of $d_{resist} \approx 130nm$ was obtained. It was important that the resist film thickness was kept at $d_{resist} < \lambda$ of the applied laser light, in order to avoid parasitic interferences.

7.4.4 Holographic grating manufacture

As already mentioned in the introduction above, the combination of photo-lithography with holographic exposure is a feasible method to manufacture gratings[6].

In this work, in order to introduce a periodic illumination condition, however, a slightly different method was used to generate the interference pattern. A single collimated monochromatic coherent light beam, after it was reflected back upon itself by placing a mirror at an angle of 45° into half the laser beam cross section, as shown in figure 7.5.

Black adhesive tape was glued flush (avoiding any bubbles) to the backside of the sample to prevent interference from reflections. The sample and the mirror (perpendicular to the sample surface) were both mounted on a rotary stage (see figure 7.5).

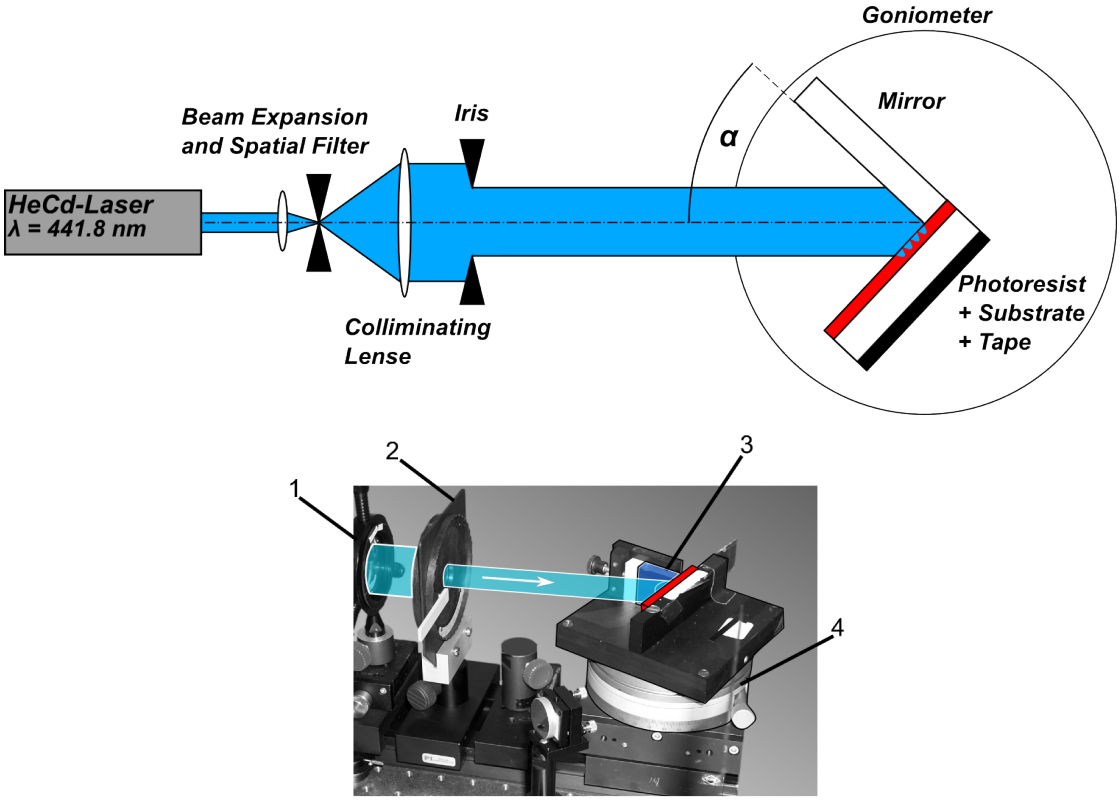

Figure 7.5: Single beam interference recording method. A collimated beam of light, incident from the right, is retro-reflected by a plane mirror, which forms a standing wave pattern whose intensity maxima are shown. A transparent blank (substrate), inclined at an angle α to the fringes, will have its surfaces exposed to a sinusoidally varying intensity pattern. The photograph depicts the real situation in the clean room, where (1) is the collimator lens, (2) the adjustable iris, (3) the mirror, and (4) the goniometer the arrangement is mounted on.

The beam of a helium-cadmium laser ($\lambda = 441.6nm$, $35mW$, 4270 NB helium-cadmium laser, LiCONiX, now a division of Melles Griot Inc.) was passed through a beam expander and a spatial filter. The Gaussian intensity profile of the parallel beam was limited by an iris to the inner part of the beam waist where the intensity profile was nearly constant. One half of this uniform beam illuminated the photoresist directly; the other half struck the mirror first, where it was reflected and then hit the sample.

A standing wave pattern was formed, with intensity maxima forming planes parallel to the wave fronts. The intersection of this interference pattern with a photoresist-covered substrate yielded an identical copy of the pattern of grooves on its surface. The spacing Λ depended on the angle θ between the substrate surface and the planes of maximum intensity, determined by the tilt angle between the optical axis and the surface normal (see Figure **7.5**). Λ and θ are for this technique also related by equation 7.17, though it must be highlighted that the interference imaging geometry behind the single-beam holographic

grating (also called Sheridon grating) is different from that of the double-beam geometry.

The profile, i.e. the groove depth can be adjusted by the following ratio:

$$h = \frac{\lambda}{2n} \tag{7.18}$$

where h is the groove depth (strictly determined by the separation distance between the intensity maxima) and λ is the wavelength of the applied laser light, n denotes the refractive index of the photoresist material.

7.4.5 Photoresist activation

The next step was the activation or development of the pattern within the photoresist layer. Since a positive photoresist was chosen for this manufacture, exposure to the laser light induced a photochemical reaction in the photoresist that promoted solubility in the developer solution (ma-D 330, microresist). The remaining unilluminated material remained insoluble. According to the sinusoidal intensity profile of the interference pattern, solubility was periodically introduced in the film. Immersion in the developer reagent translated the solubility contrast into a surface relief grating by solubilising the illuminated regions. Optimal illumination and development times depend strongly on the laser power used. Both were typically in the order of $30s$, but had to be determined precisely again for each batch. Excess developer was removed by rinsing with Milli-Q water. The remaining photoresist regions were cured by heating the substrates at $110°C$ for 30 minutes in a vacuum oven ('hard baking'). This treatment activated a thermoinitiator in the material, facilitating cross-linking.

7.4.6 Grating transfer

In order to transfer the grating structure, which was recorded into the photoresist, into the underlying glass, reactive ion beam etching (RIBE) was applied. In principle, the polymeric grating structure could also be used for spectroscopic application, however, transfer of the profile into the hard glass substrate yielded gratings of a more durable form that could be used, cleaned and re-used many times.

The working principle of the RIBE system (RR-I SQ76, Roth & Rau) is illustrated in figure 7.6.

This apparatus operated at high vacuum and was therefore flanged to a vacuum chamber (*Balzers*). The principle of operation can be outlined as: electrons were ejected from the

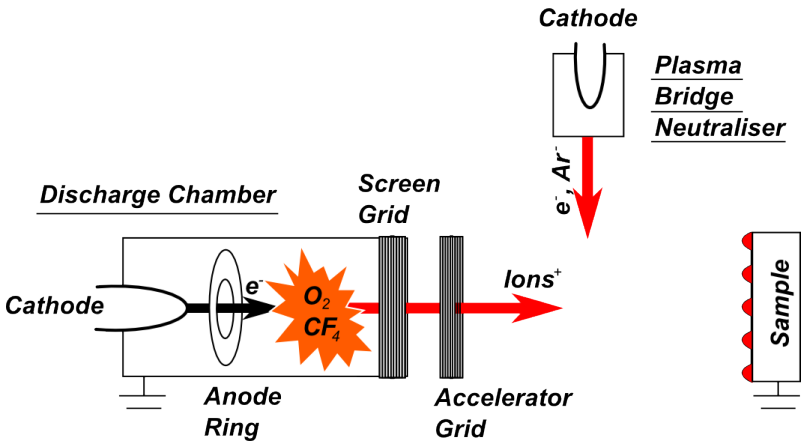

Figure 7.6: Schematic illustration of the reactive ion beam etching. This process allowes the transfer of the periodical interference pattern in the photoresist into a surface relief of the glass substrate. O_2 and CF_4 molecules are ionised by an ion beam in order to obtain reactive ions with the ability to etch the glass materials. Acceleration of these ions adds the additional effect of surface bombardment, which supports the grating manufacture.

Discharge voltage	100 V
Discharge current	0.55 A
Beam current	0.4 A
Acceleration voltage	200 V
Acceleration current	0.05 A
Plasma bridge neutraliser voltage	16 ± 4 V
Plasma bridge neutraliser current	0.53 A
Probe current	0.52 ± 0.05 A

Table 7.1: The exact parameters applied to the RIBE system.

cathode within the discharge chamber and accelerated to and through the anode ring due to its higher potential. A dilute flow of O_2 and CF_4 (Freon) was then passed through the opposite part of the chamber. Upon collision of the cathode beam with the gas molecules, the electrons were striped off and the molecules were ionised accordingly. Positive ions from this plasma were then pulled in the direction of the screen grid at ground potential. By passing this grid, they were accelerated further according to the negative potential of the acceleration grid that also served as a focusing element. The ions hit the sample perpendicularly in the form of a parallel beam with a diameter of approximately $7cm$. Charging of the probe - due to the positive ionised beam ($0.6keV$, $0.2mAcm^{-2}$) - was prevented by the injection of negative ions and electrons by the plasma bridge neutraliser. The pure bombardment of ions onto the samples is enough to ablates the material and etch into the sample. However, radicals from the plasma additionally decompose both photoresist and glass chemically. The composition of the reactive gases O_2 and CF_4 was optimised in order to attack glass effectively. One has to keep in mind that a difference in etching rates between photoresist and glass of about a ratio of $2:1$ exists[11], distorting the pattern transferred from the photoresist into the glass.

The heat load on the samples was reduced by dividing the total etching time into four 20 s periods, with a 30 s break in between, in order to allow the samples to cool down after the first treatment.

7.4.7 Grating Characterisation

Due to the modular cartridge-based system for sample mounting, the same optical setup, as used for prism-coupled OWS in Kretschmann configuration (described in detail in the experimental section) also facilitated the experimental work on grating coupled waveguides, with no further reconstructions needed.

In order to be able to simulate the optical behaviour of the fabricated gratings and accordingly to evaluate the measurements of the grating-coupled waveguide, it was necessary to experimentally determine the exact values of the properties of all components. Especially a precise knowledge of the grating constant was crucial, since it directly determined the position of the resonance modes. Hence, the grating profile and the exact grating constant were measured by AFM before the waveguiding $meso - nc - TiO_2$ film was formed on top. Detailed information about the grating profile (i.e. amplitude, shape) was important in order to refine the modelling of the coupling properties of the particular grating.

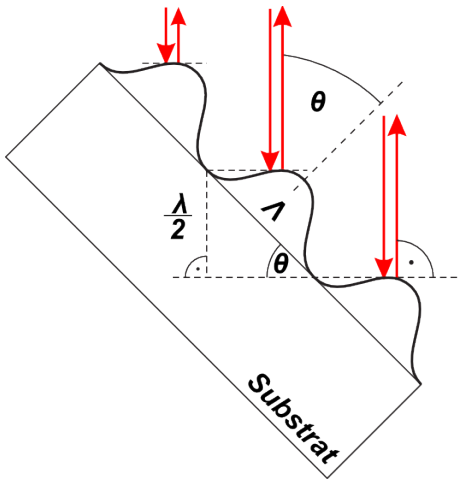

Figure 7.7: Origin of the Littrow-reflects. Simplified illustration of a grating with plane-parallel grating flanks. In an ideal case the Littrow-reflex is reflected back into the light source.

Due to the fact that the grating period was smaller than the wavelength of the allied light for the characterisation ($\lambda_{HeNe} = 632.8nm$), the grating constant could not be determined *via* diffraction of perpendicular incident light. Nevertheless, it was possible to determine the grating constant; exploiting the phenomenon of the Littrow reflects. At distinct angles of incidence, diffraction of light on a corrugated surface with a given grating constant results in constructive interference, due to reflection at multiple structural levels (see

figure 7.7). The special case in which the diffracted beam of a given diffraction order coincides with the incident beam is called the Littrow configuration. This phenomenon offers a simple and quick polarisation-independent way to conveniently determine the grating constant, and requires no modelling of any layers properties.

This angle was measured by pointing the reflected beam (for the diffraction order $m = 1$, where the diffraction peak is strongest) on (an arbitrarily chosen point on) the wall (see figure 7.8). If this is done for both rotation directions, the angular difference $\Delta\theta$ could then be determined and thus the grating constant Λ could be calculated by

$$\Lambda = \frac{\lambda_{HeNe}}{2sin\frac{\Delta\theta}{2}}. \tag{7.19}$$

In the course of this measurement $\Delta\theta/2$ was fixed as the zero-angle of the setup, where the back reflection of the laser beam was congruent with its point of origin.

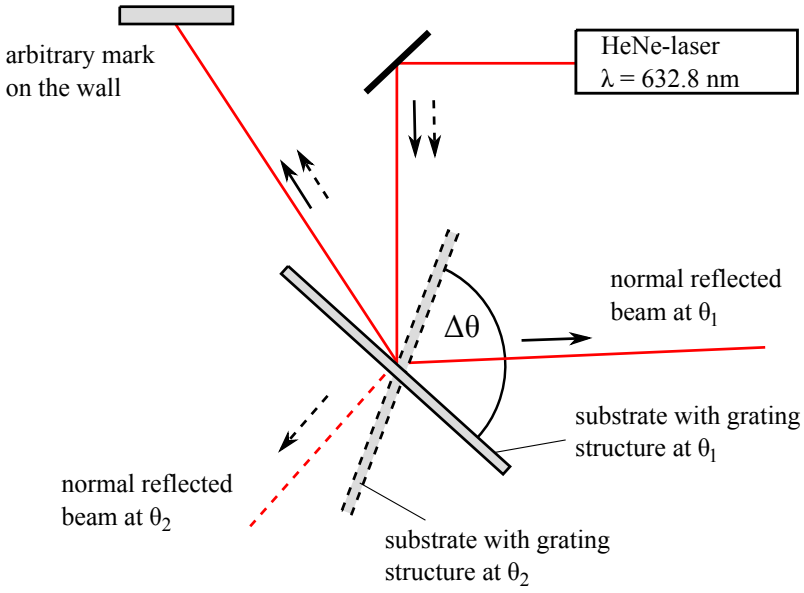

Figure 7.8: Grating characterisation via Littrow-reflections. Details in text.

In order to simulate reflectivity curves for prism coupling, the determining factors were the material properties like layer thickness and refractive index. In grating coupling, complete knowledge of the grating profile is additionally important for calculations. For the purpose of determination of the profile function of holographically manufactured gratings the surface topographies was measured by tapping mode AFM (Dimension 3100 Scanning Probe Microscope, Veeco). The obtained topographic and relief information were utilised in the modelling of the grating profile and related coupling mechanism, and accordingly integrated in the code for evaluation of grating-coupled waveguide spectroscopy.

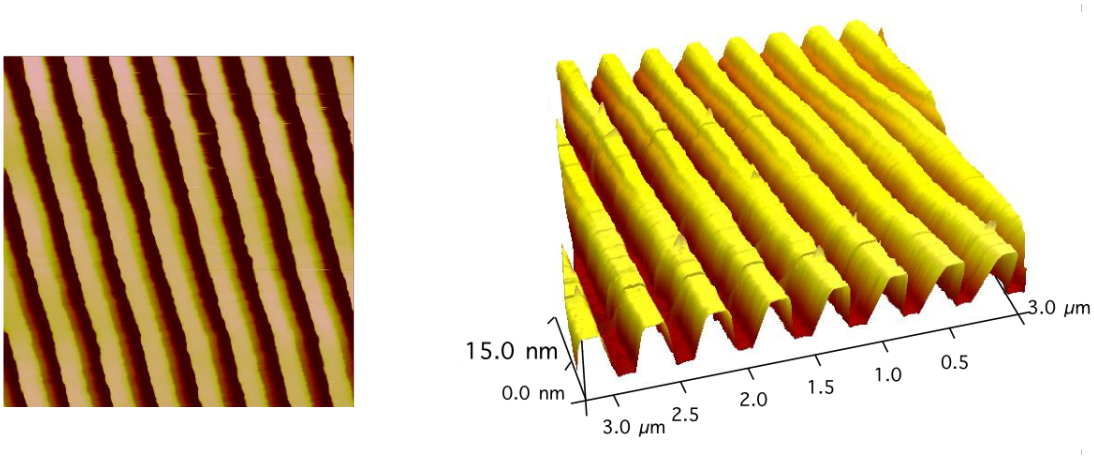

Figure 7.9: AFM images of a holographic grating, showing the topography (left) and the relief (right) of the structure. The three-dimensional view shows a $3\mu m$ by $3\mu m$ area from the centre of the glass sample. The image is disproportionately streched in z-direction (hight), therefore the axis are not equally scaled and the shallow character of the corrugation is distorted.

7.4.8 Substrate Characterisation

The exact refractive index of the glass substrate was determined by measuring of the Brewster angle, therefore the reflectivity of the prim glass surface was scanned for angles of incidence in the range of θ =53° - 58°, since the minimum was expected in this region, corresponding to a refractive index range of $n = 1.327 - 1.600$. Due to the shallow profile of the minimum, a polynomial fit was applied to the obtained data and the minimum of this fitted curve was evaluated. The experimental value for the refractive index of the glass substrate was found $n = 1.45699$, referring to the Brewster angle at found at $\theta = 55.536°$.

7.5 Grating-Coupled Optical Waveguide Spectroscopy

The Characterisation of $meso-nc-TiO_2$ in grating-coupled optical waveguide spectroscopy (GOWS) configuration was carried out on the same OWS setup as used for prism-coupled OWS, the only difference was the positioning of the photo-detector(s), due to a modified read-out scheme. Grating-coupled waveguides were operated not in reflection mode, but in the so-called 'end-fire' detection mode (see figure 7.10). This read-out technique records only the in-coupled light, which is guided within the waveguide along the x-direction, and therefore the photo-diodes were positioned at the end-faces ($y-z$-plane) of the waveguiding layer. The great benefit of this detection scheme was the minimised background noise, since only guided modes contribute to the signal, which is detected by the photo-diodes. This method was chosen (bearing in mind the development of the system for integration with DSSC) since the ultra-sharp resonances, obtained in this configuration allow an automated (binary) read-out protocol with high degree of accuracy to be implemented.

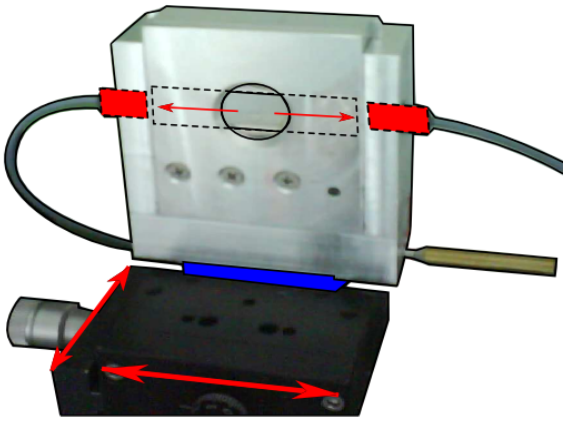

Figure 7.10: Illustration of the waveguide mounted in the exchangeable cartridge on a positioning stage. The photo-diodes at the end-faces of the waveguide are highlighted in red with arrows, pointing the propagation path of guided light along the x-axis of the waveguide. Highlighted in blue is the Peltier element, which allowed for temperature stabilisation.

7.5.1 End-Fire Operation

Operation of GOWS in end-fire configuration (as well as in reflection configuration) is affected by the influence of external conditions on the angular position of the resonances. Therefore, great importance was attached to stabilise the experiment as far as possible, hence the temperature was kept at a constant value of 25°C *via* a Peltier element at the base of the metal construction, which worked by the recirculation of temperature controlled water through the inner cavities of the cartridge (shown in figure 7.10).

Another important parameter was the constantly stable position of the impinging laser beam, since the interpretation of the recorded spectra highly depend on an exact knowledge of the absolute angles of incident. However, if symmetrical coupling gratings are used for waveguide mode excitation, the determination of an absolute zero position can be avoided by measuring the angular spectrum in both rotation directions, thus - and + position of the symmetric spectrum with respect to the absolute zero position which intrinsically underlies this approach as the 'mirror'-plane of the spectrum to both rotation direction. In spectral analysis, the absolute zero angle can be determined as half the angular difference of each pair of $\pm$ resonance features. The principle is illustrated in figure 7.11.

For the total determination of the $meso - nc - TiO_2$ waveguide system (i.e. refractive index n and film thickness d) it was necessary to have at least two different accessible resonance features (i.e. modes), in addition the optical properties of the substrate and the surrounding medium had to be known.

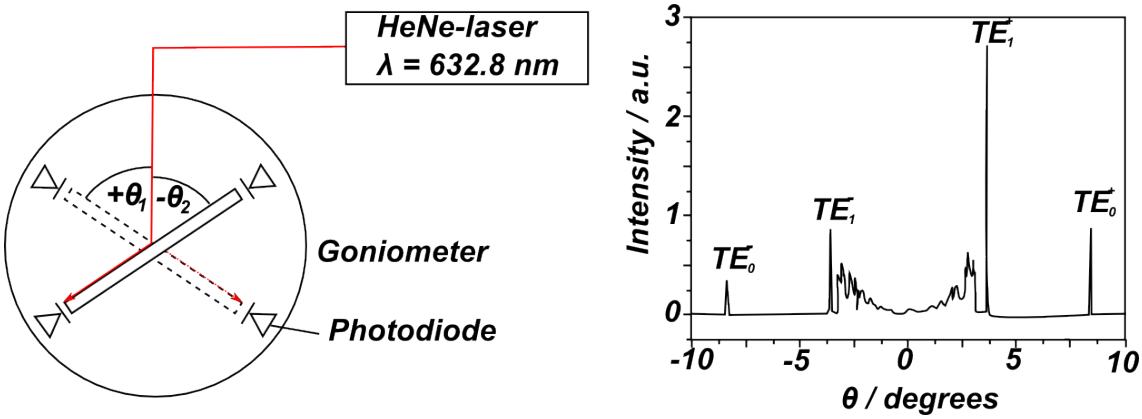

Figure 7.11: Schematic representation of the GOWS detection scheme (left). The resonance features (peaks) in the detected intensity signals are clearly distinguishable from the background. Differenc in intensity at both sides of the scan arises from unequal amplifier adjustment (right).

7.5.2 Liquid handling

GOWS experiments in liquids were performed with the same kit as introduced for the OWS experimental work (se experimental section). The liquid handling equipment allowed full optical access to the sensor surface over a broad range of azimuthal angles and to remain sealed for longer than 24 hours.

7.6 Results and Discussion

With the aim of facilitating *in-situ* experiments on DSSCs, a holographic grating-coupler element was implemented with the $meso - nc - TiO_2$ waveguide. With this step not only the Kretschmann multi-layer configuration (i.e. prism/beam-alignment, index-matching, evaporation of thin gold layer) could be avoided, but also the fundamental problem of destructive chemical interaction of the I^-/I_3^- electrolyte solution with the gold layer was resolved.

The $meso - nc - TiO_2$ were applied as waveguiding structures on top of fused silica glass slides equipped with a holographic grating-couplers. Prior to any sensing application, the $meso - nc - TiO_2$ waveguides were exposed to pure ethanol and equilibrated for ca. $24h$ to eliminate observable drift of their refractive index to lower values. This behaviour is likely to be due to minor hydrolysis and dissolution of the titanium oxide matrix of the waveguide.

7.6.1 Grating-Coupled Optical Waveguide Spectra of Mesoporous Titania Films

In order to demonstrate the functional capability of GOWS in combination with $meso - nc - TiO_2$ waveguides in principle, angular scans were performed (separately) for TM and

TE polarised light. Figure 7.12 shows the experimental resonance scan obtained from GOWS with TM polarised laser light after a $meso - nc - TiO_2$ waveguide was exposed to pure ethanol and equilibrated for 24h.

The detected intensity was found to decay as the angle of incidence increased. This behaviour was observed for all GOWS measurements, including also for non-porous film which were investigated in a series of control experiments. Therefore, it was assumed that resonances which are located closer to the absolute zero angle exhibited better coupling efficiencies, which, again, seems to be an intrinsic feature of GOWS. Scans were also taken for $meso - nc - TiO_2$ waveguides in air (not shown), however, very poor waveguiding was observed, i.e. no resonance features could be resolved.

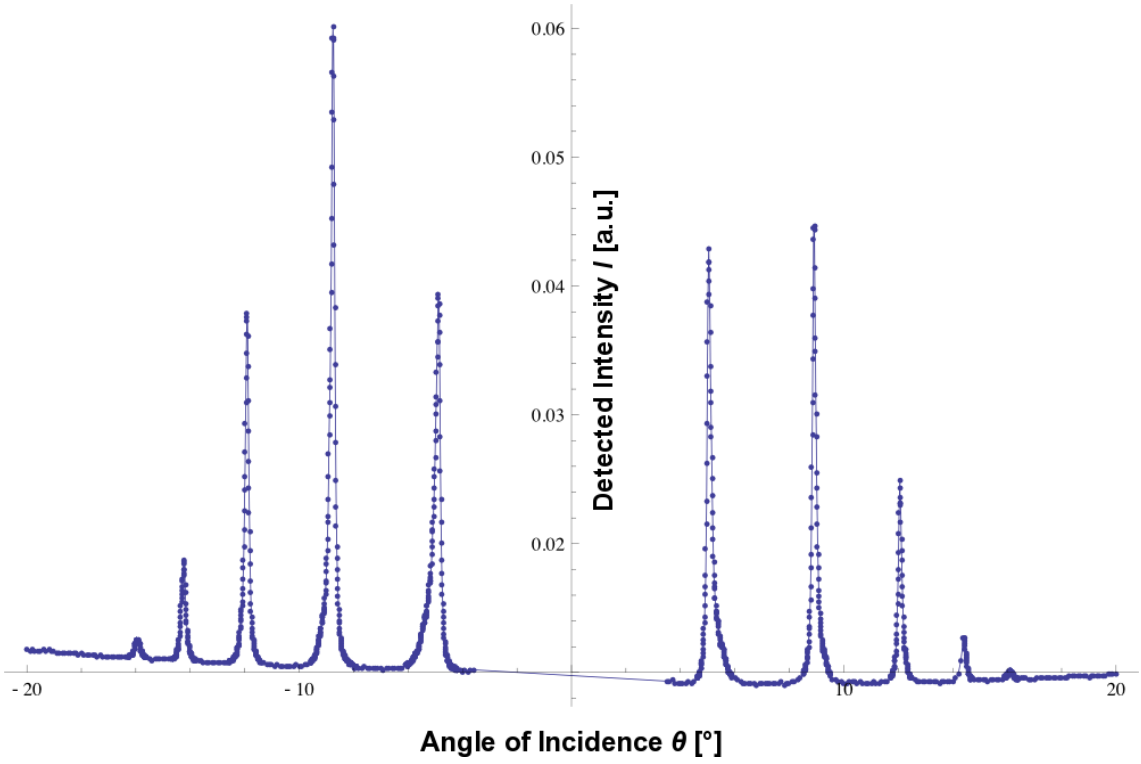

Figure 7.12: Angular spectrum of GOWS for a $meso - nc - TiO_2$ waveguide, illuminated with TM polarised light. The modes of different order (mode order decreases towards increasing angles) appear as sharp resonances at distinct angles as the light is impinged on the grating. Due to the symmetric nature of the grating coupler, the resonance peaks emerge twice for each mode, mirrored at the plane of absolute zero angle of incidence. Apparently, the detected coupling efficiency, and therefore the intensity decreases as the angle of incidence increases.

At this point it is important to mention that the photo-detectors on each side (i.e. + and - angular range) were both equipped with an amplifier to allow for separate signal intensity adjustment. Generally, the strongest resonance features on both sides of the spectrum were always tuned to ≈ 1, in this experimental spectra, however, the signal adjustment was performed proportionally for the two polarisations for the reason of direct comparison, thus to reveal the observed difference in coupling efficiencies. Comparing the angular scans for TM light in figure 7.12 with the one obtained for TE light in figure 7.13, $\approx$ 20-fold

higher intensities were measured in the case of TE light. This finding was reproduced in all experiments (with varying ratios) and appears to be an intrinsic feature of GOWS. Consequently, due to the high signal to noise ratio, TE spectra were preferably utilised for experiments.

	Thickness, d $[nm]$	Refractive Index, n $[a.u.]$	Extinction, k
Substrate	∞	1.457	-
meso-nc-Titania	1867	1.848	-
Superstrate	∞	1.3592	-

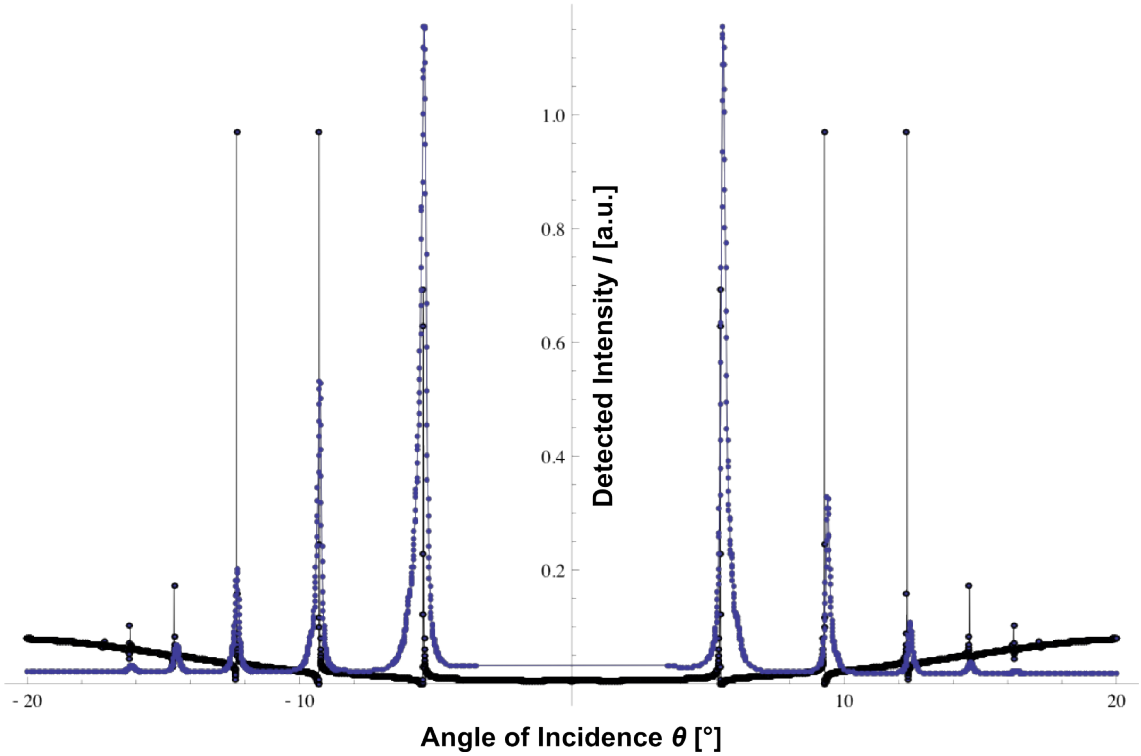

Figure 7.13: Angular spectrum of GOWS for the identical $meso - nc - TiO_2$ waveguide as shown in figure 7.12, illuminated with TE polarised light. The resonances produce sharp peaks of 20-fold intensity as compared to the spectrum obtained from illumination with TM light. The detected coupling efficiency also decreases for TE polarised light as the angle of incidence increases.

The coupling mechanism was modelled on the basis of the structural data obtained from AFM images of the grating structure profile. The grating constant was found to be $448.2nm$, based on experimentally determined Littrow-reflexes at $\theta = 44.90°$. Also due to AFM, the grating amplitude was modelled with a value of $10nm$. Furthermore, the profile function for the description of the geometric form of the grating was chosen to rather be that of an impulse then of a sine function, but with exponentially decaying slopes, rather then with immediate phase changes. The resulting shape of the function is shown in figure 7.14, accounting for the symmetrical slopes on both sides (each $50nm$) for a complete phase change, and accordingly a plateau of $248nm$.

In order to fully describe the $meso - nc - TiO_2$ waveguide with respect to refractive index, *n*, and thickness, *d*, the three-layer system with the grating at the interface of a

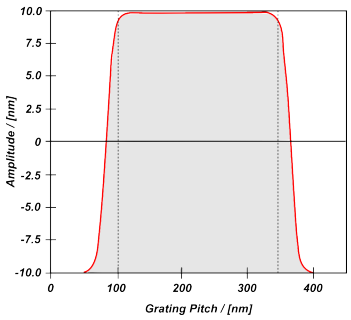

Figure 7.14: The section plot is based on averaging over the data of the full area. It yields a trapezoidal type of profile (= 478.5 nm) with an amplitude of $\pm 10nm$.

glass/$meso - nc - TiO_2$ interface was simulated and fit to the experimentally recorded data. A reasonably good fit for the shown spectra was obtained with the parameters presented in the table above figure 7.13. From the simulated fit an effective porosity of 37% of the total film volume could be calculated. The fitting of the extinction coefficient has not been possible to date, since the simulation code is still under development.

7.6.2 Dye Adsorption Measurements

In the next step, a new set of waveguides (after equilibration with pure ethanol) was exposed to $3 \cdot 10^{-4} mol\, L^{-1}$ N719 dye solutions. Before the actual sorption experiment their characteristics were determined according to the above-described procedures. In the case of the example presented here the refractive index of the $meso - nc - TiO_2$ waveguide in ethanol was found to be $n = 1.875$ with $d = 1870nm$, which correlates to a an effective porosity of 33%. Exposure to the dye solution was controlled by a peristaltic pump at low flow rate in order to allow continuous stirring and dye delivery at a constant rate. A gradual increase in refractive index was observed *via* changes in the mode coupling conditions (shown in figure 7.15). This shift was attributed to the change in the composite refractive index of the $meso - nc - TiO_2$ waveguide. Since the simulation code for the fitting routine is still under development, a certain degree of uncertainty regarding the accuracy of obtained values can not be excluded, however, the preliminary results to date yield an increase of $\Delta n = 0.022$ due to dye loading over $19h$, which is in good agreement with the results produced in the conventional Kretschmann prism-coupling configuration. Effective medium calculations (for details see introduction chapter) using the measured values predict a refractive index of $n = 1.400 \pm 0.001$ for the pore-filling medium at the time of measurement termination. This value is consistent with the calculated dye concentration in the prism coupled experiments. A steady-state was not reached during the time of adsorption.

Taking a closer look at the angular shift of the spectrum to higher angles (see figure 7.15),

a significant drop in detected intensity was apparent. However, it is not totally clear at this stage wether the intensity drop is caused by the intrinsic decrease in coupling efficiency due to the shift of the particular resonances towards higher (absolute) angles or if it is caused by the dye molecules absorbing this portion of light, or even other effects. Though it seems that the decrease is correlated, at least to a certain extent, to the presence of the dye molecules within the film. Indication therefore may be found in the changing rate of intensity decrease.

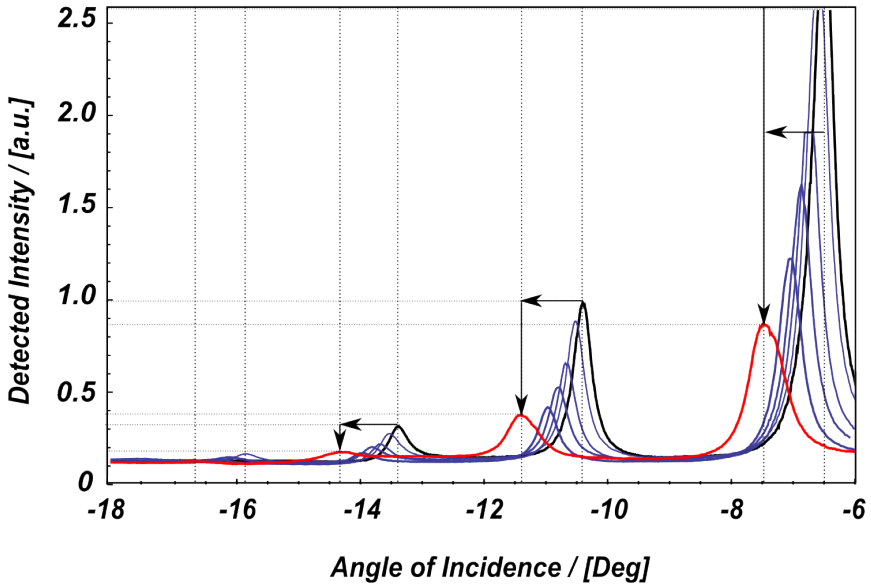

Figure 7.15: The angular shift of the spectrum to (absolute) higher angles is depicted on the example of six successively taken angular spectra during the proces of dye adsorbtion, at $t = 0, 8, 43, 54, 73, 92, 1128 min$. *The significant drop in detected intensity is apparent and much higher than expected for an intensity decrease just due to lower coupling efficiencies at (absolute) higher angles.*

7.6.3 Diffusion Kinetics Measurements

It was assumed that if the intensity drop in the resonance features related to the presence of dye molecules within the pore space, then the kinetic behaviour (analysed in detail in the previous chapter) of the shifting resonant coupling angles (i.e. composite refractive index change) must show significant distinctness from the kinetic behaviour of the intensity changes (i.e. extinction coefficient). Since the applied materials and conditions are identical to the experiments carried out in Kretschmann prism coupling configuration, distinct kinetic properties must, if they are intrinsic to the diffusive species and the matrix material (i.e. no artifact of the method) become observable.

In order to investigate the kinetics of dye adsorption onto $meso - nc - TiO_2$ pore walls with GOWS, the amount of absorbed dye was monitored (*via* resonance angle shift due

to a change of the composite refractive index of $meso-nc-TiO_2$) as a function of time. Accordingly, the experiment was run in kinetic tracking mode in order to monitor these changes. Since the extinction coefficient could not be simulated for GOWS at this stage, is was not possible to extract exact quantitative information from this measurement. Nevertheless, the qualitative determination of the characteristic differences for the two probing modes (Δn and Δk) should provide important information about mass transport in $meso-nc-TiO_2$ films and prove the validity of the GOWS method for monitoring mass transport features within mesoporous structures.

Differences between the kinetic response of n and k towards N719 dye adsorption were observed to be very pronounced, especially in the initial phase of the diffusion process. Therefore it was expected that a significant variation in the slope and shape of the time-dependant progression curve would be observed, i.e. the diffusion coefficient.

Diffusion experiments were carried out with $meso-nc-TiO_2$ waveguides from the same batch of mesoporous material as the waveguides described above in section 7.6.2. The $24h$ equilibration step in pure ethanol was followed by the exposure to $3 \cdot 10^{-4} mol\ L^{-1}$ N719 dye in ethanolic solution. Liquid handling was provided by a peristaltic pump under the same conditions as described in section 7.6.2. Figure 7.16 shows a representative time-dependant signal progression of the resonance angle change ($\Delta\theta_t/\Delta\theta_{total}$) and detected intensity change ($\Delta I_t/\Delta I_{total}$), respectively, during the initial phase of the sorption process *versus* time.

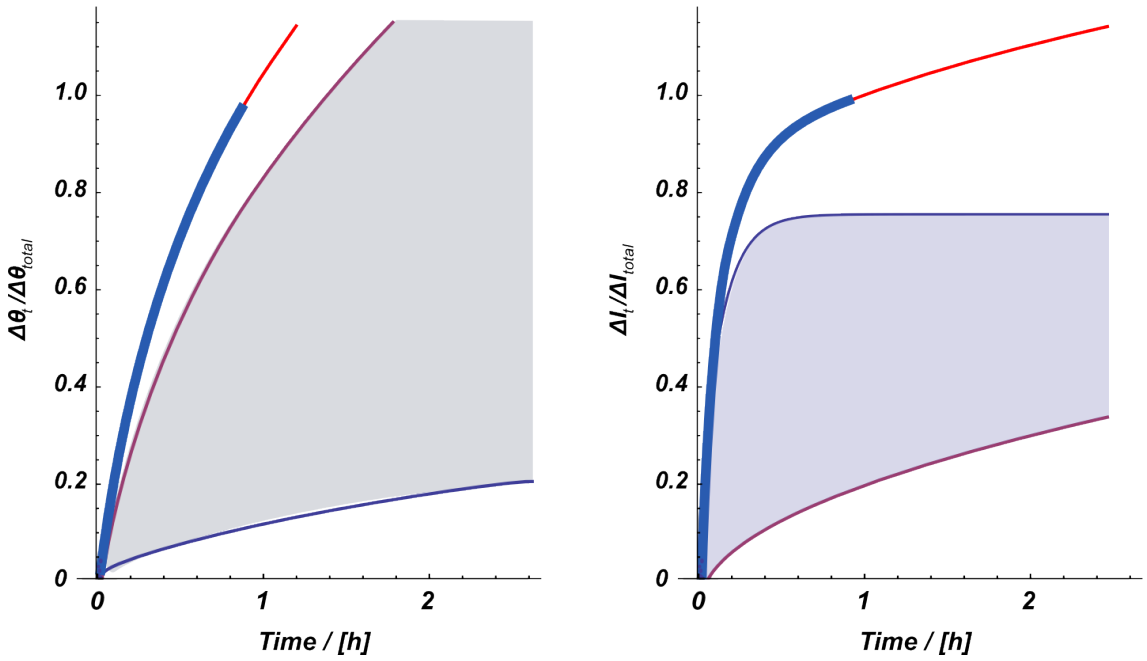

Figure 7.16: Preliminary results obtained for $meso-nc-TiO_2$ films in grating-coupled optical waveguide spectroscopy (GOWS) configuration. Plot of composite refractive index change (left), and extinction coefficient change (right) versus time.

Fitting of the kinetic curves was done using the same model as for fitting of the kinetic progression experiment in Kretschmann prism coupling configuration, i.e. with two simultaneously occurring diffusion processes (details are described in the previous chapter) and accordingly two diffusion coefficients. It was found, that the resonance angle shift was dominated by a diffusion process with a diffusion coefficient in the order of $D = 10^{-13}\,cm^2\,s^{-1}$, whereas the kinetic curve, obtained for the intensity change, was dominated by a diffusion process with a diffusion coefficient in the order of $D = 10^{-11}\,cm^2\,s^{-1}$. Equilibration of the sorption kinetics was predicted by the simulation to occur after approximately 60h, independent of the starting concentration of the dye solution.

These preliminary results, clearly show the different sensitivities of the two probing techniques (Δn and Δk) related to diffusion and adsorption processes of dye molecules into and within $meso - nc - TiO_2$ waveguide films. In order to exploit these properties efficiently for DSSC characterisation and analysis, further development is necessary.

The findings reported here were reproducible during the course of this study, and furthermore, also consistent with the results obtained from previous diffusion measurements with OWS in Kretschmann prism coupling configuration. Consequently, the transfer of the $meso - nc - TiO_2$ waveguides from prism-coupled gold substrates to grating-coupled glass substrates was achieved without observable changes in the sensing properties of the applied mesoporous films. Also it could be deduced that the integration of the grating-coupler with $meso - nc - TiO_2$ waveguides for OWS will allow *in-situ* experiments on operating DSSC systems, in order to investigate also other diffusion related processes in the DSSC under real conditions, and most notably, under illumination with a defined wavelength spectrum.

Bearing in mind the origin of the signals (as discussed in the previous chapter), it can be speculated that only a fraction of the in-diffused dye molecules within the mesopores is chemically bound to the titania surface, and hence cause a different optical signal than the isolated or physisorbed dye species. Furthermore, it is considered that (under illumination) only surface-bound dye molecules contribute to the energy conversion process of the particular DSSC, thus only surface-bound dye molecules have the ability to transfer electrons *via* electrically bonded COO groups. Generally, the incident photon-to-current efficiency (IPCE) is expected to increase linearly with the amount of adsorbed dye, basically because more adsorbed dye molecules are expected to absorb more photons, thus to finally generate more electrons. Under this aspect it might be interesting to investigate the correlation between the IPCE, or rather the absorbed photon-to-current efficiency (APCE) to the characteristics of refractive index and extinction coefficient kinetics, respectively.

7.7 Conclusion

The integration of the experimental $meso - nc - TiO_2$ OWS to a system capable of *in-situ* monitoring of changes in refractive index and extinction coefficient with the ability for integration with DSSC have been successfully demonstrated in this chapter. Moreover, this improved technique has much lower experimental complexity, and shows great potential for integration with various other techniques and applications.

Preliminary results of simulations and experimental data on refractive index and extinction measurements, as well as adsorption monitoring, and time-dependent kinetics scans were in good accordance to the previous measurements in Kretschmannconfiguration.

In order to explicitly investigate the changes and interactions of diffused dye molecules with and at the titania surface in more detail, it is strongly suggested to additionally apply an IR-light source to the OWS method. The wavelength spectrum in the IR-range is sensitive to chemical interactions (at the titania surface) which are related to the photo-catalytic processes during dye sensitisation and also during DSSC operation.

Major aspects, for example pore size/volume ratio, surface chemistry as well as surface charges, and guest-host-interactions in nano-sized environments in general have to be investigated in more detail in order to gather significant information about the transport processes within mesoporous titania. However, diffusion monitoring with OWS techniques was successfully introduced and proved to be capable of addressing spatially resolved and time-dependant processes within mesoporous materials. Moreover, the remarkable feature of spatial resolution limits beyond the diffraction limit makes this method a highly valuable tool for the investigation of fundamental material properties but also for the exploration of new phenomena in optics and opto-electronics.

Bibliography

[1] Ashcroft, N. W. & Mermin, N. D. *Solid State Physics* (International Thomson Publishing, 1976).

[2] Barnes, W. L., Priest, T. W., Kitson, S. C. & Sambles, J. R. Physical origin of photonic energy gaps in the propagation of surface plasmons on gratings. *Physical Review B* **54**, 6227–6244 (1996).

[3] Bunch, K. J., Cain, W. N. & Grow, R. W. Use of extrapolation on wave expansions to force the satisfaction of the rayleigh hypothesis,. *Journal of the Optical Society of America* **9**, 755–764 (1992).

[4] Li, L. *JOSA A* **16**, 2521–2531.

[5] Li, L., Chandezon, J., Granet, G., & Plumey, J.-P. Rigorous and efficient grating-analysis method made easy for optical engineers. *Applied Optics* **38**, 304–313.

[6] Mai, X., Moshrefzahdeh, R. S., Gibson, M. J., Stegeman, G. I. & Seaton, C. T. *Appl. Opt.* **24**, 3159 (1985).

[7] Marvin, A., Celli, V. & Hills, N. R. Optical properties of rough surfaces: General theory and the small roughness limit. *Physical Review Letters B* **15**, 5618–5626 (1977).

[8] Paulick, T. C. Applicability of the rayleigh hypothesis to real materials. *Physical Review Letters B* **42**, 2801–2824 (1990).

[9] Petit, R. & Cadilhac, M. Sur la diffraction dÕune onde plane par un r«eseau infiniment conducteur. *Comptes Rendus de lÕAcademie des Sciences B* **262**, 468–471 (1966).

[10] R. Ulrich, T. H.-H. *TU Hamburg-Harburg*.

[11] Ronggui, S. & Righini, G. C. Characterization of reactive ion etching of glass and its applications in integrated optics. *Journal of Vacuum Science and Technology* **9**, 2709–2712 (1991).

[12] Agranovitch, V. M. & Mills, D. L. (eds.) *Surface Polaritons* (North-Holland, 1982).

[13] Palmer, C. (ed.) *The Diffraction Grating Handbook* (Richardson Grating Laboratory, Thermo RGL, 2002).

[14] Petit, R. (ed.) *Electromagnetic Theory of Gratings* (Springer, 1980).

Chapter 8

8 Conclusions and Outlook

8.1 SUMMARY

A method was developed to access the interior of light-guiding structures in order to exploit the enhanced sensing potential of the highly confined electromagnetic field distributions, located within the core of a waveguide.

The work presented in this thesis explores the possibilities of optical waveguide spectroscopy utilising transparent mesoporous thin-film waveguides deposited on top of a gold layer. This multi-layer assembly is employed in a prism-coupling attenuated total internal reflection (ATR) configuration. The angular read-out of the reflected light intensity allows label-free detection schemes with high sensitivity to changes of the dielectric environment due to the presence of analyte molecules within the probing region.

The application of mesoporous materials for sensing purposes is in particular advantageous, due to the large internal surface area intrinsically inherent to these structures, which allows the target species to be accumulated within the pore volume until a density of analyte is reached that is detectable within the sensitivity limits of the probing technique. The advantage of such an approach is that the target species is confined to a three-dimensional region with dimensions on the same scale as the target itself.

Because of its porous nature, the effective refractive index of such porous structures is lower than that of bulk material. The captured molecules inside the pore volume increase the composite refractive index of the porous oxide structures thus cause a shift in the waveguide mode coupling condition and consequently manifest in an angular shift of the resonance feature that is detectable in reflectance spectra. The composite refractive index of a porous layer is related to its porosity and analysed by the Bruggeman effective medium model[?] .

Mesoporous titanium oxide in particular is a good host material for label-free optical sensing applications because its optical properties (e.g. high-refractive index, highly transparent) are highly sensitive to the presence of molecules inside the pores[?] . In order to be suitable for optical waveguiding application the mesoporous material has to have a high refractive index and pore-sizes not exceeding $\approx \lambda_{HeNe}/10$ for guiding light at visible wavelengths this restricts the pores size to the maximum allowed size, whereas the adsorption and diffusion properties of molecular restrict the pore-size to the lower limit. Consequently materials with pore-sizes between 10 and 30 nm and and completely interconnected pores were aspired.

It is shown that mesoporous titanium oxide can be used as a base material for optical waveguide applications.

8.1.1 Preparation of Mesoporous Materials

For this purpose, different forms of mesoporous titanium oxide are prepared by approaches os such as soft-templating of mesostructures, two-dimensional nanotube-arrays, and three-dimensional structures of sintered nanoparticles. Due to the sub-wavelength nature of the mesostructure, the mesoporous titanium oxide films served very well as optical waveguides. Furthermore it was possible to distinguish between processes occurring at the surface of the mesoporous films from processes within the actual mesoporous environment, due to intrinsic features of optical waveguide spectroscopy.

The best results for optical waveguide application are achieved with colloidal assemblies of nanocolloids, these materials were therefore chosen for further studies.

The material was made by *ab-initio* synthesis of nanoparticles through wet chemical synthesis. This procedure is based on colloidal chemistry, involving a sol–gel precipitation process, and provides the ability to control particle size with high monodispersity.

8.1.2 Application

The waveguiding capability of the mesoporous titanium oxide waveguide films in the prism-coupling assembly is experimentally demonstrated by very sensitive *in-situ* measurement of adsorption processes of ruthenium-based metal-organic dye ('N719') molecules on the inner surfaces of the mesoporous titania films.

Furthermore, the concept is applied to *in-situ* monitoring of diffusion kinetics of N719 dye within the confined pore geometry. It is found that diffusion is significantly slowed down in

the regime of mesopores to diffusion coefficients, as low as $10^{-11} cm^2\, s^{-1}$ and$10^{-13} cm^2\, s^{-1}$, respectively.

Diffusion kinetic studies were carried out in order to detect mass transport processes within the mesoporous titania waveguide film, thus to yield information about the sensitisation process, which is crucial for dye sensitised solar cell (DSSC) efficiency, in order to allow optimisation and accordingly higher induced photon to current efficiencies (IPCE). Therefore, the distinguishability between changes in refractive index changes, Δn, from extinction coefficient changes, Δk, within the mesoporous structured waveguide films is exploited for discrimination of surface-adsorbed dye molecules from solubilised dye molecules in the pore volume. The highly confined electromagnetic field of the resonance feature (guided mode) and its intrinsically defined intensity profile allow spatially resolved refractive index determination, thus quantification of concentration gradients with a resolution below the diffraction limit.

In the nest step, for the purpose of DSSC research and development in particular, the mesoporous waveguide system is integrated with holographic grating coupling technology, hence allowing optical waveguide spectroscopy measurements on operating DSSCs and also reduces the complexity and the required equipment for the handling of the device to a great extend.

8.2 Conclusion

The present study laid a foundation for exploiting high-performance optical sensors by using mesoporous titanium-oxide thin films. Grating coupled optical waveguide spectroscopy (GOWS) with the perspective for miniaturisation offers the mesoporous slab waveguide a potential application in the fields of integrated optical sensors for process control in future DSSC production.

8.3 Outlook

Further development of the sensing scheme is suggested in order to improve the ability of mesoporous optical waveguides to be used in automatised processes, therefore the implementation of so-called m-line spectroscopy in combination with charge-coupled device (CCD) for dynamic signal read-out is recommended. With this special technique, excitation of multiple modes is possible without angular displacement, thus without moving parts in the equipment. This can be realised by presenting a broad angular spectrum for mode

excitation by focusing the impinging laser light on the coupling device, hence, depending on the focal distance of the applied lens, an angular spectrum is added to the geometrically produced angle of incidence $\theta_i = \theta_m \pm \triangle\theta$ (see figure 8.1). As a consequence, the m-line configuration does not require moving/rotating parts for angular interrogation.

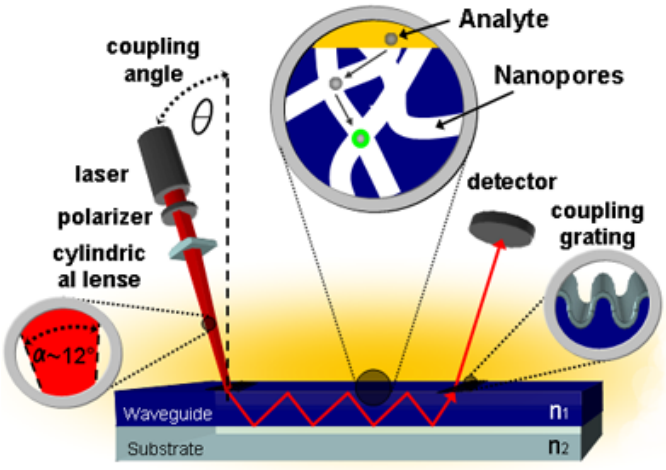

Figure 8.1: Schematic illustration of the proposed experimental setup for grating coupled m-line spectroscopy.

The guided light is detected at mode coupling angles as a very sharp peak in intensity, additionally the reflected beam (not shown in the sketch in figure 8.1), carrying the same angular spectrum as the impinging beam (and therefore also the angular intensity spectrum) can be detected by the CCD. The angular reflectance spectrum is analysed regarding its intensity distribution on the array. The method can be further extended in order to image surfaces with respect to their coupling conditions, i.e. producing two-dimensional maps of refractive index and/or thickness distribution(s) of the scanned area. Alternatively, the intensity along the path of guided light can be monitored *via* CCD for the purpose of e.g. fluorescence excitation through a range of micro arrays.

In order to explicitly investigate the changes and interactions of diffused dye molecules with and at the titania surface in more detail, it is strongly suggested to additionally apply an IR-light source to the OWS method. The wavelength spectrum in the IR-range is sensitive to chemical interactions (at the titania surface) which are related to the photo-catalytic processes during dye sensitisation and also during DSSC operation.

List of Figures

List of Tables